

TRANSPARENCY AND STABILITY PERFORMANCE IMPROVEMENT IN
HAPTIC DEVICES

A THESIS SUBMITTED TO
THE GRADUATE SCHOOL OF NATURAL AND APPLIED SCIENCES
OF
MIDDLE EAST TECHNICAL UNIVERSITY

BY

ÖZGÜR BAŞER

IN PARTIAL FULFILLMENT OF THE REQUIREMENTS
FOR
THE DEGREE OF DOCTOR OF PHILOSOPHY
IN
MECHANICAL ENGINEERING

DECEMBER 2012

Approval of the thesis:

**TRANSPARENCY AND STABILITY PERFORMANCE IMPROVEMENT
IN HAPTIC DEVICES**

submitted by **ÖZGÜR BAŞER** in partial fulfillment of the requirements for the
degree of **Doctor of Philosophy in Mechanical Engineering Department,**
Middle East Technical University by,

Prof. Dr. Canan Özgen
Dean, Graduate School of **Natural and Applied Sciences**

Prof. Dr. Süha Oral
Head of Department, **Mechanical Engineering**

Assoc. Prof. Dr. Erhan İlhan Konukseven
Supervisor, **Mechanical Engineering Dept., METU**

Examining Committee Members:

Prof. Dr. M. Kemal Özgören
Mechanical Engineering Dept., METU

Assoc. Prof. Dr. Erhan İlhan Konukseven
Mechanical Engineering Dept., METU

Prof. Dr. Tuna Balkan
Mechanical Engineering Dept., METU

Asst. Prof. Dr. Senih Gürses
Engineering Science Dept., METU

Asst. Prof. Dr. Kutluk Bilge Arıkan
Mechatronics Engineering Dept., Atılım University

Date:

I hereby declare that all information in this document has been obtained and presented in accordance with academic rules and ethical conduct. I also declare that, as required by these rules and conduct, I have fully cited and referenced all material and results that are not original to this work.

Name, Last name : Özgür BAŞER

Signature :

ABSTRACT

TRANSPARENCY AND STABILITY PERFORMANCE IMPROVEMENT IN HAPTIC DEVICES

BAŞER, Özgür

PhD, Department of Mechanical Engineering

Supervisor: Assoc. Prof. Dr. E. İlhan KONUKSEVEN

December 2012, 214 pages

Haptic devices are evaluated in terms of transparency, stability, pose and force control accuracy. Precise velocity and acceleration estimations are needed in haptic devices for accurate simulations. This thesis firstly focuses on velocity and acceleration estimations from incremental encoders and proposes two new estimation techniques. The second goal in the thesis is transparency improvement. The transparency is a metric that shows how well a virtual model is reflected to the user. Conventional force control algorithms are not sufficient for high transparency. Therefore, as alternative, a motor current based torque feedback compensator is developed. The transparency improvement efforts by using only active actuator adversely affect stability in haptic devices. In order to improve both stability and transparency, a new hybrid control algorithm is developed by employing active actuator and passive brake. Pose and force control accuracy are mostly problematic in multi-DOF haptic manipulators. Since the deviation of any kinematic parameter in Jacobian matrix adversely affects the accuracy of pose and force control, kinematic calibration is indispensable for haptic manipulators.

Besides, most of the haptic manipulators use capstan drive mechanisms in the joints due to their advantages; but cause transmission errors. Therefore, a theory is developed for the capstan drive transmission errors. Then, a closed-chain kinematic calibration technique including transmission errors is introduced for a 7 DOF haptic device. Adjustable posture ability of redundant haptic manipulators can be used for performance improvements. Finally, an optimal posture control algorithm is developed to improve the stability of the 7-DOF haptic device.

Keywords: Transparency, Stability, Pose accuracy, Force control accuracy, Velocity and acceleration estimation, Optimal posture control

ÖZ

HAPTİK CİHAZLARDA ŞEFFAFLIK VE KARARLILIK PERFORMANSININ İYİLEŞTİRİLMESİ

BAŞER, Özgür

Doktora, Makina Mühendisliği Bölümü

Tez Yöneticisi : Doç. Dr. E. İlhan KONUKSEVEN

Aralık 2012, 214 sayfa

Haptik cihazlar şeffaflık, kararlılık, konum doğruluğu ve kuvvet kontrolü doğruluğu açısından değerlendirilmektedirler. Haptik cihazlarda doğru benzetimler için hassas hız ve ivme kestirimlerine ihtiyaç vardır. Bu tez ilk olarak, hız ve ivme kestirimlerine odaklanmaktadır ve iki yeni kestirim tekniği önermektedir. Tezdeki ikinci hedef ise şeffaflık iyileştirmesidir. Şeffaflık bir sanal modelin kullanıcıya ne kadar iyi yansıtıldığını gösteren bir ölçüttür. Klasik kuvvet kontrol algoritmaları yüksek şeffaflık için yeterli değildir. Bu nedenle, alternatif olarak, motor akımı tabanlı tork geri beslemeli bir dengeleyici geliştirilmiştir. Haptik cihazlarda, sadece aktif motorları kullanarak şeffaflığı iyileştirme çabaları kararlılığı tersine etkilemektedir. Şeffaflık ve kararlılığı birlikte iyileştirmek için de, aktif motor ve pasif freni birlikte kullanarak yeni bir karma kontrol algoritması geliştirilmiştir. Çok serbestlik dereceli haptik cihazlarda konum ve kuvvet kontrolü doğruluğu çoğunlukla problemlidir. Jacobian matrisi içindeki herhangi bir kinematik parametrenin değişimi, konum ve kuvvet kontrolü doğruluğunu olumsuz etkilediği için, haptik cihazlarda kinematik kalibrasyonun gerekliliği

kaçınılmazdır. Bununla birlikte, çoğu haptik manipölatör avantajlarından dolayı eklemlerde kablo kasnak mekanizmalarını kullanmaktadır, fakat bu mekanizmalar iletim hatalarına neden olmaktadır. Bu nedenle, kablo kasnak mekanizması iletim hataları için bir teori geliştirilmiştir. Daha sonra, 7 serbestlik dereceli bir haptik cihaz için bu iletim hatalarını içeren kapalı zincir bir kinematik kalibrasyon tekniği ileri sürülmüştür. Fazlalık eklem içeren haptik manipölatörlerin ayarlanabilir duruş kabiliyeti performans iyileştirmeleri için kullanılabilir. Son olarak, 7 serbestlik dereceli haptik cihazın kararlılığını iyileştirmek için bir optimal duruş kontrol algoritması geliştirilmiştir.

Anahtar Sözcükler: Şeffaflık, Kararlılık, Konum doğruluğu, Kuvvet kontrolü doğruluğu, Hız ve ivme kestirimi, Optimal duruş kontrolü

ACKNOWLEDGMENTS

My special thanks go to my thesis supervisor Assoc. Prof. Dr. Erhan İlhan Konukseven, who was always the driving force and motivation for me. His trust and confidence from the very beginning gave me the opportunity of choosing this challenging research field.

I owe special thanks to Prof. Dr. Hakan Gürocak from School of Engineering and Computer Science, Washington State University for giving me an opportunity to work as a visiting scholar at WSU Robotics and Automation Laboratory.

I would like thank to my thesis monitoring jury members, Prof. Dr. Tuna Balkan and Asst. Prof. Dr. Senih Gürses for their guidance throughout the work.

I also thank to Asst. Prof. Dr. Melik Dölen and Dr. Ergin Kılıç for their friendly collaboration and Dr. Gökhan Bayar for encouraging me.

Finally, I am deeply grateful to my dear family, Alp Başer, Esra Teltik Başer, Kamil Başer and Evin Başer, for supporting me and for showing me their love throughout my PhD education.

TABLE OF CONTENTS

ABSTRACT.....	iv
ÖZ.....	vi
ACKNOWLEDGMENTS.....	viii
TABLE OF CONTENTS.....	ix
LIST OF TABLES.....	xiii
LIST OF FIGURES.....	xiv
LIST OF SYMBOLS.....	xx
LIST OF ABBREVIATIONS.....	xxvii
CHAPTERS	
1 INTRODUCTION.....	1
1.1 Motivation.....	1
1.2 Objectives of the Thesis.....	7
1.3 Contributions of the Thesis.....	8
1.4 Outline of the Thesis.....	10
2. VELOCITY AND ACCELERATION ESTIMATION.....	12
2.1 Introduction.....	12
2.2 Contribution	15
2.3 Overview of Conventional Estimation Methods.....	16
2.3.1 Fixed Position Method.....	16

2.3.2	Fixed Time Method.....	16
2.3.2.1	Fixed Filters.....	17
2.3.2.2	Kalman Filters.....	17
2.3.2.3	Modified State Observers.....	20
2.4	Enhanced Adaptive Windowing Method.....	20
2.5	Hybrid Method.....	25
2.6	Experimental Hardware.....	28
2.7	Simulation and Experimental Results.....	29
2.8	Conclusion.....	32
3.	TRANSPARENCY IMPROVEMENT.....	33
3.1	Introduction.....	33
3.2	Contribution.....	35
3.3	Conventional Force Control Architectures.....	35
3.4	Proposed Motor Current Based Torque Feedback Compensator....	40
3.5	System Parameter Identification of Experimental Hardware.....	42
3.6	Experimental Results.....	45
3.6.1	A Novel Transparency Metric for Haptic Devices.....	50
3.7	Application of the Algorithm to Multi-DOF Devices.....	53
3.8	Conclusion.....	61
4.	STABILITY IMPROVEMENT WITH HIGH TRANSPARENCY.....	63
4.1	Introduction.....	63
4.2	Contribution.....	70
4.3	Relation between Transparency and Stability in Haptic Devices....	71

4.4	Passive Brakes.....	76
4.5	Modified Passivity Condition and Proposed Hybrid Control Algorithm.....	77
4.5.1	Task Divider (α) and Smooth Transition Width (δ) Parameters	83
4.5.2	Artificial Neural Network Learning of Parameters for Every Impedance.....	87
4.6	Experimental Results.....	89
4.7	Implementation of Hybrid Algorithm by Using MR-Brake.....	95
4.8	Conclusion.....	100
5.	POSE AND FORCE CONTROL ACCURACY IMPROVEMENT IN MULTI-DOF CAPSTAN DRIVEN HAPTIC DEVICES.....	101
5.1	Introduction.....	101
5.2	Contribution	104
5.3	Error Sources in a 7-DOF Capstan Driven Haptic Device	105
5.3.1	Theoretical Analysis of Capstan Drive Transmission Error	106
5.3.2	Experimental Verification of Capstan Drive Transmission Error.....	113
5.3.3	Parallelogram Mechanism Transmission Error.....	125
5.4	Kinematic Modeling and Proposed Calibration Procedure	126
5.5	Kinematic Parameter Identification.....	131
5.6	Simulation of Proposed Calibration Method.....	132
5.7	Experimental Results.....	136
5.7.1	Pose Accuracy Improvement.....	139
5.7.2	Force Control Accuracy Improvement.....	141
5.8	Conclusion.....	143

6. OPTIMAL POSTURE CONTROL ALGORITHM TO IMPROVE THE STABILITY OF REDUNDANT HAPTIC DEVICES.....	145
6.1 Introduction.....	145
6.2 Contribution.....	146
6.3 Experimental Hardware	147
6.4 Optimal Posture Control Algorithm.....	148
6.5 Implementation of the Proposed Algorithm.....	153
6.5.1 Redundant Joint Maps.....	154
6.5.2 Gradually Posture Adjustment.....	156
6.6 Experimental Result.....	157
6.7 Conclusion.....	159
7. CONCLUSION AND RECOMMENDATIONS.....	160
REFERENCES.....	167
APPENDICES	184
A. HAPTIC BOX EXPERIMENTAL COMPONENTS.....	184
B. HYBRID HAPTIC DEVICE EXPERIMENTAL COMPONENTS...	189
C. 7-DOF HAPTIC DEVICE EXPERIMENTAL COMPONENTS.....	195
D. MATLAB SIMULIK FILES USED IN THE EXPERIMENTS.....	204
E. MATLAB M-FILES USED IN THE EXPERIMENTS.....	209
VITA.....	211

LIST OF TABLES

TABLES

Table 2.1	Normalized RMS of error for velocity and acceleration.....	32
Table 3.1	Average apparent inertia ($I_{app} = \text{RMS}(\text{Torque})/\text{RMS}(\text{Acc.}) - \text{gm}^2$) ...	50
Table 3.2	Apparent inertia for virtual wall experiment ($I_{app} - \text{gm}^2$).....	51
Table 5.1	D-H parameters of 7-DOF haptic device	129
Table 5.2	Simulation results for the identification of the capstan drive and parallelogram parameters	133
Table 5.3	Simulation results for the identification of the kinematic parameters	134
Table 5.4	Identification results for capstan drive and parallelogram parameters	137
Table 5.5	Identification results for kinematic parameters	138

LIST OF FIGURES

FIGURES

Figure 1.1	Surgical assistant with haptic device.....	2
Figure 1.2	Surgical Training with Haptic Device.....	2
Figure 1.3	Master-slave application	3
Figure 1.4	Computer aided industrial design application.....	4
Figure 1.5	Virtual sculpting and virtual painting application.....	4
Figure 1.6	Force feedback video game applications.....	5
Figure 1.7	Molecular docking application with haptic devices.....	6
Figure 1.8	NanoWorkbench interface for nano-manipulation.....	6
Figure 2.1	Low-pass filter applied on noisy velocity or acceleration signal	17
Figure 2.2	Prediction and correction stages of the Kalman filter	18
Figure 2.3	Structure of modified state observer	20
Figure 2.4	Curve fitting of the quantized position signal	23
Figure 2.5	Flow charts of first-order (a) and second-order enhanced (b) adaptive windowing techniques	24
Figure 2.6	Modified first order adaptive windowing technique	25
Figure 2.7	Flow chart of the proposed hybrid method	27
Figure 2.8	HapticBox for experimental tests.....	28
Figure 2.9	Experimental results of estimation methods for velocity.....	30
Figure 2.10	Experimental results of estimation methods for acceleration	30
Figure 2.11	Error map of results of estimation methods for velocity.....	31
Figure 2.12	Error map of results of estimation methods for acceleration	31
Figure 3.1	Haptic-user interaction	36
Figure 3.2	Open Loop Impedance Control (OLIC).....	37
Figure 3.3	Closed Loop Impedance Control (CLIC).....	37
Figure 3.4	Open Loop Impedance Control with model based compensator (OLIC with MBC).....	39
Figure 3.5	Closed Loop Impedance Control with model based compensator (CLIC with MBC)	40
Figure 3.6	Block diagram of Closed Loop Impedance Control with Motor Current Based Compensator (CLIC with MCBC) for a 1-DOF rotary haptic device	41

Figure 3.7	Measurements for parameter identification.....	44
Figure 3.8	Coulomb friction model (a) and proposed friction model (b)	45
Figure 3.9	Transparency performance measures for (a) free-motion, (b) virtual spring with $K=0.5$ Nm/rad, and (c) virtual damping with $B=0.1$ Nms/rad	47
Figure 3.10	Apparent inertia measure for virtual spring $K=0.5$ Nm/rad (a) OLIC, (b) OLIC with MBC, (c) CLIC, (d) CLIC with MBC, (e) CLIC with MCBC	48
Figure 3.11	Apparent inertia measure for virtual damping $B=0.1$ Nms/rad (a) OLIC, (b) OLIC with MBC, (c) CLIC, (d) CLIC with MBC, (e) CLIC with MCBC	49
Figure 3.12	Transparency measure for a virtual wall with the parameters of $K=20$ Nm/rad and $B=0.01$ Nms/rad (a) OLIC, (b) OLIC with MBC, (c) CLIC, (d) CLIC with MBC, (e) CLIC with MCBC	52
Figure 3.13	2-DOF serial planar elbow type haptic manipulator	53
Figure 3.14	Sample path applied to the 2-DOF haptic device (a), and force measurements at the handle (b, c)	55
Figure 3.15	Reconfigurable MATLAB®/Simulink model for the Force Control of 2-DOF serial planar elbow type haptic manipulator	57
Figure 3.16	MATLAB®/SimMechanics model of the 2-DOF serial planar elbow type haptic manipulator	57
Figure 3.17	Sample test scenario for 2-DOF haptic manipulator	58
Figure 3.18	Transparency performance measures of 2-DOF haptic manipulator for (a) free-motion, (b) single virtual stiffness with $K=100$ N/m, and (c) single virtual damping with $B=6$ Ns/m	59
Figure 3.19	Virtual-load transparency measure tests for various poses in the workspace	60
Figure 3.20	Transparency performance error measures of the CLIC with MCBC algorithm for (a) single virtual spring $K=100$ N/m, and (b) single virtual damping $B=6$ Ns/m in various poses	66
Figure 4.1	Typical Z-width for a 1-DOF rotational haptic interface	69
Figure 4.2	Simplified block diagram of haptic interaction	63
Figure 4.3	Experimental setup with a 1-DOF haptic device	72
Figure 4.4	Transparency measures for a virtual spring ($K=10$ Nm/rad) in frequency domain. (a) OLIC+MBC, (b) CLIC+MBC, (c) CLIC+MCBC	74
Figure 4.5	Z-width plot of transparency improvement algorithms	75
Figure 4.6	Schematic views of typical magnetic particle brake (a) and MR brake (b)	77
Figure 4.7	Overall configuration of a 1-DOF rotational haptic interface	78

Figure 4.8	Hybrid control algorithm using active actuator and passive brake for a 1-DOF rotational haptic device	83
Figure 4.9	Sample unstable virtual wall collision (a) position, (b) motor power signal, (c) high-pass filter output of motor power signal	84
Figure 4.10	Step response of the particle brake (a) and the smooth transition model of dividing parameter (b).....	86
Figure 4.11	Sample virtual wall collision after assigning a dividing parameter (a) position, (b) instantaneous torque signal, (c) high-pass filter of torque signal.....	86
Figure 4.12	Dividing parameter (a) and smooth transition bandwidth (b) estimation algorithms	87
Figure 4.13	Feed-forward ANN structures for (a) dividing parameter and (b) smooth transition bandwidth	88
Figure 4.14	Training data and ANN results for (a) task divider, (b) smooth transition width.....	89
Figure 4.15	Transparency performance measures for a virtual spring with $K=10$ Nm/rad in frequency domain. (a) CLIC+TCBMC and (b) Hybrid algorithm	90
Figure 4.16	Transparency-Z-width plots for (a) OLIC+MBC, (b) CLIC+MBC, (c) CLIC + TCBMC, (d) Hybrid algorithm.....	91
Figure 4.17	Collision experiments on a stiff virtual wall with high impedances ($K=70$ Nm/rad and $B=0.1$ Nms/rad) for (a) OLIC+MBC, (b) CLIC+MBC, (c) CLIC with passive brake, (d) CLIC + TCBMC, (e) Hybrid algorithm.....	92
Figure 4.18	Collision experiments on a concave virtual surface with high impedances ($K=70$ Nm/rad and $B=0.1$ Nms/rad) for (a) OLIC+MBC, (b) CLIC+MBC, (c) CLIC + TCBMC, (d) Hybrid algorithm	93
Figure 4.19	Precision torque achievement of the proposed algorithm for a collision experiment on a stiff virtual wall with high impedances ($K=60$ Nm/rad and $B=0.1$ Nms/rad).....	94
Figure 4.20	MR-brake with serpentine flux path.....	96
Figure 4.21	Finite element analysis of the MR-brake	96
Figure 4.22	Hybrid control algorithm using MR-brake and active actuator	97
Figure 4.23	Z-Width plot comparison between the hybrid algorithm using MR-brake and CLIC with only active actuator	98
Figure 4.24	Transparency measures for (a) CLIC with MR-brake, (b) CLIC with active actuator, (c) Hybrid algorithm for $K=10$ Nm/rad and $B=0.1$ Nms/rad	98

Figure 4.25	Collision experiments on a stiff virtual wall (a) CLIC with MR-brake (b) CLIC with active actuator, (c) hybrid algorithm.....	99
Figure 5.1	7-DOF haptic device (a) and its kinematic model (b).....	105
Figure 5.2	Capstan drive mechanism.....	107
Figure 5.3	Schematic view of a capstan drive with slip angle zones and tensions.....	108
Figure 5.4	Free body diagram of a small cable segment on the drum.....	109
Figure 5.5	Exaggerated drawing of output drum eccentricity for a capstan drive.....	112
Figure 5.6	Experimental hardware for capstan drive transmission error validation.....	114
Figure 5.7	CMM measurement of drum eccentricity	115
Figure 5.8	Eccentricity for the input (a) and output (b) drums.....	115
Figure 5.9	Cyclic tensioning of the cable that revealed an AE value of 8.1×10^3 N.....	116
Figure 5.10	Slip error without load and theoretical verification	117
Figure 5.11	Slip errors measured for four different cases	119
Figure 5.12	Theoretical verification of the slip error under the effect of an external torque for case 2	120
Figure 5.13	Theoretical verification of the slip error under the effect of an external torque for cases 3 and 4	121
Figure 5.14	Verification of the analytical model for case 3 (a) and case 4 (b)...	123
Figure 5.15	Implementation of the linear cable encoder in the haptic device calibration setup (a: Overall setup; b: measurement unit connection to end-effector; c: linear cable encoder for the distance measurement).....	127
Figure 5.16	Kinematic model of 7-DOF haptic device for calibration.....	128
Figure 5.17	External encoder connections for capstan drive (a,b) and parallelogram (c,d)	130
Figure 5.18	Flowchart of the proposed calibration procedure.....	130
Figure 5.19	Parallelogram transmission errors	135
Figure 5.20	Simulation calibration results for the positions and orientation angles of 7-DOF haptic device.....	136
Figure 5.21	Identified model and measurements of transmission errors for (a) capstan-1 (b) capstan-2 (c) capstan-3 and (d) parallelogram	139
Figure 5.22	Distance measurement and calculations before and after calibration (a) and their errors (b)	140
Figure 5.23	Closed loop impedance control for multi-DOF haptic devices.....	141

Figure 5.24	Virtual wall experiment of 7-DOF haptic device.....	142
Figure 5.25	Force control accuracy of the device before (a) and after calibration (b)	143
Figure 6.1	7-DOF haptic device kinematic model at home posture (a) and various sample postures (b).....	148
Figure 6.2	Proposed optimal posture control algorithm	153
Figure 6.3	The designed virtual environment for the implementation of the proposed algorithm.....	154
Figure 6.4	Initial map of redundant joint angles for optimal postures	155
Figure 6.5	Schematic views for the reason of ridge on the redundant joint angle	155
Figure 6.6	Smoothed map of redundant joint angles for optimal postures.....	156
Figure 6.7	Spherical offsets for the proposed optimal posture control algorithm	157
Figure 6.8	Z-width plots of 7-DOF optimal posture and 6-DOF Phantom like posture for three different regions (a, b and c) of the virtual sphere	158
Figure A.1	Maxon RE40 DC Brushes Motor Specifications	184
Figure A.2	Scancon Encoder Specifications	185
Figure A.3	Copley 413CE Servo Amplifier	186
Figure A.4	HEDS 5540A Encoder	186
Figure A.5	Humansoft MF624 Multifunction I/O card for PCI bus	187
Figure A.6	W.M.Berg Sprocket Gear.....	188
Figure A.7	W.M.Berg Polyurethane/Steel Cable Chain.....	188
Figure B.1	Parker BE232FJ brushless DC motor.....	189
Figure B.2	AMC-DPRANIE-015A400 Brushless DC servo amplifier	190
Figure B.3	Parker 2000 ppr incremental encoder.....	190
Figure B.4	Quanser Q4 Series Multifunction I/O card for PCI bus	191
Figure B.5	Placid BE15 Particle Magnetic Brake	192
Figure B.6	W.M.Berg Sprocket Gear.....	193
Figure B.7	W.M.Berg Polyurethane/Steel Cable Chain.....	193
Figure B.8	Futek FSH01987 torque transducer with $\pm 10\text{Nm}$ range	194
Figure C.1	Maxon EC-max 40 Brushless DC Motor -120W	195
Figure C.2	Maxon EC-max 40 Brushless DC Motor – 70W	196
Figure C.3	Maxon EC-max 30 Brushless DC Motor – 60W	197
Figure C.4	Faulhaber 1524012SR Coreless DC Motor.....	198
Figure C.5	DES 50/5 4-Q-EC-Servoamplifier	199
Figure C.6	LSC 4-Q-DC-Servoamplifier	200
Figure C.7	SI-50-0.5 Nano 17 6-DOF Force/Torque Transducer	201

Figure C.8	Humansoft MF624 Multifunction I/O card for PCI bus	202
Figure C.9	Maxon HEDS 5540 Encoder	203
Figure C.10	Faulhaber IE 512 Encoder	203
Figure D.1	MATLAB [®] /Simulink Model for OLIC	204
Figure D.2	MATLAB [®] /Simulink Model for OLIC+MBC	204
Figure D.3	MATLAB [®] /Simulink Model for CLIC	205
Figure D.4	MATLAB [®] /Simulink Model for CLIC+MBC	205
Figure D.5	MATLAB [®] /Simulink Model for CLIC+MCBC	205
Figure D.6	MATLAB [®] /Simulink Model for Hybrid Algorithm	206
Figure D.7	MATLAB [®] /Simulink Model inside Virtual Environment Block ...	206
Figure D.8	MATLAB [®] /Simulink Model inside Haptic Device Block	206
Figure D.9	MATLAB [®] /Simulink Model of EAW for Velocity and Acceleration Estimation	207
Figure D.10	MATLAB [®] /Simulink Model inside Device Parameters Block	207
Figure D.11	MATLAB [®] /Simulink Model for Optimal Posture Control of 7-DOF Haptic Device	208

LIST OF SYMBOLS

Q_{vp}	Resolution of fixed position based velocity
Q_{ap}	Resolution of fixed position based acceleration
f	Clock frequency in fixed position method
c	Number of clock count in fixed position method
N	Encoder pulse per revolution
Q_{vt}	Resolution of fixed time based velocity
Q_{at}	Resolution of fixed time based acceleration
T	Sampling time
K	Kalman filter gain of velocity/acceleration estimation
X	State matrix of Kalman filter
\hat{X}	Estimated state matrix of Kalman filter
K	Kalman gain matrix
Φ	State transition matrix of Kalman filter
Ψ	State input matrix of Kalman filter
Y	Measurement matrix of Kalman filter
P	Estimated variance matrix of Kalman filter
R	Variance matrix of the measurement noise
Q	Variance matrix of the system noise
H	Measured values matrix
x	Position measurement
\hat{v}	Last velocity estimate
\hat{a}	Last acceleration estimate
n	Window size of the windowing technique

k	Last sampling number
b_i	Constants of first order adaptive windowing technique
c_i	Constants of second order enhanced adaptive windowing technique
E	Error between the position estimation and position measurement
d	Maximum quantization error of the encoder
Z_M	Transmitted impedance
Z_D	Desired environment impedance
F	Force applied human user hand
F_h	Resultant user hand force
F_d	Force applied by the haptic device
F_c	Force applied by the compensator
F_{int}	Interaction force sensed in the transducer
F_{hdyn}	Force resulting from user arm dynamics
F_{ddyn}	Force resulting from device dynamics
X_h	Displacement of the user hand
X_d	Displacement of the haptic device
\dot{x}_h	Human hand velocity
\dot{x}_d	Haptic device velocity
Z_v	Virtual environment impedance
Z_d	Haptic device impedance
Z_h	Human hand impedance
\tilde{Z}_d	Estimated haptic device impedance
K_p	Controller gain of the closed loop impedance control algorithm
K_c	Compensator controller gain
$\dot{\theta}_h$	Angular velocity of the user hand
$\ddot{\theta}_h$	Angular acceleration of the user hand
$\dot{\theta}_d$	Angular velocity of the haptic device
τ_d	Desired torque command

τ_c	Compensator torque command
τ_m	Actuator torque
τ_h	Torque applied by humand hand
v_a	Motor voltage
i_m	Motor current
R_m	Motor resistance
L	Motor inductance
K_{emf}	Motor back EMF constant
K_m	Motor torque constant
τ_o	Dynamic effect of output drum
τ_i	Dynamic effect of input motor drum
τ_p	Parasitic torque
r_o	Output drum radius
r_i	Input drum radius
T_c	Coulomb friction torque
b	Viscous friction coefficient
I	Inertia
θ	Angular position
$\dot{\theta}$	Angular velocity
$\ddot{\theta}$	Angular acceleration
K	Virtual Stiffness
B	Virtual damping
$\dot{\theta}$	Crash velocity between the handle and virtual wall
θ_m	Maximum indentation on virtual wall
I_{app}	Apparent inertia
m	Link mass
L	Link length
r	Link Distance between the center of gravity and joint

τ	Dynamic torque matrix of a robot manipulator
M	Inertial matrix
C	Coriolis and centrifugal matrix
G	Gravitational vector
Y	Regressor matrix
ϕ	Device dynamic parameters matrix
δ	End-effector excitation distance
α	Task divider paramter
δ	Smooth transition width
P_{HPF}	Power measurement
T	Torque measurement
T_{db}	Desired brake torque
T_{dm}	Desired motor torque
T_d	Desired actuator torque
$\dot{\theta}_e$	Transmitted velocity to virtual environment
T_h	Torque applied by user hand
T_a	Hold actuator torque by DAC
T_e	Reference torque calculated in virtual environment,
V_h	User hand velocity
E_0	Initial energy of haptic system
G_T	Transparency transfer function
F_D	Desired force
F_M	Measured force
V_D	Desired velocity
V_M	Measured velocity
ϕ_{VF}	Cross power spectral density between motion input and force output
ϕ_{VV}	Power spectral density of motion inputs
AE	Stiffness/length of cable

D	Distance between the two drums
dF	Differential tension
dL	Differential length
dN	Differential normal force
$d\theta$	Differential angle
$d\delta$	Differential elongation of cable
e	Overall slip error
e_e	Slip error due to eccentricity
e_{e_i}	Slip error of input drum due to eccentricity
e_{e_o}	Slip error of output drum due to eccentricity
e_l	Slip error due to the applied load
F	Cable tension
F_{load}	Tension due to applied load
$F_{preload}$	Cable preload tension
ΔF	Additional tension
L	Original free length of cable used for tensile test measurement
L_{free}	Free length of cable not in contact with either drum
ΔL	Length deflection
R_{input}	Input drum radius
R_{output}	Output drum radius
r_i	Radius of the input drum eccentricity
r_o	Radius of the output drum eccentricity
δ	Cable elongation on the drum
ε	Cable strain
μ	Coefficient of friction between the cable and drum
θ_{slip}	Deformation region in the loaded cable on the drum
θ_{slip1}	Angle of the cable in slip region 1
θ_{slip2}	Angle of the cable in slip region 2

$\theta_{no-slip}$	Region without any deformation or slip
θ_{wrap}	Total angle of cable wrapped around drum
β_i	Phase angle of the input drum
β_o	Phase angle of the output drum
θ_i	Rotation angle of the input drum
θ_o	Rotation angle of the output drum
α_i	Eccentricity angle of the input drum
α_o	Eccentricity angle of the output drum
α_{ii}	Initial eccentricity angle of the input drum
α_{oi}	Initial eccentricity angle of output drum
a_i	Link lengths
d_i	Link offsets
n	Measurement number
\underline{C}	Orientation matrix
D	Distance between the drums
L_i	Link lengths of parallelogram
\underline{P}	Position matrix
R	Capstan drive transmission ratio
R_d	Cable encoder drum radius
R_e	Deviation in the transmission ratio
$R(x_i, \alpha_i)$	4x4 rotation matrices around x axis
$R(y_i, \beta_i)$	4x4 rotation matrices around y axis
$R(z_i, \theta_i)$	4x4 rotation matrices around z axis
e_c	Error after calibration
e_{nc}	Error before calibration
$T(a_i, 0, d_i)$	4x4 transformation matrix throughout x and z axes
α_i	Twist angles
δ	Norm of the position matrix

δ_{ic}	Computed distance
δ_{im}	Measured distance
Δa_i	Deviation in link lengths
Δd_i	Deviation in link offsets
ΔL_i	Deviations in parallelogram links
$\Delta \alpha_i$	Deviations in twist angles
$\Delta \theta_{caps}$	Transmission error of capstan drive
$\Delta \theta_i$	Joint variable offsets
$\Delta \theta_{i-ecc}$	Error due to input drum eccentricity
$\Delta \theta_{o-ecc}$	Error due to output drum eccentricity
$\Delta \theta_{offset}$	Error due to joint offset
$\Delta \theta_{ratio}$	Error due to ratio inaccuracy
η_i	Input vector of joint variables
θ_a	Actuated angle of the parallelogram
λ_a	Actual value of the i^{th} parameter
λ_n	Nominal value of the i^{th} parameter
λ_o	Estimated value of the i^{th} parameter
σ_e	Maximum quantization error
σ_m	Accuracy of the measurement system
φ	Parameter vector to be identified
J	Jacobian Matrix
T_{dc}	Desired torque of critical elbow joint
F_d	Desired force
θ_R	Redundant joint angle
θ_U	redundant joint angle upper limi
θ_L	redundant joint angle upper limi

LIST OF ABBREVIATIONS

FOAW	First order Adaptive Windowing
EAW	Enhanced Adaptive Windowing
MAW	Modified Adaptive Windowing
HM	Hybrid Method
FP	Fixed Position
FT	Fixed Time
RMS	Root Mean Square
LMS	Least Mean Square
LPF	Low Pass Filter
KKF	Kinematic Kalman Filter
FPGA	Field Programmable Gate Array
KF	Kalman Filter
MSO	Modified State Observer
DF	Differentiation + Filtering
DOF	Degrees of Freedom
AUI	Active User Interaction
PUI	Passive User Interaction
AC	Admittance Control
IC	Impedance Control
OLIC	Open Loop Impedance Control

CLIC	Closed Loop Impedance Control
MBC	Model Based Compensator
MCBC	Motor Current Based Compensator
AIS	Analog Input Shaper
AOL	Analog Output Limiter
PO/PC	Passivity Observer/Passivity Controller
EAB	Energy Bounding Algorithm
FBA	Force Bounding Algorithm
PSPM	Passive Set-Position modulation
MR	Magneto-Rheological
HPF	High Pass Filter
ANN	Artificial Neural Network
CMM	Computer Measuring Machine

CHAPTER 1

INTRODUCTION

1.1 Motivation

Haptic technology is a tactile feedback technology which takes advantage of the sense of touch by applying forces to the user. This mechanical stimulation can be used to in the sense of virtual objects in a computer simulation and the remote control of machines and devices.

Haptic devices produce force and/or torque feedback to users for the simulation of virtual or remote environments. They sense motion and force/torque at the end-effector and provide feeling of touch to the user based on the virtual or remote environment. An environment containing physical elements such as spring, damping and mass can be simulated through the force/torque feedback capability of haptic devices. Wide range of haptic applications is available in present day for the fields of engineering, medical, teleoperation and entertainment. New application fields are reproduced and the scope of haptic applications looks like to grow further with the new high performance haptic devices.

First significant haptic applications where haptic devices are employed are medical implementations. Most of surgical operations are carried out worldwide by using specially designed robotic equipments. These robotic equipments including haptic devices enable fine control on precise movements and more accurate detection for a surgical operation [1].

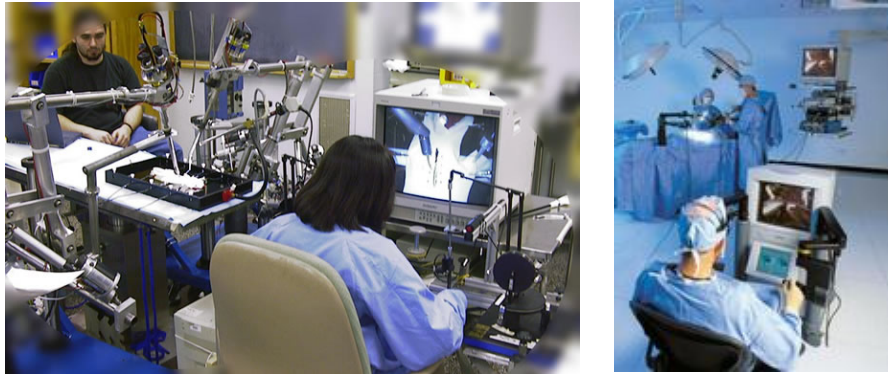


Figure 1.1 Surgical assistant with haptic device

Haptic technology has great potential in medical training, which includes the teaching of spatial and functional anatomy and the experience of surgical procedures such as penetrating, cutting and probing. Using a virtual reality training environment reduces the need for cadaver-based training and the use of live patients in clinical training [1].



Figure 1.2 Surgical Training with Haptic Device

Haptic devices are also used for remote control of robots (teleoperation applications) [2]. These types of applications are adapted for telesurgery, remote control of industrial robots, remote control of aircraft tools in aerospace engineering etc. In a teleoperated manipulation system, the user needs not only a visual feedback but also a haptic feedback of a system existing in a remote

environment. Typically, a teleoperation system comprises a master robotic device (haptic device) detecting the user's movements/forces and a slave robot trying to mimic the motions of the master.

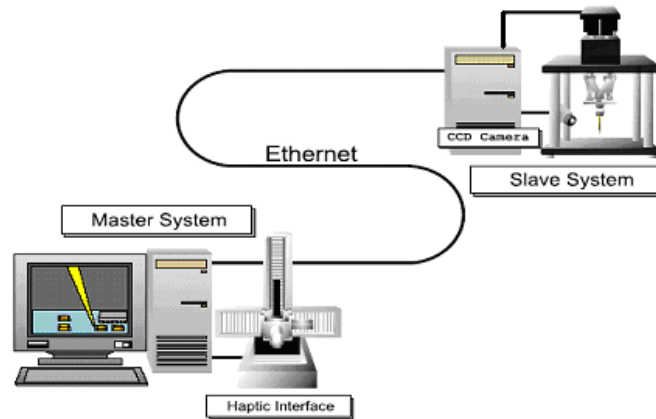


Figure 1.3 Master-slave application

The communication between master system and slave system is performed by an internet connection. In this way, haptic simulations have great potential not only in virtual reality, but also for augmenting user interfaces in actual telerobotic systems.

In the field of CAD/CAM (Computer Aided Design / Computer Aided Design), haptic technology has become a significant issue for combining physical and digital modeling [3]. Using haptic devices in 3D CAD modeling, a user can import solid models directly from design packages, then convert specific regions to clay and rapidly add complex shapes manually. Also, the CAD models can be assembled in the virtual environment by the help of haptic devices for checking before manufacturing. Then, the designed complex models can be used for rapid prototyping or CAM.



Figure 1.4 Computer aided industrial design application

Another interesting application is the field of art where haptic devices are employed as art tools (Virtual sculpting and virtual painting etc.) [4, 5]. The virtual clay is used in a virtual sculpting operation and it is deformed by the virtual tool. The deformable virtual clay is modeled as a real object. Thus, the user can shape it with the feeling realistic touch. Virtual painting is similar to the virtual sculpting and haptic handles are used as the art tool in these applications.

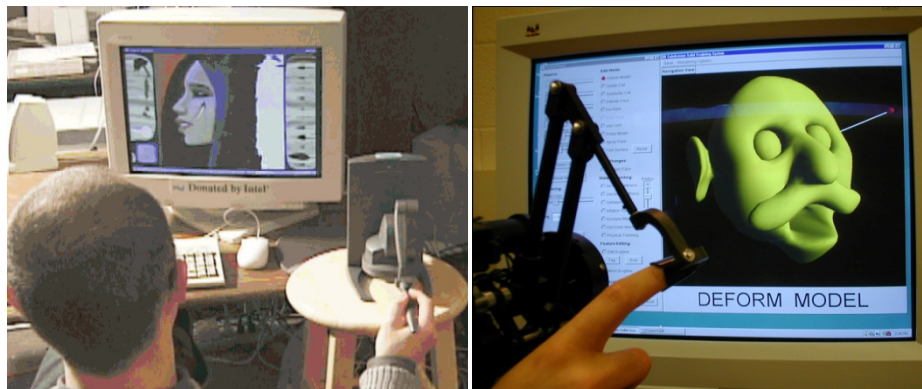


Figure 1.5 Virtual sculpting and virtual painting application

Force feedback technology is commonly used in video games. Simple haptic devices are in the form of game controllers, joysticks, and steering wheels for

these applications. Many newer generation console controllers and joysticks are built in the feedback devices. The first consumer 3D touch device with three-dimensional force feedback, Novint Falcon, allowed the haptic simulation of objects, textures, recoil, momentum, and the physical presence of objects in the video games [6].

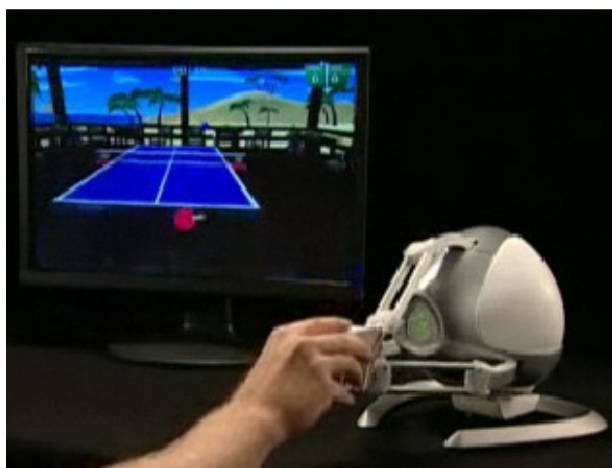


Figure 1.6 Force feedback video game applications

In recent years, besides using the visualization techniques, there has been increasing interest in using the haptic interface to facilitate the exploration and analysis of molecular docking and assembly. Molecular docking is defined as the process by which two molecules bind each other in an orientation and position determined by their geometric shape and local physicochemical properties. The geometric shapes of molecules define how well the binding surfaces complement each other while the physicochemical properties define how well the binding strength of the interaction energies holds molecules together. Hence, the goal in molecular docking studies is to determine whether two molecules interact and if so, the binding position and orientation of molecules such that the surface area of interaction is maximized while the interaction energy is minimized. Nowadays, it is possible to explore and manipulate molecular models in virtual environments with the use of haptic devices enabling force interactions [7].

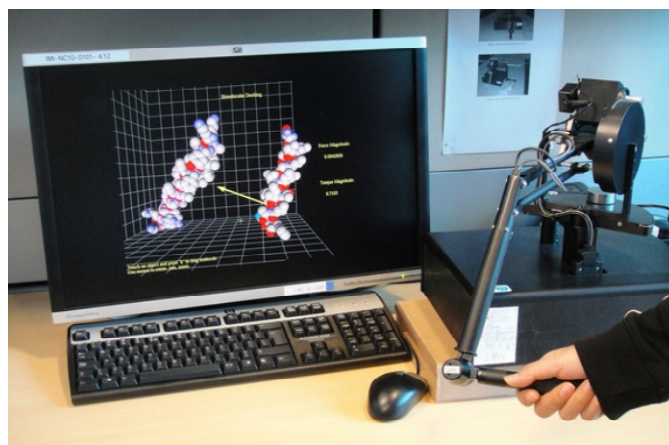


Figure 1.7 Molecular docking application with haptic devices

Another application field where haptic devices are used is the nano-manipulation. Grant et. al. designed the first NanoWorkbench interface for nano-manipulator [8]. The nano-manipulator application provided an intuitive interface to scanning-probe microscopes, enabling scientists from a variety of disciplines to examine and manipulate nanometer-scale structures. It displayed a 3D rendering of the data as it arrives in real time. Using haptic feedback controls, a scientist could feel the surface representation to enhance understanding of surface properties and to modify the surface directly. The nano-manipulator greatly increased productivity by acting as a translator between the scientist and the instrument being controlled.

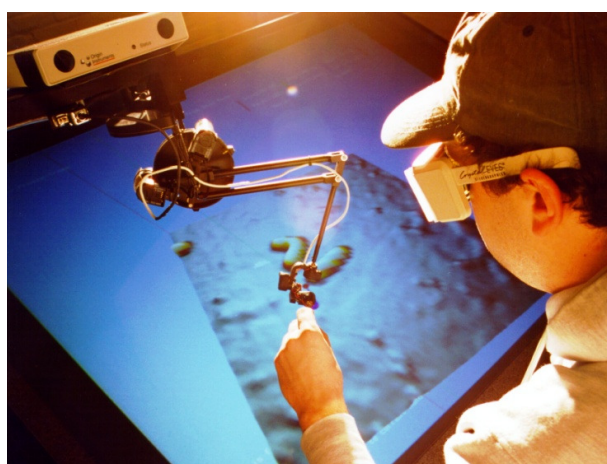


Figure 1.8 NanoWorkbench interface for nano-manipulation

In brief, haptic devices enable users to touch any virtual or remote environment. This facility of haptic devices created different applications in the field of industry, medical, education, art and entertainment. Furthermore, new applications will be explored over time. Therefore, the demand on high performance haptic devices increases more and more. This thesis is dedicated to the performance improvement of haptic devices.

1.2 Objectives of the Thesis

Since force/torque and tactile feedback facilities of haptic devices create new application fields, high performance requirement in haptic devices grows increasingly. First of all, precise velocity and acceleration estimations are necessary for accurate simulation of virtual model elements such as damping and mass. These estimations are also employed in model based compensators to reject the haptic device dynamics. Therefore, at the first step of the thesis, it is aimed to develop new estimation techniques. Usually, haptic devices are evaluated in terms of transparency and stability. The transparency is the most significant performance criteria for haptic devices and it is defined as the ratio between the transmitted impedance and desired impedance of the virtual environment. Ideally, this ratio should be unity. In order to improve the transparency, the dynamical effect of the device needs to be minimized. Conventionally, the model based compensators are employed for that purpose. However, this approach suffers from non-precise velocity/acceleration estimation and inaccurate system identification. Accordingly, at the second step of the thesis, it is aimed to develop a new compensation algorithm where the system model is not used. The transparency improvement efforts using only active actuators in haptic devices adversely affect the stability. On the other hand, it is well known that passive brakes provide high stability for haptic interactions. Therefore, it is aimed to develop a new hybrid algorithm using both active actuator and passive brake to improve stability without distorting transparency at the third step of the thesis. Multi-DOF capstan driven haptic manipulators suffer from pose accuracy and force control accuracy.

The Jacobian matrix including kinematic parameters is employed in pose calculations and force control algorithms in multi-DOF haptic manipulators. Besides, capstan drive mechanisms used in the haptic manipulators cause transmission errors in the joints. In order to improve the pose and force control accuracy of multi-DOF capstan driven haptic manipulators, it is aimed to develop a theoretical analysis for capstan drive transmission errors and an easy to implement kinematic calibration including capstan drive transmission errors at the fourth step of the thesis. Redundant haptic manipulators can reach any point in the workspace with different postures. The posture selection facility of redundant haptic manipulators can improve the haptic performance. In this context, the last objective of the thesis is to develop an optimal posture control algorithm to improve the stability of redundant haptic devices. In this thesis, the hybrid algorithm research to improve both stability and transparency is achieved with the opportunities of Robotics and Automation Laboratory in School of Engineering and Computer Science of Washington State University, Vancouver, WA, USA and all other researches are conducted in Mechatronics Laboratory in Mechanical Engineering Department of Middle East Technical University, Ankara, Turkey.

1.3 Contributions of the Thesis

This thesis aims to improve the performance criterions of haptic devices such as transparency, stability, pose accuracy and force control accuracy. In this scope, the following contributions have been made:

- Precise velocity and acceleration estimations are required in haptic devices to reflect virtual model elements accurately (such as spring, damping and mass). Usually, incremental encoders, which provide quantized position signal, are used in haptic devices. The quantization effect in the incremental encoders makes the precise velocity and acceleration estimation difficult with conventional methods. Therefore, two new methods, enhanced adaptive windowing and hybrid technique, were developed for precise estimation.

- The transparency is primary performance criteria for haptic devices and quantify that how well the remote or virtual environments are reflected to the user. It is defined as the ratio between the reflected impedance and environment impedance, and the ideal ratio is unity for a desired frequency bandwidth. Force feedback control algorithms and the model based compensators are frequently employed in haptic controllers to maximize the transparency. However, they are not sufficient for every frequency range. As alternative, a motor current based torque feedback compensator was developed and its superiority was shown experimentally on a 1-DOF HapticBox.
- The stability is another performance criterion in haptic devices. However, there is an inverse correlation between the transparency and stability when only active actuators are employed in haptic devices. An ideal haptic device should reflect wide range of virtual impedances stably and with high transparency. In order to improve both stability and transparency of haptic devices, a hybrid control algorithm was developed by employing active actuator and passive brake. The developed algorithm was tested on a 1-DOF hybrid haptic device and it can reflect higher range of virtual impedances stably and with high transparency than the conventional control algorithms.
- Pose and force control accuracy are critical for multi-DOF haptic manipulators for the accurate simulation of virtual environments. The controllers of multi-DOF haptic manipulators employ kinematic Jacobian matrix for pose calculation and force control algorithms. Since any deviation in the Jacobian elements affect the accuracy of pose calculation and force control, kinematic calibration is indispensable for haptic manipulators. Most of the haptic manipulators use capstan drive mechanisms for power transmission due to their advantages, but causes transmission errors in the joint space, which additionally affect the Jacobian matrix. A theory of the capstan drive transmission errors was developed and it was validated

experimentally on a 1-DOF capstan drive mechanism. Then, an easy to implement kinematic calibration technique including the capstan drive transmission errors was introduced for a 7-DOF haptic device. This calibration technique improves the pose and force control accuracy of the haptic manipulators significantly.

- Redundant haptic manipulators like 7-DOF haptic device can reach any point in the workspace with different postures. The different posture selection of redundant haptic manipulators can be used to improve the performances of haptic devices. Therefore, an optimal posture control algorithm was developed in this thesis to improve the stability of a 7-DOF haptic device. This algorithm significantly improves the stable impedance range of the redundant haptic devices.

1.4 Outline of the Thesis

In the first chapter, the brief information about the motivation, objectives, contributions and outline of the thesis are presented. The detailed presentation of each study can be found in following chapters. The next chapter is related to the velocity and acceleration estimation from incremental encoders, which has vital importance for realistic haptic simulations. Two new methods, enhanced adaptive windowing and hybrid technique, are developed. The detailed literature survey, mathematical derivations and results of the proposed estimation algorithms are presented in this chapter. Chapter 3 focused on the transparency improvement of haptic devices. In this chapter, firstly, a literature survey of the existing transparency improvement studies and an overview of conventional force control algorithms (open loop, closed loop, and model based impedance algorithms) are presented. Then, a new transparency improvement algorithm, motor current based torque feedback control algorithm, is introduced and the proposed algorithm is tested in MATLAB[®]/SimMechanics environment for a multi-DOF haptic manipulator. Chapter 4 is about the stability improvement without distorting the transparency. In this chapter, existing stability improvement studies and inverse

correlation between the stability and transparency are introduced, and the developed new hybrid control algorithm using both active actuator and passive brake are presented together with the experimental results conducted on 1-DOF hybrid haptic device. Chapter 5 presents a calibration study to improve the pose and force control accuracy of a multi-DOF capstan driven haptic device. In this chapter, firstly a theoretical analysis is developed for a 1-DOF capstan drive mechanism and this theory is validated by experiments. Then, an easy to implement calibration technique is developed. Finally, a set of experimental results are presented to show that how the proposed calibration technique improves the pose and force control accuracy of a 7-DOF capstan driven haptic device. In Chapter 6, an optimal posture control algorithm is developed to improve the stability of redundant haptic manipulators and the proposed algorithm is implemented on a 7-DOF haptic device. A general conclusion and recommendations about the researches carried out in this thesis is presented in Chapter 7. A list of reference about the literature survey and an appendix section about the equipments and MATLAB[®] models of the algorithms used in the thesis can be found after Chapter 7.

CHAPTER 2

VELOCITY AND ACCELERATION ESTIMATION

2.1 Introduction

Accurate estimations of velocity and acceleration are necessary for realistic haptic simulation of virtual elements [9], model-based disturbance compensation [10, 11] or robust motion control [12]. The position measurements of optical incremental encoders are employed in the estimations that suffer from the quantization effects introduced by these devices and their interfaces. The resolution of the encoders primarily relies on the design of grids on the encoder disc. The encoder design as well as the data acquisition/processing interface introduce quantization error to the position measurements. Since the direct calculation of velocity and acceleration using numerical differentiation from the quantized position is not sufficient, some signal processing and estimation techniques are needed.

There are different methods in the literature for estimating velocity and acceleration from the quantized position measurements. Low-pass filters are commonly used to reduce the noise of numerical differentiation of quantized position signals. In the effort of filtering this noisy signal, low-pass filters cause phase lag in the velocity estimation, which is not desirable for many applications. Some predictive numeric calculation methods can be applied on the quantized position signals in the estimations [13]. These methods enable selecting estimation precision and adjusting the time delay. The transition-rate logic

algorithm is another method to estimate velocity [14]. This technique addressed a major velocity estimation problem of reversal and sparse position measurements such that their intervals can never be known. Higher sampling frequency than the rate of the encoder pulses is needed in this technique. Dual-sampling rate observers and advanced Kalman filters, which require accurate dynamic system model to estimate velocity and acceleration, are proposed in the literature [15, 16]. The principle of these methods is to predict the state variables between the encoder pulses based on the dynamical model of the system and to correct the estimation error when the next encoder event is occurred. In addition, there are some other observers using nonlinear system models in the literature to estimate velocity [17-19]. Some sliding-mode observers are presented in [20, 21]. Model-based estimation methods are not preferred for haptic interfaces. The system model of haptic interfaces cannot be completely known since the human hand and haptic device are coupled in a haptic application. Modified state observers, which don't use the system model, can be employed for such applications [22]. Lastly, neural network [23, 24] and fuzzy logic [25] methods are also implemented for velocity estimation from the position information.

The velocity and acceleration calculation methods are classified into two groups in the literature: Fixed Position (FP) and Fixed Time (FT) methods [26]. In FT method, the number of encoder pulses is counted at a constant sampling time. In FP method, the time duration to travel the distance between the successive encoder slides is measured by an external high-frequency clock source.

Janabi-Sharifi et. al. [27] proposed a first-order adaptive windowing technique based on FT method to estimate velocity. This method is the best of FT methods and overcomes tradeoff problems among noise reduction, control delay, estimate accuracy, reliability, computational load, transient preservation. However, the first-order adaptive windowing technique does not provide acceleration estimation and needs to be enhanced for both velocity and acceleration estimation.

Field Programmable Gate Arrays (FPGAs) reducing the effect of time quantization by high frequency clock improve the performance of fixed-position method. Precise velocity estimation can be achieved by fixed-position technique using high frequency clock. Tanaka et. al. [28] used FPGA to estimate velocity and acceleration at relatively low frequencies. Velocity and acceleration estimation can be achieved precisely by FP technique using high-frequency clock source. However, it suffers from two problems. This technique results in low acceleration resolution at higher frequencies and causes an impulsive change in acceleration estimates whenever the sign of velocity changes. These problematic cases can be improved by adaptive windowing technique of FT method.

In this chapter, two improvements are achieved. Primarily, first-order adaptive windowing technique is enhanced to estimate both velocity and acceleration using quantized encoder position. This method is called as enhanced adaptive windowing technique and it is a kind of FT method which can be used without needing FPGAs. Secondly, a hybrid algorithm is developed to use advantages of FP and FT methods in a single technique for entire operation region. In this technique, first-order adaptive windowing is modified to compute acceleration from the velocity estimates obtained via a FP method (modified adaptive windowing technique) and enhanced adaptive windowing technique is used to eliminate impulsive change of acceleration on the region of the velocity sign changes. Consequently, in the hybrid algorithm, three approaches are utilized for precise velocity and acceleration estimation: (1) the FP method for velocity estimation, (2) the first-order extended adaptive windowing using FP based velocity for acceleration estimation and (3) second order enhanced adaptive windowing using encoder position to eliminate the problems encountered when the velocity sign changes. By integrating these approaches, this algorithm presents a hybrid estimation method for precise velocity and acceleration estimation where the transition between the methods is achieved by a parametric distribution.

The rest of this chapter is organized as follows: The contribution is explained in the following section. Next section presents an overview of the conventional

estimation methods. In the following sections, enhanced adaptive windowing technique and hybrid approach are introduced. Lastly, test results and discussions are presented to compare the performance of the methods. The last section is related to the conclusion part of the research.

2.2 Contribution

In the literature, fixed-time (FT) and fixed-position (FP) methods are used to estimate velocity and acceleration from the quantized position signal. One of the FT methods, adaptive windowing estimation method yields the best solution for velocity estimation; however, does not provide acceleration estimation. The first contribution of this chapter is the second order enhanced adaptive windowing method which was developed to estimate both velocity and acceleration in a single algorithm. The experimental results show that the enhanced method is superior over other FT methods. As a second contribution, a hybrid method was developed to use the advantages of FT and FP methods for different operating regions. Using FPGAs with high-frequency clock sources can reduce the effect of temporal quantization and improve the estimation performance of FP methods. However, it has low resolution for acceleration estimation especially at high frequencies and causes an impulsive change of acceleration estimation when the direction of motion dynamically changes. Adaptive windowing estimation method can solve these problematic cases of FP method. These two methods are rolled into a single technique by applying a parametric smooth transition in order to estimate velocity and acceleration for entire operating region. This chapter was adapted from our previously published papers titled with “A Hybrid Method to Estimate Velocity and Acceleration using Low-Resolution Optical Incremental Encoders” [29] and “An Enhanced Adaptive Windowing Technique for Velocity and Acceleration Estimation using Incremental Position Encoders” [30].

2.3 Overview of Conventional Estimation Methods

Basically, there are two classes of conventional methods to estimate velocity and acceleration from discrete position signal: (1) Fixed position (FP) and (2) Fixed time (FT) method. The summaries of the methods are presented below. Note that the model based estimation methods are not covered since they are not applicable for haptic interfaces.

2.3.1 Fixed Position Method

Dividing the distance between two successive encoder slides by the measured time between these slides using high-frequency clock gives the velocity data in FP method. The resolution of velocity and acceleration of FP method (Q_{vp} , Q_{ap}) is calculated by Eq.(2.1) which is formulated by Tanaka et. al [28].

$$Q_{vp} = \frac{2\pi f}{N} \frac{1}{c(c-1)}, \quad Q_{ap} = \frac{3c-1}{(c+1)} \frac{N}{2\pi} Q_{vp}^2 \quad (2.1)$$

f , c and N denote the clock frequency, the number of clock count, and the number of encoder pulse per revolution, respectively. Note that Eq.(2.1) should give smaller values for higher resolutions. Therefore, FP method is only effective at low frequencies, since the acceleration resolution of this method decreases when the velocity increases [28].

2.3.2 Fixed Time Method

Dividing the number of pulses by a constant sampling time gives the velocity data in FT method. The rate of change in velocity directly yields the acceleration. The resolution of velocity and acceleration of FT method (Q_{vt} , Q_{at}) can be calculated by Eq.(2.2) [28];

$$Q_{vt} = 2\pi/NT , \quad Q_{at} = Q_{vt}/T \quad (2.2)$$

N and T denote the number of encoder pulse per revolution and the sampling time, respectively. Since the calculations using FT method cause noisy estimates when the resolution is not sufficiently high, some filtering or estimation techniques are required to smooth velocity and acceleration.

2.3.2.1 Fixed Filters

Fixed low-pass filters are applied on the velocity and acceleration calculated using the first and second order numerical differences of a position signal to clean noisy components of the signal. However, they suffer from fundamental tradeoffs between time lag, phase distortion, attenuation, and cutoff precision. They should be tuned for each application and operating condition

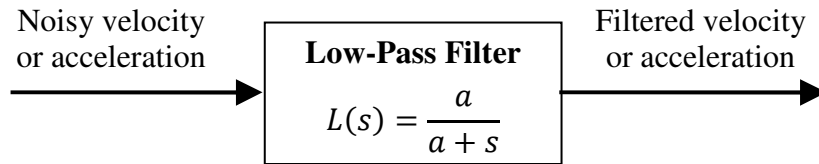


Figure 2.1 Low-pass filter applied on noisy velocity or acceleration signal

2.3.2.2 Kalman Filters

Kalman Filters can be used as model based estimators in which the model parameters and disturbances are known accurately; however, they are not applicable for haptic devices since the system model is not fully known. Therefore, constant velocity and constant acceleration models can be employed in Kalman filters, which do not require system information. These methods, which use kinematic models, are also called kinematic Kalman filters (KKF) [31].

Kinematic Kalman filter estimates a state variable according to previous value and recent measurement of that state. A gain K called as Kalman gain is employed for that purpose in the algorithm. Figure 2.2 shows a diagram of the estimation loop of a Kinematic Kalman filter [32].

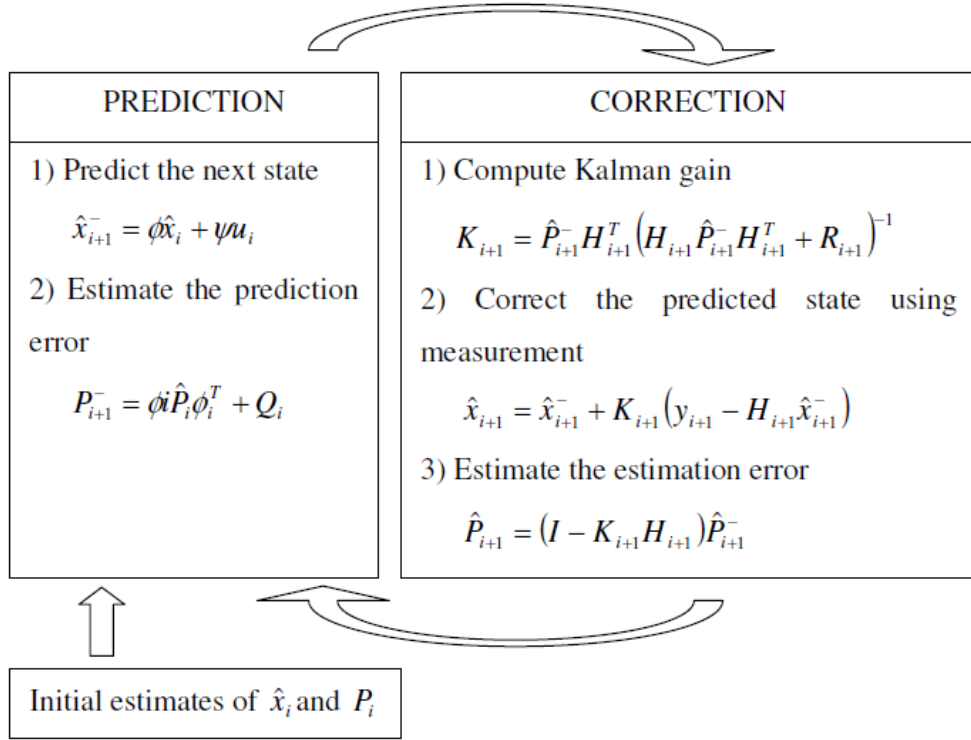


Figure 2.2 Prediction and correction stages of the Kalman filter [32]

where $X, \hat{X}, K, \phi, \psi, Y, P, R, Q, H$ denote state matrix, estimated state matrix, kalman gain matrix, state transition matrix, state input matrix, measurement matrix, estimated variance matrix, variance matrix of the measurement noise, variance matrix of the system noise, measured values matrix respectively. Note that the superscripts denoted by (-) in the correction stage represent the prediction coming from prediction stage in Figure 2.2.

A constant acceleration model is used in KKF to estimate velocity and acceleration simultaneously. Eq.(2.3) represents the state transition matrix of this approach:

$$\Phi = \begin{bmatrix} 1 & T & T^2 \\ 0 & 1 & T \\ 0 & 0 & 1 \end{bmatrix} \quad (2.3)$$

The predicted states can be formulated through Eq(2.4-2.6) in that case:

$$\hat{x}_{i+1}^- = \hat{x}_i + T\hat{\dot{x}}_i + (T^2/2)\hat{\ddot{x}}_i \quad (2.4)$$

$$\hat{\dot{x}}_{i+1}^- = \hat{\dot{x}}_i + T\hat{\ddot{x}}_i \quad (2.5)$$

$$\hat{\ddot{x}}_{i+1}^- = \hat{\ddot{x}}_i \quad (2.6)$$

After prediction of P and calculation of K , the corrections are performed as given in Eq.(2.7), Eq.(2.8) and Eq.(2.9) for position, velocity and acceleration:

$$\hat{x}_{i+1} = \hat{x}_{i+1}^- + K_{i+1}(y_{i+1} - \hat{x}_{i+1}^-) \quad (2.7)$$

$$\hat{\dot{x}}_{i+1} = \hat{\dot{x}}_{i+1}^- + K_{i+1}(\dot{y}_{i+1} - \hat{\dot{x}}_{i+1}^-) \quad (2.8)$$

$$\hat{\ddot{x}}_{i+1} = \hat{\ddot{x}}_{i+1}^- + K_{i+1}(\ddot{y}_{i+1} - \hat{\ddot{x}}_{i+1}^-) \quad (2.9)$$

In the experiments, the acceleration measurement obtained by the second order numerical derivative of the position is also given to the filter. However, 20 steps back is traced to make it smoother. Q and R matrices are selected as:

$$Q = \begin{bmatrix} 0.1 & 0 & 0 \\ 0 & 0.1 & 0 \\ 0 & 0 & 0.1 \end{bmatrix}, \quad R = \begin{bmatrix} 0.01 & 0 & 0 \\ 0 & 0.1 & 0 \\ 0 & 0 & 1 \end{bmatrix} \quad (2.10)$$

2.3.2.3 Modified State Observers

Tilli et. al. proposed a modified state observer to estimate velocity and acceleration from encoder position measurements without using a detailed system model [22]. Figure 2.3 shows the block diagram of the proposed algorithm. The algorithm minimizes the effect of the quantization noise with a large bandwidth. A very narrow low-pass filtering of the estimations is performed when the velocity and acceleration signals have a narrow bandwidth, while a lead network type controller (referred as regulator in Figure 2.3) is applied when the signals have large bandwidth. The smooth switching between the two kinds of filtering is based on the position estimation error. If this error is inside an interval which is equal to the encoder resolution, the low-pass filter is applied; otherwise, the fast filtering is enabled. Note that the abbreviations of DIF, LPF, INT and REG in Figure 2.3 mean the differentiator, low-pass filter, integrator and regulator.

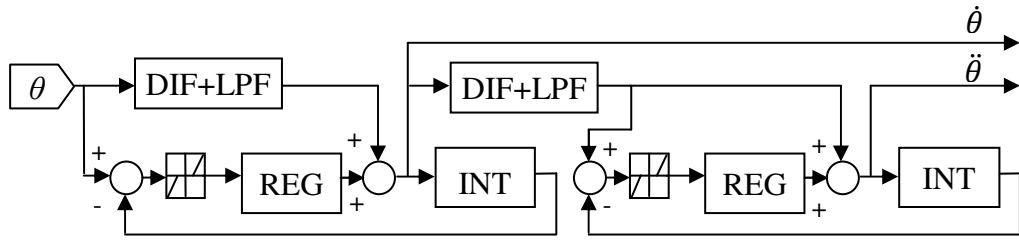


Figure 2.3 Structure of modified state observer [22]

2.4 Enhanced Adaptive Windowing Method

First-order adaptive windowing method (FOAW) proposed by Janabi-Sharifi et. al. [27] is an optimal method in the sense that it minimizes the velocity error variance while maximizing the accuracy of the estimates. Since the method does not provide accurate acceleration estimation, an enhanced adaptive windowing is developed for the estimation of acceleration from the quantized position measurements in this section. Hence, a numerical solution is derived for the EAW method.

If two samples used in the velocity calculation are far apart, the Euler approximation of derivation provides more precise estimation. Besides, as the position measurement window size gets the larger, the variance of the velocity and acceleration gets the smaller due to the averaging effect of the last n velocity and acceleration estimates ($\hat{v}_k, \hat{v}_{k-1}, \dots, \hat{v}_{k-n}$ and $\hat{a}_k, \hat{a}_{k-1}, \dots, \hat{a}_{k-n}$), which are obtained from the finite difference method. The velocity and acceleration are calculated for a window size (n) as follow:

$$\hat{v}_k = \frac{1}{n} \sum_{j=0}^{n-1} \hat{v}_{k-j} = \frac{x_k - x_{k-n}}{nT} \quad (2.11)$$

$$\hat{a}_k = \frac{1}{n} \sum_{j=0}^{n-1} \hat{a}_{k-j} = \frac{\hat{v}_k - \hat{v}_{k-n}}{nT} \quad (2.12)$$

Enlarging window size (n) leads to a significant decrease in quantization noise. However, it decreases the estimation accuracy as the mean is computed in a larger window, and introduces a significant phase lag in the process. Consequently, if the velocity is high, the window size should be short or it should be increased when the velocity is low.

The first-order adaptive windowing technique aims to determine a line passing all intermediate samples ($\hat{x}_k, \hat{x}_{k-1} \dots \hat{x}_{k-n}$) as formulated in Eq.(2.13) such that all intermediate samples are in an uncertainty band defined by the peak norm of the noise [27]. Thus, this technique fits a line on the quantized position signal and the constants of this technique is calculated in the sense of the least mean squares (LMS) of error as given in Eq.(2.14) and (2.15) [27]:

$$\hat{x}_{k-1} = b_1(k-1)T + b_2 \quad (2.13)$$

$$b_1 = \frac{n \sum_{i=0}^n x_{k-i} - 2 \sum_{i=0}^n i x_{k-i}}{n(n+1)(n+2)/6} \quad (2.14)$$

$$b_2 = \frac{kx_{k-n} + (n-k)x_k}{n} \quad (2.15)$$

Similarly, a second-order curve can be fitted on the position measurement for the acceleration estimation:

$$\hat{x}_{k-1} = c_1(k-1)^2T^2 + c_2(k-i)T + c_3 \quad (2.16)$$

Eq.(2.17) gives the error that minimizes the difference between the fitted curve and the sampled position measurement:

$$E = \sum_{i=0}^n (x_{k-i} - \hat{x}_{k-i})^2 \quad (2.17)$$

x_i is the i_{th} position sample before the last sample as illustrated in Figure 2.4. The partial derivatives of the error (E) in terms of three variables are equal to zero in the sense of the least mean squares:

$$\frac{\partial E}{\partial c_1} = 0, \quad \frac{\partial E}{\partial c_2} = 0, \quad \frac{\partial E}{\partial c_3} = 0 \quad (2.18)$$

The solution of Eq.(2.18) gives the parameters of Eq.(2.16);

$$c_1 = 30 \frac{n(n-1) \sum_{i=0}^n x_{k-i} - 6n \sum_{i=0}^n ix_{k-i} + 6 \sum_{i=0}^n i^2 x_{k-i}}{T^2 n(n-1)(n+1)(n+2)(n+3)} \quad (2.19)$$

$$c_2 = 6 \frac{A \sum_{i=0}^n x_{k-i} + B \sum_{i=0}^n ix_{k-i} + C \sum_{i=0}^n i^2 x_{k-i}}{Tn(n-1)(n+1)(n+2)(n+3)} \quad (2.20)$$

$$c_3 = 3 \frac{D \sum_{i=0}^n x_{k-i} + E \sum_{i=0}^n i x_{k-i} + F \sum_{i=0}^n i^2 x_{k-i}}{n(n-1)(n+1)(n+2)(n+3)} \quad (2.21)$$

where the factors in these equations are given as follow:

$$A = 3n(2n^2 - n - 1) - 10kn(n - 1)$$

$$B = -4n(8n + 1) - 6(10kn + 1)$$

$$C = 30(n - 2k)$$

$$D = 10k^2n(n - 1) - 6kn(2n^2 + n - 1) + n(3n^3 - n - 2)$$

$$E = 8kn(8n + 1) - 6n(2n^2 - n - 1) - 12k(5kn + 1)$$

$$F = 10n(n - 1) + 60k(k - n)$$

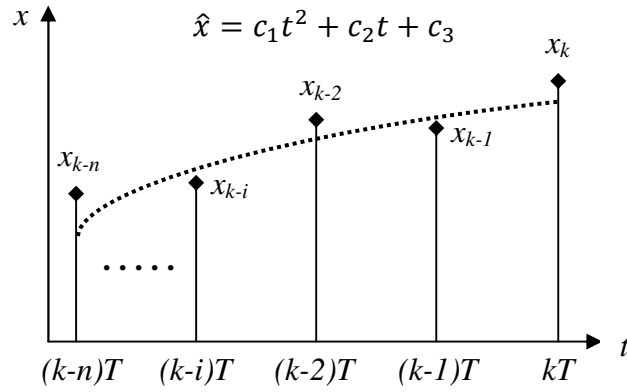


Figure 2.4 Curve fitting of the quantized position signal [30]

The position, velocity and acceleration can be defined in terms of these parameters as;

$$\hat{x}(kT) = c_1(kT)^2 + c_2(kT) + c_3 \quad (2.22)$$

$$\hat{v}_k = \left. \frac{d\hat{x}}{dt} \right|_{t=kT} = 2c_1(kT) + c_2 \quad (2.23)$$

$$\hat{a}_k = \left. \frac{d^2 \hat{x}}{dt^2} \right|_{t=kT} = 2c_1 \quad (2.24)$$

The velocity and acceleration estimations are the approximations of LMS as shown in Eqs.(2.23) and (2.24), and hence the method is named as Enhanced Adaptive Windowing. Here, it is aimed to find a window size (n) with maximum length, such that all position estimation errors within the selected window line inside a tolerance band (d) which is the upper bound of the quantization error (i.e. half of the encoder resolution). Note that Ref. [27] shows that the PDF for the errors introduced by an ideal quantization process is uniform between $-d$ and d . Figure 2.5 shows the flow charts of the first order and second order enhanced adaptive windowing estimation techniques.

$$|x_{k-i} - \hat{x}_{k-i}| \leq d, \quad i \in \{1, 2, \dots, n\} \quad (2.25)$$

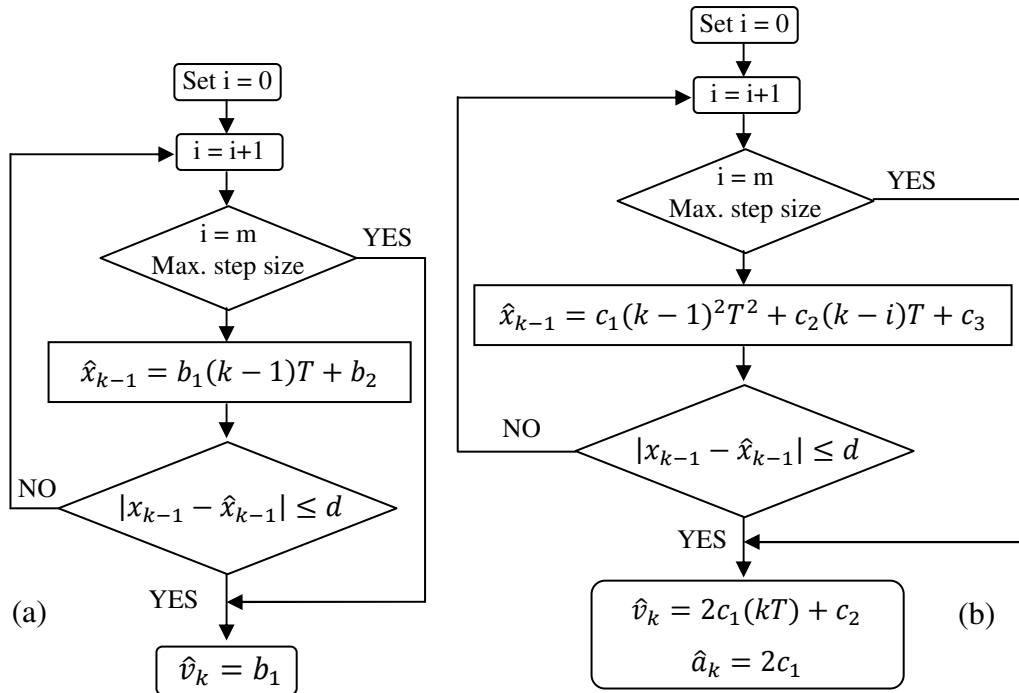


Figure 2.5 Flow charts of first-order (a) and second-order enhanced (b) adaptive windowing techniques

2.5 Hybrid Method

Most of the methods, which are proposed in the literature, necessitate tradeoffs among noise reduction, control of delay, estimation accuracy, reliability, computational load, and bandwidth. Adaptive windowing techniques, which were presented in previous section, are used to overcome these difficulties. In these techniques, discrete position data window is increased until the difference between position measurement and least square based position estimates falls under the maximum quantization error “ d ” for velocity and acceleration estimation. Since the first-order adaptive windowing method does not provide acceleration estimation, it could be modified to estimate acceleration estimation using FP based velocity. Figure 2.6 shows the flowchart of this modified technique. It uses of FP based velocity as input where v_k denotes last value of exact position-based velocity while \hat{v}_k represents the last value of calculated velocity using least square method.

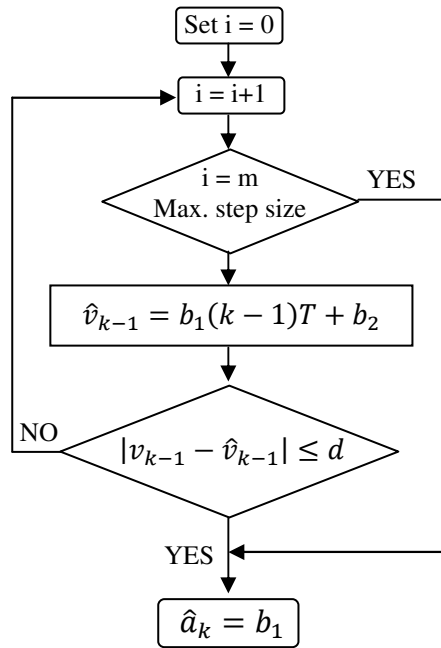


Figure 2.6 Modified first order adaptive windowing technique

The modified method leads to an impulsive change in acceleration around zero velocity when the sign of velocity changes, since it uses the FP based velocity. Therefore, acceleration around zero velocity should be estimated by a different method. A second-order adaptive windowing technique can be used as an alternative to estimate velocity and acceleration in this problematic region.

The hybrid method (HM) proposed in this study is the combination of FP and FT methods. Three different techniques are utilized in this method. These are the fixed position (FP) technique for velocity estimation, the first-order modified adaptive windowing (MAW) using FP based velocity and second-order enhanced adaptive windowing (EAW) using encoder position.

The flow chart of the hybrid method is depicted in Figure 2.7. In this algorithm, firstly, the FP technique estimates the velocity for entire operating region except for around zero velocity. Then, the FP based velocity is used in the first-order modified adaptive windowing (MAW) for high resolution acceleration estimation. Lastly, the impulsive change in acceleration estimation of MAW and discontinuity in FP based velocity around zero velocity are corrected by the second-order enhanced adaptive windowing method (EAW). However, these all techniques should be transited smoothly in HM method. Therefore, a parametric transition curve is proposed in the second step of the algorithm for the smooth transition between these techniques. The second step of the algorithm generates a transition parameter (k) according to the operating velocity (referring FP based velocity) by using the proposed smooth transition curve. Then, this transition parameter (k) is used in the third step of the algorithm for resultant estimations. Note that the smooth transition curve is formed as Gaussian distribution between transition velocity limits (10 rad/sec and 20 rad/sec), and hence it enables smooth shifting among the techniques while the velocity is between 20 rad/sec and 10 rad/sec. Consequently, three different techniques are utilized for different operating regions: (1) the second-order enhanced adaptive windowing technique is used under 10 rad/sec for velocity and acceleration estimation, (2) the FP technique estimates velocity above 20 rad/sec, (3) the first-order modified

adaptive windowing technique using FP based velocity estimates the acceleration above 20 rad/sec. The smooth transition between the techniques is achieved by the proposed parametric transition curve.

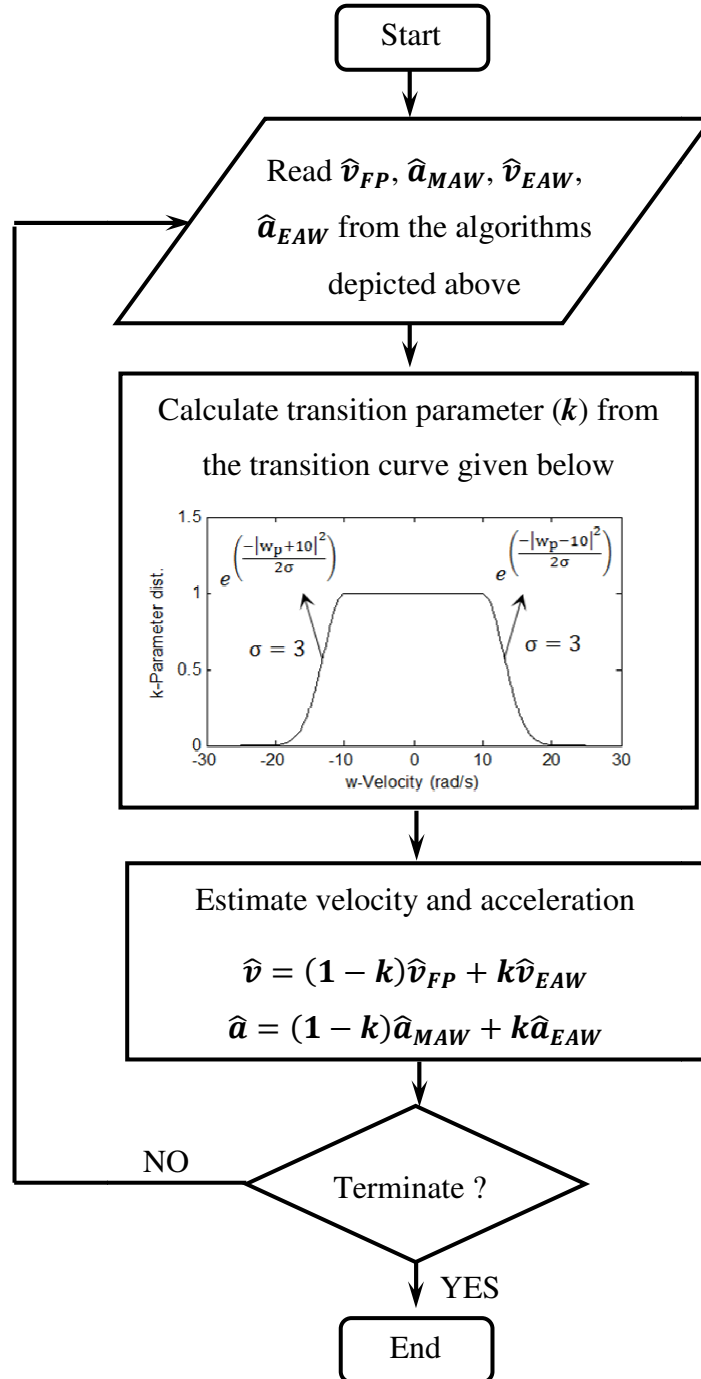


Figure 2.7 Flow chart of the proposed hybrid method

2.6 Experimental Hardware

1-DOF rotary HapticBox shown in Figure 2.8 is used in experimental test of the velocity/acceleration estimation algorithms. This device can simulate only one degree of freedom rotational virtual or remote environments.

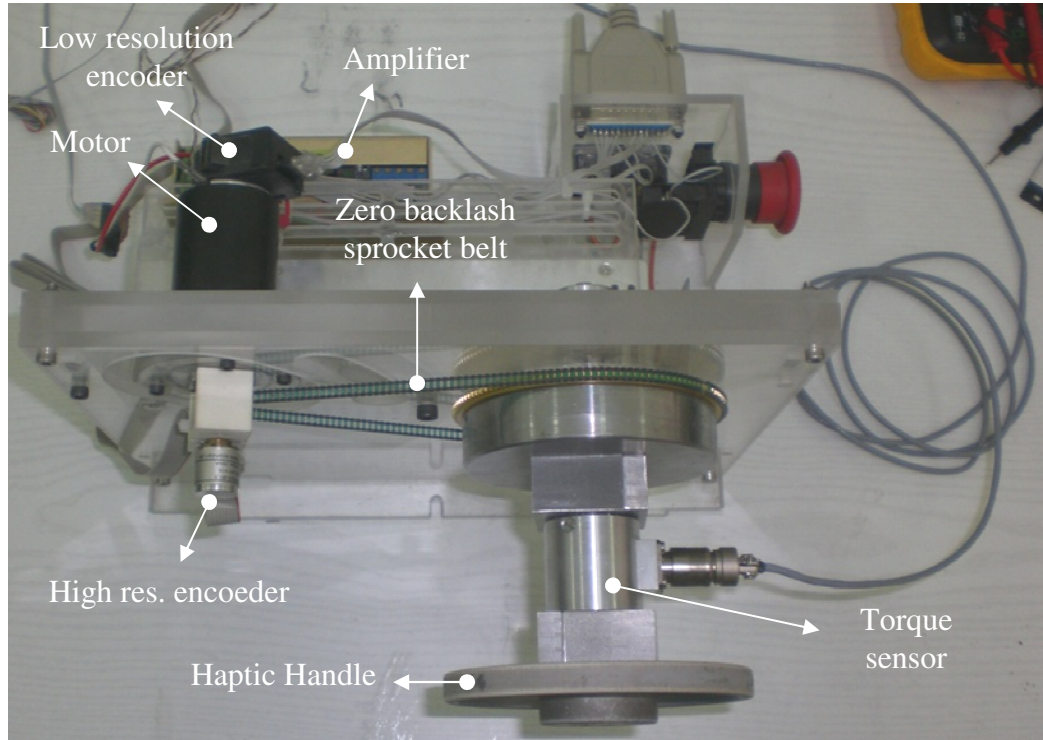


Figure 2.8 HapticBox for experimental tests

There are two encoders in HapticBox: a high resolution with 5000 ppr and low resolution with 500 ppr. Low resolution incremental encoder was used to test the proposed and conventional velocity/acceleration estimation algorithms. The motion inputs are given to device by the user so that the position data were stored for later use. For the evaluation of the velocity and acceleration estimation results, offline forward-backward filtering of the differentiated velocity and acceleration signals of the high resolution encoder is used to generate reference. The “*filtfilt*” function in Matlab's Signal Processing Toolbox is used as Forward-backward

filtering technique for implementing zero-phase filter [33]. The device is actuated by a *MaxonRE40* DC brush motor with a 150W power, which is driven by a *Copley413CE* DC Brush Servo Amplifier. A zero backlash sprocket and chain with a 128/18 gear ratio is used to increase the motor torque. A torque transducer with a range of 10 Nm torque load is used at the handle of the box. The control algorithm is implemented on HapticBox by means of Real-Time Windows Target Toolbox of MATLAB[®]. The technical properties of computer used in application are Intel Core 2 Quad CPU Q9400 @ 2.66 GHz processor, 4 GB Ram, NVIDIA GeForce 9500 GT graphics card. Humusoft MF-624 multifunction I/O card is used to acquire signals coming from the sensors and to send reference signal to motor amplifier at 1 kHz sampling frequency.

2.7 Simulation and Experimental Results

For the comparison of the proposed methods to conventional methods, 3D plots of velocity and acceleration results are generated (Figures 2.9 and 2.10). The reference signal and results of the methods in the figures are shown by blue solid and red dotted lines, respectively. In order to show the results much clearly, the error color maps of the methods are plotted on a graph throughout the simulation time. The colored error maps, Figures 2.11 and 2.12, give a good idea to the readers for the comparison of the methods. As it can be seen in the colored error maps, the following remarks can be given: (1) the phase distortion effect of the Differentiation+filtering (DF) at high operating frequency leads to the higher estimation errors, (2) the modified state observer (MSO) and Kalman filter (KF) cannot effectively reduce the noise, (3) second-order enhanced adaptive windowing (EAW) yields relatively good performance, (4) the proposed hybrid method (HM) is best when compared to the others. For further evaluation of the results, a normalized RMS error of each method is summarized in Table 2.1. Note that normalized RMS error means the ratio between RMS of errors of the examined method and RMS of the reference signal. The normalized RMS error

table shows that the proposed hybrid velocity and acceleration estimation method leads to minimum estimation error.

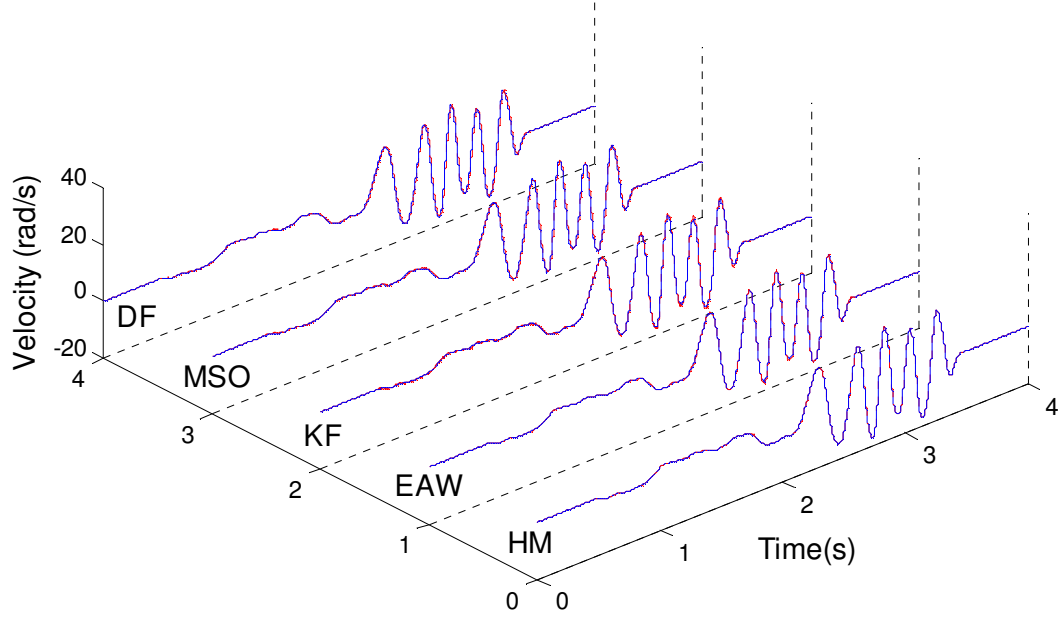


Figure 2.9 Experimental results of estimation methods for velocity

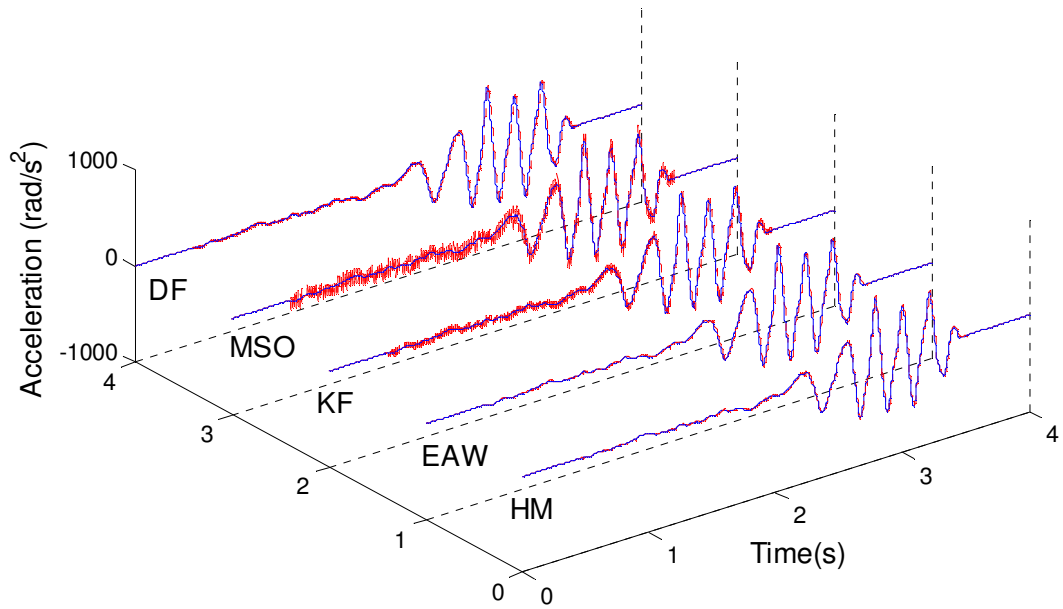


Figure 2.10 Experimental results of estimation methods for acceleration

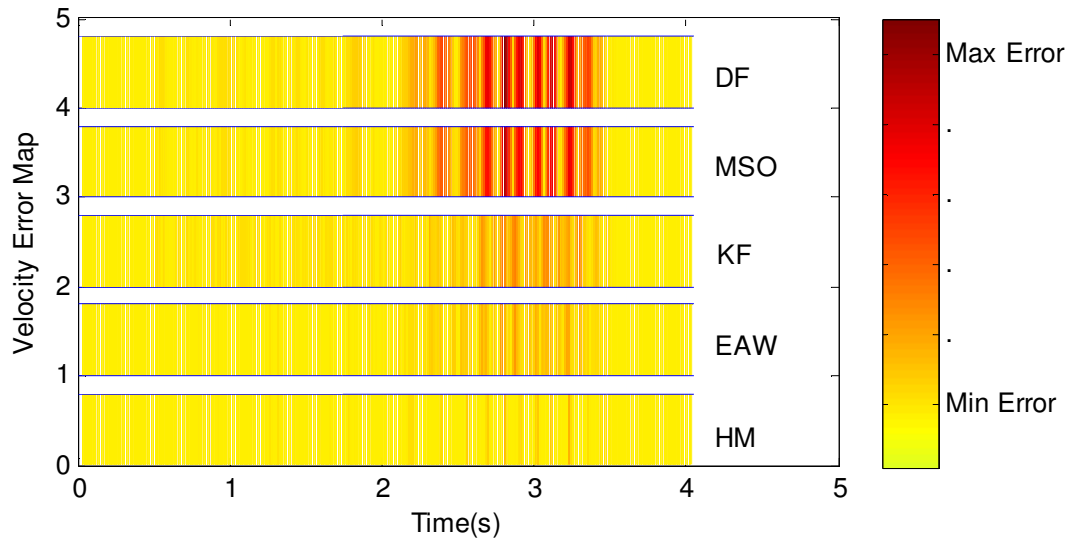


Figure 2.11 Error map of results of estimation methods for velocity

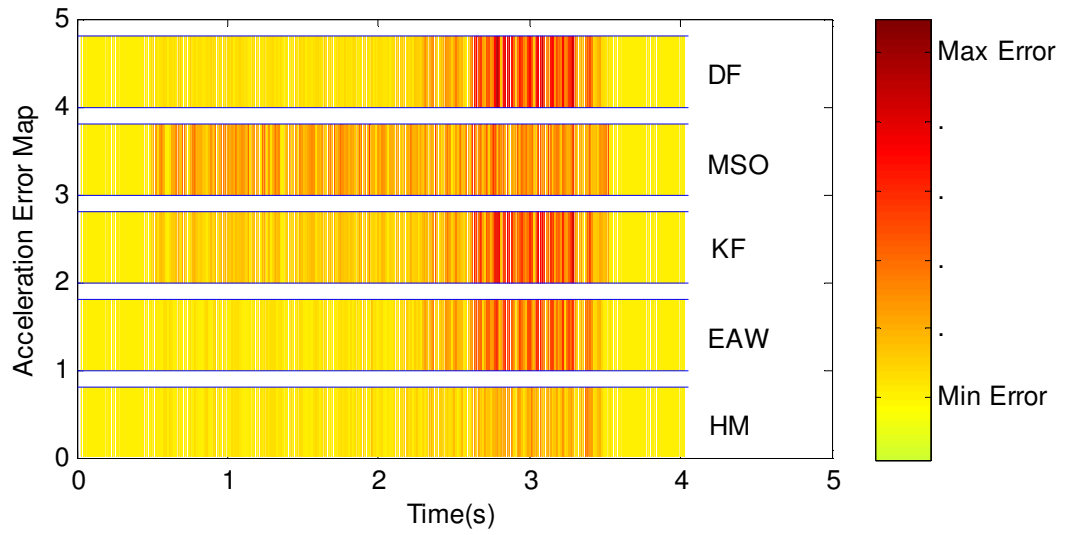


Figure 2.12 Error map of results of estimation methods for acceleration

Table 2.1 Normalized RMS of error for velocity and acceleration

Methods	Norm. Vel. RMS (Res.RMS/Ref.RMS)	Norm. Acc. RMS (Res.RMS/Ref.RMS)
DF	0.2920	3.5134
MSO	0.2562	3.2167
KF	0.1004	3.2696
EAW	0.0619	2.6379
HM	0.0242	1.2821

2.8 Conclusion

This chapter proposed an enhanced second-order adaptive window (EAW) technique and hybrid estimation method (HM) to estimate not only velocity but also acceleration from position signals of a low resolution incremental encoder. The EAW could easily be implemented by applying Real-Time Windows Target Toolbox of MATLAB[®] on a multifunction I/O card facilitating incremental encoder readings. The hybrid method necessitates the use of FPGAs. Basic estimation methods (FP and FT) cannot provide good estimations alone for the entire operating frequencies. For instance, high resolution acceleration estimation is not possible at high velocity region and an impulsive change of acceleration estimation is inevitable when the sign of velocity changes in FP methods. On the other hand, the first-order modified and second-order enhanced adaptive windowing methods are efficient at the problematic regions of FP method. Hence, the proposed hybrid method incorporates these three techniques (Fixed position, modified adaptive windowing, and enhanced adaptive windowing) into a single technique to use the bests of them on different operating regions. The performance of the proposed techniques is comparatively evaluated through a detailed simulation and experimental study. In the comparison of the algorithms, it is shown that the enhanced adaptive windowing and hybrid methods yield the best estimation performance for velocity and acceleration.

CHAPTER 3

TRANSPARENCY IMPROVEMENT

3.1 Introduction

The transparency is the first performance criteria of haptic interfaces and quantify that how well the remote or virtual environments are reflected to the user. The dynamics of a haptic interface should be minimized for maximum transparency. For the transparent simulation of a remote or virtual environment, there are two approaches. These are to redesign the haptic device to minimize dynamic effects, or to improve the performance of the controller to meet the requirements [34-36]. Lawrence [37] explains the transparency as the ratio between the transmitted impedance (Z_M) and environment impedance (Z_D) such that the ideal ratio is unity for a desired bandwidth. The transparency subject is firstly studied in the field of teleportation. Various compensators are proposed in the literature to improve the transparency. Ref. [38] proposed to incorporate a loop-shaping compensator and local feedback loops at the master and slave manipulations to ensure stability and high transparency in a teleoperator system. Loop-shaping approach used in this study increase transparency bandwidth and stability robustness in a bilateral telemanipulation system. Other types of compensators are adaptive control schemes to increase transparency performance criteria [39]. An adaptive controller does not require the parameters of the robot and environment dynamics, and can estimate them in continuous contact simulations. In this way the proposed algorithm provides transparent interaction. Another transparency-optimized control law for an impedance-impedance type of teleoperation system is presented

in [40]. In the literature, either closed loop feedback or open loop with model based compensators is commonly used for transparency improvement of haptic devices [10, 41 and 42]. McJunkin classified haptic interaction into two groups for the evaluation of the transparency characteristics: (1) active user interaction (AUI) and (2) passive user interaction (PUI) [43, 44]. In an AUI application, haptic user gives motion to the device, this motion is sensed by the device and a force is generated based on the virtual model. In PUI case, the user does not generate motion. The passive user interacts with a virtual object defined by an active force. Haptic tennis game can be given as an example for PUI. Maximization of transparency in both interaction types can only be performed by minimizing the disturbance torques/forces resulting from the device dynamics.

Haptic force control algorithms usually employ model based compensators in haptic interfaces to eliminate the inertia and friction of the system [10]. These compensators have two major drawbacks. System dynamics parameters cannot be identified perfectly, and velocity and acceleration cannot be estimated perfectly due to the quantized encoder measurements. Besides, the controller gains in the closed loop controllers cannot be increased to high values due to the inherent device dynamics. These difficulties limit the implementation of model based and closed loop control algorithms. In this chapter, as an alternative, a motor current based torque compensator is developed to increase the transparency.

The rest of the chapter is organized as follow: The contribution is explained in the following section. The next two sections present an overview of the conventional controller architectures and proposed control algorithm. Then, the system identification of the experimental hardware is given in detail. The experimental results and performance evaluations are presented in the fourth section. Applicability of the proposed algorithm to multi-DOF haptic manipulators is shown in the fifth section. The last section is related to the conclusion part of the research.

3.2 Contribution

Force feedback control algorithms and model based compensators are frequently employed in haptic controllers to maximize the transparency. However, the model based control algorithms have some drawbacks such as estimation errors of the disturbance model and velocity/acceleration estimation inaccuracies causing incorrect disturbance compensation. On the other hand, since the controller gains of the force feedback control algorithm cannot be increased to high values due to the inherent dynamics of the system, it is not sufficient alone to cancel the disturbances. The main contribution of this chapter is the motor current based torque feedback compensator which was developed instead of model based compensators to maximize the transparency. The developed algorithm was experimentally tested on a 1-DOF HapticBox. The results show that the proposed algorithm provides the better performance than the conventional algorithms. Furthermore, the motor current based torque feedback compensator is also tested on a MATLAB/SimMechanics[®] model of a 2-DOF serial planar elbow type haptic manipulator to show that it is applicable for multi-DOF haptic devices. This chapter was mainly adapted from our previously published paper titled with “Utilization of Motor Current based Torque Feedback to Improve the Transparency of Haptic Interfaces” [45].

3.3 Conventional Force Control Architectures

Two basic control algorithms are used in haptic interfaces: (1) admittance and (2) impedance type control algorithms [10, 46]. In the admittance control (AC), the motion is controlled to reflect the virtual environment. A reference motion is computed based on the virtual environment model, and sent to the actuator drivers. In the impedance type control (IC), the user motion is sensed and a reference force is computed based on the virtual environment model. Force-feedback loop using a force transducer improves the accuracy of this type of control strategy. It is called as closed loop impedance control (CLIC). AC and CLIC algorithms require the use of force/torque transducers. Appropriate control

algorithm should be selected based on the virtual environment and the device itself. The proposed method in this chapter is implemented on CLIC which is mostly preferred for haptic interfaces.

Figure 3.1 shows the components in a haptic-user interaction. User applies a force F_h to move the device handle. X_h and X_d are the displacement of the user hand and haptic device. F_d is the force applied by the device based on the virtual environment model. The dynamic of the user hand and device affects the haptic interaction force. Force transducer attached to the end-effector sense the user force. However, the user changes the force to overcome the dynamic effects. Thus, the force sensed by the transducer includes the dynamic effects of the device and the user arm. Moreover, the user's fingers may not hold the handle tightly. In such a case user and device motion (X_h and X_d) might be different. This phenomenon should be taken into consideration in the design of a haptic interface controller.

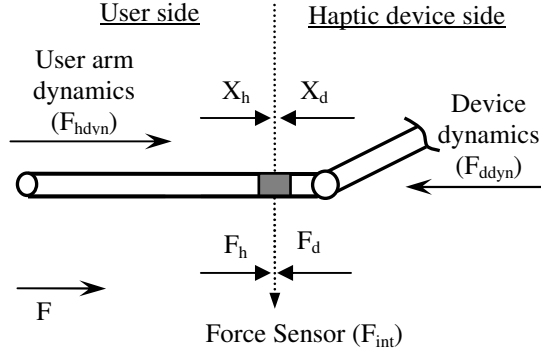


Figure 3.1 Haptic-user interaction

Figure 3.2 shows typical haptic interface architecture for the open loop impedance type control (OLIC). The interface is composed of the human operator, haptic device and virtual environment. The user receives force-feedback when imposes motion on the device. Incremental encoders on the device sense position and these measurements are then used to compute the desired forces and corresponding motor torques based on the virtual environment model.

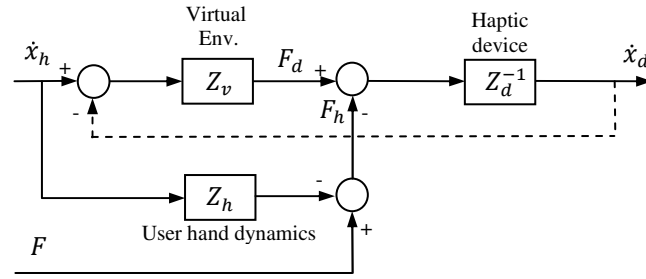


Figure 3.2 Open Loop Impedance Control (OLIC)

The block diagram in Figure 3.2 includes the virtual environment, haptic device and user impedances (Z_v , Z_d , Z_h) and can be used to determine the equivalent impedance of the haptic interface. The equivalent impedance (Z_{eq}) is the relationship between force applied by the operator (F_h) and device displacement (x_d), and can be defined as the summation of the virtual environment, human and the device impedances (Eq.3.1). Thus, the user feels the dynamics of haptic device and user arm in addition to the virtual environment.

$$Z_{eq} = Z_v + Z_d + Z_h \quad (3.1)$$

In the closed loop impedance controller, the sensed force is used as feedback in the controller (Figure 3.3) and equivalent impedance can be determined as:

$$Z_{eq} = Z_v + (1 + K_p)^{-1}Z_d + Z_h \quad (3.2)$$

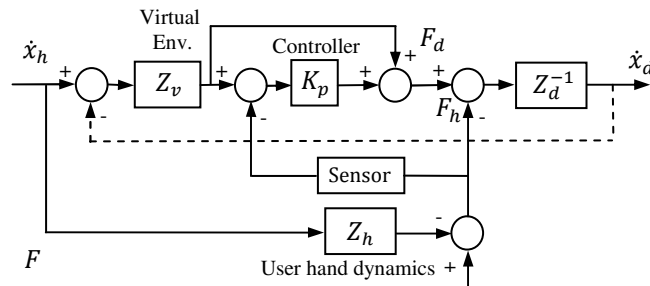


Figure 3.3 Closed Loop Impedance Control (CLIC)

The errors due to the dynamics of the haptic device are inversely proportional to the controller gain, K_p . If the gain is set to zero, then the controller turns into open-loop. The controller gain can be set as high as possible for a realistic haptic interaction. However, high gain may cause instability which depends on the inherent dynamics of the system (i.e. device dynamics, sensor noises and inaccurate velocity/acceleration estimation) [10].

The closed loop block diagram shown in Figure 3.3 uses a proportional controller. McJunkin explained that it is not possible to use traditional (PID, PD, PI) control law with force/torque sensors in haptic interfaces [34]. In a PD control application using a force/torque transducer the derivative term may create difficulty due to the noise of the sensor signal. The numerical differentiation of the sensor signal amplifies noise and thus the derivative term of the controller causes instability. On the other hand, PI control has also practical difficulties in implementation. The PI control law can be used to correct the steady state error in a system. However, a user who explores a haptic environment generally may not maintain static contact with an object consistently.

Another controller type to eliminate the dynamic effect of the device felt by the user is to apply a model-based compensator on open loop control as shown in Figure 3.4. This type of controller is called as open loop impedance control with model based compensator (OLIC with MBC). The equivalent impedance can be determined as:

$$Z_{eq} = Z_v + Z_d - \tilde{Z}_d + Z_h \quad (3.3)$$

In order to eliminate the dynamic effect of the haptic device, identified device impedance (\tilde{Z}_d) should be equal to the actual impedance of the device (Z_d). Therefore, model based controller requires a good identification to compensate the dynamic and frictional effects of the haptic device.

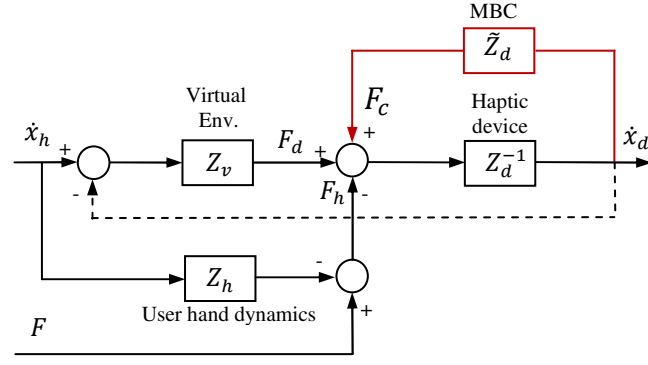


Figure 3.4 Open Loop Impedance Control with model based compensator (OLIC with MBC)

The model-based feedforward controller contributes the transparency improvement of the haptic devices. However, it is problematic due to some certain drawbacks. First, it is very susceptible to modeling errors. If the estimated parameters of the haptic model are incorrect, the estimated force will also be incorrect. Another drawback of this algorithm is the fact that velocity and acceleration cannot be estimated perfectly due to the quantized encoder signals.

As shown in Figure 3.5, model-based compensator can also be applied to the closed loop impedance control (CLIC with MBC) [47]. The equivalent impedance can be determined as:

$$Z_{eq} = Z_v + (1 + K_p)^{-1}(Z_d - \tilde{Z}_d) + Z_h \quad (3.4)$$

Since the velocity and acceleration can be estimated better using the quantized position signal at high-velocities, model based compensator tends to work well for high-velocity; however, closed loop force feedback works well for low velocity [47]. Therefore a hybrid force controller can be used to combine the advantages of these two modes. Nevertheless, they may be coupled in an application and create instable effects.

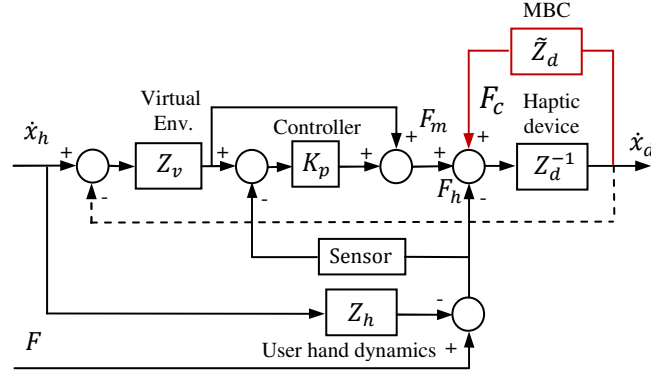


Figure 3.5 Closed Loop Impedance Control with model based compensator (CLIC with MBC)

3.4 Proposed Motor Current Based Torque Feedback Compensator

In the literature, the transparency of haptic devices is maximized by linear model-based compensation algorithms and force feedback control algorithms [10]. The model-based methods are not sufficient due to some drawbacks as mentioned in the previous section. For the force feedback control algorithms, only proportional controller is preferred since haptic interactions generally do not have steady state equilibrium and the transducer noise is inevitable [34]. Besides, the proportional gain of the closed loop controller cannot be increased to high values for transparency maximization because of the system dynamics. On the other hand, the force feedback control is implemented on the tip point, since the force transducer is attached to the end-effector of a haptic manipulator. This technique has certain difficulties in estimating the interaction torque at each joint for effective transparency. Alternatively, torque feedback control can be implemented on each joint by means of separate torque sensors attached to every joint. However, it increases the inertia and the cost of the haptic devices. In this section, motor current based torque-feedback compensator is employed in the closed loop impedance controller to improve the transparency of the haptic interfaces. The proposed control algorithm is applied on the joint space. The block diagram of the proposed method for 1-DOF rotary haptic device is shown in Figure 3.6.

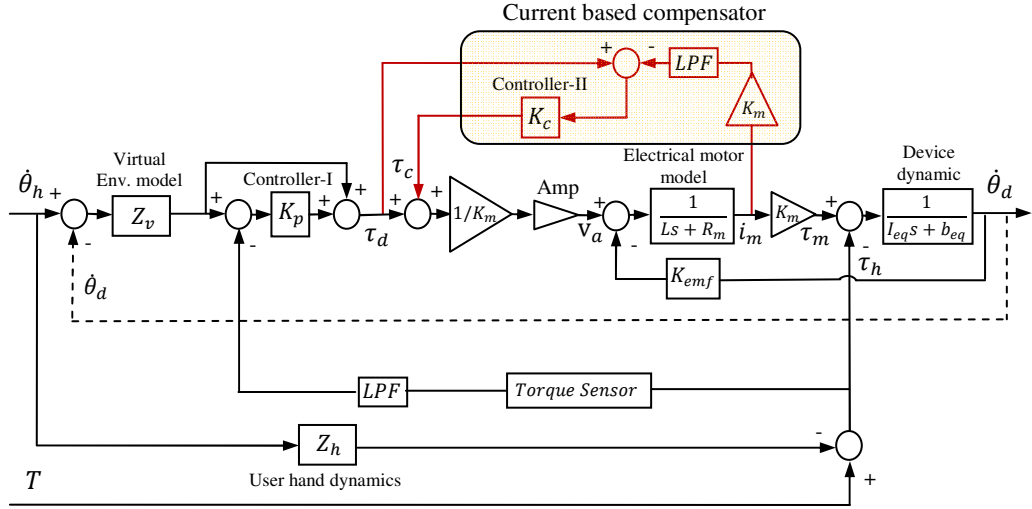


Figure 3.6 Block diagram of Closed Loop Impedance Control with Motor Current Based Compensator (CLIC with MCBC) for a 1-DOF rotary haptic device

The block diagram comprises the virtual model, device dynamics, user dynamics, actuator models, force feedback controller (Controller-I) and motor current based compensator (Controller-II). The actuator torque can be measured by means of a low-cost current sensor and the actuator torque constant. This torque measurement is compared with the output of Controller-I and the error between them is compensated by Controller-II of the current based compensator. A low-pass filter (LPF) is employed to reduce the vibration effect of the noisy feedback. In the experiments, a fully integrated hall-effect current sensor (Allegro[®] ACS712) is used for the current measurements. Z_v , Z_h , K_p , K_c , $\dot{\theta}_h$, $\dot{\theta}_d$, F_h , τ_d , τ_c , τ_m , τ_h , v_a , i_m , R_m , L , K_{emf} , K_m symbols in Figure 3.6 denote impedance of virtual environment, impedance of user hand, gain of controller-I, gain of controller-II, motion of the user hand, motion of the haptic device, human user force, desired torque command, compensator torque command, joint torque applied by motor, joint torque applied by human user, motor voltage, motor current, motor resistance, motor inductance, motor back EMF constant, motor torque constant, respectively.

3.5 System Parameter Identification of Experimental Hardware

1-DOF HapticBox was used in the experimental comparison of the control algorithms. All details about the HapticBox are mentioned in Chapter 2. The system parameters of a haptic device should be identified precisely to implement a model-based compensation algorithm. In experimental system identification of a robot, there are two methods: (1) implicit and (2) explicit methods [48]. Training a neural network is an example to implicit experimental system dynamics identification of a robot [49, 50]. In explicit methods the robot dynamics is formulated in terms of system parameters and they are identified based on a series of measurements. Nonlinear least squares estimation technique is commonly used to identify the system parameters of the robots. In this section, Gauss-Newton nonlinear least square optimization algorithm [51] is implemented on the measured torque, velocity and acceleration of the device for the system identification (parameter estimation) of the HapticBox.

Inertial and frictional effects of output drum (τ_o) and input motor drum (τ_i) of our 1-DOF experimental hardware (HapticBox) causes parasitic torque (τ_p) during interaction. Sprocket mechanism used in the HapticBox magnifies the parasitic torque effect of input drum by the transmission ratio (r_o/r_i). Hence, Eq.(3.5) represents the total parasitic torque of the HapticBox:

$$\tau_p = \tau_o + \frac{r_o}{r_i} \tau_i \quad (3.5)$$

The parasitic torques of each drum can be expressed in terms of Coulomb friction (T_c), viscous friction coefficient (b) and inertia (I) as follow:

$$\tau_o = \text{sgn}(\dot{\theta}_o) T_{c_o} + b_o \dot{\theta}_o + I_o \ddot{\theta}_o \quad (3.6)$$

$$\tau_i = \text{sgn}(\dot{\theta}_i) T_{c_i} + b_i \dot{\theta}_i + I_i \ddot{\theta}_i \quad (3.7)$$

where $\dot{\theta}_i = \frac{r_o}{r_i} \dot{\theta}_o$, $\ddot{\theta}_i = \frac{r_o}{r_i} \ddot{\theta}_o$.

Total parasitic forces can be expressed as give in Eq.(3.8) by using Eqs.(3.6) and (3.7). Then the equivalent Coulomb friction, equivalent viscosity friction constant and equivalent inertia can be derived as follow:

$$\tau = \text{sgn}(\dot{\theta}_o) \left(T_{c_o} + \frac{r_o}{r_i} T_{c_i} \right) + \left(b_o + \frac{r_o^2}{r_i^2} b_i \right) \dot{\theta}_o + \left(I_o + \frac{r_o^2}{r_i^2} I_i \right) \ddot{\theta}_o \quad (3.8)$$

$$T_{c_{eq}} = \left(T_{c_o} + \frac{r_o}{r_i} T_{c_i} \right), b_{eq} = \left(b_o + \frac{r_o^2}{r_i^2} b_i \right) \text{ and } I_{eq} = \left(I_o + \frac{r_o^2}{r_i^2} I_i \right) \quad (3.9)$$

A simple experiment was conducted to identify these equivalent parameters. In this experiment, the user rotated haptic handle at various velocity and acceleration. The torque measurements and the estimations of velocity and acceleration of the handle are plotted as given in Figure 3.7. Note that enhanced adaptive windowing (EAW) technique explained in Chapter 2 is employed to estimate velocity and acceleration of the handle. Gauss-Newton nonlinear least-square estimation technique [51] (MATLAB[®] “*lsqnonlin*”) is applied on Eq.(3.8) by using the torque, velocity and acceleration measurements to estimate the equivalent parameters. Hence, the cost function of the problem can be defined as:

$$\begin{aligned} \min \left\| f \left(T_{c_{eq}}, b_{eq}, I_{eq} \right) \right\|_2^2 \\ = \min \left\{ f_1 \left(T_{c_{eq}}, b_{eq}, I_{eq} \right)^2 + \dots + f_n \left(T_{c_{eq}}, b_{eq}, I_{eq} \right)^2 \right\} \end{aligned} \quad (3.10)$$

where $f_i \left(T_{c_{eq}}, b_{eq}, I_{eq} \right) = \tau_{mi} - \text{sgn}(\dot{\theta}_{o_mi}) T_{c_{eq}} - b_{eq} \dot{\theta}_{o_mi} - I_{eq} \ddot{\theta}_{o_mi}$

Subscript “ m_i ” in Eq.(3.10) denotes the i^{th} measured data. Initial values of the parameters are set to zero for parameter estimation. As a result, equivalent static

friction, viscous friction and inertia parameters are found as ($T_{ceq}=0.0097$ Nm, $b_{eq}=0.0046$ Nms, $I_{eq}= 0.0025$ kgm²).

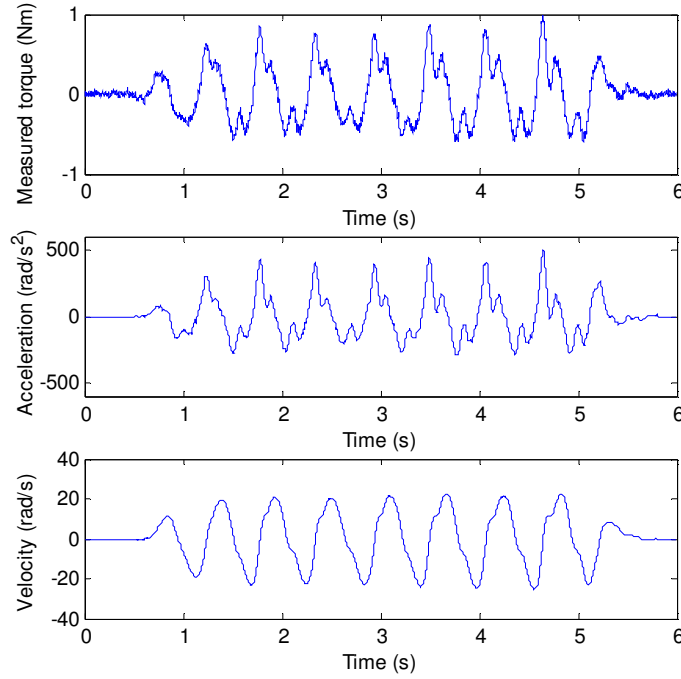


Figure 3.7 Measurements for parameter identification

The classic Coulomb friction model causes a discontinuity around zero velocity and this discontinuity produces unstable oscillations in haptic interfaces [52]. Therefore, Coulomb friction model is modified according to the boundary conditions ($\dot{\theta}_l$) using a continuous smooth transition function in the dead-zone (Figure 3.8) to eliminate the oscillation problem. The model based compensator implemented in this chapter uses this modified friction model as follow:

if $|\dot{\theta}| < \dot{\theta}_l$

$$T_c = \text{sgn}(\dot{\theta}) \left[-\left(\frac{T_{ceq} - b_{eq}\dot{\theta}_l}{\dot{\theta}_l^2} \right) |\dot{\theta}|^2 + \left(\frac{2T_{ceq} - b_{eq}\dot{\theta}_l}{\dot{\theta}_l} \right) |\dot{\theta}| \right] \quad (3.11)$$

else $T_c = \text{sgn}(\dot{\theta}) [T_{ceq} + b_{eq}(|\dot{\theta}| - \dot{\theta}_l)]$

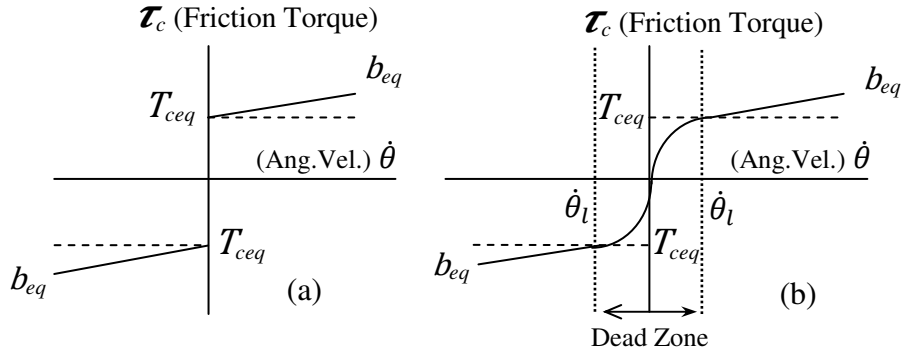


Figure 3.8 Coulomb friction model (left) and proposed friction model (right)

3.6 Experimental Results

In order to compare the proposed algorithm to conventional algorithms, we carried out a set of experiments. In the first set, virtual stiffness (K) and damping (B) elements of the virtual model are set to zero. The results are presented in the form of interaction torque measurements versus angular rotation of the handle and so-called free-motion transparency measure. It is expected that the device does not produce any parasitic torque in the experiments. The haptic user cycled the handle around ± 1 rad. within 6 seconds and the measurements were stored with varying velocity and acceleration. The interaction torque measurements are desired to be close as possible to the horizontal axis for maximum transparency in the free-motion transparency measures. Second experiment was conducted under the effect of two separate virtual load simulations: (1) a single virtual spring ($K=0.5$ Nm/rad) and (2) a single virtual damping ($B=0.1$ Nms/rad). For high transparency performance, the haptic device should produce the accurate torque required for the virtual environment simulation. Thus, it is desired that the measured torque should be close as possible to the reference torque calculated for the virtual model. The motion of handle in these experiments is generated by the user at high velocities and accelerations to test the algorithms effectively.

The results are presented as 3D graphs to compare the algorithms simply (Figures.3.9). Figure 3.9a presents the free-motion transparency measures for OLIC, OLIC with MBC, CLIC, CLIC with MBC and CLIC with MCBC algorithms. It shows that closed loop algorithms give relatively good performance. However, the proposed CLIC with MCBC algorithm is the best. For the virtual-load experimental results, the measured and reference torque values are shown on the same figure (Figures 3.9b and 3.9c). The closeness of them gives an idea about the transparency performances of the algorithms. According to the virtual load experimental results, it can be concluded that: (1) MBC does not improve the haptic interaction effectively due to the identification inaccuracies and non-precise velocity/acceleration estimations, (2) the transparency performance of the CLIC is not satisfactory because of the fact that proportional gain cannot be increased to high values due to the inherent device dynamics, (3) MCBC improve the transparency performance of CLIC significantly. Consequently, CLIC with MCBC method gives the highest transparency performance for the haptic interactions. Note that the proposed algorithm used in the experiments contains two different proportional controllers. They use transducer torque feedback and motor current based torque feedback. Proportional gains of these controllers are set to high values as possible provided that the system is stable.

The results of virtual-load experiments were also evaluated in detail using double axes figures where left and right axes show the torque error and angular acceleration versus time. Figures 3.10a-e and 3.11a-e are presented to illustrate the apparent inertia achieved by the algorithms for virtual stiffness and damper simulations. The torque errors during interaction can be followed up throughout the angular acceleration of the handle in these figures and it can be seen that the torque error changes similarly with angular acceleration. Therefore, the minimum torque error means the minimum apparent inertia achieved by the algorithms. Consequently, Figure 3.10 and 3.11 show that CLIC+MCBC provides minimum apparent inertia which can be interpreted as the highest transparency performance.

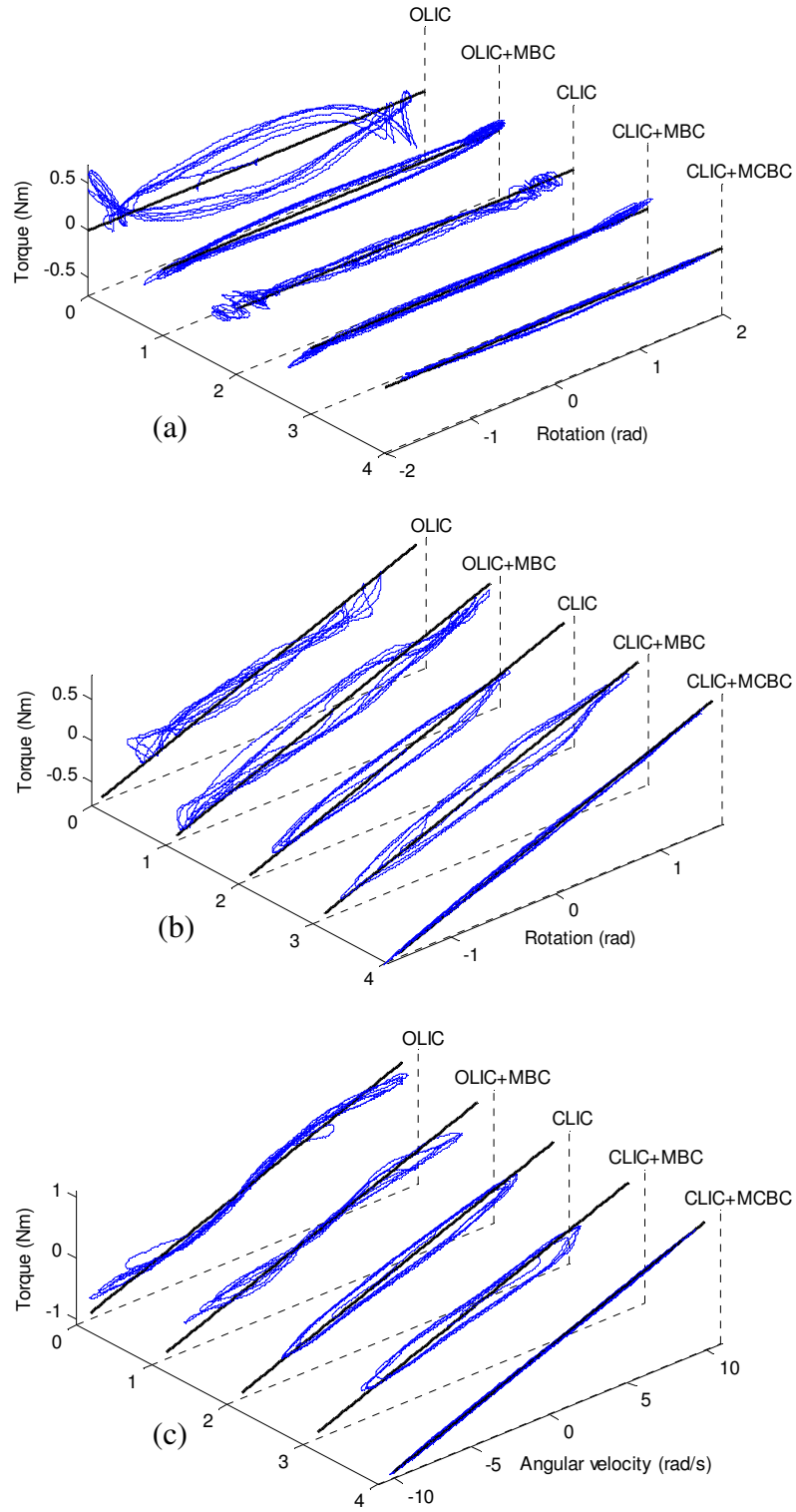


Figure 3.9 Transparency performance measures for (a) free-motion, (b) virtual spring with $K=0.5 \text{ Nm/rad}$, and (c) virtual damping with $B=0.1 \text{ Nms/rad}$

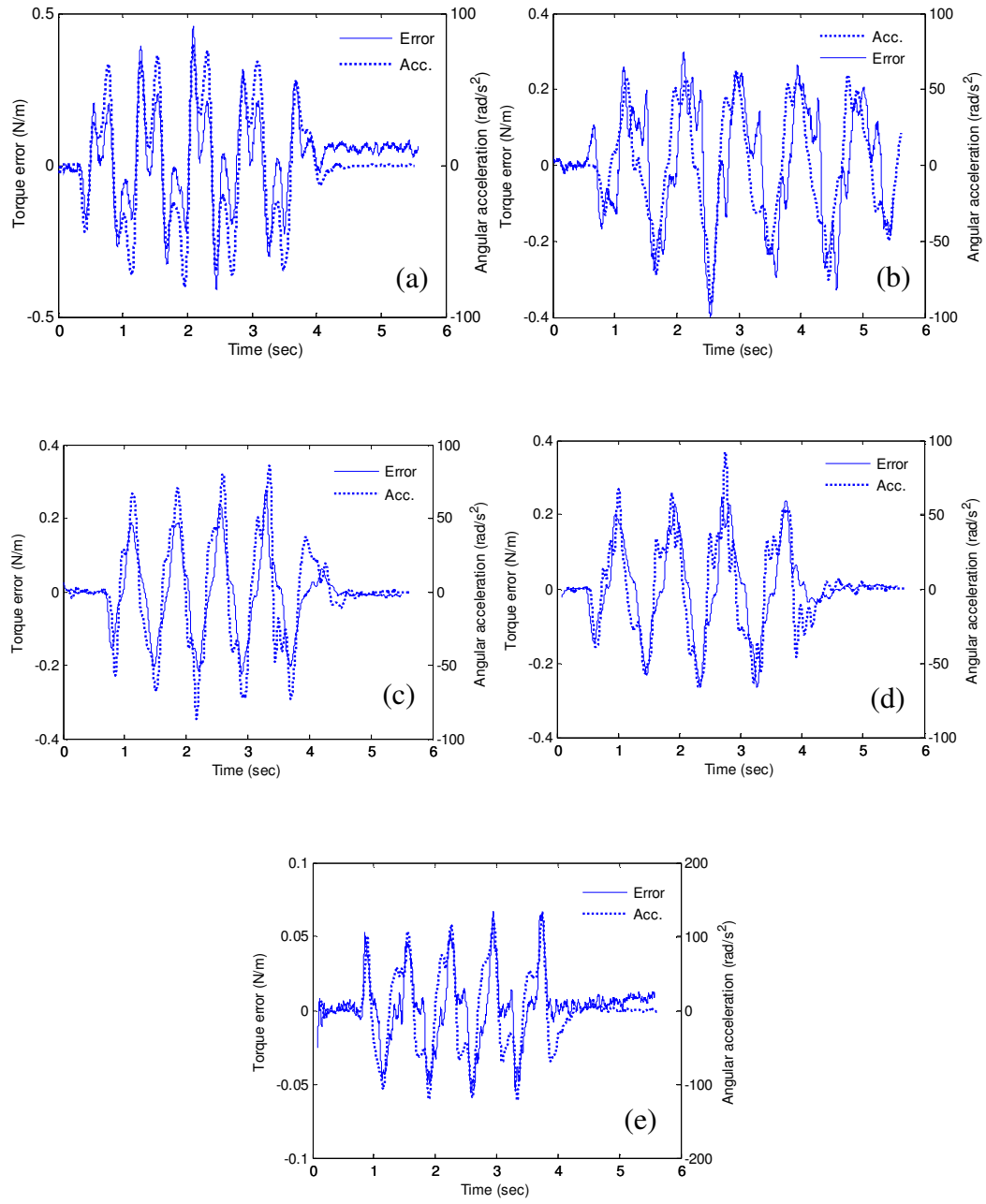


Figure 3.10 Apparent inertia measure for virtual spring $K=0.5 \text{ Nm/rad}$ (a) OLIC, (b) OLIC with MBC, (c) CLIC, (d) CLIC with MBC, (e) CLIC with MCBC

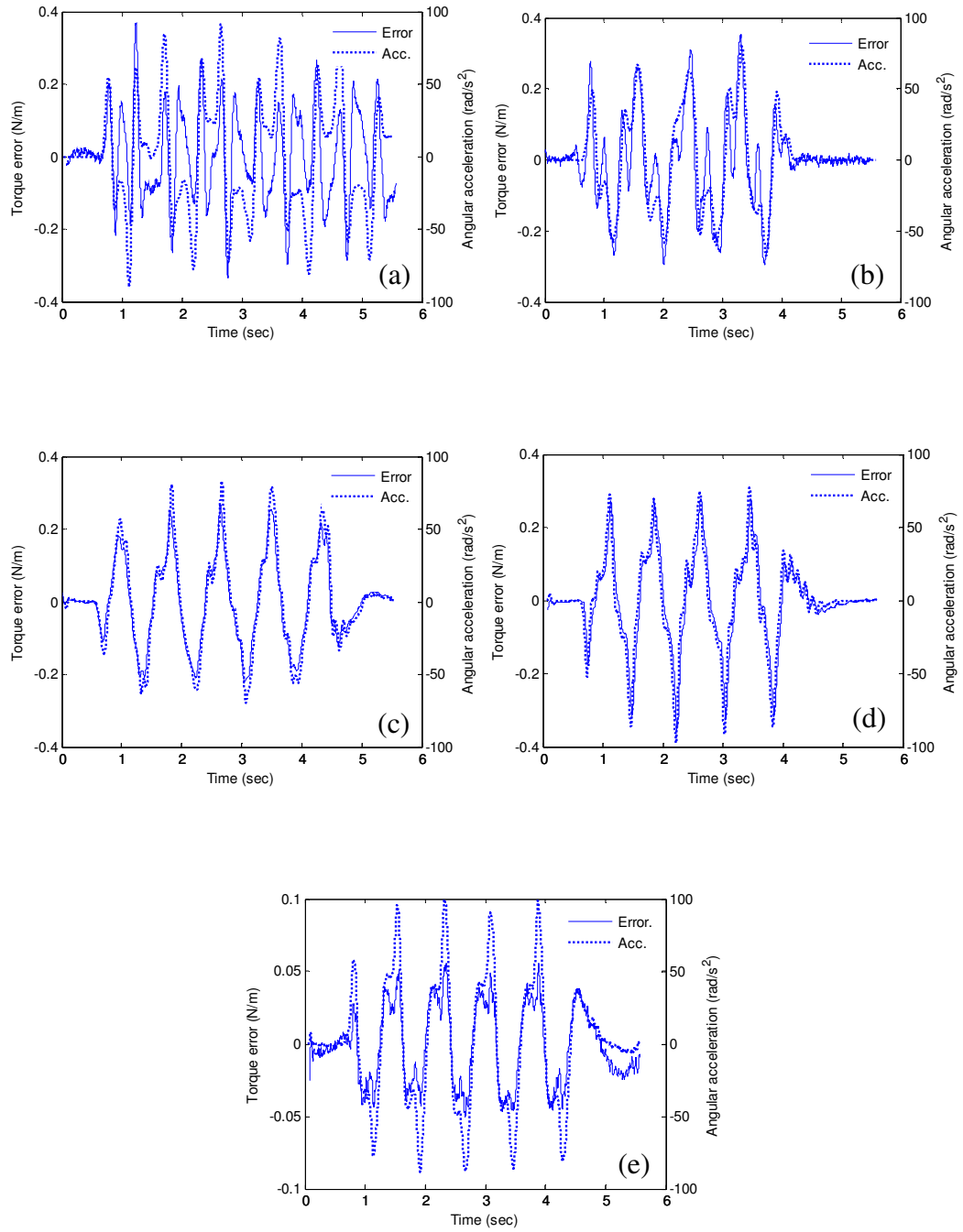


Figure 3.11 Apparent inertia measure for virtual damping $B=0.1 \text{ Nms/rad}$ (a) OLIC, (b) OLIC with MBC, (c) CLIC, (d) CLIC with MBC, (e) CLIC with MCBC

In order to further interpret the double axes figures given in Figures 3.10 and 3.11, the average apparent inertias of the algorithms are presented in Table 3.1. Note that the average apparent inertia means the ratio between RMS of the torque errors and RMS of the acceleration of the handle during the experiments. According to Table 3.1, the minimum apparent inertia is achieved by CLIC+MCBC and hence it can be concluded that the proposed algorithm is superior in terms the transparency.

Table 3.1 Average apparent inertia ($I_{app} = RMS(Torque)/RMS(Acc.) - gm^2$)

Virtual Model	OLIC	OLIC+MBC	CLIC	CLIC+MBC	CLIC+MCBC
K = 0.5 Nm/rad	4.4	3.8	3.5	2.7	0.042
B= 0.1 Nms/rad	3.9	3.2	3.7	3.4	0.062

3.6.1 A Novel Transparency Metric for Haptic Devices

In this section, a novel transparency metric is proposed for haptic devices. The conservation of energy at the time of crash of a solid object with a virtual wall is considered in this method. A solid object hurled through a wall can penetrate into the wall at the crash, depending upon the kinetic energy of the object and the virtual wall parameters (stiffness - K and damper - B). The kinetic energy of the object is absorbed by the wall. Hence, the conservation of energy is formulated as given in Eq.(3.12) for the crash of a rotational 1-DOF solid object with a virtual wall in terms of inertia of the object (I), crash velocity with the virtual wall ($\dot{\theta}_c$), virtual stiffness parameter (K), virtual damping parameter (B), maximum indentation (θ_m), rotation of the object after crash (θ) and velocity of the object after crash ($\dot{\theta}$). Left side term represents the kinetic energy just before crash while right side terms represent the work done by the virtual wall parameter after crash.

$$\frac{1}{2}I\dot{\theta}_c^2 = \frac{1}{2}K\theta_m^2 + \int_0^{\theta_m} B\dot{\theta} d\theta \quad (3.12)$$

Maximum transparency necessitates minimum apparent inertia in haptic devices. To find the apparent inertia of the device as a transparency metric, Eq.(3,12) can be rearranged as given in Eq.(3.13).

$$I_{app} = \frac{K\theta_m^2 + 2 \int_0^{\theta_m} B\dot{\theta} d\theta}{\dot{\theta}_c^2} \quad (3.13)$$

A set of experiments was carried out on a virtual wall to test the algorithms in terms of the proposed transparency metric. The stiffness and damper parameters of the wall were selected as $K=20 \text{ Nm/rad}$, $B=0.01 \text{ Nms/rad}$. The user hurled the haptic handle through the wall at nearly same velocity for each experiment. Figure 3.12a-e shows the position and velocity measurements of the handle for each experiment. Virtual wall contact velocity of the handle and maximum indentation depth are shown by data cursor in the same figures. Using Eq.(3.13), the apparent inertia of the device is presented in Table 3.2 for virtual wall experiment of each algorithm. According to Table 3.2, the proposed algorithm (CLIC with MCBC) provides the minimum apparent inertia which is required for maximum transparency.

Table 3.2 Apparent inertia for virtual wall experiment (I_{app} – gm^2)

Virtual Wall	OLIC	OLIC+MBC	CLIC	CLIC+MBC	CLIC+MCBC
K = 20 (Nm/rad) B = 0.01 (Nms/rad)	2.41	1.57	1.50	1.09	0.69

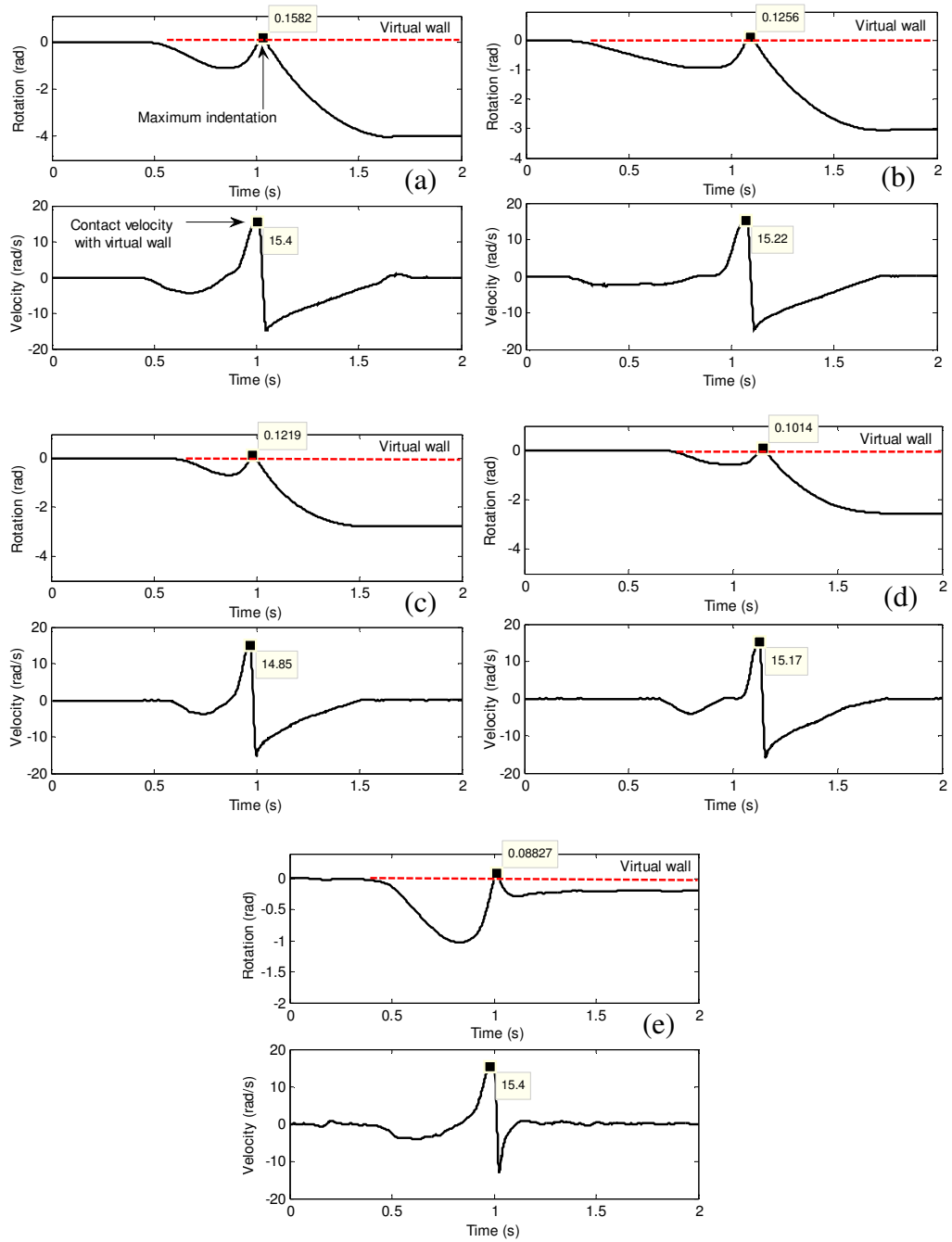


Figure 3.12 Transparency measure for a virtual wall with the parameters of $K=20 \text{ Nm/rad}$ and $B=0.01 \text{ Nms/rad}$ (a) OLIC, (b) OLIC with MBC, (c) CLIC, (d) CLIC with MBC, (e) CLIC with MCBC

3.7 Application of the Algorithms to Multi-DOF Haptic Devices

In order to show that the proposed MCBC is applicable for multi-DOF systems, the algorithms are tested for a 2-DOF serial planar elbow type haptic manipulator in the simulation environment (Figure 3.13). MATLAB/SimMechanics[®] Toolbox is used in the simulation since it enables us to realize the forward dynamics of the haptic device. Besides, the virtual actuators, virtual end-point force sensor, virtual joint position sensors of the MATLAB/SimMechanics[®] Toolbox can be employed for a realistic haptic device simulation.

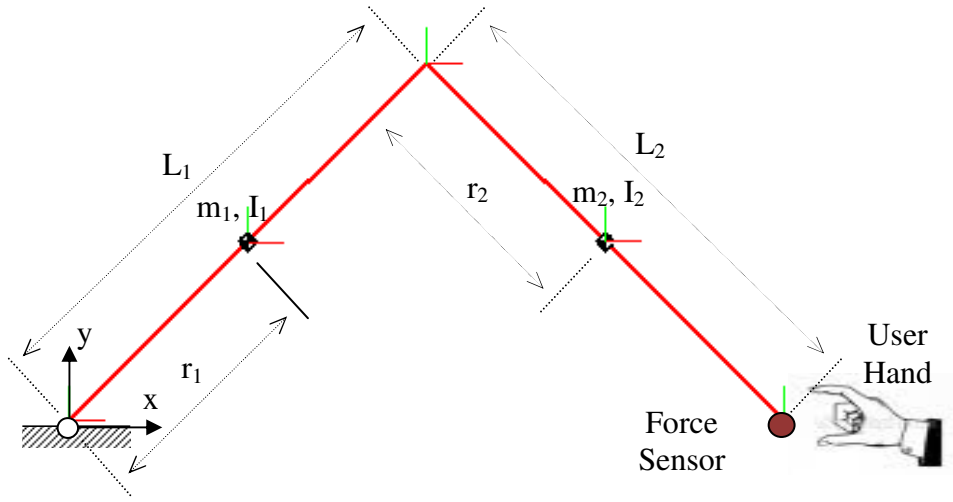


Figure 3.13 2-DOF serial planar elbow type haptic manipulator

In this section, firstly dynamic model of the device was derived. Then, the linearized dynamic parameters to be used in model-based control algorithm are identified. Finally, conventional and the proposed algorithms are implemented on the SimMechanics[®] model of the device to compare the results.

The dynamics of the robot manipulators is expresses as follow [53]:

$$\tau = M(\theta)\ddot{\theta} + C(\theta, \dot{\theta})\dot{\theta} + G \quad (3.14)$$

where M , C , and G denote the inertial matrix, the Coriolis and centrifugal matrix, and the gravitational vector respectively. $\tau = [\tau_1, \tau_2]^T$, $\Theta = [\theta_1, \theta_2]^T$ are torque vectors generated by the motors and the vector of joint angles.

The equations of motion of a 2-DOF serial manipulator can be derived as given in Eq.(3.15) by using the Euler-Lagrange method:

$$\begin{bmatrix} \tau_1 \\ \tau_2 \end{bmatrix} = \begin{bmatrix} M_{11} & M_{12} \\ M_{21} & M_{22} \end{bmatrix} \begin{bmatrix} \ddot{\theta}_1 \\ \ddot{\theta}_2 \end{bmatrix} + \begin{bmatrix} C_{11} & C_{12} \\ C_{21} & C_{22} \end{bmatrix} \begin{bmatrix} \dot{\theta}_1 \\ \dot{\theta}_2 \end{bmatrix} + \begin{bmatrix} G_1 \\ G_2 \end{bmatrix} \quad (3.15)$$

$$\begin{aligned} M_{11} &= m_1 r_1^2 + m_2 (L_1^2 + r_2^2 + 2L_1 r_2 \cos \theta_2) + I_1 + I_2 \\ M_{12} &= M_{21} = m_2 (r_2^2 + L_1 r_2 \cos \theta_2) + I_2 & M_{22} &= m_2 r_2^2 + I_2 \\ C_{11} &= -2m_2 L_1 r_2 \sin \theta_2 \dot{\theta}_2 & C_{12} &= -m_2 L_1 r_2 \sin \theta_2 \dot{\theta}_2 \\ C_{21} &= m_2 L_1 r_2 \sin \theta_2 \dot{\theta}_1 & C_{22} &= 0 \\ G_1 &= (m_1 r_1 + m_2 L_1) g \cos \theta_1 + m_2 g r_2 \cos \theta_{12} & G_2 &= m_2 g r_2 \cos \theta_{12} \end{aligned}$$

The Coulomb and viscous friction models are employed in the friction model. T_{ci} and b_i represent the Coulomb and viscous friction coefficients for joint i :

$$\tau_f = T_{ci} \text{sgn}(\dot{\theta}_i) + b_i \dot{\theta}_i \quad i = 1, 2 \quad (3.16)$$

In order to identify the device dynamic parameters, Eq.(3.16) should be linearly parametrized so that it can be represented by the multiplication of two matrices which are composed of joint variables and device dynamic parameters respectively. Consequently, Eq.(3.16) can be rewritten as given in Eq.(3.17):

$$\tau = Y(\Theta, \dot{\Theta}, \ddot{\Theta})_{2 \times 9} \phi_{9 \times 1} \quad (3.17)$$

where Y is a regressor matrix and ϕ is a vector of nine unknown parameters as:

$$y_{11} = g \cos \theta_1 \quad y_{12} = \ddot{\theta}_1 \quad y_{13} = L_1^2 \ddot{\theta}_1 + L_1 g \cos \theta_1$$

$$\begin{aligned}
y_{14} &= 2L_1 \cos \theta_2 \ddot{\theta}_1 + L_1 \cos \theta_2 \ddot{\theta}_2 - 2L_1 \sin \theta_2 \dot{\theta}_1 \dot{\theta}_2 - L_1 \sin \theta_2 \dot{\theta}_2^2 + g \cos \theta_{12} \\
y_{15} &= \ddot{\theta}_1 + \ddot{\theta}_2 & y_{16} &= \dot{\theta}_1 & y_{17} &= 0 \\
y_{18} &= \text{sign}(\dot{\theta}_1) & y_{19} &= 0 & y_{21} &= y_{22} = y_{23} = 0 \\
y_{24} &= L_1 \cos \theta_2 \ddot{\theta}_1 + L_1 \sin \theta_2 \dot{\theta}_1^2 + g \cos \theta_{12} & y_{25} &= \ddot{\theta}_1 + \ddot{\theta}_2 \\
y_{26} &= 0 & y_{27} &= \dot{\theta}_2 & y_{28} &= 0 \\
y_{29} &= \text{sign}(\dot{\theta}_2) & \varphi_1 &= m_1 r_1 & \varphi_2 &= m_1 r_1^2 + I_1 \\
\varphi_3 &= m_2 & \varphi_4 &= m_2 r_2 & \varphi_5 &= m_2 r_2^2 + I_2 \\
\varphi_6 &= b_1 & \varphi_7 &= b_2 & \varphi_8 &= T_{c1} & \varphi_9 &= T_{c2}
\end{aligned}$$

φ components can be identified by means of force, velocity and acceleration measurements. A sample path is applied to the end-effector as shown in Figure 3.14a and corresponding force measurements are given in Figures 3.14b and 3.14c. The sample path is generated by two sine/cosine functions that are given in the figure. An artificial Gaussian noise with 0.075N standard deviation and zero mean in the range of ± 15 N is added to virtual force sensor measurement.

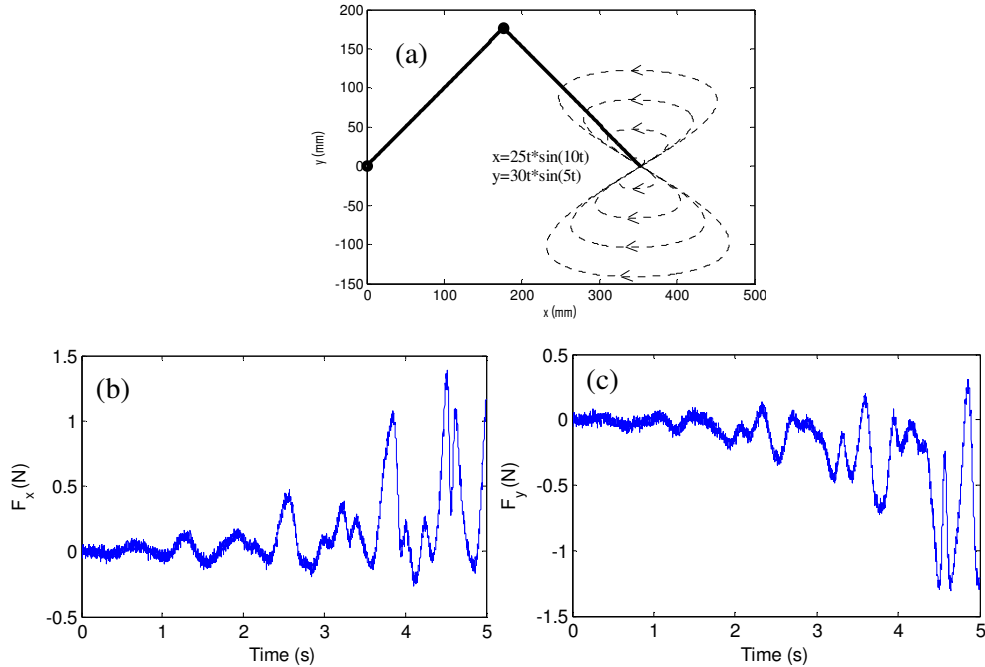


Figure 3.14 Sample path applied to the 2-DOFhaptic device (a), and force measurements at the handle (b, c)

Gauss-Newton nonlinear least-square estimation technique in [51] (MATLAB® “*lsqnonlin*”) is used to identify the parameters (φ_i) using the linearized equation of the motion based on the joints parasitic torque, velocity and acceleration data. As a result, real and identified values of the device parameters are given below:

Real parameters:

$$\begin{aligned} m_1 = m_2 &= 0.25 \text{ kg}, I_1 = I_2 = 0.0013 \text{ kgm}^2, r_1 = r_2 = 0.125 \text{ m} \\ T_{c1} = T_{c2} &= 0.009 \text{ Nm}, b_1 = b_2 = 0.004 \text{ Nms} \\ \varphi_1 &= 0.03125, \varphi_2 = 0.00521, \varphi_3 = 0.25, \varphi_4 = 0.03125, \varphi_5 = 0.00521 \\ \varphi_6 &= 0.009, \varphi_7 = 0.004, \varphi_8 = 0.009, \varphi_9 = 0.004 \end{aligned}$$

Identified parameters:

$$\begin{aligned} \hat{\varphi}_1 &\cong 0.03016, \hat{\varphi}_2 \cong 0.00512, \hat{\varphi}_3 \cong 0.24100, \hat{\varphi}_4 \cong 0.03198, \hat{\varphi}_5 \cong 0.00543 \\ \hat{\varphi}_6 &\cong 0.00912, \hat{\varphi}_7 \cong 0.00371, \hat{\varphi}_8 \cong 0.00872, \hat{\varphi}_9 \cong 0.00412 \end{aligned}$$

Figure 3.15 and 3.16 show the reconfigurable MATLAB®/Simulink model for the force control of a 2-DOF haptic manipulator. This Simulink model can be configured for different control algorithms by manual switches (OLIC, OLIC+MBC, CLIC, CLIC+MBC, CLIC+MCBC). Since a multi-DOF haptic manipulator should employ separate current based compensators in its each joint, two separate current based compensators are used for the 2-DOF haptic manipulator model. All current and force feedback signals have a Gaussian distributed noise with zero mean and 0.5% variance of the maximum range of the virtual sensors. These feedback signals are filtered by a low-pass filter with a 50 Hz cut-off frequency. Velocity and acceleration are estimated based on the enhanced adaptive windowing technique using 500 ppr artificial encoder model.

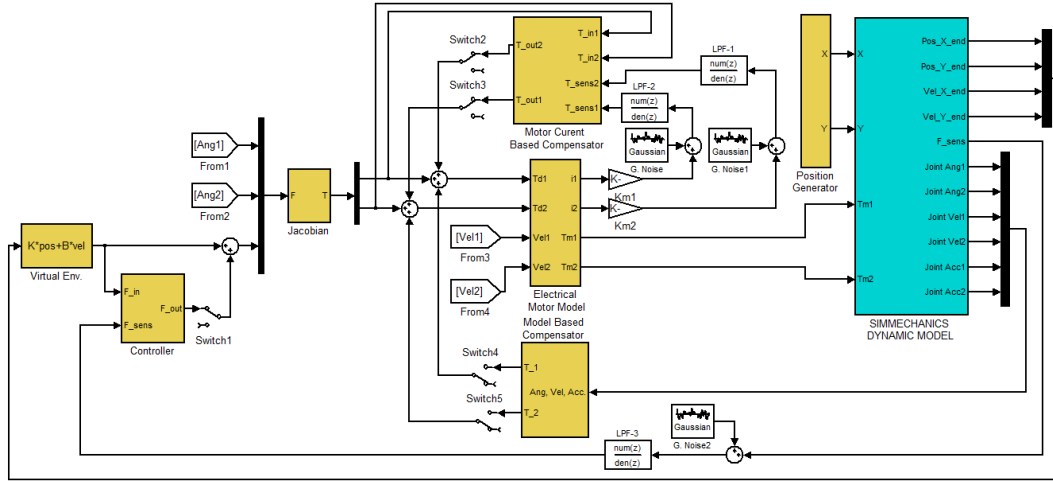


Figure 3.15 Reconfigurable MATLAB[®]/Simulink model for the Force Control of 2-DOF serial planar elbow type haptic manipulator

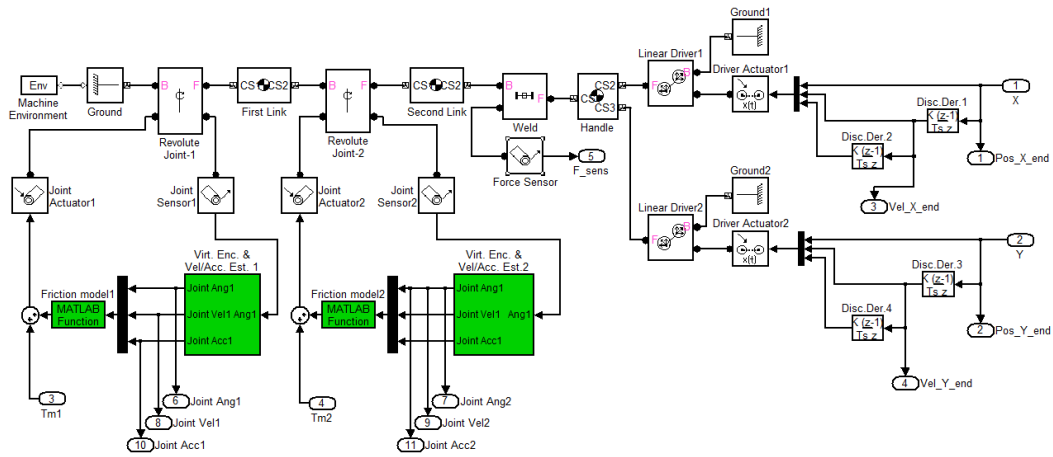


Figure 3.16 MATLAB[®]/SimMechanics model of the 2-DOF serial planar elbow type haptic manipulator

A sample test scenario was carried out in MATLAB[®]/SimMechanics to evaluate the performance of the proposed control algorithm. A virtual model with a stiffness (K) and damping (B) is located horizontally as shown in Figure 3.17 ($x=0$). End-point of the device is moved ± 100 mm range with different velocities and accelerations on the horizontal direction ($x = \pm \delta = \pm 100$ mm) by using the virtual drivers and actuators in MATLAB[®]/Simulink environment.

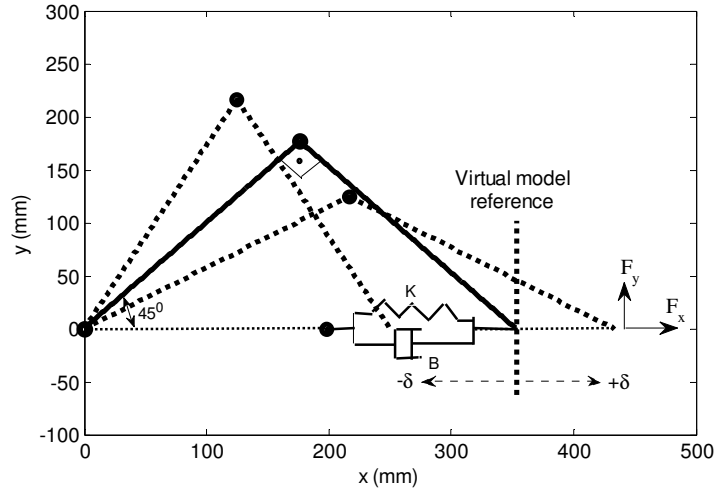


Figure 3.17 Sample test scenario for 2-DOF haptic manipulator

Using virtual drivers and actuators in MATLAB[®]/SimMechanics Toolbox, the robot handle is excited by using a chirp signal with continuous trajectories generated by $(\delta=0.1\sin(\pi t^2/2))$ m). The tests were conducted for two separate cases as mentioned in the experimental results section: (1) free-motion, where virtual stiffness - K and damping - B parameters are set to zero and (2) virtual-load is designated by defining stiffness - K and damping B .

Figure 3.18a presents the free-motion transparency measures for the proposed and alternative algorithms. It is desired that the device does not produce any parasitic forces. The results show that the proposed CLIC with MCBC algorithm is superior when compared to the others. Figure 3.18b and 3.18c show the virtual-load test results. The closeness of the measured and reference force values gives an idea about the quality of algorithms in terms of transparency. According to the test results, MCBC overcome the insufficiency of CLIC, it improves the transparency significantly. Consequently, it can be said that the proposed control algorithm is effective also for multi-DOF haptic systems.

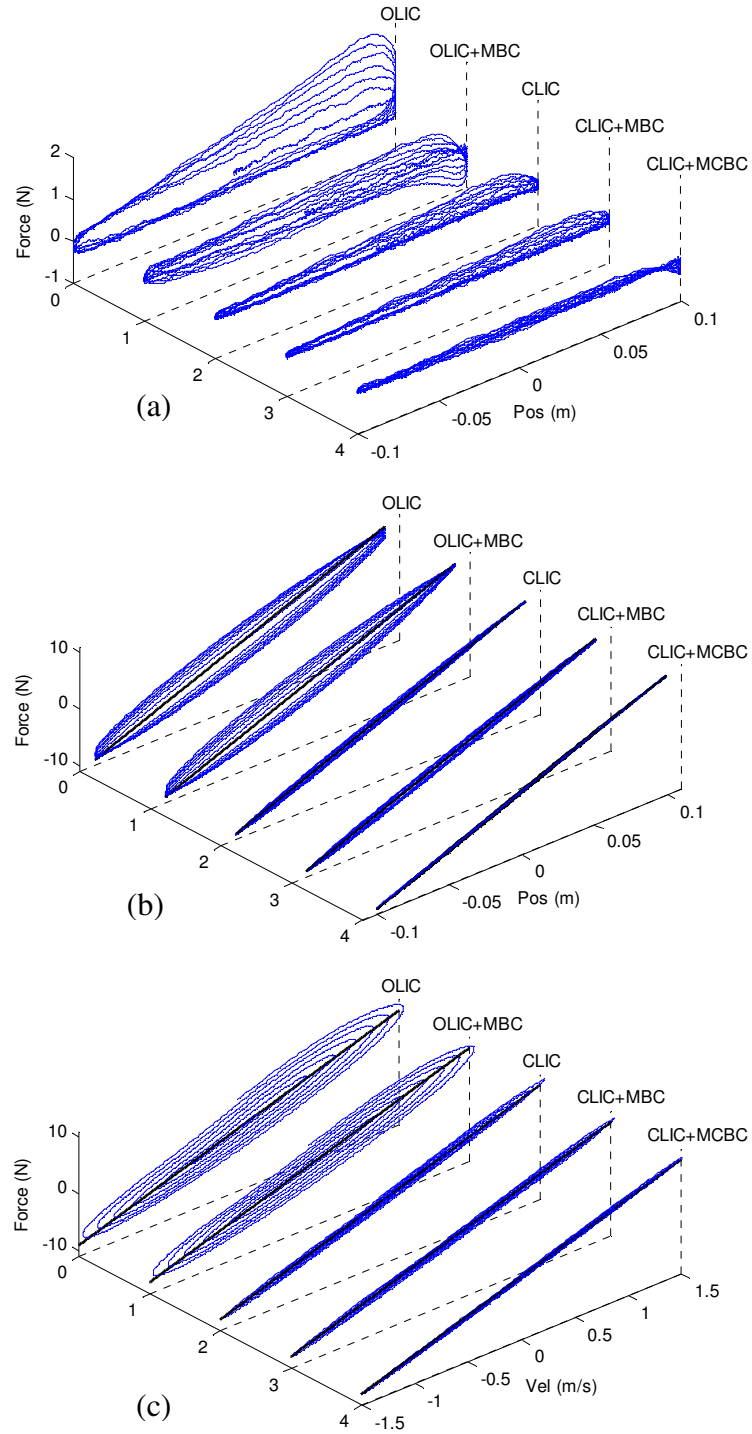


Figure 3.18 Transparency performance measures of 2-DOF haptic manipulator for (a) free-motion, (b) single virtual stiffness with $K=100\text{ N/m}$, and (c) single virtual damping with $B=6\text{ Ns/m}$

The proposed algorithm should be tested with different poses to show that it is effective in the whole workspace of the haptic device. For that purpose, same virtual model was located on the different coordinates with different poses. Figure 3.19 shows the sample five poses which were selected on a spiral path. The arrow shows the moving direction of the end-effector of the 2-DOF planar haptic device model. The same trajectory and motion characteristics defined in the previous tests were re-used. Figures 3.20a and 3.20b show the force error measurements of the virtual-load transparency tests achieved by the proposed CLIC and MCBC. The results show that the proposed algorithm keeps the transparency at high level in different poses of multi-DOF haptic system.

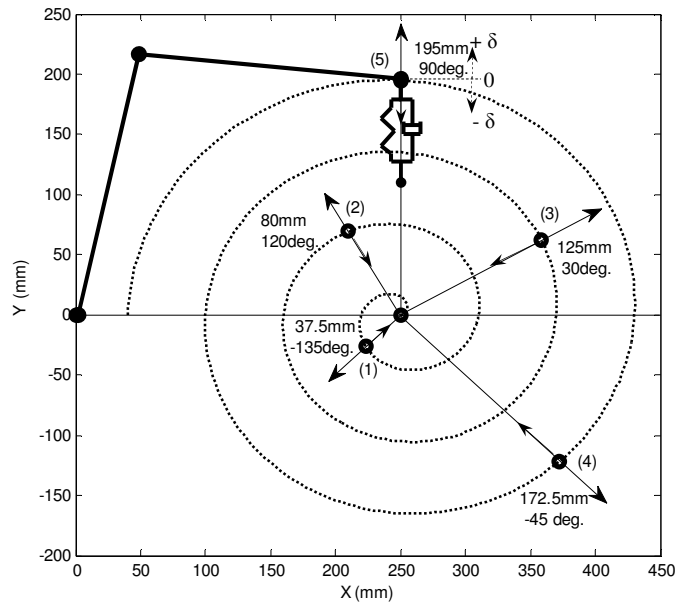


Figure 3.19 Virtual-load transparency measure tests for various poses in the workspace

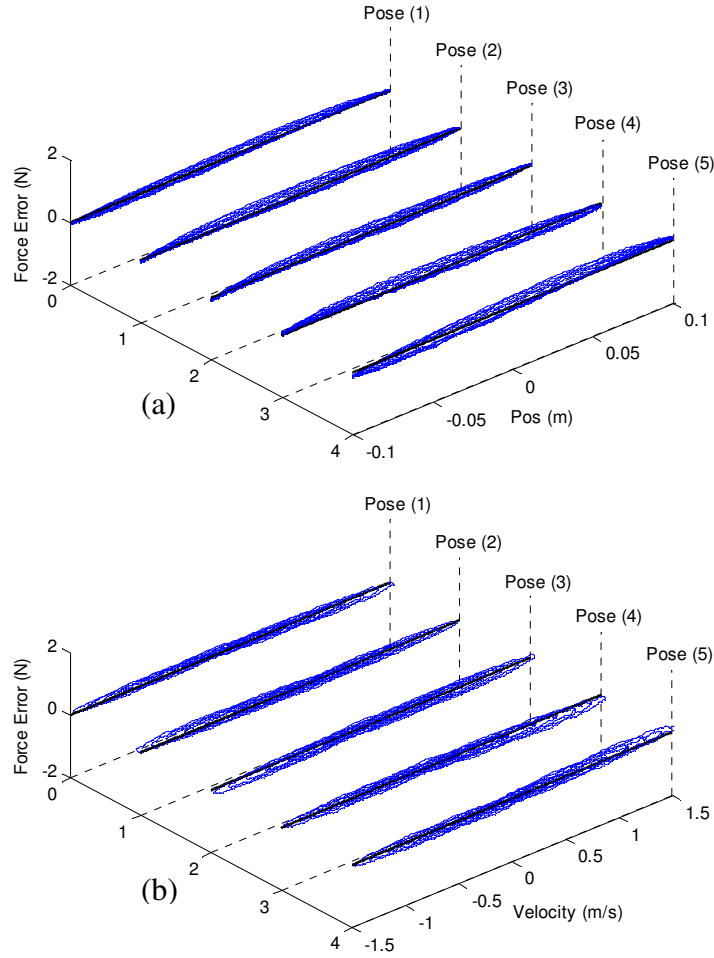


Figure 3.20 Transparency performance error measures of the CLIC with MCBC algorithm for (a) single virtual spring $K=100\text{ N/m}$, and (b) single virtual damping $B=6\text{ Ns/m}$ in various poses

3.8 Conclusion

Closed loop force control algorithms and model-based compensators are used in haptic interfaces to increase virtual environment simulation accuracy through the improvement of transparency. Since the proportional gain of the closed loop controller cannot be increased to high values due to the inherent dynamics of the haptic interface, the closed loop force control is not sufficient alone for the transparency. As an alternative, the model based compensators with disturbance parameter estimation are employed. However, they have some drawbacks too due

to the inevitable estimation errors in the disturbance model, velocity and acceleration. In this study, a motor current based torque feedback compensator is employed instead of model-based compensators to maximize the transparency. This technique works as a secondary controller in the closed loop impedance algorithm. The proposed algorithm is implemented on a 1-DOF HapticBox and showed in the simulation that it can be applied for muti-DOF haptic systems. The results show that the proposed algorithm is more effective than the conventional algorithms for the transparency maximization of the haptic interfaces.

CHAPTER 4

STABILITY IMPROVEMENT WITH HIGH TRANSPARENCY

4.1 Introduction

Since the haptic devices are evaluated in terms of stable impedance range and transparency, both of them should be improved together. However, the studies in the literature focused on either increasing stable impedance range or transparency improvement for haptic devices. In this section, firstly the passivity condition, which is required for the stable haptic interaction, is explained, then a literature survey about the stability improvement is presented and finally the transparency subject is reviewed over again.

The first parts of this section are dedicated to the the reason of instability in haptic interfaces and they are adapted from “Stability of Haptic Displays” Chapter in the book of “Haptic Rendering: Foundations, Algorithms, and Applications”, written by David Weir and Edward Colgate and edited by Ming Lin and Miguel Otaduy in order to explain clearly [54].

The objects in the real world interact based on the physical laws that govern their behavior. However, this interaction is only approximated in the virtual world. Even though the approximate behavior may be very close to the real behavior, the sum of these errors can lead to a considerable effect. Instability and limit cycle oscillations are two common ways in which haptic interactions deviate from their physical counterparts, both of which result from non-passivity. Everyday

interaction with common objects involves experiencing a wide range of impedances. Moving in free space implies almost zero resistance to motion, while interacting with tables, walls, and other massive objects provides almost complete resistance to motion. The aim in the haptic technology is to design haptic interfaces that can reflect as wide a range of dynamic impedances as possible.

Haptic interfaces are sampled-data systems. They combine a continuous-time mechanical system with a discrete-time controller. The effects of sampling, even assuming ideal sensors and actuators in the continuous-time plant, cause a haptic interface to lose passivity. The virtual wall is the standard haptic task. Since most interaction with virtual environments can be simplified to interaction with a virtual wall of varying stiffness and damping, the virtual wall is commonly used as a performance metric for haptic interfaces.

Simulating a stiff virtual wall is a difficult task due to the nature of sampling. The following example characterizes the general problem. As a general rule, there is always some penetration of the position of the haptic display into the virtual wall. As a consequence, at the next sampling interval, the discrete controller detects the wall penetration, and the virtual environment computes large output forces normal to the wall surface. This large force has a tendency to rapidly push the haptic display outside of the virtual wall into free space. This situation now reverses, where at some future sampling interval; the position of the haptic display is outside the virtual wall, so the forces return to zero. Oscillations arise when this cycle of free space and wall penetration is repeated. Sampling prevents detecting the exact time when the haptic display contacts the surface of the virtual wall, and position sensing resolution has the effect of quantizing penetration distance into the virtual wall, both of which are destabilizing effects. These errors can lead to energy generation and active, non-passive behavior. One consequence of optical encoders used in haptic interfaces is that position information is quantized based on the encoder resolution. The distinction between sampling and sensor quantization should be emphasized. Sampling introduces uncertainty with respect to when events occur and what happens between sampling intervals. Sensor

quantization causes a loss of information due to sensing only discrete changes in the value of a signal. Another effects which cause loss of information in haptic interfaces are the time delays due to the computational loads and network communications. The physical damping in the haptic display is critically important due to its role in counteracting the energy generation from errors introduced by sensing and discrete-time control. The disturbance compesation algorithms reduce the amount of physical damping in haptic interfaces; hence, increase the instability possibility. Additionally, the noisy and phase-lagged sensory signals are the other sources for the instability of haptic interfaces. In brief, the main factors for haptic devices to generate excess energy are:

- Information loss in A/D and D/A converters
- Computational delay
- Non-zero noise and non-zero phase-lag in velocity/acceleration estimators
- Non-zero noise and non-zero phase-lag in transducer signal filters
- Communication delays
- Disturbance compensation algorithms

Haptic interaction is a kind of a bi-directional energy flow system as the haptic devices operate in contact with the user's hand. The total of the energy contribution during the interaction should not exceed the initially stored energy to keep the haptic system passive and avoid the unstable vibrations. In other words, the energy flowing in a haptic system should not be below the initial energy to keep the system stable as formulated in Eq.(4.1). This equation represents the passivity condition that should be satisfied for stable interaction [55]. $F_h(\tau)$, $V_h(\tau)$ and E_0 in the equation represent the user hand force, user hand velocity and initial energy of the system at $t = 0$ respectively.

$$\int_0^t F_h(\tau)V_h(\tau)d\tau \geq -E_0 \quad \text{for } t > 0 \text{ and all admissible } F_h(t) \quad (4.1)$$

The passivity of haptic devices means that the actuators used in the haptic system should not generate excess energy causing undesired vibration to the user.

“Z-Width” plots are used for the evaluation of the stability in haptic devices. This evaluation technique is proposed by Colgate et. al. and it is defined as the passive impedance range that can be simulated stably by a haptic interface [56]. Thus, the Z-width plot illustrates the stable achievable limits of stiffness parameters (K) versus damping parameters (B) for a virtual wall collision (Figure 4.1).

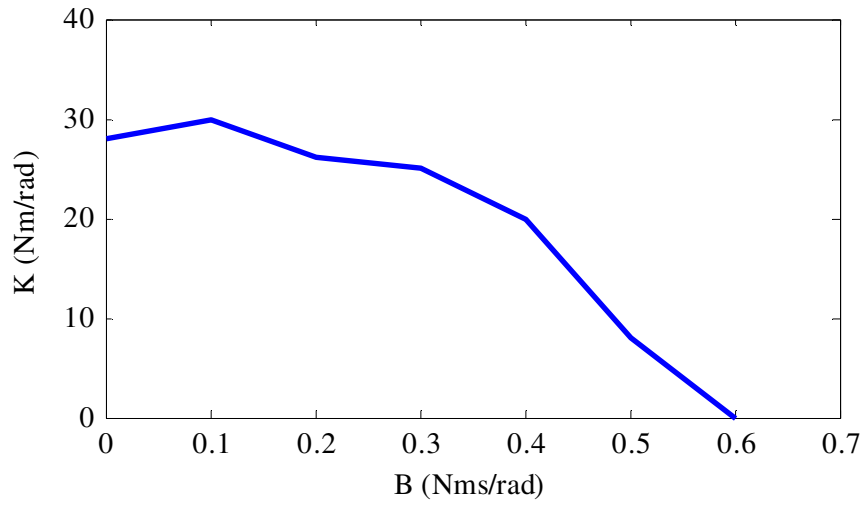


Figure 4.1 Typical Z-width for a 1-DOF rotational haptic interface

The physical damping of haptic systems dissipates the energy resulting from instability; consequently it changes achievable impedance range. Eq.(4.2) is the passivity criteria proposed by Colgate et. al. in terms of physical damping of haptic device (b), virtual model parameters (stiffness - K and damping - B) and sampling time (T). This equation indicates that increasing the physical damping “ b ” in the system improves the achievable impedance range of the haptic interface [56].

$$b > \frac{KT}{2} + B \quad (4.2)$$

Various methods are proposed in the literature to increase the stable impedance range of haptic devices. Colgate et. al. proposed passive and active electrical damping to satisfy the passivity condition [57, 58]. The occurrence of limit cycle oscillations can be reduced by electrical damping at especially high virtual impedances. Besides, the design of electrical damping is very simple and it can be made frequency dependent so that it does not adversely affect a device's low impedance range. Passive electrical damping generates frequency dependent damping by employing an electrical resistance and capacitance in parallel with the motor, but it is limited because of the resistance of the motor winding. Active electrical damping circumvents the limitation of the rotor resistance. It produces a continuous artificial damping proportional to motor velocity for excess energy dissipation. An analogue input shaper (AIS) is proposed by Lim et. al for stably increasing the displayable impedance range of haptic interfaces. [59]. The AIS employs a nonlinear low-pass filter for the purpose of a frequency-dependent dissipative element to eliminate these undesired high-frequency vibrations during haptic interaction. This proposed nonlinear low-pass filter is placed in the signal stage of the system so that it can be designed independently from motor parameters. Also, this AIS includes two linear half-wave rectifiers to enable a fast decrease of impedance and avoid negative input to the haptic interface when a haptic handle moves away for the virtual wall. Adjusting output limiter (AOL) is another control technique for stable haptic interaction [60]. Especially in the simulations of virtual models which changes in the geometry and/or impedance of the deformation model, such as cutting or suturing, a fast computation of the accurate impedance of deformable objects is not guaranteed always. These computational delays trigger the instabilities for haptic interaction. The proposed AOL ensures stable interaction with deformable objects of unknown and/or varying impedance. The controller adjusts the maximum allowable force to ensure the passivity of the haptic system at every sampling instant. The AOL controls only the final force output, and it is independent from the properties of the employed virtual model. This makes the proposed control method applicable to haptic systems involving deformable objects with unknown, nonlinear, and/or time-varying impedance. However this method suffers from oscillations for very

stiff walls due to the accumulation of past remaining dissipation in the memory. Another method is a time-domain passivity algorithm including a passivity observer and controller proposed by Ryu et al. [61-63]. The energy of the system is computed online at the passivity observer stage of the algorithm and the level of the energy is tested to decide whether it exceeds the initial energy or not at every sampling time. When excess energy occurs, it is dissipated by changing the reference actuator torque with a parameter employed in the passivity controller. This technique deviates the transmitted torque from the reference torque. However, the desired torque should be transmitted to the user transparently. Besides, the PO/PC technique is a velocity dependent approach and is problematic at low velocities due to the well-known difficulties of estimating noiseless velocity. Energy bounding algorithm (EBA) is another approach proposed by Kim and Ryu [64, 65]. The EBA restricts the energy generated by a sample-and-hold operator by the effective damping elements in the haptic interfaces. Besides, the algorithm provides that the virtual environment and controller are passive. Therefore, much stiffer contact simulation can be implemented. These guarantees stable haptic interactions, regardless of the sampling frequency and its variations; however, compromise the achievable impedance range. Kim and Ryu et. al also proposed a force bounding approach (FBA), which uses a derived force bounding equation depending upon the passivity condition to provide stable interaction [66]. Another study is the passive set-position modulation (PSPM) framework proposed for interactive robotic systems [67]. The PSPM modulates the set-position signal to its modulated version that is permissible by the available energy in the system for passivity in such a way that the modulated version is close as possible to the real set-position signal as possible for the performance [67]. The authors defined an artificial energy tanks to extract energy into them by using a constant viscous damper. The excess extracted energy is artificially dissipated by thresholding the level of the energy tank. All of these studies improve the stability. However, the effect of the improved stability on the transparency of the device has not been investigated. Recently, Franken et. al. [68, 69] proposed a two-layer control technique which is proposed to optimize the transparency and the stability of bilateral telemanipulation systems. This technique splits the control

algorithm into two separate layers: a transparency layer hierarchically on the top and a passivity layer on the lower. The proposed two-layer algorithm has an adjustment stage limiting the transparency layer torque. These limiting made by the adjustment stage to the commands of the bilateral controller can have a negative effect on the achievable transparency in the telemanipulation system [68].

The impedance of the virtual environment should be transmitted to the user without parasitic torque effects (device dynamics, friction and gravity) to keep the transparency high. Figure 4.2 shows the simplified block diagram of a haptic interaction including virtual environment impedance and transmitted impedance [34]. The ratio of the transmitted impedance - Z_M (the desired force $-F_D$ over input velocity $-V_D$) and the virtual environment impedance – Z_D (the measured force F_M over output velocity V_M) should be a gain of near unity over its maximum bandwidth [37].

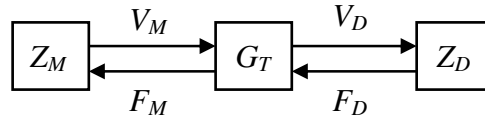


Figure 4.2 Simplified block diagram of haptic interaction [34]

The transfer function (G_T) of transparency can be defined by the ratio of the impedances. This transfer function can be used to test the transparency of haptic interfaces.

$$G_T = \frac{Z_M}{Z_D} \quad (4.3)$$

This equation enables to find the transparency bandwidth to evaluate the transparency performance of the haptic system. It is defined as 3dB crossover frequency from 0dB for the transfer function [34]. A haptic system can simulate

the virtual environment properly at the frequencies within the transparency bandwidth. Since the parasitic torques/forces coming from the mass/inertia, friction and gravity decrease the magnitude of transparency bandwidth, they need to be reduced or eliminated. The transparency improvement studies in the literature are already mentioned in Chapter 3.

In this chapter, firstly, it is explored that there is an inverse correlation between the transparency and achievable impedance range in the case that only active actuators are used in the force control algorithms. According to this exploration, the transparency improvement algorithms employing only active actuators decrease the stable impedance range. On the other hand, passive brakes can transmit high impedances in stable, but are not sufficient for transparency. In this chapter, secondarily, it is proposed to utilize both active actuator and passive brake in a haptic device to improve the transparency and stable impedance range together. A new hybrid control technique is developed to divide the task between the actuators for that purpose. There are several studies in the literature employing hybrid actuators; however, they focused on the stability improvement and did not investigate how the transparency is affected [70, 71]. Nam et. al. [72] proposed to improve the transparency by a hybrid actuation using friction compensation algorithm depending upon velocity measurements, but they did not examine their algorithm in high frequencies.

The rest of the paper is organized as follows: The contribution is explained in the following section. The next section presents an overview of the transparency improvement and the relation between the transparency and stable impedance range in haptic interfaces. Then the proposed hybrid algorithm is introduced. The experimental results and performance evaluations are discussed in the next section. The last section is related to the conclusion part of the research.

4.2 Contribution

When using active actuators in haptic devices, transparency improvement algorithms tend to decrease the range of achievable impedances. On the other

hand, passive brakes can provide stable interaction even for high virtual impedances, but are not sufficient for transparency. There exist an inverse correlation between the stable impedance range and transparency in haptic interfaces employing only one type of actuator. The first contribution of this chapter is a hybrid control algorithm employing both active actuator and passive brake to incorporate their advantages in a single haptic interface. In this algorithm, the active actuator helps increase the transparency while the passive brake reduces the demand on the active actuator to improve the stability. Second contribution of the chapter is a novel transparency metric plot so-called *transparency Z-width plot* to evaluate the stable impedance range and transparency together. This plot shows the transparency bandwidths of the achievable impedances as colored maps and gives an idea to the readers about both the stable impedance limit and the magnitude of transparency bandwidth under this limit. The proposed algorithm was experimentally compared with the conventional force control algorithms on a 1-DOF hybrid haptic device. The results show that proposed algorithm provides larger stable impedance ranges with higher transparency than the others.

4.3 Relation between Transparency and Stability in Haptic Devices

The closed loop impedance control (CLIC) algorithms and model-based compensators (MBC) are frequently employed in haptic devices for the transparency improvement. Besides, a current based compensator (MCBC), which is superior over them, is proposed in Chapter 3. All details about these algorithms are explained in the previous chapter. In this section, the performances of these algorithms are compared in frequency domain on an experimental hardware including an excitation motor and explored how they affect the stable impedance range.

A 1-DOF hybrid haptic device was designed in this study; it is a simply rotary handle as shown in Figure 4.3. The handle is actuated by active actuator and passive brake. While the rear end of the device driven by active actuator and

passive brake operates haptic simulation, another actuator attached on the front end is used to excite the handle for the frequency domain transparency tests.

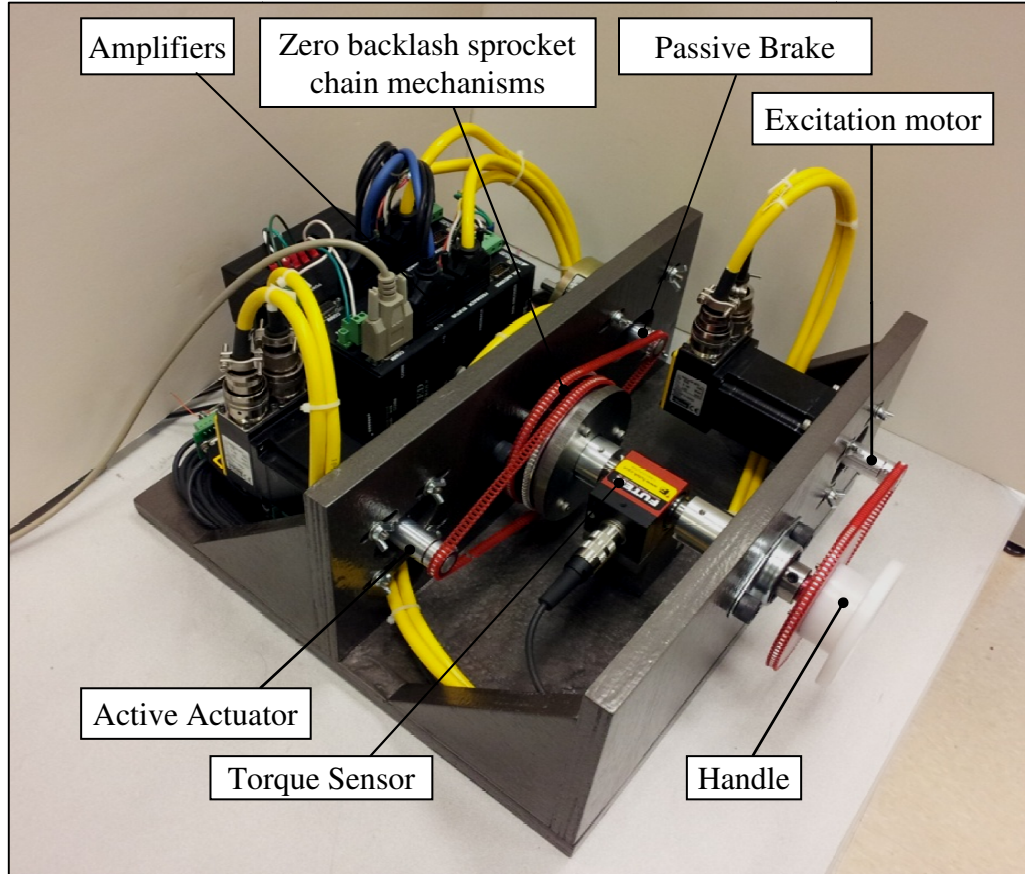


Figure 4.3 Experimental setup with a 1-DOF haptic device

In the hardware, the active actuating unit is a *Parker BE232FJ* brushless DC motor with a 473W power. It is connected to a *AMC-DPRANIE-015A400* Brushless DC Servo Amplifier. The actuator torque is increased using sprocket and chains with a 96/20 gear ratio. The passive actuating unit is *Placid BE15 Particle Magnetic Brake* with 1.7 Nm maximum torque. There are optical encoders attached to the motors with 2000 pulses per revolution. *Futek FSH01987* torque transducer with $\pm 10\text{Nm}$ range is attached to the handle. The control algorithm is implemented by means of Quarc v2.2 software. The technical properties of computer used in application are Intel[®] Core[™] i7-2600 (3.40 GHz, 8

MB cache, 4 cores), 4 GB Ram, AMD Radeon HD 6350 (512 MB) graphics card. The PC has one Quanser Q4 Series I/O cards which is used to acquire signals coming from the sensors and send reference signals to the amplifiers.

The equivalent inertial and frictional parameters of the experimental hardware should be identified, and velocity/acceleration should be estimated with an efficient method to implement the MBC algorithms on the setup. The second order enhanced adaptive windowing method is used to estimate the velocity and acceleration for model-based compensation. The details of this method can be found in Chapter 2 [29]. Besides, Gauss-Newton nonlinear least-square estimation technique explained in Chapter 3 [51] was applied on the torque, velocity and acceleration measurements of a simple free motion experiment. As a result, equivalent inertia, viscous friction and static friction parameters were found as ($I_{eq}=0.001 \text{ kgm}^2$, $b_{eq}=0.005 \text{ Nms/rad}$ and $T_{Ceq}=0.15 \text{ Nm}$).

A set of experiments was carried out to find the transparency bandwidth of the algorithms for a virtual load simulation. Since the user's hand cannot excite the device at high frequencies, it is not possible to find exact transparency bandwidth with the experiments excited by the user hand [43, 44]. Therefore, an excitation motor is attached to the front end of the device to be used in the transparency bandwidth experiments. The excitation motor produces a white noise torque input to the handle in these experiments; then the transmitted impedance, Z_M , was estimated as a function of the frequency by using Eq.(4.4). Nominator and denominator of this equation represent the cross power spectral density (Φ_{VF}) between the motion input and force output and the power spectral density (Φ_{VV}) of the motion input, respectively [73, 74]. Finally, the transparency transfer function can be estimated by dividing the transmitted impedance Z_M by the desired impedance Z_D . The desired impedance in the experiments were set to $K=10 \text{ Nm/rad}$ and $B=0 \text{ Nms/rad}$ for the entire frequency range. Figure 4.4 shows the bode diagrams of algorithms obtained from the transparency bandwidth experimental results. The CLIC+MCBC algorithm gives the maximum bandwidth and the phase difference remains almost zero within this increased bandwidth.

$$Z_M(j\omega) = \frac{\phi_{VF}(j\omega)}{\phi_{VV}(j\omega)} \quad (4.4)$$

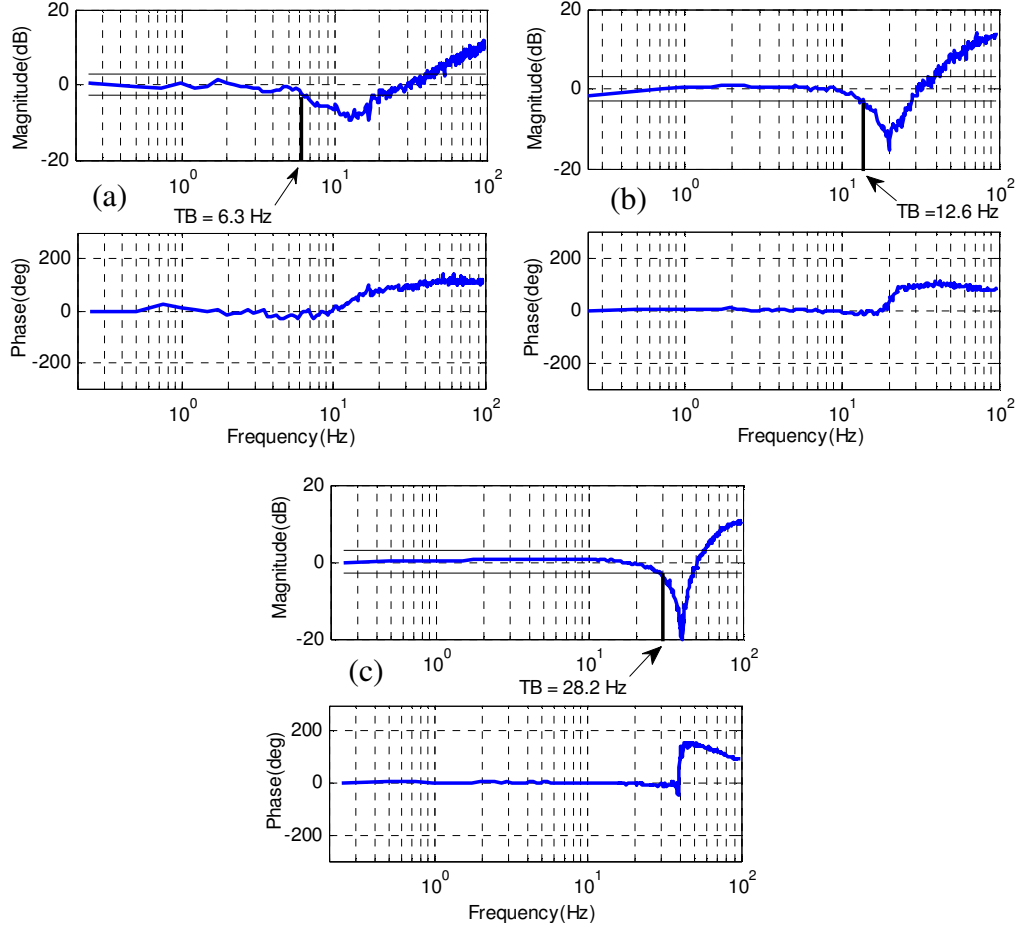


Figure 4.4 Transparency measures for a virtual spring ($K=10 \text{ Nm/rad}$) in frequency domain. (a) OLIC+MBC, (b) CLIC+MBC, (c) CLIC+MCBC

Secondarily, it needs to be investigated that how the stable impedance range is affected by different control algorithms and what is the relation between the stability and transparency. For that purpose, Z-width plots of the force control algorithms were generated as given in Figure 4.5. Each algorithm was tested on various virtual walls which are designed with different impedances (K - B) to generate these plots. The Z-width plots show the limits where unstable vibrations (over 50 Hz) start for the different algorithms. The results can be interpreted such

that: (1) CLIC+MCBC, which is superior in transparency, resulted in minimum stable impedance range, (2) the OLIC+MBC, which is poor in transparency, can simulate the largest range. The main reasons of the decrease in the achievable impedance range while the increase in the transparency is that the transparency maximization algorithms entail sensory feedback data which are generally noisy and eliminate the physical damping of the system.

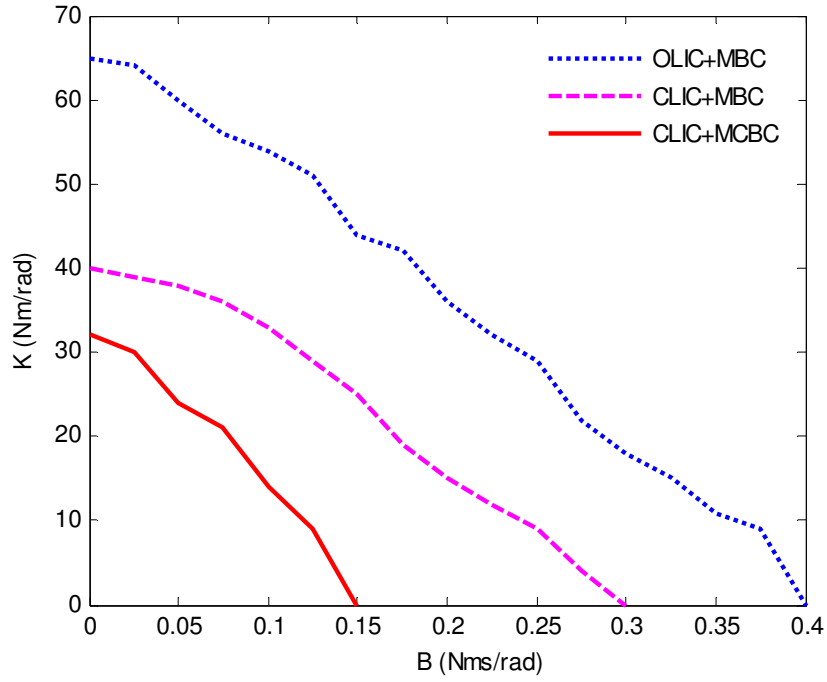


Figure 4.5 Z-width plot of transparency improvement algorithms

As it can be seen from the transparency bandwidth and Z-width plots, the stability and transparency criteria need to be considered and improved together. Thus, high impedances should be transmitted stably and with high transparency in haptic interfaces. Therefore, a hybrid control algorithm was developed by employing both active actuator and passive brake in this chapter. The following sections are devoted to explaining the passive brakes, proposed hybrid algorithm and its experimental results.

4.4 Passive Brakes

As mentioned in the previous section, the haptic devices employing only active actuators such as electrical motors provide transparent haptic interaction but suffer from the instability when high virtual impedances needs to be simulated. Alternatively, passive brakes are used in haptic device designs due to their stable response even for high virtual impedances. There are two main passive brakes in the literature: (1) Magnetic particle brakes and (2) Magnetorheological (MR) brakes.

Magnetic particle brakes are superior in their design over other electromechanical brakes as they provide the wider operating torque range with smaller size [75]. The torque to voltage is almost linear in the magnetic particle brakes and the torque can be controlled much accurately than the electromechanical brakes. This makes them promising candidates for torque control applications. Figure 4.6a shows a schematic view of a magnetic particle brake. Magnetic particles such as iron filings are located in the powder cavity of the brake. When voltage/current is applied to the coil, the magnetic flux is created, and this magnetic flux starts to combine the particles together. As the voltage/current is increased, the combining particles become stronger. The brake rotor passes through these bound particles. As the particles start to combine together, a resistant force is created on the rotor, and hence creates a resistance torque on the output shaft.

Magnetorheological (MR) brakes change the viscosity of a MR-fluid inside the brake by magnetic field to produce resistance torque [76]. Although the viscosity of this fluid is similar to low viscosity oil in the inactive state, the magnetic field changes the viscosity of the fluid with a consistency similar to peanut butter. MR-brakes have very desirable characteristics, such as high torque-to-volume ratio, inherent stability, easy control, and simple interface between the mechanical and electrical systems. Therefore, they are frequently employed in many applications including civil engineering, haptics, exercise equipments, automobile suspensions,

vibration control, prosthetics, and tactile displays. Figure 4.6b shows the schematic view of a typical MR brake.

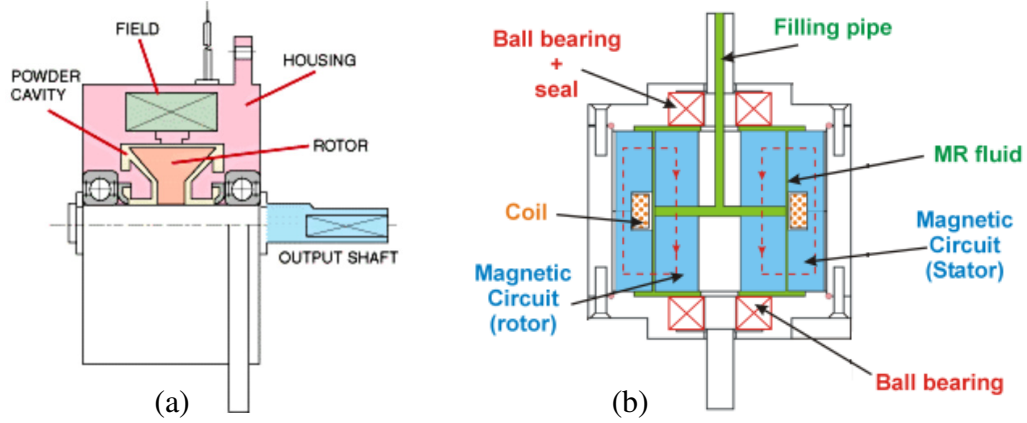


Figure 4.6 Schematic views of typical magnetic particle brake [75] (a) and MR brake [77] (b)

Although passive brakes have some major advantages such as high torque-to-volume ratio, inherent stability, easy control, and simple interface, they have some difficulties to be handled such as slow response time, sticking, and hysteresis effect. The hybrid algorithm which will be explained in the next section overcomes these disadvantages while improving the stability characteristic of active actuators.

4.5 Modified Passivity Condition and Proposed Hybrid Control Algorithm

The CLIC+MCBC algorithm proposed in Chapter 3 is superior over other conventional algorithms to transmit the desired impedances transparently at even high frequencies; but this algorithm adversely affects the achievable impedance range. The reason for this adverse effect is based on the passivity criteria. In this section, the mathematical derivations to explain the passivity criteria and the concept of the proposed hybrid algorithm are presented.

Figure 4.7 shows the simplified 1-DOF rotational haptic interface configuration. An overall haptic interface configuration can be represented by the combination of haptic device, sample/hold unit, controller and virtual environment. $\dot{\theta}_h$, $\dot{\theta}_d$, $\dot{\theta}_e$, T_h , T_d , T_a , T_e , b , T_c , I symbols in this figure denote the user hand velocity, device velocity, transmitted velocity to virtual environment, torque applied by user hand, desired actuator torque, hold device actuator torque by DAC, reference torque calculated in virtual environment, viscosity, Coulomb friction and inertia, respectively.

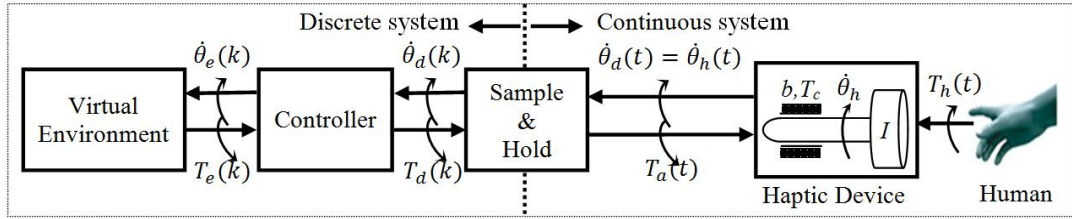


Figure 4.7 Overall configuration of a 1-DOF rotational haptic interface

The basic passivity condition is briefly mentioned in the first section and it is represented by Eq.(4.1) which means that the energy-flow in a haptic system should not exceed the initial energy in the haptic interfaces. However, this equation is inexplicit to develop a new passivity based force control algorithm. This equation can be rewritten by considering dynamic equilibrium of the 1-DOF rotational haptic device configuration during $0 \leq t \leq nT$ through Eqs.(4.5-4.7).

Dynamics equilibrium of a haptic device can be expressed as follow:

$$T_h(t) = I\ddot{\theta}_h(t) + b\dot{\theta}_h(t) + \text{sgn}[\dot{\theta}_d(t)]T_c + T_a(t) \quad (4.5)$$

By substituting Eq.(4.5) into Eq.(4.1), the passivity condition can be rewritten as:

$$\int_0^{nT} [I\ddot{\theta}_h(t) + b\dot{\theta}_h(t) + \text{sgn}[\dot{\theta}_d(t)]T_c + T_a(t)] \dot{\theta}_h(t) dt \geq -E_0 \quad (4.6)$$

Since the velocities/accelerations of the device and human hand are the same in a haptic interaction ($\dot{\theta}_d(t) = \dot{\theta}_h(t)$), the passivity condition can be expressed as:

$$\begin{aligned} \int_0^{nT} I \ddot{\theta}_d(t) \dot{\theta}_d(t) dt + \int_0^{nT} b \dot{\theta}_d^2(t) dt + \int_0^{nT} \text{sgn}[\dot{\theta}_d(t)] T_c \dot{\theta}_d(t) dt \\ + \int_0^{nT} T_a(t) \dot{\theta}_d(t) dt \geq -E_0 \end{aligned} \quad (4.7)$$

The first term in Eq.(4.7) indicates energy storage by the inertia and it has finite nonnegative value for finite velocity motion. Therefore, it can be rewritten as given in Eq.(4.8). Note that in our experiment since the total initial energy E_0 at $t = 0$ includes the initial kinetic energy by the inertia, the term of $(I\dot{\theta}_d^2(0)/2)$ was eliminated in Eq.(4.8).

$$\begin{aligned} \int_0^{nT} I \ddot{\theta}_d(t) \dot{\theta}_d(t) dt &= I \int_0^{nT} \dot{\theta}_d(t) \frac{d\dot{\theta}_d}{dt} dt = I \int_0^{nT} \dot{\theta}_d(t) d\dot{\theta}_d \\ &= \frac{1}{2} I \dot{\theta}_d^2(n) - \frac{1}{2} I \dot{\theta}_d^2(0) = \frac{1}{2} I \dot{\theta}_d^2(n) \end{aligned} \quad (4.8)$$

The second term of Eq.(4.7) indicates energy dissipation by the viscous damper and it can be rewritten by Cauchy-Schwarz inequality [78] as;

$$\begin{aligned} \int_0^{nT} b \dot{\theta}_d^2(t) dt &= \sum_{k=0}^{n-1} b \int_{kT}^{(k+1)T} \dot{\theta}_d^2(k) dt \geq \sum_{k=0}^{n-1} \frac{b}{T} \left[\int_{kT}^{(k+1)T} \dot{\theta}_d(k) dt \right]^2 \\ &= \frac{b}{T} \sum_{k=0}^{n-1} [\theta_d(k+1) - \theta_d(k)]^2 \end{aligned} \quad (4.9)$$

The third term of Eq.(4.7) represents the energy dissipation by the Coulomb friction of the system and it can be rewritten as:

$$\begin{aligned}
\int_0^{nT} \text{sgn}[\dot{\theta}_d(t)] T_c \dot{\theta}_d(t) dt &= T_c \sum_{k=0}^{n-1} \text{sgn}[\dot{\theta}_d(k)] \left[\int_{kT}^{(k+1)T} \dot{\theta}_d(k) dt \right] \\
&= T_c \sum_{k=0}^{n-1} \text{sgn}[\dot{\theta}_d(k)] [\theta_d(k+1) - \theta_d(k)]
\end{aligned} \tag{4.10}$$

The last term of Eq.(4.7) indicates energy flow into the subsystem which is composed of sample and hold, controller, and virtual environment. When ZOH is used for hold operator, it can be rewritten as given in Eq.(4.11). It is assumed that the actuator torque is equal to the desired actuator torque at the sample/hold unit for Eq.(4.11) ($T_d = T_a$).

$$\begin{aligned}
\int_0^{nT} T_a(t) \dot{\theta}_d(t) dt &= \sum_{k=0}^{n-1} \left[\int_{kT}^{(k+1)T} T_a(t) \dot{\theta}_d(k) dt \right] \\
&= \sum_{k=0}^{n-1} T_d(k) [\theta_d(k+1) - \theta_d(k)]
\end{aligned} \tag{4.11}$$

The passivity condition can be expressed in discrete time using Eqs.(4.8-4.11) as given in Eq.(4.12). This passivity condition also includes an initial energy term (E_0) on the right hand side since the system may have stored an initial energy at $t=0$ such as potential energy from a compressed virtual spring or kinetic energy from an accelerated physical inertia, etc.

$$\begin{aligned}
\frac{1}{2} I \dot{\theta}_d^2(n) + \frac{b}{T} \sum_{k=0}^{n-1} \Delta \theta_d^2(k+1) + T_c \sum_{k=0}^{n-1} \text{sgn}[\dot{\theta}_d(k)] \Delta \theta_d(k+1) \\
+ \sum_{k=0}^{n-1} T_d(k) \Delta \theta_d(k+1) \geq -E_0
\end{aligned} \tag{4.12}$$

where n is the last sampling and $\Delta \theta_d(k+1) = [\theta_d(k+1) - \theta_d(k)]$. The first three terms are always positive in Eq.(4.12) and the only last term is the excess

energy source by actuator employed in the device. If the extracted energy exceeds the initially stored energy, the device starts to produce undesired vibrations, which cause instability. Especially, when high impedances need to be simulated, the desired actuator torque increases and the passivity criterion formulated in Eq.(4.7) cannot be met. The energy by active actuator must not exceed the passivity limit for the stability.

In this study, it is proposed to use a hybrid technique employing both active actuator (such as motor) controlled by CLIC+MCBC algorithm and passive (brake) actuator controlled by only CLIC algorithm. The hybrid algorithm provides a task sharing between the actuators. In this way, the desired torque is guaranteed for high transparency and the passivity leading to stability is ensured. Besides, this proposed algorithm overcomes the disadvantages of the passive brake such as residual torque and hysteresis effects. A task divider parameter (α) is employed to share the task between the active actuator and passive brake. The active actuator is fully activated if α is equal to zero. Similarly, the passive brake is fully active when α is equal to one. In the hybrid control, the desired actuator torque T_d is achieved transparently by the sum of passive (brake torque - T_{db}) and active actuator torques (motor torque - T_{dm}), as formulated in Eq.(4.13).

$$\begin{aligned} T_d(t) &= T_{db}(t) + T_{dm}(t) \text{ such that} \\ T_{db}(t) &= \alpha T_d(t) \text{ and } T_{dm}(t) = (1 - \alpha)T_d(t) \end{aligned} \quad (4.13)$$

In this way, a modified passivity condition can be derived for the proposed hybrid algorithm through Eqs.(4.14)and (4.15).

The last term in Eq.(4.12) can be divided into two parts:

$$\frac{1}{2}I\dot{\theta}_d^2(n) + \frac{b}{T} \sum_{k=0}^{n-1} \Delta\theta_d^2(k+1) + T_c \sum_{k=0}^{n-1} \text{sgn}[\dot{\theta}_d(k)]\Delta\theta_d(k+1) \quad (4.14)$$

$$+ \sum_{k=0}^{n-1} T_{db}(k) \Delta \theta_d(k+1) + \sum_{k=0}^{n-1} T_{da}(k) \Delta \theta_d(k+1) \geq -E_0$$

Then, the modified passivity condition can be represented by including task divider parameter (α) as:

$$\begin{aligned} \frac{1}{2} I \dot{\theta}_d^2(n) + \frac{b}{T} \sum_{k=0}^{n-1} \Delta \theta_d^2(k+1) + T_c \sum_{k=0}^{n-1} \text{sgn}[\dot{\theta}_d(k)] \Delta \theta_d(k+1) \\ + \sum_{k=0}^{n-1} \alpha T_d(k) \Delta \theta_d(k+1) + \sum_{k=0}^{n-1} (1 - \alpha) T_d(k) \Delta \theta_d(k+1) \geq -E_0 \end{aligned} \quad (4.15)$$

Only the last term in the modified equation, which corresponds to the energy contributed by the active actuator (motor), is the excess energy source. The first three terms represents the energy contribution by the passive elements (inertia, damping and friction). The task divider parameter (α) balances the energy contribution levels in Eq.(4.15) to satisfy the passivity condition when unstable vibration starts. In the meantime, the desired torque is achieved transparently by the CLIC+MCBC part of the hybrid algorithm.

Figure 4.8 shows block diagram of the hybrid algorithm. The upper branch of the block diagram after Controller-I represents the passive brake control loop while the lower one is for the active actuator. The details of the active actuator loop (CLIC+MCBC) are presented in Chapter 3. Passive brake control loop comprises look-up, current amplifier and particle brake blocks. The look-up block in the diagram represents the current vs. desired brake torque characteristics, which is taken from the technical specification documents of the particle brake, and is used to calculate the amount of reference current for a desired brake torque in the brake control stage. Particle brake block shows the physical particle brake producing the required torque in hybrid algorithm.

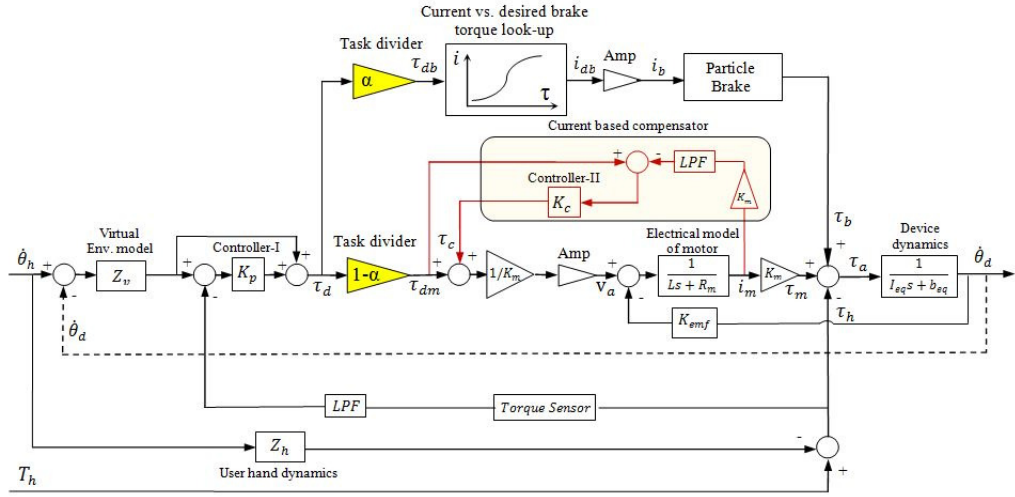


Figure 4.8 Hybrid control algorithm using active actuator and passive brake for a 1-DOF rotational haptic device

4.5.1 Task Divider (α) and Smooth Transition Width (δ) Parameters

Since all instability triggering effects (i.e. the loss of information in the sample/hold unit, noisy sensory data, inaccurate velocity estimation, computational load, and dynamics compensation algorithms) are coupled in a haptic interface, it is very hard to estimate task divider parameter mathematically. Therefore, an experimental estimation technique is proposed for the task divider parameter (α). In this technique a high pass filter is employed as a unstable vibration detector. Unstable interaction causes undesired vibrations in the device and the monitored motor power signal ($P=i^2R$) oscillates with high frequency. The oscillating parts of the signal can be extracted by the high pass filter employed in the proposed estimation technique. In this way, unstable vibrations can be detected. Since the human hand senses the vibrations above frequencies of 50 Hz [79] and the vibrations under this limit do not deteriorate the smooth interaction, the cut-off frequency of the detector was set to 50 Hz. Figure 4.9a-c shows sample active actuator power measurements and its high-pass filter output for a virtual wall collision with very high impedances.

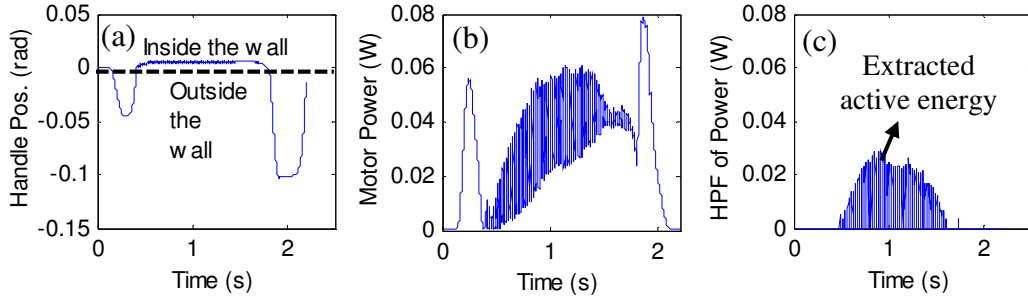


Figure 4.9 Sample unstable virtual wall collision (a) position, (b) motor power signal, (c) high-pass filter output of motor power signal (P_{HPF})

Non-zero output of the unstable vibration detector (P_{HPF}) indicates that there exists undesired active energy to be removed from the system. In the proposed estimation technique, the value of the task divider is increased when the detector senses an unstable vibration until it is eliminated. Hence, the modified passivity condition in Eq.(4.15) is satisfied for stable interaction.

Another problem in the implementation of hybrid algorithm is a jumping effect in wall collisions, resulting from the threshold between the brake and motor response times. The motor is activated suddenly when just moving out of the wall for full transparency in free-motion. On contrary the brake cannot be deactivated quickly due to its slow response (Figure 4.10a). This jumping effect in the hybrid algorithm can be handled by applying a smooth transition of the task divider parameter around the virtual wall. The proposed smooth transition model around the virtual wall is shown in Figure 4.10b. This model primarily starts the activation of the brake a while before touching the virtual wall. A smooth transition width (δ) is employed to achieve this early activation, which is defined as total traveling distance required for full activation of the brake. The integration of the device velocity ($\dot{\theta}_d$) over response time (t_r) gives the required smooth transition as formulated in Eq.(4.16). The amount of the smooth transition width depends on the approach velocity since longer traveling distance is required at higher velocities to complete full activation in the brake response time.

$$\delta = \int_0^{t_r} \dot{\theta}_d dt \quad (4.16)$$

The task distribution achieved by the proposed smooth transition model during transition is formulated in Eq.(4.17) where θ and $\hat{\alpha}$ denote the handle position and estimated value of the task divider parameter, respectively. Using this smooth transition model enables elimination of the jumping effect when just moving out of the wall. The proposed model also provides quick response for the hybrid device.

$$\begin{aligned} T_{db} &= \hat{\alpha} \left| \frac{2\theta - \delta}{2\delta} \right| T_a \text{ for all } \theta \text{ between } \mp \delta/2 \\ T_{dm} &= \left(1 - \hat{\alpha} \left| \frac{2\theta - \delta}{2\delta} \right| \right) T_a \text{ for all } \theta \text{ between } \mp \delta/2 \end{aligned} \quad (4.17)$$

In order to implement the proposed transition model to eliminate the jumps around the virtual wall surface, the smooth transition width (δ) should be estimated carefully. Like experimental task divider parameter estimation, a secondary algorithm is proposed to estimate the width for the smooth transition. The high pass filter output of the instantaneous torque measurements (T_{HPF}) is used to detect the jumps when moving away from the wall. Figure 4.11a-c shows a sample instantaneous torque measurement and its high-pass filter output when moving away from the virtual wall. The smooth transition width is increased until the jumps are completely cleared away. This technique is called as smooth transition width estimation algorithm. Figure 4.12 shows the flow charts of these task divider parameter and smooth transition width estimation algorithms.

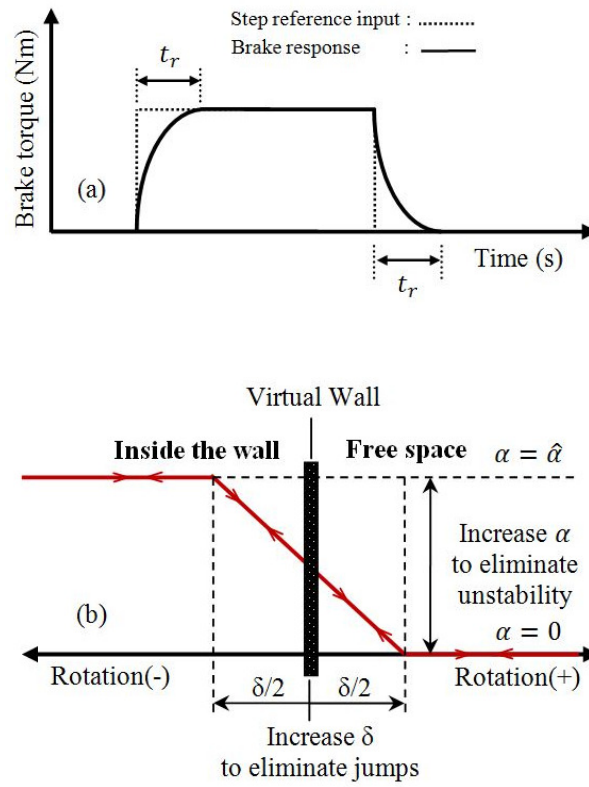


Figure 4.10 Step response of the particle brake (a) and the smooth transition model of dividing parameter (b)

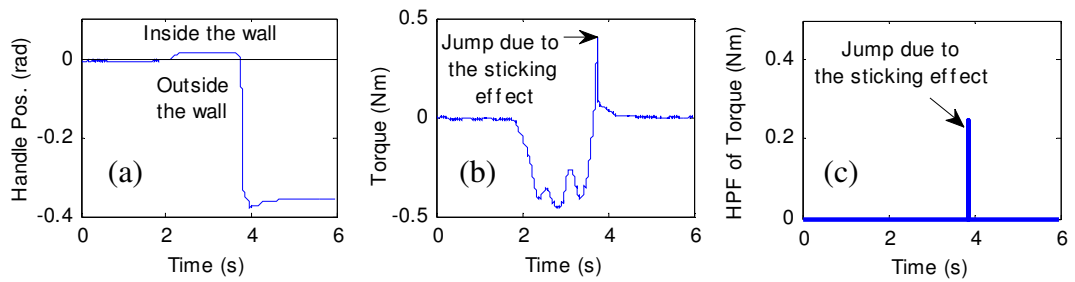


Figure 4.11 Sample virtual wall collision after assigning a dividing parameter (a) position, (b) instantaneous torque signal, (c) high-pass filter of torque signal

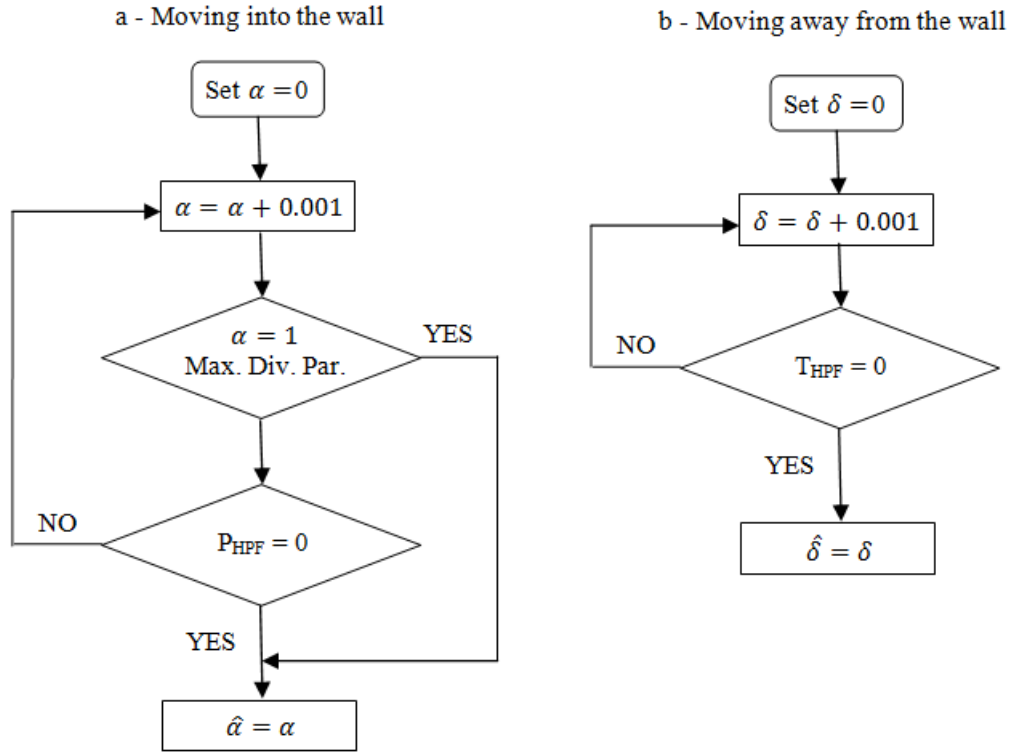


Figure 4.12 Dividing parameter (a) and smooth transition bandwidth (b) estimation algorithms

4.5.2 Artificial Neural network Learning of Parameters for Every Impedance

Using Artificial Neural Network (ANN) learning algorithm instead of repeating the estimation experiments is preferred in this study to estimate the task divider and smooth transition parameters for the entire range of achievable impedances. To this end, sample collision experiments were conducted to determine the most influential input training parameters. Two main observations were made after performing these experiments: (1) the task divider changes with virtual model impedances ($K-B$) and the approach velocity and (2) the smooth transition width changes only with the estimated dividing parameter. Correspondingly, two separate neural network cells were trained: (1) for the task divider by using virtual model impedances and approach velocity as three inputs, and (2) for the smooth transition width by using the dividing parameter as only one input. A two-layer feed-forward network structure with tan-sigmoid hidden neurons and linear output

neurons, which are shown in Figure 4.13, was selected and MATLAB[®] NFtool was used in these learning tasks. The number of hidden layer neurons for the first and second ANN cells were selected as 30 and 10, respectively since they present the best learning performance. 420 and 150 samples were collected for the task divider and smooth transition width respectively (Figure 4.14a-b). These trainings stopped when the validation error increased for six iterations, which occurred at epoch iterations 38 and 20. The training results are acceptable since the final mean-square error was quite small ($0.238\text{e-}006$ and $7.334\text{e-}007$). The test set error, validation set error and training set error all have similar characteristics in the NFtool. ANN training results are shown in Figure 4.14a-b together with the learning samples.

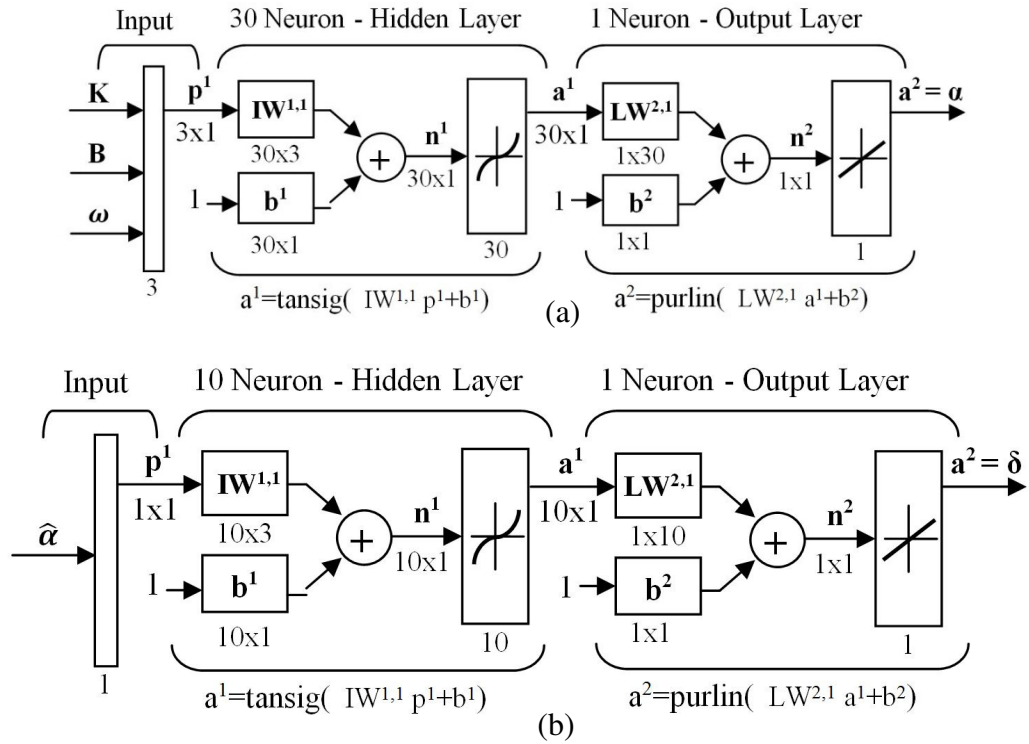


Figure 4.13 Feed-forward ANN structures for (a) dividing parameter and (b) smooth transition bandwidth

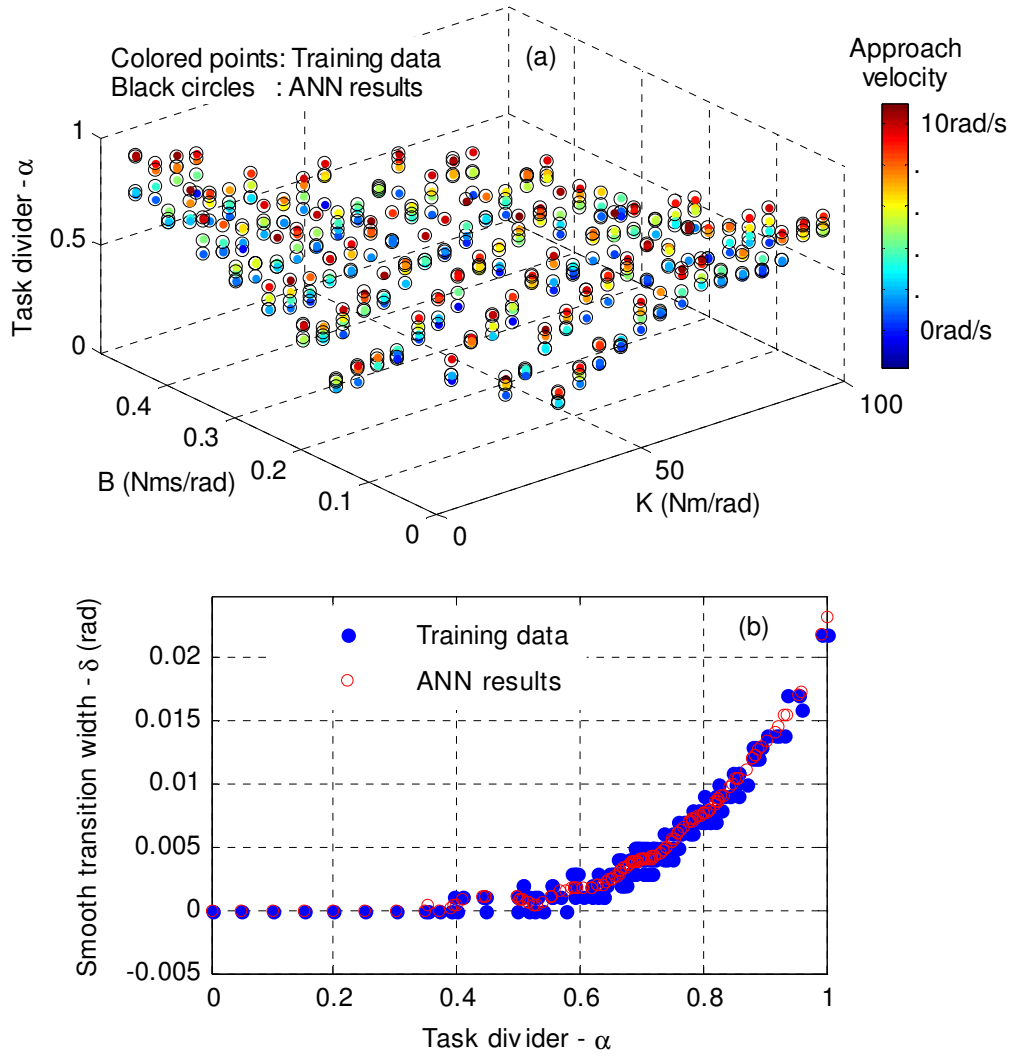


Figure 4.14 Training data and ANN results for (a) task divider, (b) smooth transition width

4.6 Experimental Results

In this section, three sets of experiments were carried out to show the performances of the algorithms for the transparency, stability (Z-width) and virtual wall collision.

Firstly, in order to show how the hybrid algorithm changes the transparency bandwidth, the same experiment mentioned in Section 4.3 was repeated using the

proposed hybrid algorithm. The transparency performance measures of the CLIC+MCBC and hybrid algorithms are shown in Figure 4.15a-b for the comparison. As a result, the transparency bandwidth of the hybrid algorithm (27.1 Hz) is very close to the CLIC+MCBC's transparency bandwidth (28.2 Hz).

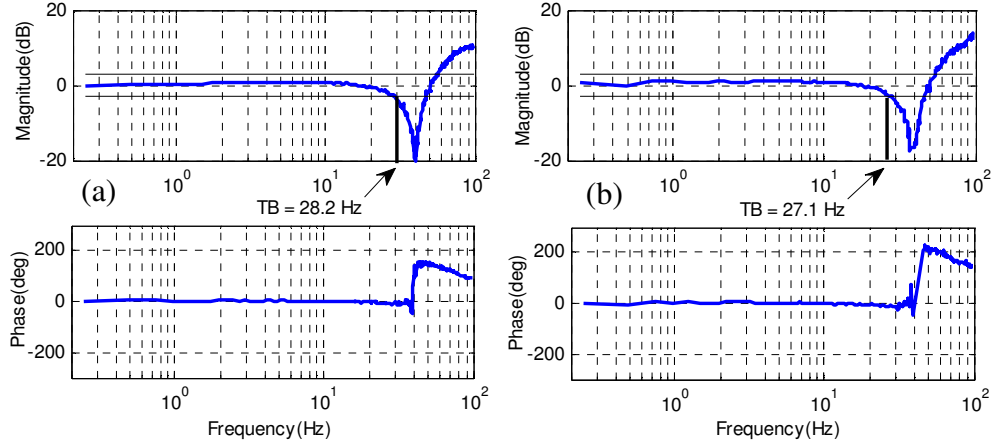


Figure 4.15 Transparency performance measures for a virtual spring with $K=10$ Nm/rad in frequency domain. (a) CLIC+TCBMC and (b) Hybrid algorithm

The transparency bandwidth of a haptic device rather changes with the virtual model being simulated. Thus, it is not a fixed value for all virtual model impedances since the effect of device dynamics on the transparency changes with the virtual model impedances being simulated. The effect of device dynamics is much more dominant for the low impedances and decreases when the impedance values are increased. Therefore, the transparency performance of any algorithm should be evaluated for all achievable impedances. On the other hand, the stable impedance range, Z-width, is another performance criterion to be considered. A new “transparency-Z-width” plot is proposed in this section to evaluate the transparency and Z-width of any algorithm together. This plot shows the limit of stable impedances with full line and transparency measures with colored maps under this limit. The transparency-Z-width plots of all algorithms are presented in Figure 4.16a-d. Different virtual model impedances are selected as shown with the red points on the Z-width plots and transparency bandwidth measures of them are

stated as hot scale colors on the same plots. As a result, the hybrid algorithm provides the larger stable impedance range than the other algorithms and high transparency as much as CLIC+MCBC. Note that higher smooth transition widths (δ) are required for higher impedances as shown in Figure 4.14. Excessive smooth transition width (δ) values increase the torque demand on active actuator and thereby cause unstable vibrations which limit the stable impedance range of hybrid control algorithm.

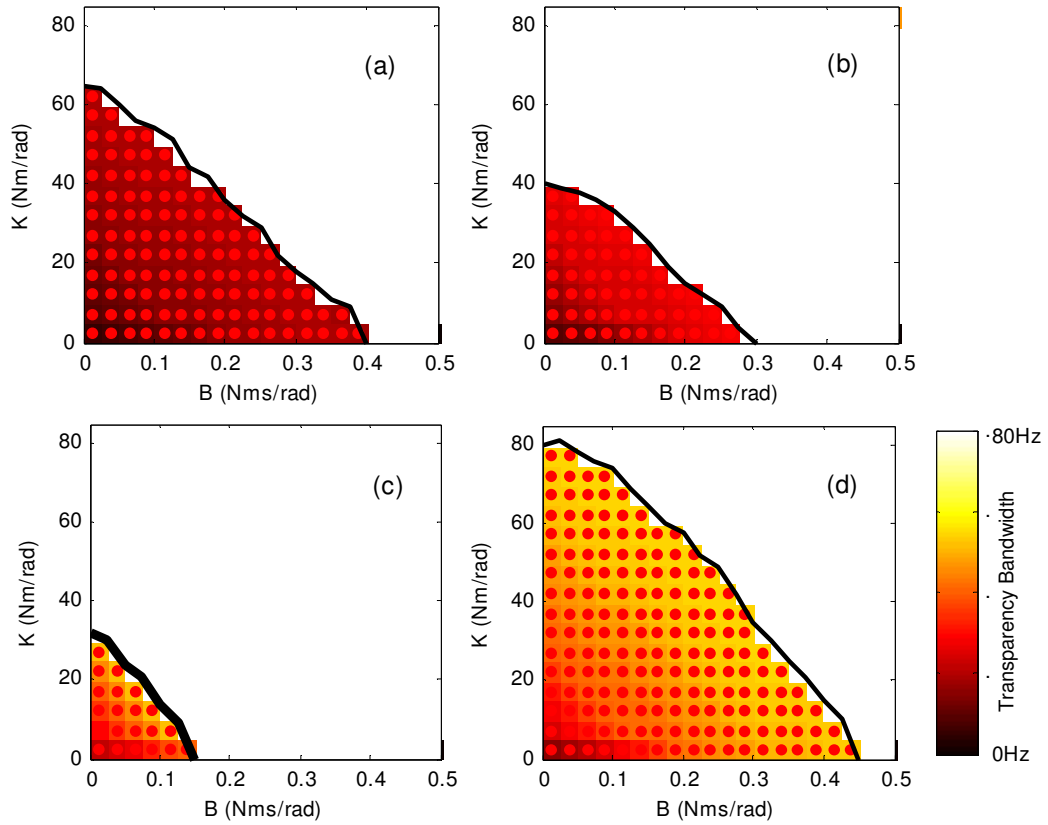


Figure 4.16 Transparency-Z-width plots for (a) OLIC+MBC, (b) CLIC+MBC, (c) CLIC + TCBMC, (d) Hybrid algorithm

The algorithms should be examined on a stiff virtual wall with high impedances to evaluate their stability performance inside the wall and transparency performance outside the wall. For that purpose, a virtual impedance, which is lower than the limit of the hybrid algorithm and higher than the others in Figure 4.16, is selected for testing ($K=70$ Nm/rad and $B=0.1$ Nms/rad). The handle was collided to the wall several times by the user to present a real human-haptic interaction. The

torque measurements versus position are shown in Figure 4.17. The nearness of the measures to the vertical and horizontal axes represents the stability and transparency performances, respectively. Therefore, the magnitude of the deviations can be defined as the stability and transparency widths as shown in Figure 4.17a. They should be lowest for the maximum performance. As a result, the hybrid algorithm provides minimum distortion for stability and transparency. Additionally, CLIC with only the passive brake is included to the experiments to show the sticking and residual effect of the passive brake (Figure 4.17c). The hybrid algorithm eliminates these disadvantages as shown in Figure 4.17e.

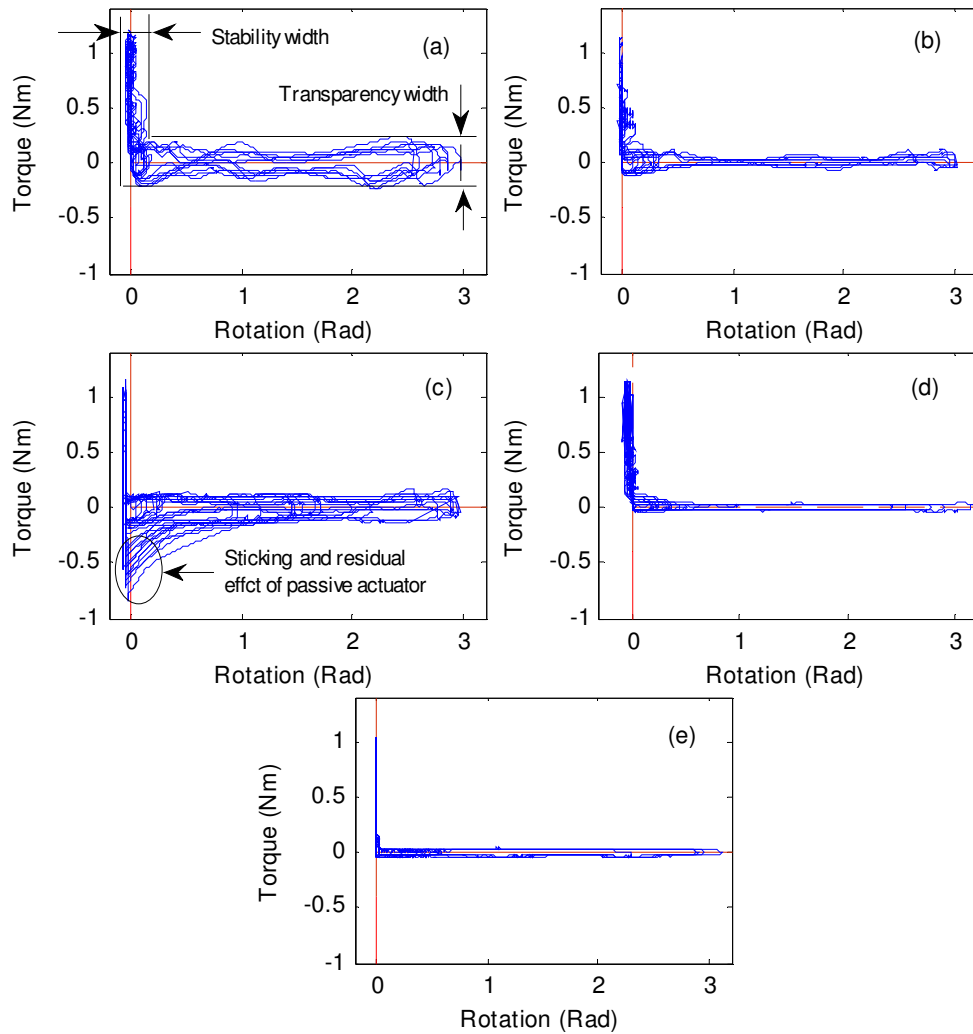


Figure 4.17 Collision experiments on a stiff virtual wall with high impedances ($K=70 \text{ Nm/rad}$ and $B=0.1 \text{ Nms/rad}$) for (a) OLIC+MBC, (b) CLIC+MBC, (c) CLIC with passive brake, (d) CLIC + TCBMC, (e) Hybrid algorithm

The algorithms should also be examined on the narrow concave surfaces since it is nearly impossible for the user to get away from any narrow concave surface when the instability occurs. The magnitude of oscillation increases suddenly and it may damage the device or injure the user. Therefore, a V-shaped concave surface (± 0.05 rad.) with high impedances ($K=70$ Nm/rad and $B=0.1$ Nms/rad) was designed to test the algorithms. The handle was moved with high velocity to hit the sides. The results of these experiments were shown in Figure 3.18. The algorithms employing only active actuator produced high-magnitude oscillations which may be dangerous for the device and the user. Only hybrid algorithm does not generate unstable interaction for a V-shaped concave surface.

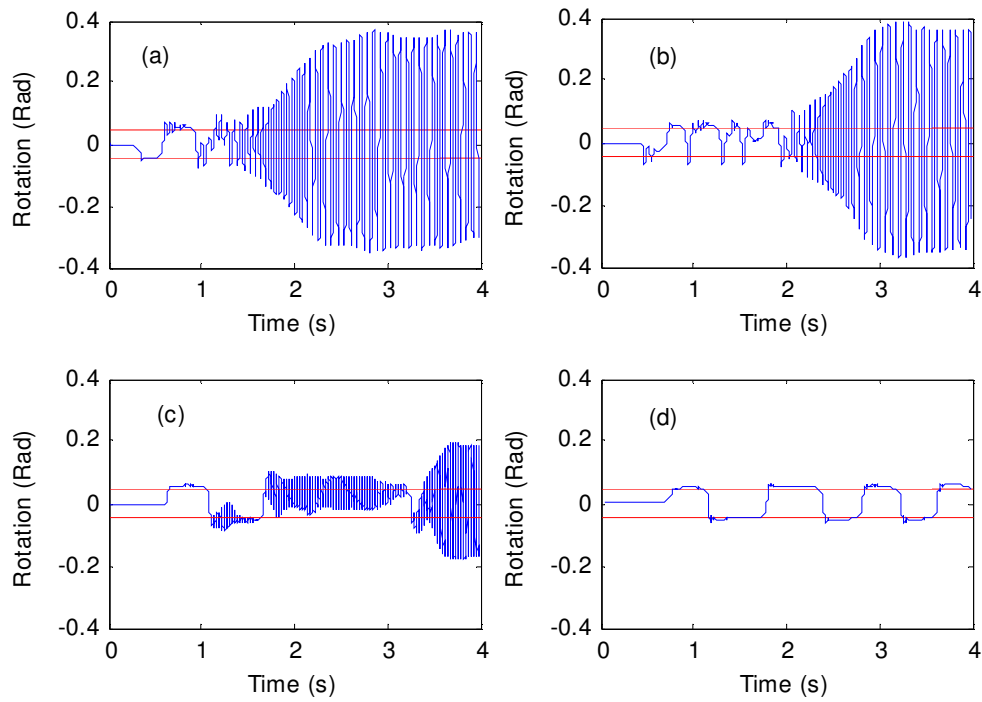


Figure 4.18 Collision experiments on a concave virtual surface with high impedances ($K=70$ Nm/rad and $B=0.1$ Nms/rad) for (a) OLIC+MBC, (b) CLIC+MBC, (c) CLIC + TCBMC, (d) Hybrid algorithm

In order to show how well the proposed hybrid algorithm follows the reference torque while ensuring passivity, another collision experiment was carried out on a stiff virtual wall with high impedances ($K=60$ Nm/rad and $B=0.1$ Nms/rad). The

reference torque, interaction torque measurements, and handle position are plotted versus time in Figure 4.19a-b. This figure shows that the proposed algorithm provides a stable smooth interaction and precise interaction torque response. In the experiment, the proposed algorithm sets the task divider parameter (α) to a high value, which means that much of the desired torque is achieved by the passive brake to provide stable interaction and the active actuator finely tunes the remaining portion of the desired torque for precise interaction. In this way, it can be concluded that the high transparency while ensuring stability can be achieved by the hybrid algorithm even for high virtual impedances.

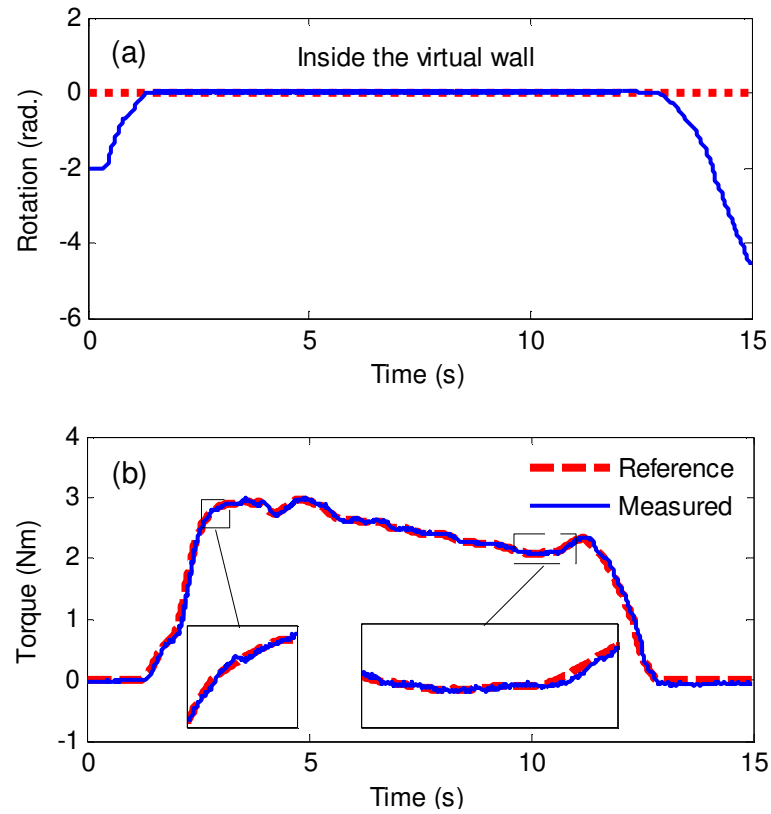


Figure 4.19 Precision torque achievement of the proposed algorithm for a collision experiment on a stiff virtual wall with high impedances ($K=60$ Nm/rad and $B=0.1$ Nms/rad)

4.7 Implementation of Hybrid Algorithm by Using MR Brake

Magnetorheological (MR) brakes are alternative passive brakes in haptic devices [80]. They are promising candidates for haptic devices due to the advantages of high torque to volume ratio, passivity, stability and ease of control [81, 82]. However, MR-brakes don't provide high transparency performance and uneven interaction occurs if MR-brakes are used alone in haptic devices. The main factors of this adverse effect are that MR-fluid increases the viscous friction and residual torque remains on the actuator when magnetic field is turned off. Besides, MR-brakes suffer from the sticking and hysteresis effect due to its slow response. In this section, the hybrid algorithm is implemented by using MR-brake instead of particle brake to show that how the proposed algorithm is effective when MR-brakes are used as passive brake. This section was mainly adapted from our previously published paper titled with "Stability and Transparency Improvement in Haptic Device Employing both MR-Brake and Active Actuator" [83].

MR-brakes contain an amount of MR-fluid between their rotor and housing. The viscosity of the MR-fluid is changed to generate braking torque. The fluid has a viscosity similar to low viscosity oil in the inactive state. Upon exposure to magnetic field, it changes to a thick consistency creating friction between the rotor and the housing [76].

In the MR-brake used in this study, the serpentine flux path approach [84, 85] was used to reduce the size of the brake while increasing the torque output. In this design, the MR-fluid fills the small cylindrical gap between the drum and the stator as shown in Figure 4.20. The magnetic flux is generated in the steel core by the coil and it pass through the MR-fluid 4 times to increase the torque generation. The brake was modeled by using the MagNet FEM software by Infolytica Corp (Figure 4.21) [86] and the design was optimized for 1.5N torque at 1A current. The final design had 50.2mm outer diameter, 40.5mm length and used a coil made of 535 turns of 26-gauge wire.

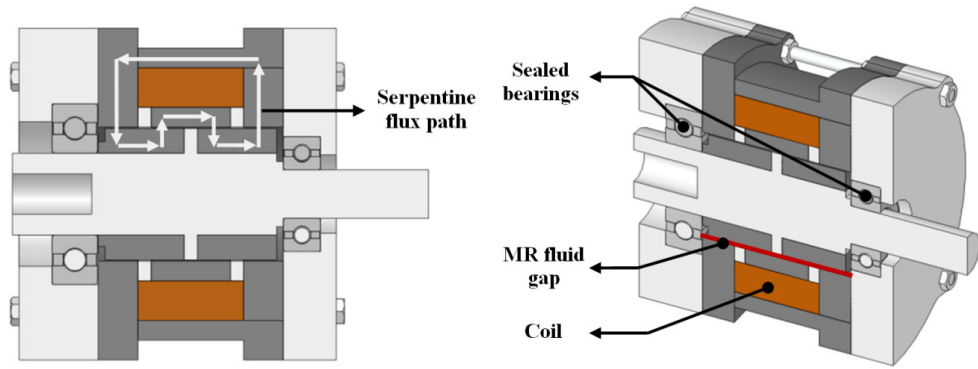


Figure 4.20 MR-brake with serpentine flux path

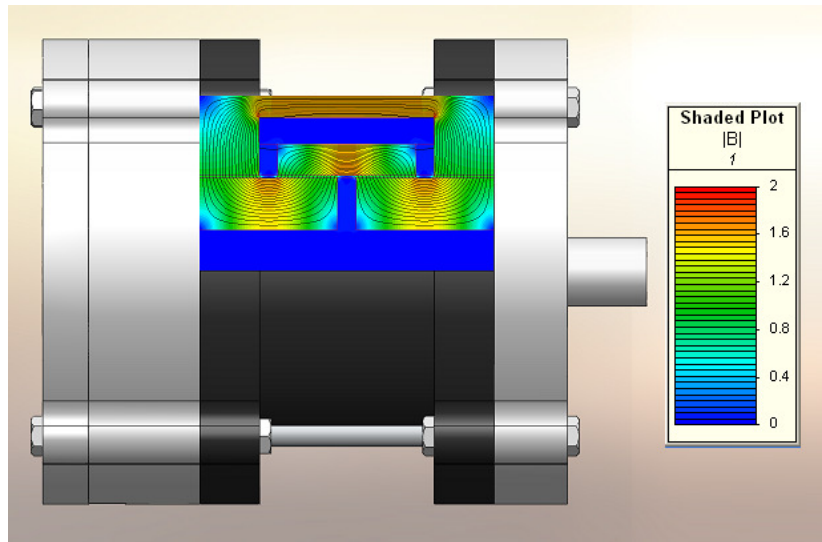


Figure 4.21 Finite element analysis of the MR-brake

This serpentine flux path MR-brake was used in the implementation of the hybrid algorithm as shown in Figure 4.22. Note that the active actuator control loop of the algorithm does not include motor current based compensator (MCBC) in this implementation; hence the hybrid algorithm is compared with only CLIC algorithm. The same values of task dividing and smooth transition parameters which are estimated in the previous sections are used in the new implementation.

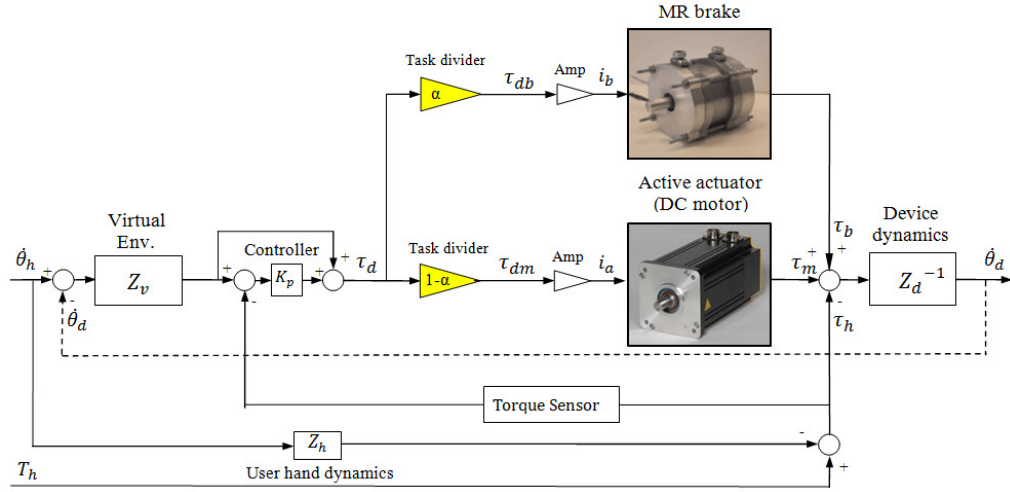


Figure 4.22 Hybrid control algorithm using MR-brake and active actuator

Three set of experiments were carried out again to show the performance of the algorithms. In the first experiment, the stability performances are compared. Figure 4.23 shows the Z-width comparison between the hybrid algorithm and CLIC. Since CLIC use non-perfect sensory feedback data and eliminates physical damping of the haptic device, its stable impedance range is very limited when only active actuators are used. The proposed hybrid algorithm shared the required torque between the MR-brake and active actuator; hence it significantly increases the range of achievable impedances.

The next set of experiments is the transparency performance test. In these experiments, white noise torque inputs were generated to the handle under the effect of a virtual load (Point-X in Figure 4.23, $K=10 \text{ Nm/rad}$ and $B=0.1 \text{ Nms/rad}$) by means of the excitation motor at the front end of the experimental hardware. Then, the transparency bandwidths of the algorithms were measured with the same method mentioned in Section 4.3, and their bode-plots are given in Figure 4.24. As a result, the hybrid algorithm makes the transparency bandwidth of the MR-brake very closer (from 10.2 Hz to 17.7 Hz) to the transparency bandwidth of the active actuator (18.2 Hz).

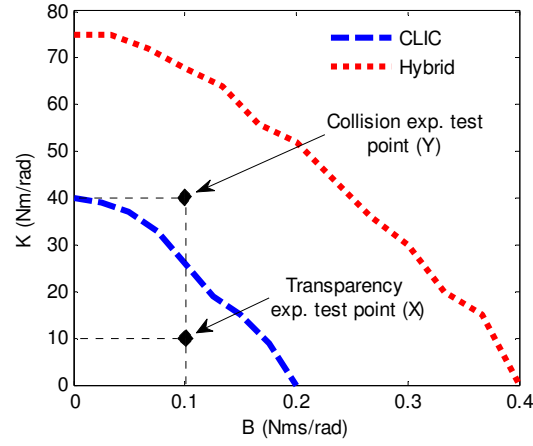


Figure 4.23 Z-Width plot comparison between the hybrid algorithm using MR-brake and CLIC with only active actuator

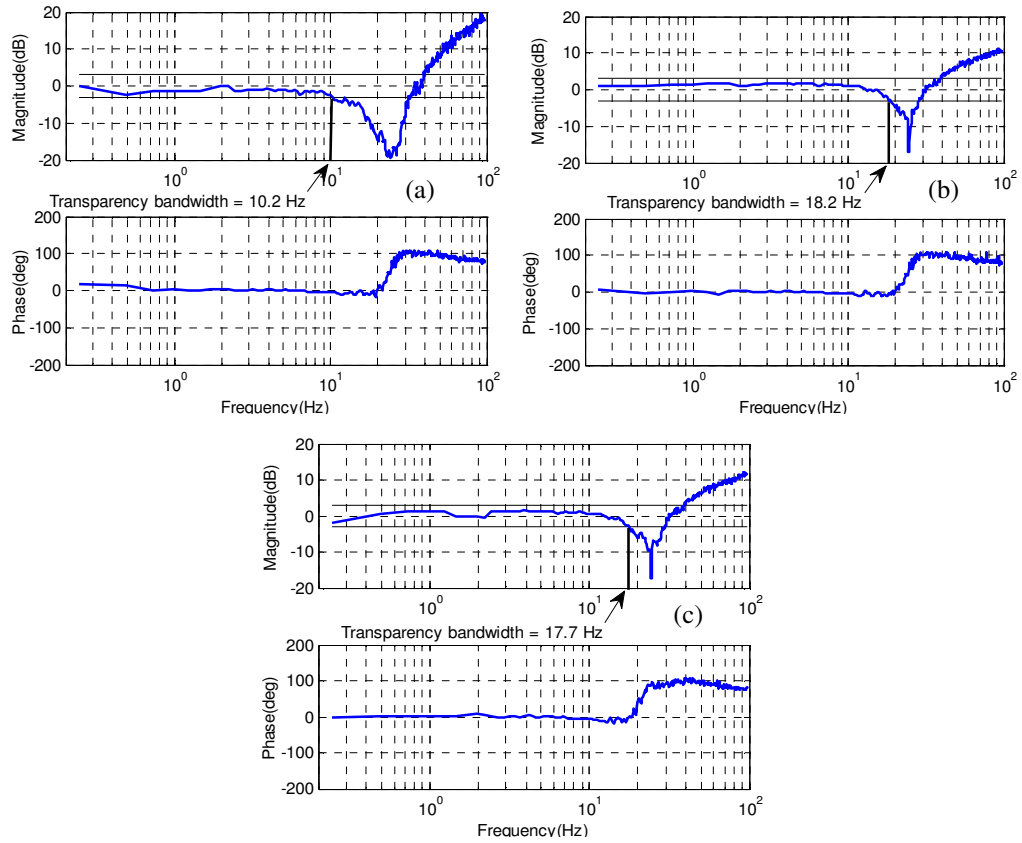


Figure 4.24 Transparency measures for (a) CLIC with MR-brake, (b) CLIC with active actuator, (c) Hybrid algorithm for $K=10$ Nm/rad and $B=0.1$ Nms/rad

Finally, a collision experiment was conducted on a stiff virtual wall with high impedances as shown in Figure 4.23 (Point-Y). The rotation and torque measurements of this experiment are plotted versus time in Figure 4.25 for CLIC with MR-brake, CLIC with active actuator and hybrid algorithm. According to the results, it can be concluded that (1) MR-brake suffers from sticking and hysteresis effect, residual torque and poor transparency, (2) active actuator cannot provide stable interaction on the virtual wall, and (3) the proposed hybrid algorithm provides smooth stable interaction and improves the transparency by eliminating the disadvantages of one type of actuator.

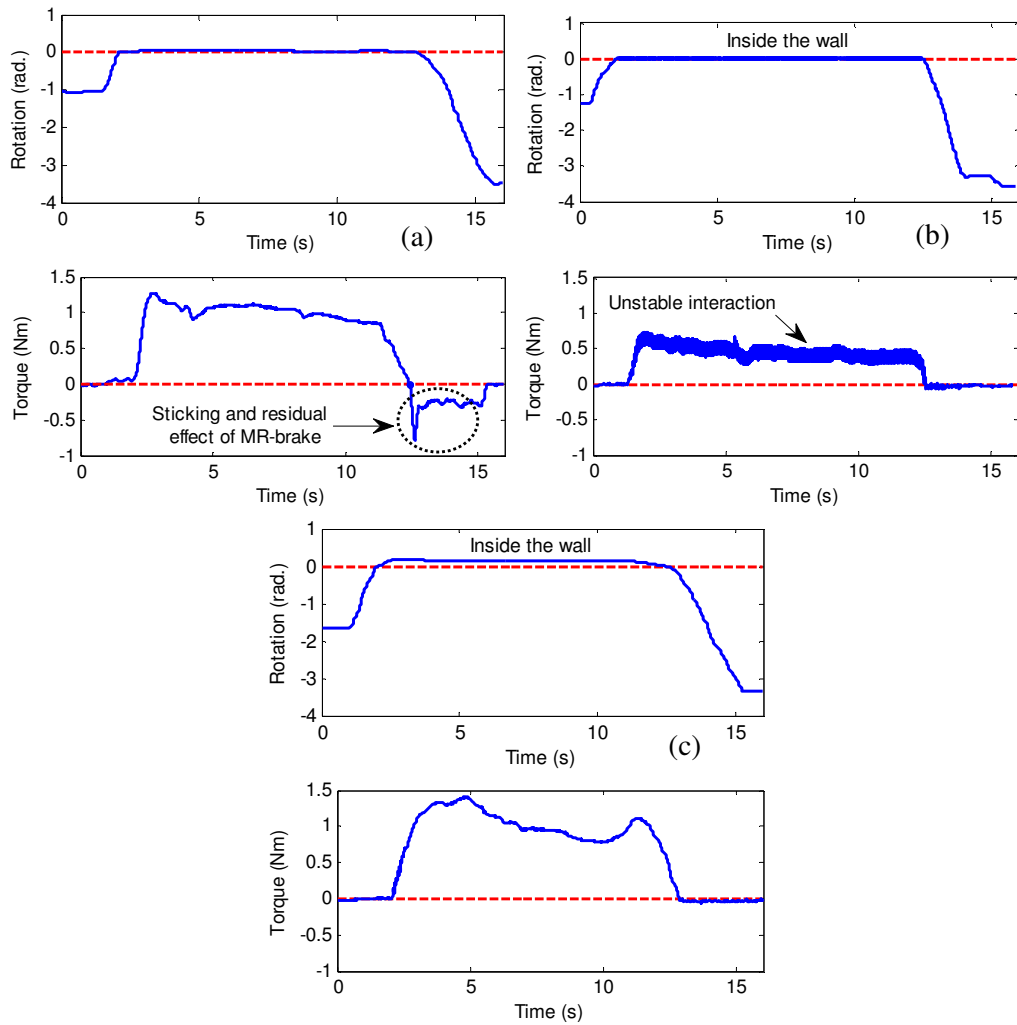


Figure 4.25 Collision experiments on a stiff virtual wall (a) CLIC with MR-brake (b) CLIC with active actuator, (c) hybrid algorithm

4.8 Conclusion

Stability and transparency are major performance criterions in haptic interfaces and they should be evaluated together. An ideal haptic device should simulate wide range of stable virtual impedances with high transparency. Usually, the model based compensators and closed loop impedance control algorithms with only active actuators are used in haptic interfaces for high transparency. However, these algorithms decrease the range of stable impedances since they eliminate the physical damping of the system which is required in passivity and employ non-perfect velocity/acceleration estimations and noisy sensor signals. On the other hand, passive brakes provide stable interaction; however, they not sufficient for high transparency. There is an inverse correlation between the stable impedance range and transparency in haptic interfaces driven by only one type actuator. In this chapter, a hybrid force control algorithm employing both active actuator and passive brake is proposed to improve both the stable impedance range and transparency in haptic devices. Besides, a new transparency-Z-width plot was proposed to evaluate the stable impedance range and transparency together. The proposed hybrid control algorithm uses some parameters (task divider and smooth transition parameters) to share the torque demand between two actuators smoothly. These parameters were estimated experimentally and an artificial neural network (ANN) learning tool was used to extend them to the entire achievable impedance range. The algorithms were tested experimentally on a 1-DOF hybrid haptic device. An excitation motor located at the front side of the device was employed to evaluate the algorithms in the frequency domain. These frequency domain test results were shown with colored maps on the proposed transparency-Z-width plot. Moreover, some collision results were presented for a straight stiff virtual wall and a concave stiff virtual surface. The results show that the proposed hybrid control algorithm provides higher range of stable impedances with higher transparency than the conventional algorithms.

CHAPTER 5

POSE AND FORCE CONTROL ACCURACY IMPROVEMENT IN MULTI-DOF CAPSTAN DRIVEN HAPTIC DEVICES

5.1 Introduction

Multi-DOF capstan driven haptic manipulators suffer from pose and force control accuracy. Jacobian matrix including kinematic parameters is employed in haptic controllers for pose calculation and force control. The deviations in kinematic parameters and joint transmissions change the Jacobian matrix, and effect adversely pose and force control accuracy. This problem necessitates the calibration for haptic devices. The calibration process is carried out by modifying the robot software instead of modifying the mechanical structure or robot design. In general, robot calibration can be classified into two groups; model-based parametric and non-parametric calibrations. Since the most accuracy problems result from the variations in kinematic parameters, the calibration studies are concentrated on the model-based calibration. Model-based calibration considered as a global method consists of four sequential steps: (1) modeling, (2) measurement, (3) parameter identification and (4) compensation or correction [87].

Modeling, which is used to calculate end-effector pose in terms of kinematic and non-kinematic parameters, is the first step for the robot calibration. There are a lot of studies showing that pose inaccuracies of manipulators mainly come from the kinematic inaccuracies [88-95]. Non-kinematic parameters of joint compliance,

backlash and gear transmission errors are included in robot calibration by Whitney et al. [96] for the first time. There are also model-less method such as neural network algorithm where the previous measured data is used to estimate pose errors [97].

Pose measurement is the second step for robot calibration. The measurement system plays a vital role for both identification and performance evaluation. The measurement systems preferred in the robot calibration are generally laser trackers, optical, photogrammetric, cable systems, coordinate measuring machines and theodolites [90-92, 95, 97-103]. Instead of using these measurement systems Khalil et al. [103] emphasized the self-calibration method where the robot calibration can be performed without using any external measurement system. However, the performance of this calibration method is lower than the calibration methods using external measurement system [103].

Parameter identification is the third step in the calibration procedure. It is a kind of regression problem which minimizes the error between the identified model and the measured tool position data. Gauss-Newton algorithm can be used for nonlinear models [104, 51]. However, Levenberg-Marquardt algorithm, [105, 106] a modified version of the Gauss-Newton algorithm, is better than Gauss-Newton algorithm in case of singular or ill-conditioned matrices resulting from unidentifiable parameters, insufficient measurements and/or poor scaling issues. In this study, MATLAB[®] “*lsqnonlin*” command serving as Levenberg-Marquardt algorithm is employed for the identification procedure.

Compensation or correction of the errors is the final step for the robot calibration. There are two alternatives: (1) updating the identified model parameters of the robot used in the robot controller and (2) changing the robot program using the fake targets. Since the haptic handle is manipulated by the user in haptic rendering applications, the first alternative is preferred.

Some haptic applications such as microsurgery and teleoperation applications require accurate posing and precise force control [107-109]. Some haptic libraries

created by producers (i.e. GHOST[®] SDK and OpenHaptics[®] Toolkit, Force Dimension[®] SDK and MHaptic[®]) enable to calibrate encoder offsets of their devices [110-113]. However, encoder offset calibration is not sufficient alone to improve the pose and force control accuracy. In the literature there are some calibration methods which are developed for the pose accuracy improvement of haptic devices and they can be classified into two main groups: (1) tracker-based and (2) tracker-less calibration techniques [114-118]. In the tracker-based techniques, infrared optical tracking device is employed for pose measurements of haptic handle to be used in the calibration. In other technique, instead of tracking the handle, some physical planar constraints and single planar or two perpendicular planar calibration grids are employed to correct the handle pose. The tracker-less methods use only encoder measurements. These proposed methods are implemented on Phantom haptic devices. Moreover, parallel mechanisms such as Delta, Cartesian and R-Cube type are ideal candidates to be used in haptic devices for precise positioning applications; however they need to be calibrated too [119, 120]. Yanhe et. al. emphasized the necessity of calibration for parallel haptic devices and proposed a self-calibration method for a Delta-type parallel haptic device [121]. All these haptic calibration studies in the literature only focused on the kinematic parameter calibration. However, the transmission errors of capstan drives and the effect of calibration on force control accuracy are not considered in the literature.

The calibration improves both pose and force control accuracies in haptic devices, since the interaction force is measured at the handle and driving torques are calculated by a Jacobian matrix containing kinematic parameters. In this study, firstly the transmission error of capstan drives is determined and experimentally validated for a single DOF capstan drive mechanism. Secondly, an enhanced closed-chain calibration method including the transmission errors of capstan drives of a 7-DOF haptic device is presented and the effect of calibration on force control accuracy is analyzed experimentally. All identifiable kinematic parameters (joint offsets, link offsets, link lengths and twist angles) are identified using a linear cable encoder, which has certain advantages such as easy implementation

and low cost. Additionally, the parameters of transmission error resulting for the parallelogram mechanism and capstan drive mechanisms are identified by using external encoders attached to the output joints of the transmission mechanisms.

The rest of the paper is organized as follows: The contribution is explained in the following section. The next section presents the error sources for a 7-DOF haptic device and the determination of capstan drive transmission error. Then the kinematic modeling and calibration procedure are presented together with simulation and experimental results. The last section is related to the conclusion part of the chapter.

5.2 Contribution

Accurate pose estimation and precise force control requirements necessitate kinematic calibration in multi-DOF haptic devices. Although there are several kinematic calibration studies in the literature for haptic devices, none of them include the transmission errors of the capstan drives. Besides, the effect of kinematic calibration on the force control has not been investigated in these studies. The first contribution of this chapter is the theoretical and experimental determination of capstan drive transmission errors. As a second contribution, an easy to implement kinematic calibration technique is presented for a 7-DOF Phantom like haptic device including the capstan drive transmission errors. The improvements in pose and force control accuracy are shown using both simulation and experimental results. This chapter is mainly adapted from our previously published papers titled with “Theoretical and Experimental Determination of Capstan Drive Slip Error” [122] and “Kinematic Model Calibration of a 7-DOF Capstan Driven Haptic Device for Pose and Force Control Accuracy Improvement” [123].

5.3 Error Sources in a 7-DOF Capstan Driven Haptic Device

7-DOF haptic device used in this study is a kind of hybrid link mechanism (Figure 5.1). The first 3-DOF serial mechanism at the base of the device is linked to another 3-DOF serial mechanism at the wrist by a parallelogram mechanism. In the design, a static balance is ensured to minimize the apparent mass of the entire system in such a way that all mobile motors are used as counterweights to avoid extra load usage.

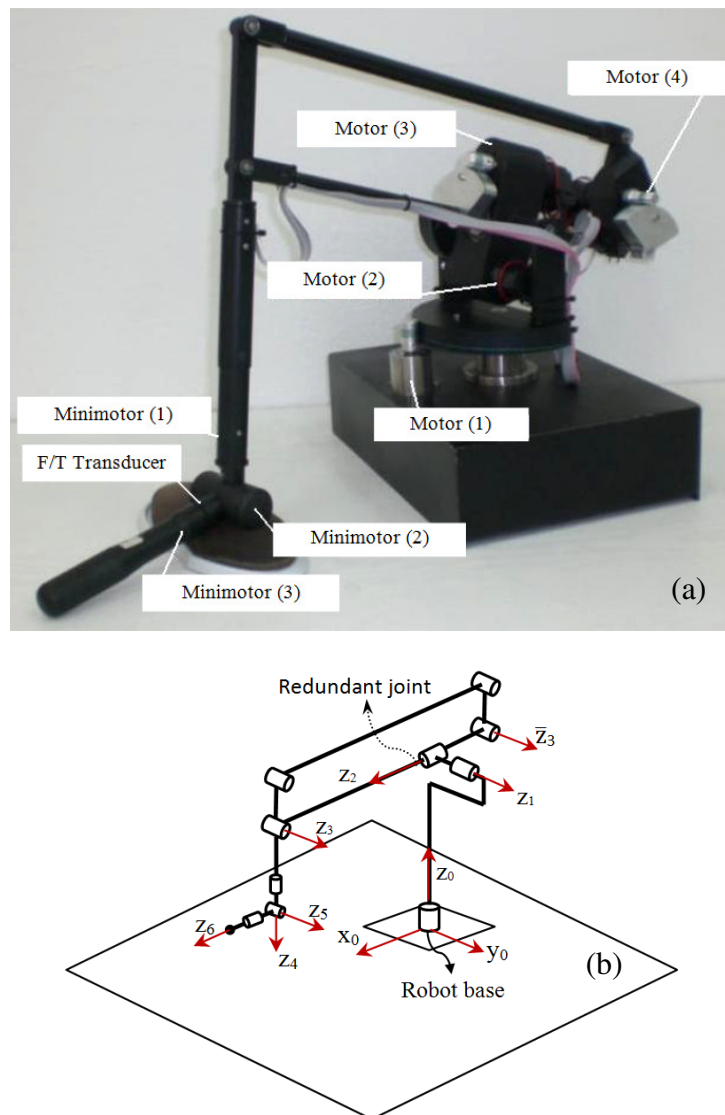


Figure 5.1 7-DOF haptic device (a) and its kinematic model (b)

The mechanical structure of the 7-DOF haptic device is similar to 6-DOF Phantom haptic device; it has only one extra DOF that corresponds to the joint of the motor (3) as shown in Figure 4.1. 7-DOF haptic device becomes similar to a 6-DOF Phantom haptic device at the home position. The redundant joint of the device increases the workspace approximately 20% without compromising the other design criteria [124]. This redundancy provides different posture selection to reach positions within the workspace. The optimal posture ability of the device can improve the haptic performance such as maximum stiffness or transparency, minimum inertia or power consumption, and singularity or obstacle avoidance [125].

Although the interaction forces are measured at the end-effector of haptic devices, the force control is achieved by the torque control applied on the actuators at joints. Therefore, the force control algorithm employs Jacobian matrix to calculate actuator torque commands according to the desired and measured forces [10]. Therefore, the kinematic parameter deviations and joint transmission errors may cause incorrect calculation of the actuator torque commands. This redoubles the importance of the calibration for haptic devices.

Error sources in any multi-DOF capstan driven haptic device are the deviations in kinematic parameters and the joint transmission errors resulting from the capstan drive and parallelogram mechanisms. Kinematic parameter calibration is already studied so many times in the literature. However, a theoretical analysis and its experimental validation are needed for the transmission errors of capstan drive mechanisms.

5.3.1 Theoretical Analysis of Capstan Drive Transmission Error

Cable capstan drives are frequently used in haptic devices as rotary transmission elements. Figure 5.2 shows a typical capstan drive mechanism used in a haptic device. The cable on the capstan drive mechanisms is wrapped around the input

and output drums in a figure-eight pattern and is the principle component for power transmission. They provide several advantages for haptic devices:

- *Low inertia* is desired in terms of dynamics in haptic devices. The use of cables for power transmission minimizes the mass and inertia of the device.
- *High stiffness* is required for precise positioning in haptic devices. The use of cables provides high rigidity in the joints.
- *Low backlash* is another design consideration in haptic devices for positioning accuracy. Gearboxes are not preferred for transmission in haptic devices due to its disadvantage of backlash. Capstan drives minimize this drawback.
- *Structural simplicity* is another advantage of capstan drives in haptic device design: Use of cables simplify the design because of the cable flexibility.

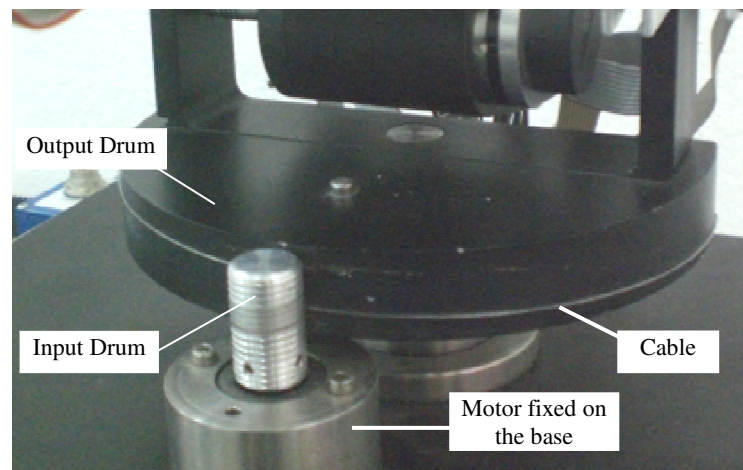


Figure 5.2 Capstan drive mechanism

Werkmeister et. al. investigated theoretical and experimental validation of capstan drive stiffness [126]. Similarly, this section presents a theory on the transmission error of a capstan drive for thaptic devices. A capstan drive system is composed of

an input drum (radius R_{input}) and an output drum (radius R_{output}) which are connected by a cable. The cable can be wrapped once or multiple times on the input or output drums and fixed to one of them to yield segments of finite length. A schematic view of a capstan drive, its slip angle zones and the cable tension loads in these zones are depicted in Figure 5.3.

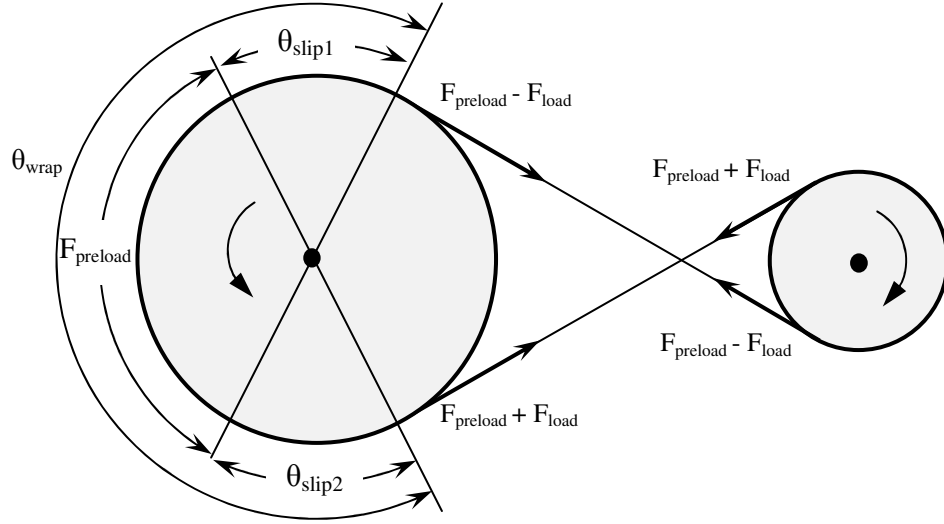


Figure 5.3 Schematic view of a capstan drive with slip angle zones and tensions

The stiffness of the capstan drive is provided by a preload force ($F_{preload}$) that is loaded initially on the cable. An external torque (T_{ext}) which is applied to the drums stretches one part of the cable and slacks the other part according to the direction of the torque. This stretch–slack action of the cable results from the change (F_{load}) in tension of the cable segments.

F_{load} can be derived using the torque balance on the capstan drive:

$$T_{ext} = [F_{preload} + F_{load} - (F_{preload} - F_{load})]R \Rightarrow F_{load} = \frac{T_{ext}}{2R} \quad (5.1)$$

Since the capstan drive system is in equilibrium without any external torque, the initial length with preload force can be considered as the original cable length.

When external torque is applied on the mechanism, it extends the cable more. This should be considered in determining the slippage of the cable on the drum. The free body diagram of a small cable segment including dN (normal force between the cable and drum) and μdN (drag force due to friction between the cable and the drum) is depicted in Figure 5.4.

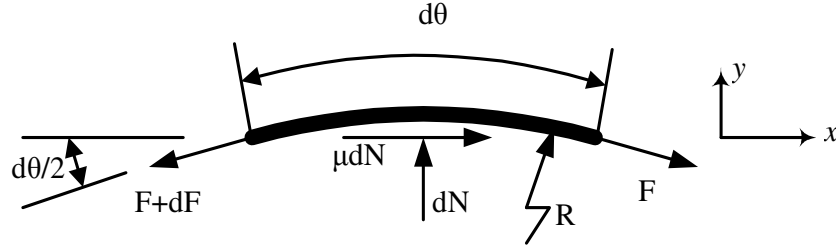


Figure 5.4 Free body diagram of a small cable segment on the drum

Force equilibrium on the cable segment can be expressed as:

$$\sum F_x = F \cos\left(\frac{d\theta}{2}\right) + \mu dN - (F + dF) \cos\left(\frac{d\theta}{2}\right) = 0 \quad (5.2)$$

$$\sum F_y = dN - F \sin\left(\frac{d\theta}{2}\right) - (F + dF) \sin\left(\frac{d\theta}{2}\right) = 0 \quad (5.3)$$

Since $d\theta$ and dF are infinitesimally small:

$$\frac{dF}{F} = \mu d\theta \quad (5.4)$$

The cable tension at any angle in the slip zone can be derived as given in Eq.(5.5) and Eq.(5.6). In this integration, the tension and angle boundaries are selected as (from $F(\theta)$ to a tension F) and (from 0 to θ_{slip}), respectively.

$$\int_{F(\theta)}^F \frac{dF}{F} = \mu \int_0^{\theta_{slip}} d\theta \quad (5.5)$$

$$F(\theta) = F e^{-\mu\theta_{slip}} \quad (5.6)$$

The Eq.(5.6) determines the elongation of the cable on the drum slip zones, which are called the slip regions (θ_{slip1} for the stretch side and θ_{slip2} for the slack side) and also known as the classic capstan equation. Hence, the slip angles of a capstan drive and the cable tension at any point on the slip zones are derived as follows:

$$\theta_{slip1} = \frac{1}{\mu} \ln \left(\frac{F_{preload} + F_{load}}{F_{preload}} \right) \Rightarrow F = e^{-\mu\theta} (F_{preload} + F_{load}) \quad (5.7)$$

$$\theta_{slip2} = -\frac{1}{\mu} \ln \left(\frac{F_{preload} - F_{load}}{F_{preload}} \right) \Rightarrow F = e^{\mu\theta} (F_{preload} - F_{load}) \quad (5.8)$$

The cable elongation on the drums is required to derive the slip error of the mechanism. Hooke's Law is used in the derivations as follows:

$$\varepsilon = \frac{F}{AE} = \frac{d\delta}{dL} = \frac{d\delta}{Rd\theta} \quad (5.9)$$

A modulus of AE is defined as the product of the modulus of elasticity E and the effective area A since the cross-sectional area of the cable rope is difficult to determine.

The elongation δ under tension can be derived as follow:

$$\delta = \int \frac{FR}{AE} d\theta \quad (5.10)$$

The elongation is the extension of the cable due to the external torque (T_{ext}) or tension applied to the cable (F_{load}). The preload force exists in all segments of the capstan drive, and therefore the elongation component due to the preload force can be subtracted. Cable extension due to the external torque (δ_e) should be considered only to determine slippage. Hence, the elongation resulting from the cable tension (F_{load}) due to the external torque (T_{ext}) is equal to the difference between the elongation component caused by the preload force and the total elongation:

$$\delta_e = \int \frac{e^{-\mu\theta}(F_{preload} + F_{load})R}{AE} d\theta - \int \frac{F_{preload} R}{AE} d\theta \quad (5.11)$$

Since the slip error depends on absolute extension of the transformed cable due to rotation of the drums the cable contraction in the slack region should also be derived for the absolute extension of the transformed cable:

$$\delta_c = \int \frac{F_{preload} R}{AE} d\theta - \int \frac{e^{\mu\theta}(F_{preload} - F_{load})R}{AE} d\theta \quad (5.12)$$

The total absolute cable extension of a capstan drive is the sum of cable extension and cable contraction:

$$\delta = \int \frac{e^{-\mu\theta}(F_{preload} + F_{load})R}{AE} d\theta - \int \frac{e^{\mu\theta}(F_{preload} - F_{load})R}{AE} d\theta \quad (5.13)$$

Consequently, the dividing the absolute extension of the transformed cable by the drum radius gives the total slip error resulting from the external torque:

$$e_l = \frac{\delta}{R} \quad (\text{rad.}) \quad (5.14)$$

In addition to the external torque, the eccentricity of the drums extends the cable further during motion. Hence, the drum eccentricity should be considered and one

more derivation is needed for the slip error due to the eccentricity of the output and input drums based on the drum geometry as shown in Figure 5.5.

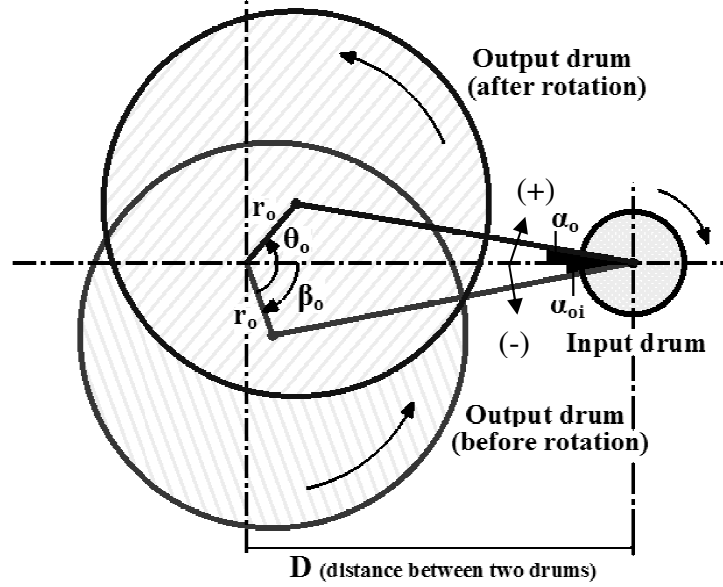


Figure 5.5 Exaggerated drawing of output drum eccentricity for a capstan drive

The eccentricity angle (α_o) and initial eccentricity angle (α_{oi}) of the output drum can be defined in terms of geometric parameters of the drum as follow:

$$\alpha_o = \arctan \left[\frac{r_o \sin(\theta_o + \beta_o)}{D - r_o \cos(\theta_o + \beta_o)} \right] \quad (5.15)$$

$$\alpha_{oi} = \arctan \left[\frac{r_o \sin(\beta_o)}{D - r_o \cos(\beta_o)} \right] \quad (5.16)$$

The slip error of the output drum due to the eccentricity can be derived by using Eqs.(5.15) and (5.16):

$$e_{e_o} = \alpha_o - \alpha_{oi} \quad (5.17)$$

Using the index “*i*” instead of “*o*” in Eqs.(5.15)–(5.17) for the input drum, the same slip error equations can be used for the input drum.

Consequently, the total slip error due to the eccentricity can be determined for a capstan drive:

$$e_e = e_{e_o} + e_{e_i} \quad (5.18)$$

Finally, the overall transmission error of a capstan drive mechanism resulting from the cable slip on the drums can be defined as the sum of slip error due to the external load [Eq.(5.14)] and eccentricity [Eq.(5.18)] as follow:

$$\begin{aligned} e = & \int \frac{e^{-\mu\theta}(F_{preload} + F_{load})}{AE} d\theta - \int \frac{e^{\mu\theta}(F_{preload} - F_{load})}{AE} d\theta \\ & + \left\{ \arctan \left[\frac{r_o \sin(\theta_o + \beta_o)}{D - r_o \cos(\theta_o + \beta_o)} \right] - \arctan \left[\frac{r_o \sin(\beta_o)}{D - r_o \cos(\beta_o)} \right] \right\} \\ & + \left\{ \arctan \left[\frac{r_i \sin(\theta_i + \beta_i)}{D - r_i \cos(\theta_i + \beta_i)} \right] - \arctan \left[\frac{r_i \sin(\beta_i)}{D - r_i \cos(\beta_i)} \right] \right\} \end{aligned} \quad (5.19)$$

This equation can be used in the calibration porocess of any capstan driven haptic device for compensation of transmission errors of capstan drives.

5.3.2 Experimental Verification of Capstan Drive Transmission Error

An experimental hardware was constructed for the verification of the capstan drive slip error theory developed in the previous section (Figure 5.6). This hardware is a 1-DOF capstan drive mechanism consisting of a 0.35-mm steel cable wrapped around two drums (15 mm and 150 mm diameter) and fixed to the output drum ends. In the hardware, the shaft of a DC brushless motor is used as an input drum to provide the desired position trajectory for the experiments. The output drum is assembled to the base. This experimental hardware contains a load pulley attached to the output drum to hang an external load on the output side.

Besides, two different encoders with 1000 ppr and 5000 ppr are attached to the motor shaft and output drum respectively to measure the relative motion (transmission error) between the drums.

MATLAB[®] Simulink and xPC Target are used for the experimental procedure. An NI 6025 I/O board and NI 6602 counter/timer board were installed in the target PC. A Simulink model was constructed on the host PC to enable the user to give a reference position. The user can also change the external load on the output drum pulley.

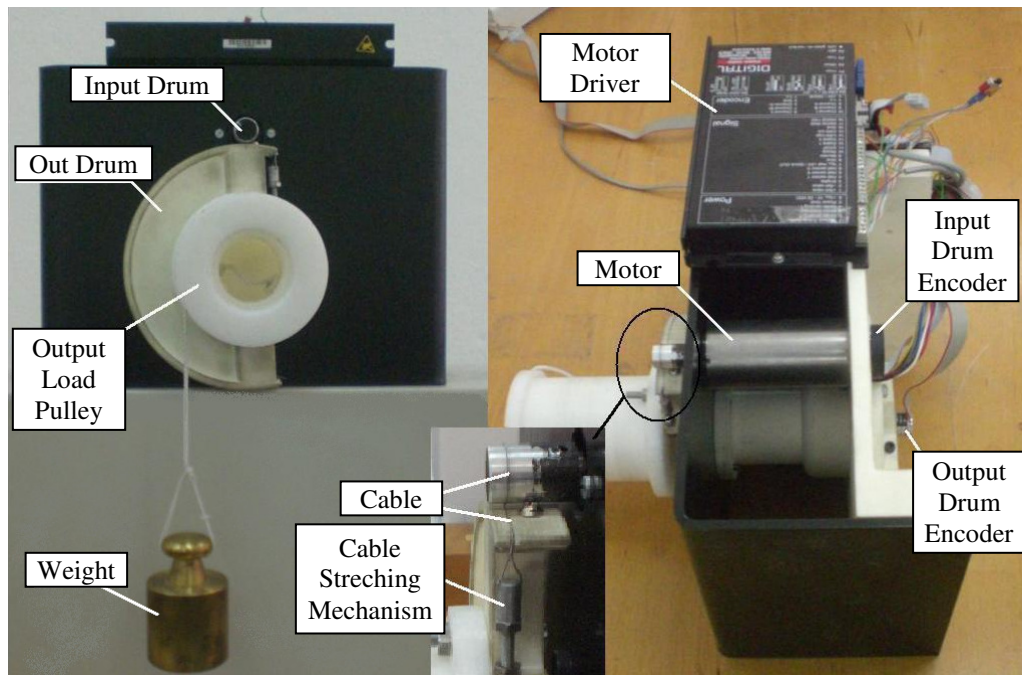


Figure 5.6 Experimental hardware for capstan drive transmission error validation

In the experimental validation, firstly, the drum eccentricity geometries such as the eccentricity radius and phase angle should be measured precisely to estimate the slip error resulting from the drum eccentricity. A computer measuring machine (CMM) was used to determine these parameters (Figure 5.7). Many measurements were collected from the forehead surfaces of two drums while they rotate in reverse directions. The eccentricity measurements on the drums and corresponding cosine curve fittings are shown in Figures 5.8. As a result, the

eccentricity radiuses and phase angles of the output and input drums were found as (0.7 mm and -105°) and (0.05 mm and -15°), respectively. Note that the measurements on the forehead surfaces of the drums deviate from cosine curve fit in some regions, which may cause little difference between the theory and experiment.

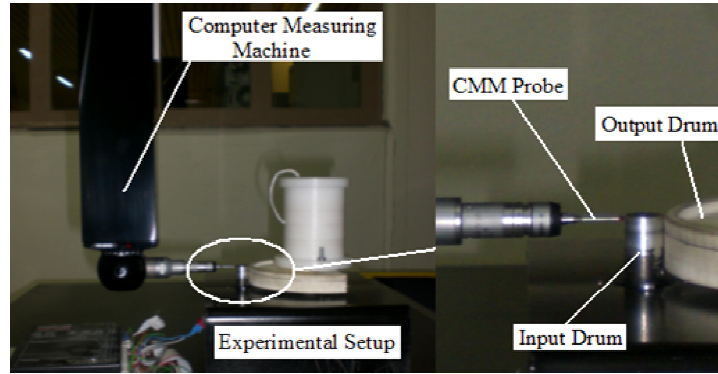


Figure 5.7 CMM measurement of drum eccentricity

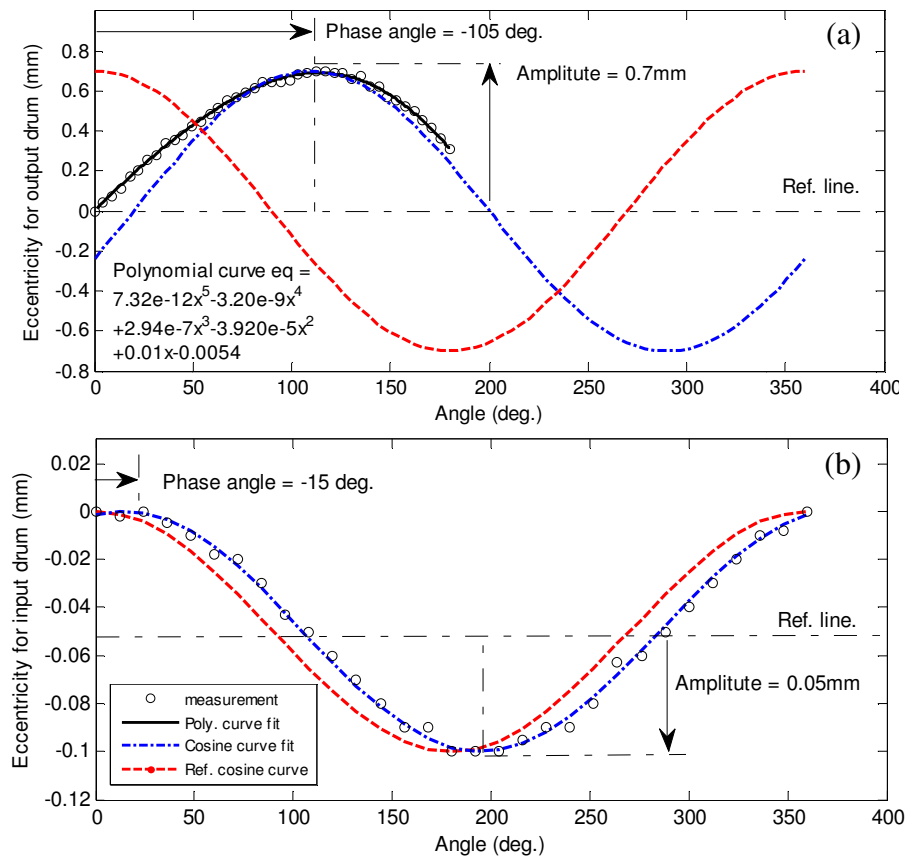


Figure 5.8 Eccentricity for the input (a) and output (b) drums

The effective cable modulus (AE) was determined from Hookes Law (Eq.(5.20)) by loading the cable to 50 N and recording the displacement of the load. Hence, it was measured as 8.1×10^3 N for a 150-mm-long and 0.35-mm-diameter cable. The cable was cycled six times to 50 N in the experiment (Figure 5.9). Although the cycling load is in the range of 0 and 50 N, the effective cable modulus was calculated using the actual cable loading region between 5 and 30 N. Note that the cable self-adjustment on the test machine causes a discontinuity marked by a triangle in Figure 5.9.

$$F = \frac{AE}{L} \delta \Rightarrow AE = \frac{FL}{\delta} \quad (5.20)$$

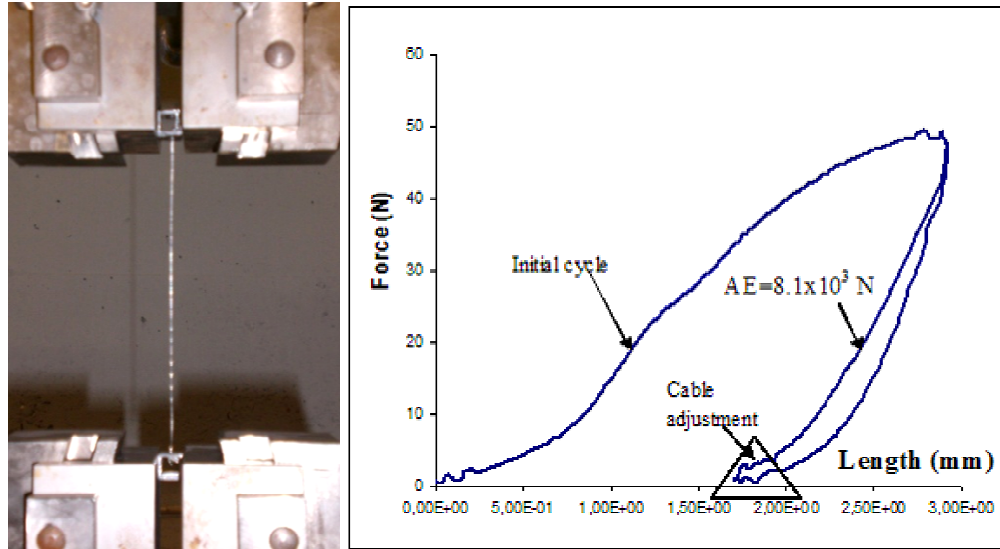


Figure 5.9 Cyclic tensioning of the cable that revealed an AE value of 8.1×10^3 N

The effect of the external load on slip error depends on the load direction and magnitude. Hence, as a first step, the theory of the slip error due to the eccentricity should be verified. To this end, an experiment was conducted without any external load. In this experiment, a desired position profile is achieved by the position control applied on the input drum motor and the slip error is recorded using the difference between two encoder measurements. The reference position and transmission error of the capstan drive versus time are shown in Figures 5.10.

It can be seen from the figure that output and input drum eccentricities cause one large and five small error waves in each direction respectively. Also, various error ripples occurred due to the asynchronous increments between the encoders. Since the encoders are discrete measurement units, asynchronous encoder increments cause these error ripples. Figures 5.10 also shows the theoretical error graphs drawn by using Eqs.(5.15-5.18). Nevertheless, there is a small difference between the experimental and theoretical results based on the cosine curve fit (Figure 5.10) since the actual drum eccentricity measurements do not fit to cosine curve. For more accurate estimation of eccentricity, alternatively, a fifth order polynomial curve fit was used. The theoretical error calculated using this polynomial curve fit shown in the same figure follows the experimental results more accurately than the other. The theory based on cosine curve fit is used in the rest of this research for simplicity.

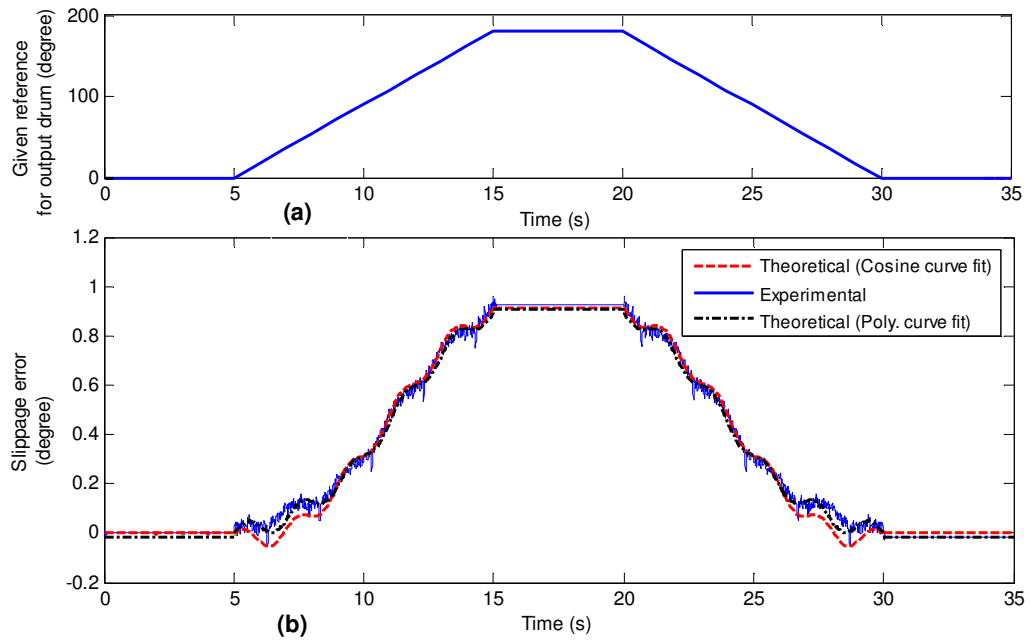


Figure 5.10 Slip error without load and theoretical verification

A load pulley was used on the output drum to determine the effect of a known external load on the transmission error so that the desired external torque could be applied by an external load hanged on the pulley.

Four different experimental cases were considered for further analysis of slip error and each case was conducted with six repetitions. Figure 5.11 shows the reference output drum position and slip error versus time for all cases. Preliminary observations of each experiment are given right after the explanation of each case as follows:

- **Case 1:** The experiment was conducted without any external load.

For case 1, some slip error occurred depending upon the position of the output drum due to eccentricity. The system compensated this error itself when the drum returned to the starting position.

- **Case 2:** The experiment was conducted with an external load (0.907 kg) which is applied in the same direction of the output drum rotation.

For case 2, additional slip errors occurred due to the external load in the forward direction and the drum returned to the starting position without any error since the load direction was inverted while the drum was returning. el_2 in Figure 5.11 denotes the magnitude of this temporary slip error for a half cycle (rotation from 0° to 180°) of the output drum in case 2.

- **Case 3:** The experiment was conducted with an external load (0.907 kg) which is applied in the permanent direction (External torque is clockwise while the drum rotates clockwise or counterclockwise).
- **Case 4:** Same experiment defined in Case 3 was repeated with a higher external load (1.361 kg)

For cases 3 and 4, the slip error due to the load increased regularly. el_3 and el_4 in Figure 5.11 denote the magnitude of the permanent slip error due to the external load for one cycle (rotation from 0° to 180° and return to the starting position) of the output drum for cases 3 and 4, respectively.

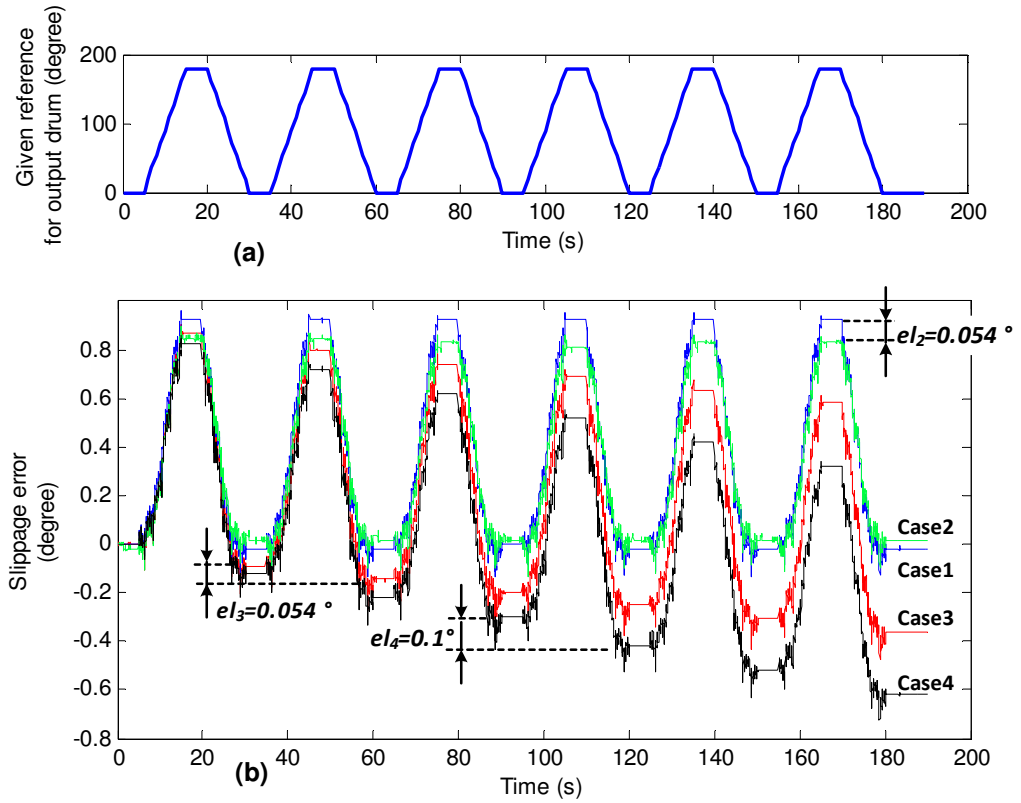
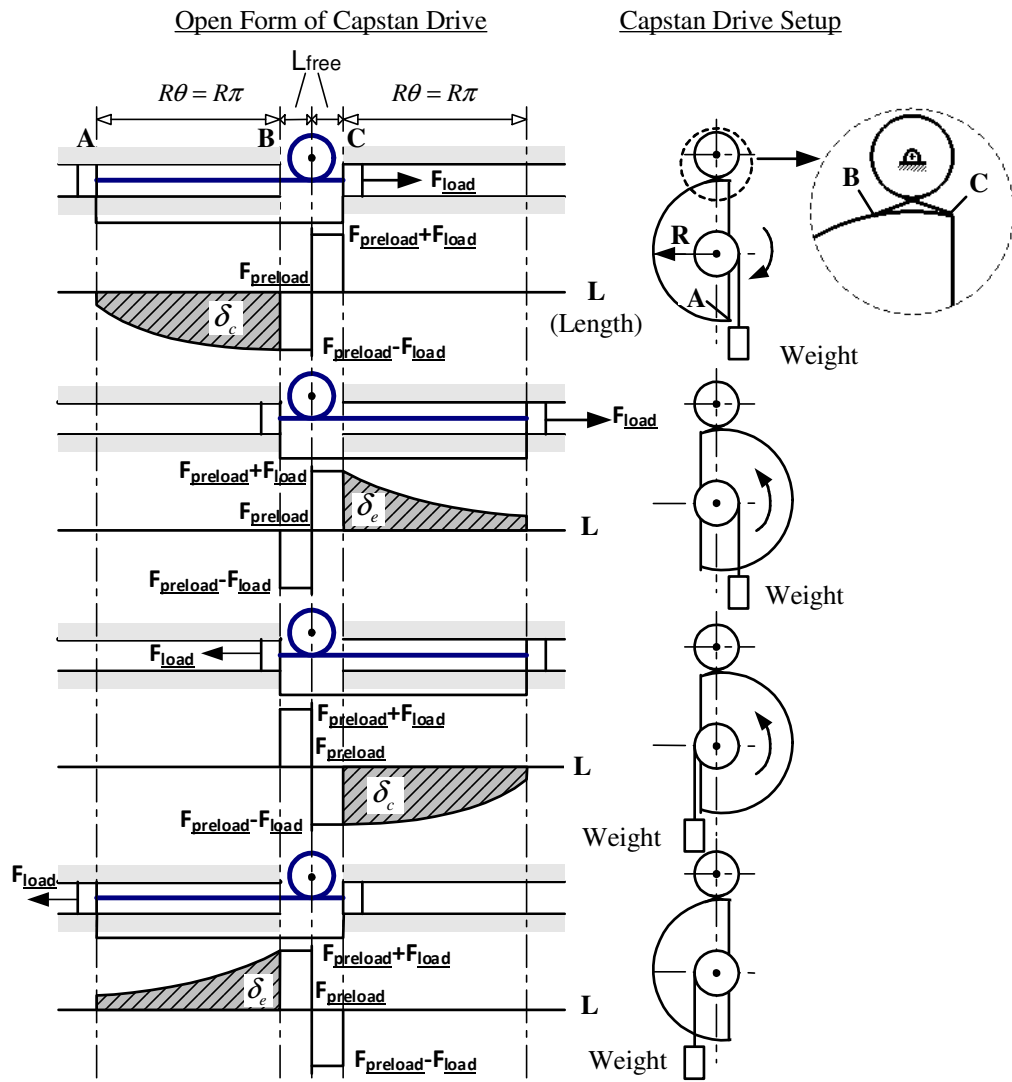


Figure 5.11 Slip errors measured for four different cases

The theory derived in the previous section estimates the slip error due to the external torque for the experiments. Figures 5.12 and 5.13 depict open forms of a capstan drive mechanism for four different positions of one cycle to explain the procedure used for cases 2, 3 and 4. The drawings in the left side are the open forms of the capstan drive position shown in the right side. These figures also show the cable tension variation versus cable length for the sample positions.



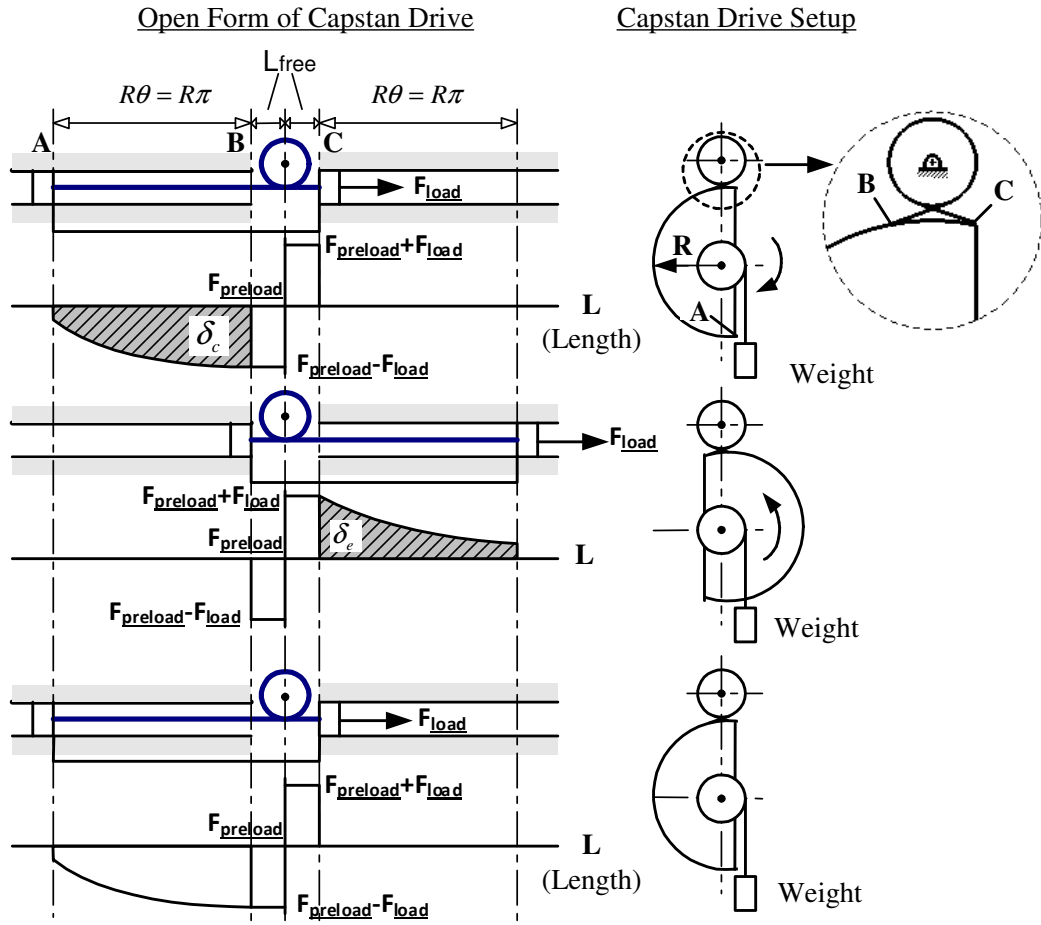


Figure 5.13 Theoretical verification of the slip error under the effect of an external torque for cases 3 and 4

Since θ_{slip1} and θ_{slip2} calculated by Eqs.(5.7) and (5.8) for the loads of 0.977 and 1.361 kg are greater than π rad., the cable tension during experiments does not reach the preload force on the output drum. The cross-hatched areas in Figures 5.12 and 5.13 give the cable extension and contraction (δe , δc). In the experimental hardware, the cable is wrapped around the drums one time and it was assumed that the diameter of the input drum is quite small in comparison to the output drum. Thus, it was assumed that the input drum diameter is infinitesimally small for simplicity. Therefore, the cable extension on the input drum is neglected.

As a result, the interpretations of experimental results given in Figure 5.12 for the cases 2, 3 4 can be given as:

- For Case 2, the slip error occurred at the clockwise and counterclockwise output drum rotation is in reversed directions. In other words, the cross-hatched areas in Figure 5.12 cancel each other at the end of one full cycle and the temporary slip error (el_2) due to the load is lost after each cycle. The error cancellation at the end of the cycle is evident as shown in the cable tension graphs in Figure 5.12.
- For cases 3 and 4, the slip error increases over time in both directions. The cross-hatched area in Figure 5.13 can be calculated to verify the experimental slip error. For this purpose, $F_{preload}$, F_{load} , AE , μ and the slip regions should be defined clearly. For cases 3 and 4, the loads of 0.977 and 1.361 kg are applied on the output drum. Using the load pulley radius (35 mm) and Eq.(5.1), F_{load} was calculated as approximately 2.08 and 3.12 N, respectively. A cable of 350 mm in length was wrapped around the drums and stretched by 0.4 mm using a cable stretching mechanism. $F_{preload}$ was calculated as 9.26 N using this elongation and the cable modulus. The sum of the cross-hatched areas ($\delta e + \delta c$) in Figure 5.13 gives the permanent slip error due to the load for one cycle. Moreover, the temporary slip error for cases 2 and 3 is the same ($el_2 = el_3$) because the load is equal and slip due to the load occurs only when the rotation direction is through the direction of the load. Values of the slip error for cases 2, 3 and 4 calculated with Eq.(5.14) agrees with the experimental values el_2 , el_3 and el_4 in Figure 5.11 within 10%. The measured and estimated values are ($el_2 = el_3 = 0.054^\circ$, $el_4 = 0.1^\circ$) and ($el_2 = el_3 = 0.06^\circ$, $el_4 = 0.107^\circ$), respectively.

$$\begin{aligned}
 el_2 = el_3 &= \int_0^\pi \frac{e^{-0.05\theta}(9.26 + 2.08)}{8.1 \times 10^3} d\theta - \int_0^\pi \frac{e^{0.05\theta}(9.26 - 2.08)}{8.1 \times 10^3} d\theta \quad (5.21) \\
 &\cong 1.05 \times 10^{-3} \text{ rad.} \cong 0.06 \text{ deg.}
 \end{aligned}$$

$$el_4 = \int_0^{\pi} \frac{e^{-0.05\theta}(9.26 + 3.12)}{8.1 \times 10^3} d\theta - \int_0^{\pi} \frac{e^{0.05\theta}(9.26 - 3.12)}{8.1 \times 10^3} d\theta \quad (5.22)$$

$$\cong 1.86 \times 10^{-3} \text{ rad.} \cong 0.107 \text{ deg.}$$

The theory derived for slip error due to eccentricity and loading can be used to predict the overall transmission error for capstan drives. Figure 5.14a,b shows the consistency between theory and experiment under a permanent load for cases 3 and 4, respectively. This verification shows that the transmission error in a capstan drive mechanism can be corrected successfully by using the analytical model developed in this chapter.

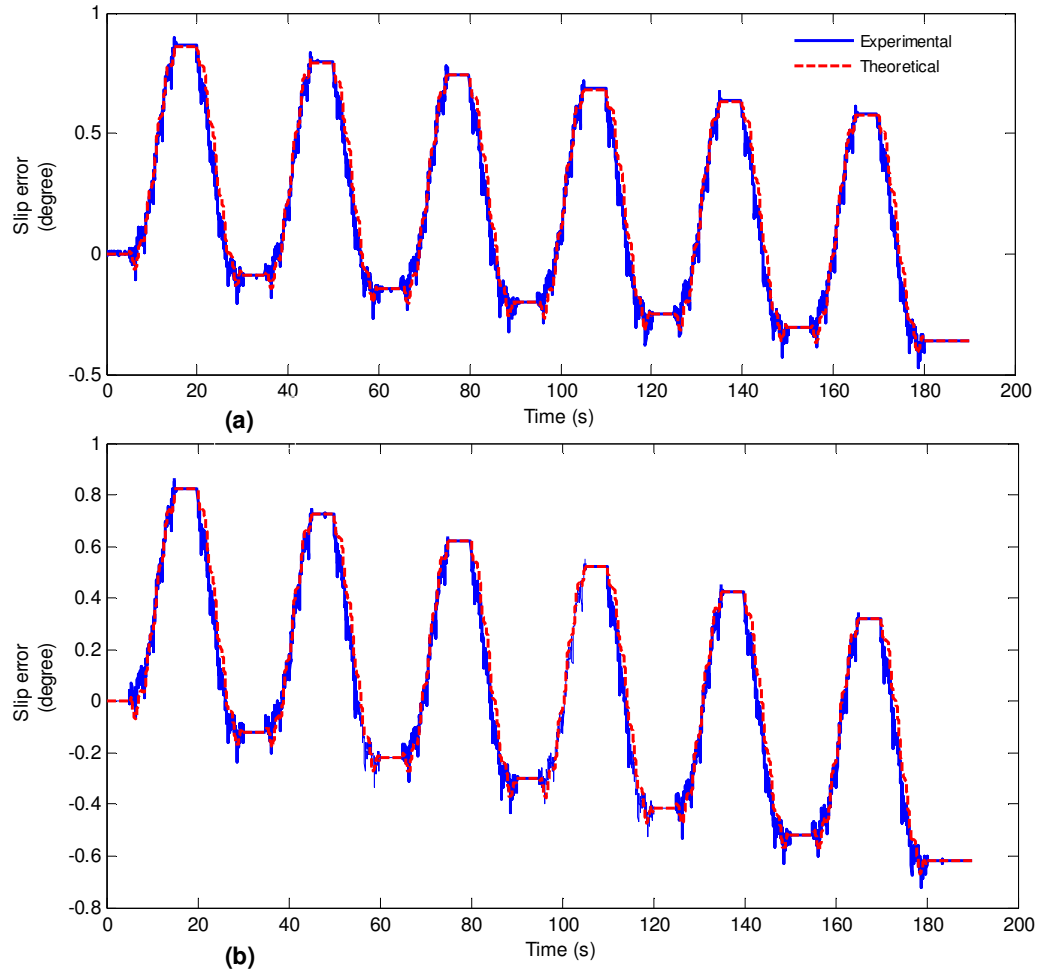


Figure 5.14 Verification of the analytical model for case 3 (a) and case 4 (b)

In general, the transmission error of a capstan drive mechanism is caused by the drum eccentricities and external load applied on the output drum. However, it should be noted that the effect of external load on the transmission error is ignored in the calibration of 7-DOF haptic device since only free-motion and static virtual model simulations are considered in this study. Consequently, the transmission error in the capstan drive mechanisms of 7-DOF haptic device can be expressed by Eq.(5.23). $\Delta\theta_{offset}$, $\Delta\theta_{ratio}$, $\Delta\theta_{o-ecc}$, $\Delta\theta_{i-ecc}$ in this equation represent the transmission errors caused by the joint variable offsets relative to the home position, error in transmission ratio, output drum eccentricity and input drum eccentricity, respectively.

$$\Delta\theta_{caps} = \Delta\theta_{offset} + \Delta\theta_{ratio} + \Delta\theta_{o-ecc} + \Delta\theta_{i-ecc} \quad (5.23)$$

where

$$\Delta\theta_{offset} = c$$

$$\Delta\theta_{ratio} = \left[\frac{-R_e}{R_e + R} \right] \theta$$

$$\Delta\theta_{o-ecc} = \left\{ atan \left[\frac{r_o \sin(\theta + \beta_o)}{D - r_o \cos(\theta + \beta_o)} \right] - atan \left[\frac{r_o \sin(\beta_o)}{D - r_o \cos(\beta_o)} \right] \right\}$$

$$\Delta\theta_{i-ecc} = \left\{ atan \left[\frac{r_i \sin(R\theta + \beta_i)}{D - r_i \cos(R\theta + \beta_i)} \right] - atan \left[\frac{r_i \sin(\beta_i)}{D - r_i \cos(\beta_i)} \right] \right\}$$

5.3.3 Parallelogram Mechanism Transmission Error

Another error source distorting the calibration of 7-DOF haptic device is inaccuracies in the kinematic parameters of a parallelogram mechanism. Schroer et al. simplified the parallelogram mechanism to a closed-chain planar mechanism linkage [127]. Similarly, the parallelogram mechanism used in our haptic device is considered as a planar mechanism to obtain the joint dependency. In this way, the transmission error between the actuated and transmitted joint angles of the parallelogram can be expressed in terms of link lengths as follows:

$$\Delta\theta_{par} = \left[\frac{L_1^2 + s^2 - L_2^2}{2L_1s^2} \right] + \left[\frac{L_4^2 + s^2 - L_3^2}{2L_4s^2} \right] - \frac{\pi}{2} - \theta_a \quad (5.24)$$

where $s = \left(L_1^2 + L_2^2 - 2L_1L_2 \cos\left(\frac{\pi}{2} - \theta_a\right) \right)$

Schroer et al. reported that only one link length parameter from among five parameters of a planar parallelogram (four link lengths and one joint angle) is identifiable [127]. The parallelogram joint in 7-DOF haptic device is limited with $\pm 45^\circ$. Besides, a capstan drive mechanism is employed in the parallelogram mechanism used in our device for the actuation. This complicates the transmission error model. Therefore, a higher order polynomial is used to represent the transmission error of the parallelogram to simplify the identification process. The transmission error model of the parallelogram in 7-DOF haptic device involves ten parameters coming from the parallelogram ($\Delta L_1, \Delta L_2, \Delta L_3, \Delta L_4, \Delta\theta$) and capstan drive models ($R_e, r_o, r_i, \beta_o, \beta_i$), and hence a tenth order polynomial is selected to represent the transmission error. It should be noted that a polynomial with a higher order than ten might increase the computational load unnecessarily.

5.4 Kinematic Modeling and Proposed Calibration Procedure

In this research, for easy implementation, a closed-chain calibration method is used to identify kinematic parameters. The distance measured between the end-effector and a reference frame located on the cable encoder measurement unit is employed for a closed-chain kinematic calibration. The maximum quantization error of the cable encoder limits the accuracy of the measurements. Figure 5.15 shows the overall calibration setup, cable encoder and its connection to the hardware. The accuracy of the cable encoder (σ_m) can be calculated by the multiplication of the unit drum circumference and the maximum quantization error of the optical incremental encoder used inside of the cable encoder. As a result, it is found as ($\sigma_m = 2\pi R_d * \sigma_e = 2\pi * 0.015 * 2\pi / 20000$).

Figure 5.16 shows the schematic view of the 7-DOF haptic device at home position, the location of the measurement system and their coordinate frames. The kinematic model of the structure is established using the Denavit-Hartenberg (D-H) convention [128]. A reference frame “(-1)” is attached to the starting point of the cable encoder for the closed-chain kinematic structure. In the kinematic model, the line connecting the robot base origin “(0)” to the measurement system origin “(-1)” is selected as the common x direction for the device and measurement system. The D-H parameters of the device are given in Table 5.1.

According to the D-H convention, each homogeneous transformation matrix A_i is expressed by the product of four basic transformations;

$$A_i = R(z_i, \theta_i).T(a_i, 0, d_i).R(x_i, \alpha_i)R(y_i, \beta_i) \quad (5.25)$$

$\theta_i, a_i, d_i, \alpha_i, \beta_i$ in Eq.(5.25) represent the joint variable, link length, link offset, twist angle and Hayati parameter which is used for the sequential parallel joints, respectively [129]. 7-DOF haptic device does not include any parallel joints; hence the last term of the homogeneous transformation matrix is not used in our kinematic model.

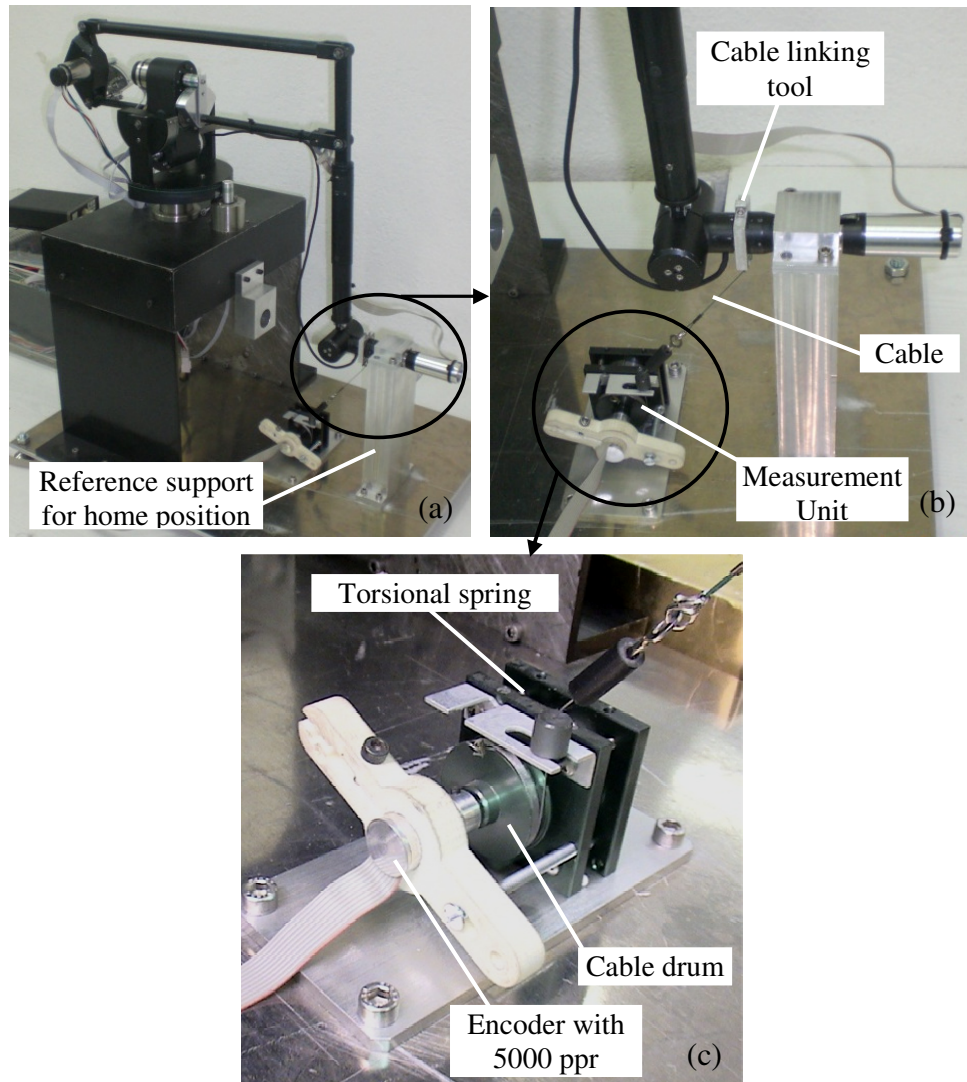


Figure 5.15 Implementation of the linear cable encoder in the haptic device calibration setup (*a*: Overall setup; *b*: measurement unit connection to end-effector; *c*: linear cable encoder for the distance measurement)

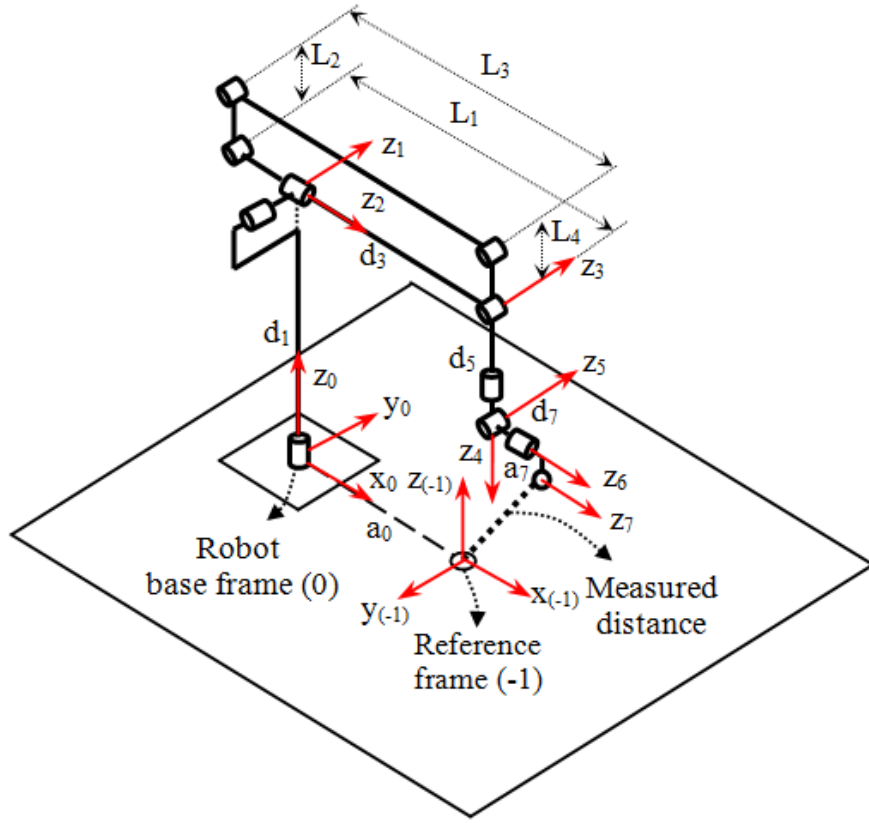


Figure 5.16 Kinematic model of 7-DOF haptic device for calibration

Eq.(5.26) gives the transformation matrix including the position (\underline{P}) and orientation matrix (\underline{C}) of the end-effector, which are relative to the reference frame attached to the starting point of the cable encoder. The distance (δ) between the end-effector and reference frame of the measurement system is the norm of position matrix \underline{P} as given in Eq.(5.27) ;

$$= A_0 A_1 A_2 \dots A_6 A_7 = \begin{bmatrix} \underline{C} & \underline{P} \\ \underline{0} & 1 \end{bmatrix} \quad (5.26)$$

$$\delta = \sqrt{P_x^2 + P_y^2 + P_z^2} \quad (5.27)$$

Table 5.1 D-H parameters of 7-DOF haptic device

Link	a_i	α_i	d_i	θ_i
w	a_0	$-\pi/2$	0	θ_0
1	0	$-\pi/2$	d_1	θ_1
2	0	$+\pi/2$	0	θ_2
3	0	$-\pi/2$	d_3	θ_3
4	0	$+\pi/2$	0	θ_4
5	0	$-\pi/2$	d_5	θ_5
6	0	$+\pi/2$	0	θ_6
7	a_7	0	d_7	θ_7

Transmission error parameters of the capstan drives and parallelogram mechanism make the identification procedure quite difficult. The measurement unit used in the experiments does not have high accuracy for the entire workspace. Therefore, using only distance measurements in a closed-chain kinematic model cannot identify all parameters effectively. Alternatively, it is proposed to use external encoders to be attached on the output joint rotation axes for the identification of the transmission error parameters of the capstan drives and parallelogram mechanism separately. In the implementation of calibration, a high resolution external encoder is used to measure the transmission error on the capstan drives and parallelogram mechanism (Figure 5.17). This encoder is assembled to the output joint rotation axes of the transmission mechanisms with reconfigurable special parts so that same encoder can be used for each transmission mechanism of the device in sequence.

Consequently the calibration of 7-DOF haptic device is conducted by stages. In the first stage, the parameter identification and correction of transmission errors are carried out with external encoder measurements; secondly the identification and correction of kinematic model parameters are implemented with linear cable encoder measurements. This proposed calibration procedure is depicted with a flowchart in Figure 5.18.

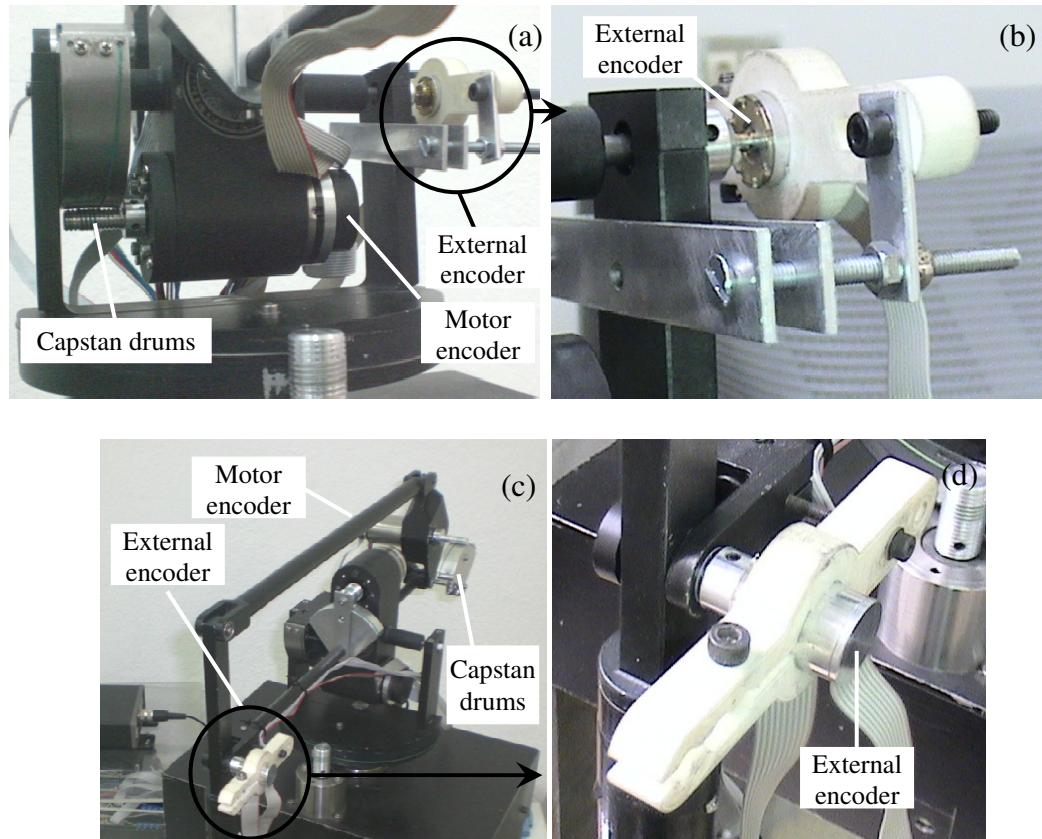


Figure 5.17 External encoder connections for capstan drive (a,b) and parallelogram (c,d)

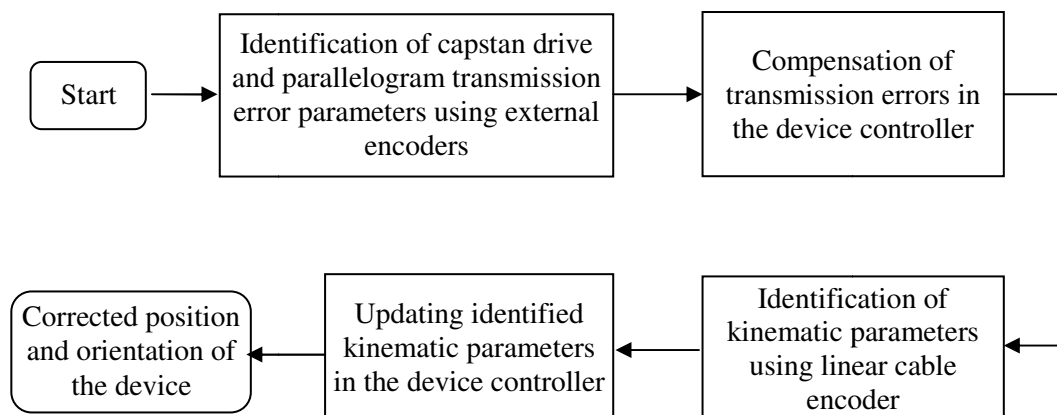


Figure 5.18 Flowchart of the proposed calibration procedure

5.5 Kinematic Parameter Identification

Nonlinear least square estimation technique is used to estimate the deviations in kinematic model parameters in this study. The base of this technique is to minimize the error between the measured (δ_{im}) and computed distances (δ_{ic}) from Eq.(5.28) for the closed-chain kinematic model using. The nonlinear least square optimization problem can be solved by Gauss-Newton or Levenberg-Marquardt algorithm [52]. Eq.(5.29) defines the nonlinear model of our optimization problem. The least-square solution estimates the parameter vector (φ) by minimizing the sum of squares of the error between n number of measurements and computations corresponding to n number of joint variables (η_i).

$$\delta_{ic} = f(\varphi, \eta_i) \quad (i = 1, \dots, n) \quad (5.28)$$

$$S(\varphi) = \sum_{i=1}^n \|\delta_{im} - f(\varphi, \eta_i)\|^2 \quad (5.29)$$

Non-identifiable kinematic model parameters are determined by using the method presented by Khalil et al. [103]. According to this, the first and last twist angles of the kinematic model (α_0 and α_7) and first joint offset (θ_0) are not identifiable since they do not have any effect on the distance calculations which are used in the identification. The line connecting the robot base origin to the cable encoder origin was selected as common x axes in the kinematic model. Therefore, the link offset between them (d_0) is always zero and it is not included in the identification. The other non-identifiable parameters are also not included in the parameter vector to be identified. However, their effects on the measurements should be considered in any simulation study.

5.6 Simulation of Proposed Calibration Method

In order to show the validity of the proposed calibration procedure, a simulation study was conducted by using the optimization function “*lsqnonlin*” of the MATLAB/Optimization Toolbox[®]. Some pre-defined deviations are added to the nominal kinematic parameters and virtual transmission errors are defined for all transmission mechanisms to construct a non-calibrated haptic device in the simulation. Furthermore, for a realistic simulation, a measurement data set should be generated for this non-calibrated device. Therefore, normal noise distributions with zero mean and a standard deviation are added to the deviated output joint angles of transmission mechanisms and deviated distances of the closed-chain kinematic model. The assigned transmission error parameters and the deviations from the nominal parameters are shown in Table 5.2 and 5.3 respectively. It is assumed that an encoder with 20000 ppr is used in the measurement of the transmission mechanism and linear cable measurement units. The standard deviation of the encoder is taken as one-third of the maximum quantization error of the encoder ($\sigma_e = 2\pi/20000/3$). This can be used directly for the output joint angle measurements of the transmission mechanisms, but for the distance measurement of the closed-chain kinematic model, this maximum quantization error is multiplied by the cable encoder drum circumference as shown in Figure 5.15-c and it can be found as ($\sigma_m = 2\pi R_d * \sigma_e = 2\pi * 0.015 * 2\pi/20000/3$). As mentioned in the previous section, transmission error of the parallelogram mechanism is represented by the tenth order polynomial model since it contains non-identifiable parameters. In the simulation, 200 random pose measurements are generated with these specifications for each transmission mechanism and end-effector of the device. The identification result of the transmission mechanism model parameters and the kinematic parameter deviations are given in Table 5.2 and 5.3. These tables also present percentage improvements (*I*) to show how much the error of each parameter is improved and Eq.(5.30) was used in these calculations.

$$I\% = \left(1 - \frac{|\lambda_a - \lambda_i|}{|\lambda_a - \lambda_n|}\right) \times 100 \quad (5.30)$$

where λ_a , λ_o and λ_n represent the actual, identified nominal values of each parameter. In the calculation results 100% improvement means that the parameter is estimated without any error. It should be noted that α_o , α_7 are non-identifiable parameters for the proposed closed-chain model.

Table 5.2 Simulation results for the identification of the capstan drive and parallelogram parameters

Parameters	Assigned	Identified	I (%)
Re ₁	-0.025	-0.024929	99.72
Re ₂	-0.020	-0.020291	98.54
Re ₃	0.015	0.013933	92.89
ro ₁ (mm)	0.200	0.200470	99.76
ro ₂ (mm)	0.250	0.248206	99.28
ro ₃ (mm)	0.200	0.209968	95.02
ri ₁ (mm)	0.005	0.004968	99.36
ri ₂ (mm)	0.0025	0.002522	99.12
ri ₃ (mm)	0.004	0.003990	99.75
βo ₁ (deg)	-105	-104.724022	99.74
βo ₂ (deg)	-10	-9.921826	99.22
βo ₃ (deg)	150	151.2022	99.20
βi ₁ (deg)	-15	-14.585499	97.24
βi ₂ (deg)	140	139.9904	99.99
βri ₃ (deg)	-100	-99.1451	99.14
The parameters of fourth drum eccentricity and deviations of parallelogram ro ₄ (mm)=0.1 ΔL ₁ (mm)= -0.0005 ri ₄ (mm)=0.002 ΔL ₂ (mm)= -0.0007 βo ₄ (deg)=-40° ΔL ₃ (mm)= 0.001 βi ₄ (deg)=-120° ΔL ₄ (mm)= 0.0003 Re ₄ =0.02		10 th order polynomial coefficients of the transmission error k10=1.191804 k4=-0.391253 k9=0.633845 k3=-0.100185 k8=-2.185038 k2=0.040587 k7=-0.983788 k1=-0.005159 k6=1.436945 k0=0.000043 k5=0.508398	

Table 5.3 Simulation results for the identification of the kinematic parameters

Parameters	Assigned	Identified	I (%)
$\Delta\alpha_0$ (mrad)	1.500	-	-
$\Delta\alpha_1$ (mrad)	-1.500	-1.477	98.47
$\Delta\alpha_2$ (mrad)	1.300	1.309	99.30
$\Delta\alpha_3$ (mrad)	-1.400	-1.396	99.73
$\Delta\alpha_4$ (mrad)	1.200	1.424	81.35
$\Delta\alpha_5$ (mrad)	-1.100	-1.320	80.01
$\Delta\alpha_6$ (mrad)	-1.600	-1.546	96.60
$\Delta\alpha_7$ (mrad)	1.700	-	-
Δa_0 (mm)	1.900	1.901	99.99
Δa_1 (mm)	-1.100	-1.089	98.97
Δa_2 (mm)	1.600	1.592	99.47
Δa_3 (mm)	-1.200	-1.199	99.99
Δa_4 (mm)	1.400	1.408	99.44
Δa_5 (mm)	-1.500	-1.499	99.99
Δa_6 (mm)	1.400	1.402	99.86
Δa_7 (mm)	-1.300	-1.301	99.99
Δd_1 (mm)	1.200	1.206	99.44
Δd_2 (mm)	-1.500	-1.504	99.71
Δd_3 (mm)	1.300	1.308	99.37
Δd_4 (mm)	-1.300	-1.269	97.64
Δd_5 (mm)	1.400	1.406	99.55
Δd_6 (mm)	-1.200	-1.201	99.99
Δd_7 (mm)	1.000	1.001	99.92
$\Delta\theta_1$ (mrad)	1.000	1.006	99.44
$\Delta\theta_2$ (mrad)	1.700	1.756	96.69
$\Delta\theta_3$ (mrad)	-1.300	-1.187	91.29
$\Delta\theta_4$ (mrad)	1.000	0.972	97.24
$\Delta\theta_5$ (mrad)	-1.200	-1.245	96.22
$\Delta\theta_6$ (mrad)	-1.000	-1.093	90.66
$\Delta\theta_7$ (mrad)	1.100	0.841	76.45

It is not possible to evaluate the transmission error results of the parallelogram mechanism by percentage improvement as it is represented by a tenth order polynomial in the calibration procedure. Therefore, the simulation measurements and identified polynomial are plotted on the same figure. Figure 5.19 shows that the identified tenth order polynomial follows the transmission error of the parallelogram mechanism accurately.

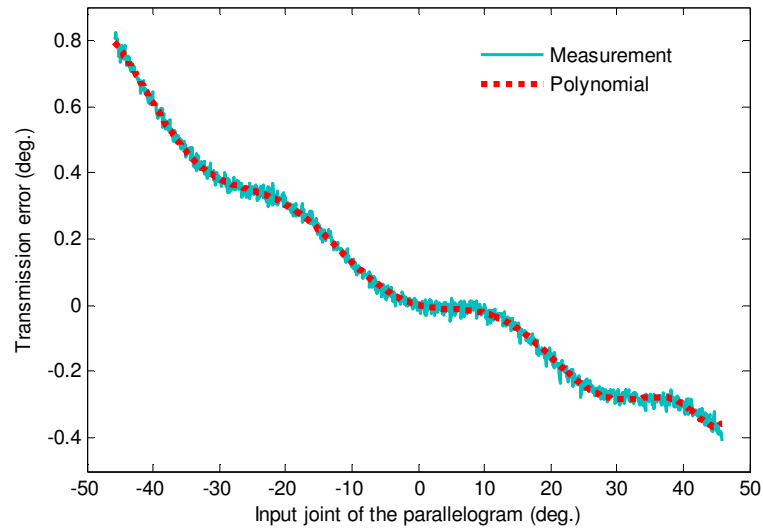


Figure 5.19 Parallelogram transmission errors

For further evaluation of the proposed kinematic calibration performance, 200 various poses and the corresponding measurements, which are different from those used in the identification step, are generated in the simulation. The position and orientation errors before and after calibration for these poses are shown in Figure 5.20. Additionally, the percentage improvements in the RMS errors are also presented on the same plots. It can be concluded from the results that the proposed kinematic calibration technique improves the position and orientation accuracy of the device significantly.

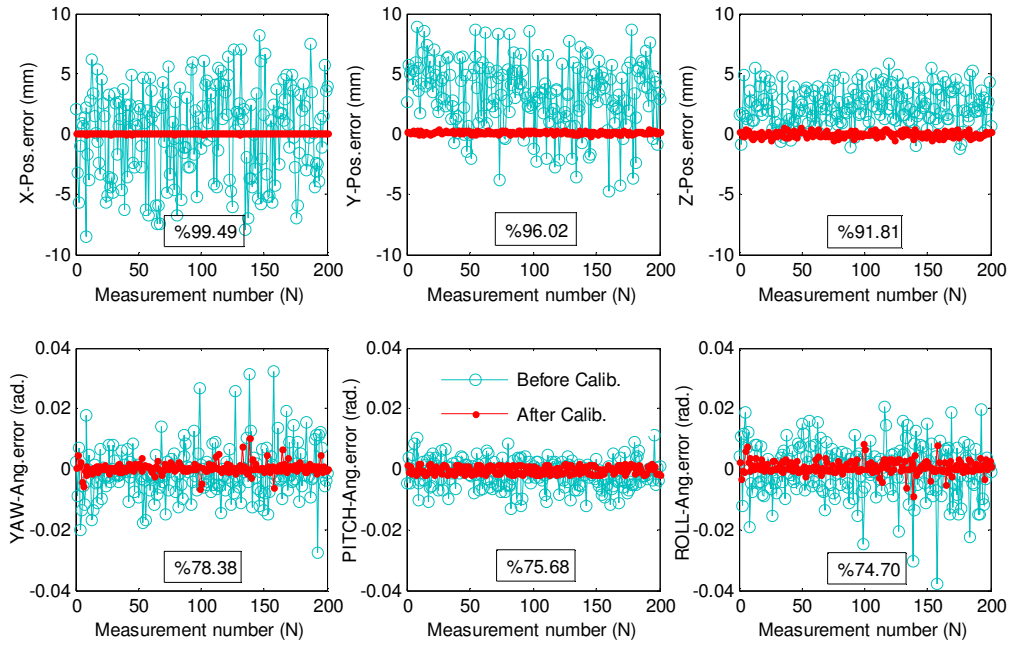


Figure 5.20 Simulation calibration results for the positions and orientation angles of 7-DOF haptic device

5.7 Experimental Results

Jacobian matrix is employed in the controllers of 7-DOF haptic device to calculate the handle pose and implement the force control algorithm. Since any deviation in the Jacobian elements affect the accuracy of pose calculation and force control, kinematic calibration has a great importance. In this section experimental parameter identification was conducted for 7-DOF haptic device, and its effect on the pose and force control accuracy is presented sequentially.

In the experimental identification, cable encoder distance, output joint angle of the transmission mechanisms and the corresponding device joint angles were measured while the device is moved by the user such that all joints swept their entire working range. Like simulation study, the identification is implemented by using the optimization function “*lsqnonlin*” of the MATLAB/Optimization Toolbox[®] by using 200 random measurements. The parameter identification results are given in Table 5.4 and 5.5. In order to evaluate the parameter

identification results of transmission mechanisms, the output joint measurements and their theoretical calculations using the identified parameters are plotted in Figure 5.21. This figure shows that identified joint angles of the transmission mechanism can correct their transmission errors effectively.

Table 5.4 Identification results for capstan drive and parallelogram parameters

Parameters	Identified
Re_1	0.339383
Re_2	0.226663
Re_3	0.09557
$ro_1(mm)$	1.498938
$ro_2(mm)$	1.158217
$ro_3(mm)$	0.3918
$ri_1(mm)$	0.004212
$ri_2(mm)$	0.007451
$ri_3(mm)$	0.0228
$\beta_{o1}(deg)$	-153.60
$\beta_{o2}(deg)$	-168.40
$\beta_{o3}(deg)$	-171.38
$\beta_{i1}(deg)$	-110.64
$\beta_{i2}(deg)$	98.00
$\beta_{ri3}(deg)$	80.68
<p>10th order polynomial coefficients of the transmission error</p> <p> $k_{10}=4.758752$ $k_4= 0.494506$ $k_9= 3.410843$ $k_3=-0.159660$ $k_8= 5.476355$ $k_2=-0.033388$ $k_7=-3.421651$ $k_1=-0.038000$ $k_6=-2.458614$ $k_0= 0.000000$ $k_5= 1.186850$ </p>	

Table 5.5 Identification results for kinematic parameters

Parameters	Identified
$\Delta\alpha_0$ (mrad)	-
$\Delta\alpha_1$ (mrad)	-2.866
$\Delta\alpha_2$ (mrad)	1.133
$\Delta\alpha_3$ (mrad)	4.550
$\Delta\alpha_4$ (mrad)	14.818
$\Delta\alpha_5$ (mrad)	-1.223
$\Delta\alpha_6$ (mrad)	-26.794
$\Delta\alpha_7$ (mrad)	-
Δa_0 (mm)	-4.195
Δa_1 (mm)	-0.402
Δa_2 (mm)	-2.966
Δa_3 (mm)	-1.225
Δa_4 (mm)	-2.584
Δa_5 (mm)	-0.076
Δa_6 (mm)	0.340
Δa_7 (mm)	-0.522
Δd_1 (mm)	-2.907
Δd_2 (mm)	2.017
Δd_3 (mm)	-3.242
Δd_4 (mm)	-0.179
Δd_5 (mm)	-1.164
Δd_6 (mm)	-1.021
Δd_7 (mm)	1.948
$\Delta\theta_1$ (mrad)	-6.088
$\Delta\theta_2$ (mrad)	5.648
$\Delta\theta_3$ (mrad)	13.363
$\Delta\theta_4$ (mrad)	-22.663
$\Delta\theta_5$ (mrad)	0.125
$\Delta\theta_6$ (mrad)	5.941
$\Delta\theta_7$ (mrad)	-51.718

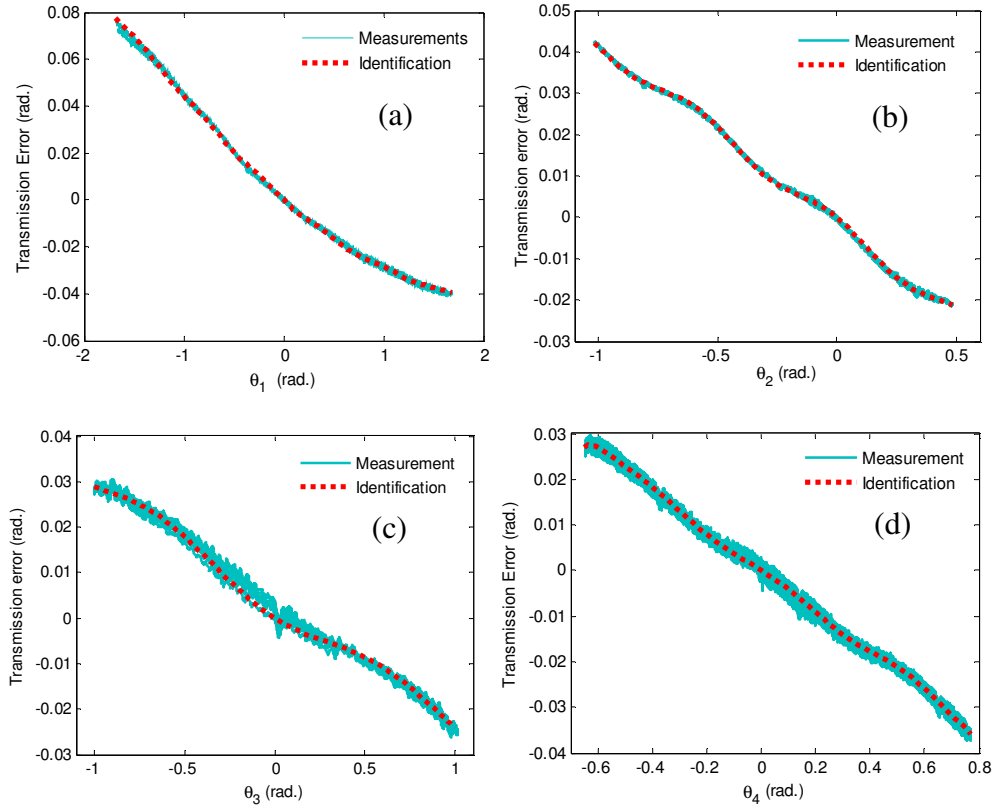


Figure 5.21 Identified model and measurements of transmission errors for (a) capstan-1 (b) capstan-2 (c) capstan-3 and (d) parallelogram

5.7.1 Pose Accuracy Improvement

The last step of the calibration is to compensate pose errors and correct the device poses by using the identified parameters. To this end, the identified parameters were directly used in the device controller to correct the model errors. For the evaluation of the pose accuracy improvement, the device handle was moved by the user randomly in the workspace for about 100 sec. The calibrated and non-calibrated kinematic models are run at 1 kHz by MATLAB/RealTime Windows Toolbox[®]. Meanwhile, the cable encoder measurements were stored. The measured and computed closed loop kinematic model distances and their corresponding errors are plotted on the on Figure 5.22. In this experiment, both full calibration and the calibration where the transmission errors are not included are run separately to show the effect of transmission errors on calibration. It can be seen from Figure 5.22, the errors while starting and finishing are very low

since these measurements are taken while the device is motionless at the home position. When the device is moved away from the home position, the non-calibration model and calibration model without transmission correction produces excessive error due to the transmission errors.

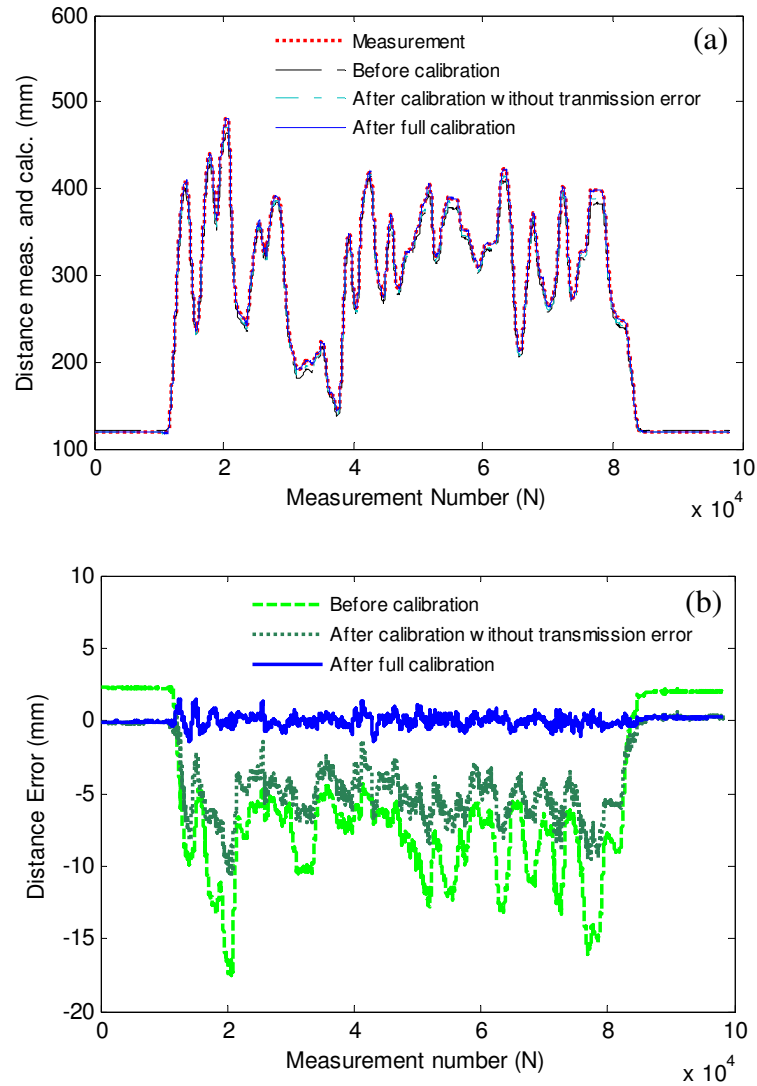


Figure 5.22 Distance measurement and calculations before and after calibration (a) and their errors (b)

In order to evaluate the pose accuracy results further (distance errors), the percentage improvement in the RMS of the distance errors are calculated by using

Eq.(5.31). The symbols of e_c and e_{nc} in this equation denote calibrated model and non-calibrated model errors respectively.

$$I\% = \left(\frac{|RMS(e_c) - RMS(e_{nc})|}{|RMS(e_{nc})|} \right) \times 100 \quad (5.31)$$

The results show that: (1) the full calibration provides 96.6% improvement and (2) the calibration without including transmission errors provides 44.7% in the pose accuracy. This indicates that almost half of the distance errors results from the transmission errors of the capstan drives and parallelogram mechanisms.

5.7.2 Force Control Accuracy Improvement

The kinematic calibration improves the accuracy of force control as well as pose in haptic devices. In this section, the effect of calibration on the force control is investigated. Usually, CLIC is preferred in the capstan driven haptic devices for effective force control. Figure 5.23 shows the block diagram of CLIC for multi-DOF haptic devices, which includes the virtual environment (Z_v), haptic device (Z_d), controller (G) and Jacobian blocks (J). Since the Jacobian block includes the kinematic parameters, the calibration should also improve the force control.

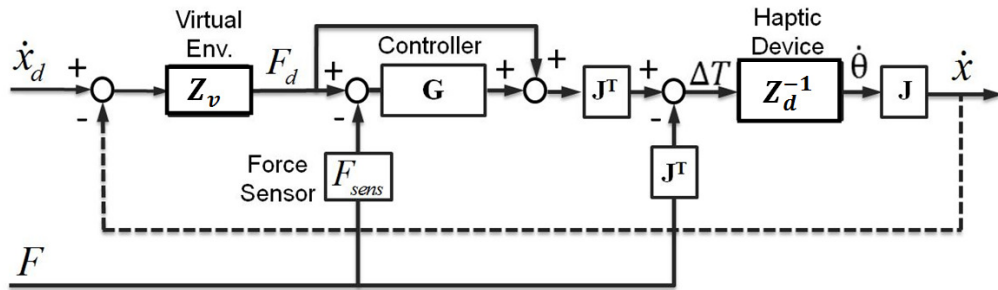


Figure 5.23 Closed loop impedance control for multi-DOF haptic devices

For experimental evaluation of the effect of calibration on the force control accuracy, a simple virtual environment scenario is defined. In this scenario, a virtual wall constructed with only a spring constant ($K=100$ N/m) is moved 20 mm in the z-axis direction of the haptic handle while the handle is fixed on a stationary point as shown in Figure 5.24. Same experiment is carried out with both full calibrated and non-calibrated models in order to show the effect of calibration on the performance of controller. In the experiments, the handle is fixed and the virtual wall is moved to provide same positioning in both experiments.

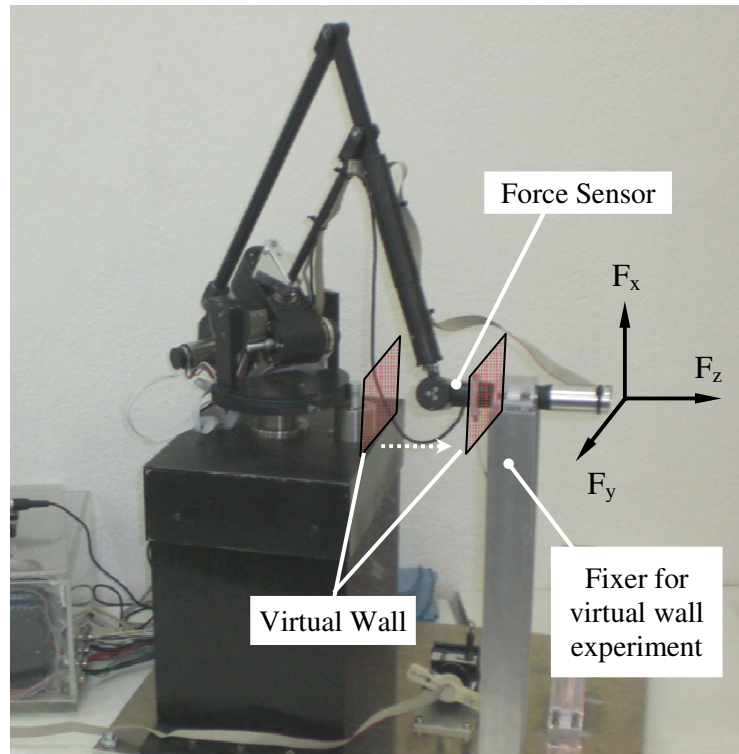


Figure 5.24 Virtual wall experiment of 7-DOF haptic device

In this experiment, only a one dimensional force should be measured in the z-direction of the handle and the force measurements in other (x and y) directions should be zero. Figure 5.25-b shows the experimental results. These results show that the calibration improves the force control by eliminating the transverse forces

(F_x and F_y) on the handle. Note that the redundant joint of the device is locked at the home position and same controller parameters are used in all experiments.

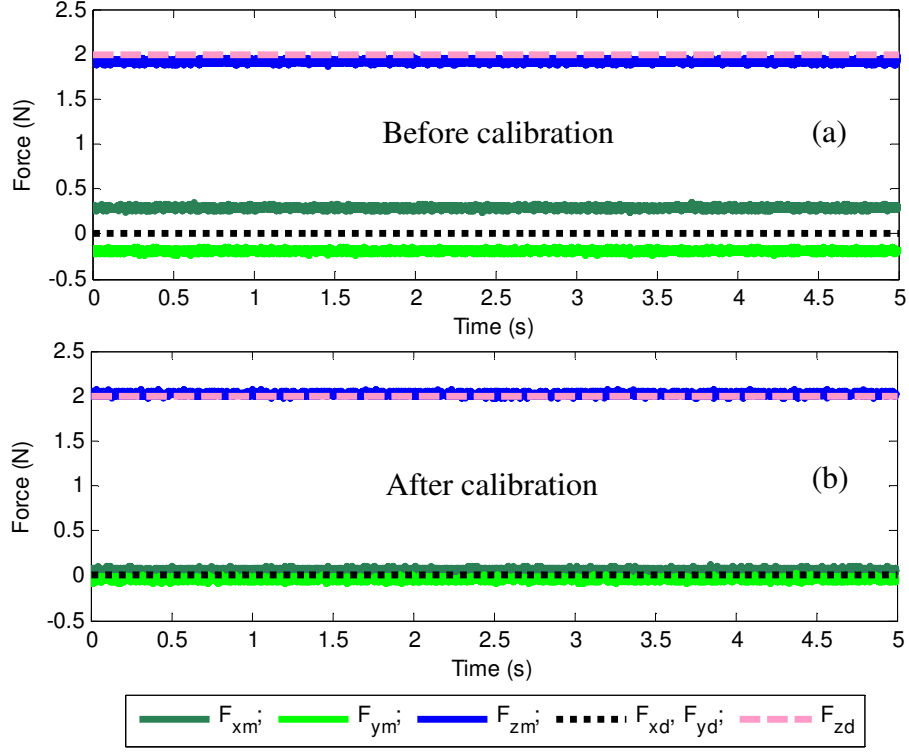


Figure 5.25 Force control accuracy of the device before (a) and after (b) calibration (m: measured, d: desired)

5.8 Conclusion

In this chapter both simulation and experimental calibration results are presented for a 7-DOF capstan driven haptic device to improve the pose and force control accuracy. Primarily an analytical method was successfully developed to model the slip error of a capstan drive and it was validated by a set of experiments conducted on a 1-DOF capstan drive hardware. Then, a closed-chain kinematic structure is established on the 7-DOF haptic device by means of a low cost and easy to implement linear cable encoder. The developed calibration method includes not only the deviation of kinematic model parameters, but also

transmission error parameters for the capstan drives and parallelogram mechanism. They are identified using the measurements of cable encoder and external encoders. The simulation and experimental results show that the kinematic calibration of a haptic device improves the pose and force control accuracy significantly. The proposed calibration method in this chapter can be implemented easily to improve both pose and force control performance of the haptic devices with capstan drives and parallelogram mechanisms.

CHAPTER 6

OPTIMAL POSTURE CONTROL ALGORITHM TO IMPROVE THE STABILITY OF REDUNDANT HAPTIC DEVICES

6.1 Introduction

As mentioned in Chapter 4, the stability is the major requirement in haptic interfaces for a realistic simulation. The energy exchanges between the user and haptic device as the user cooperates with the device. The excess energy flowing towards the user can lead to undesired vibrations. Smooth interaction without any vibration for any virtual environment is only possible provided that the passivity of haptic interface is guaranteed. For a passive haptic system, the energy flowing into the system should not be less than initially stored energy as formulated in Eq.(6.1) for 1-DOF rotational systems. This equation refers to the passivity condition of the haptic system. T_h , $\dot{\theta}_h$, E_0 in the equation denote the user torque, user hand angular velocity and initially stored energy in the system.

$$\int_0^t T_h(\tau) \dot{\theta}_h(\tau) d\tau \geq -E_0 \quad \text{for } t > 0 \text{ and all admissible } T_h(t) \quad (6.1)$$

Various studies are proposed in the literature to ensure passivity for stability improvement such as electrical damping [57, 58], analog input shaper (AIS) [59], analog output limiter (AOL) [60], passivity observer / passivity controller (PO/PC) [61-63], energy bounding algorithm (EAB) [64, 65], force bounding

algorithm (FBA) [66] and the passive set-position modulation (PSPM) framework [67]. The detailed discussions of these algorithms are presented in Chapter 4.

Principally, stability improvement studies can be classified into two major techniques in the literature: (1) increasing the level of damping and (2) modulating the command force or set-position. However, these techniques suffer from the deterioration of transparency since the desired forces calculated in the virtual/remote environment cannot be provided in the actuators due to the damping or modulating processes. For multi-DOF haptic devices passivity condition must be satisfied on each actuator to provide stable interaction. Unsatisfied passivity in any actuator makes the whole system unstable. In redundant haptic manipulators it is possible to keep the system stable without changing the level of damping and bounding the command force. This study proposes to use the posture adjustment ability of a redundant haptic manipulator to keep the actuators passive. In this proposed approach, the posture of the redundant device is optimally controlled to minimize the torque requirement on the critical actuator in terms of stability. Golden section search algorithm [130] is employed to estimate redundant joint angles between its limits for optimal postures. The cost function of the optimization algorithm is based on the passivity condition provided in Chapter 4.

The rest of the paper is organized as follow: The contribution is explained in the following section. The next section explains 7-DOF haptic device used in the experiments. Then the optimal posture control algorithm is introduced. The experimental results and performance evaluations are discussed in the next section. The last section is related to the conclusion.

6.2 Contribution

Passivity plays a vital role in haptic interfaces to provide wide range of stable virtual environment impedances. The passivity should be ensured for each actuator of a multi-DOF haptic device to achieve stable interaction. In this study,

an optimal posture control algorithm was developed to guarantee the passivity for each actuator and thereby maximize the stability performance of a redundant haptic device. In the proposed algorithm, the device posture is adjusted online based the optimal postures which are previously estimated by a golden section search algorithm. The proposed control algorithm was experimentally implemented on a virtual sphere using a 7-DOF redundant haptic device. Z-width stability performance metric was used for the evaluation of the proposed algorithm and the results showed that it improves significantly stable impedance range of a 7-DOF redundant haptic device. As a result, the optimal posture control approach can be used to improve the stability performance of redundant haptic devices.

6.3 Experimental Hardware

In this chapter, 7-DOF redundant haptic device, which is initially introduced in Chapter 5 (Figure 5.1) was used. It is similar to 6-DOF Phantom haptic device in terms of mechanical structure; except that it has only one redundant joint that corresponds to the last joint of the shoulder (z_2 axis) as shown in Figure 6.1a. The redundancy enables the device to reach any position in the workspace with various postures. Figure 6.1b shows the sample right, left and home postures of the device.

The actuating units of the device are *Maxon* brushless DC motors for positioning stage and *Faulhaber* DC mini-motors for orientation stage. They are driven by *Maxon* 4QEC DES 50/5 and LSC 4Q DC 30/2 servoamplifiers respectively. The motor powers are increased using capstan drive mechanisms in positioning stage and zero-backlash gearheads in orientation stage. There are two types of optical encoders attached to the brushless DC motors with 1000 ppr and DC mini-motors with 512 ppr. A 6-DOF *ATI-NANO-17* force/torque transducer is employed at the handle of the device. The control algorithm is implemented on the device by means of Real-Time Windows Target Toolbox of MATLAB[®]. The technical properties of the computer used in the application are Intel Core 2 Quad CPU

Q9400 @ 2.66 GHz processor, 4 GB Ram, NVIDIA GeForce 9500 GT graphics card. Humusoft MF-624 multifunction I/O card is used for the acquisition of the signals at 1 kHz sampling frequency.

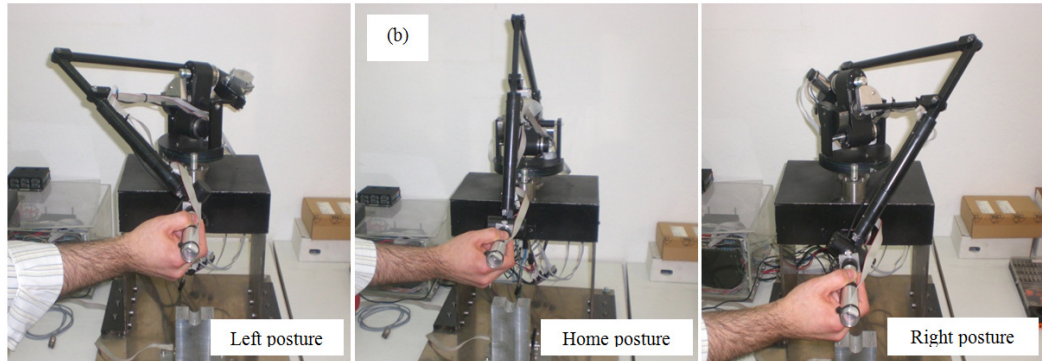
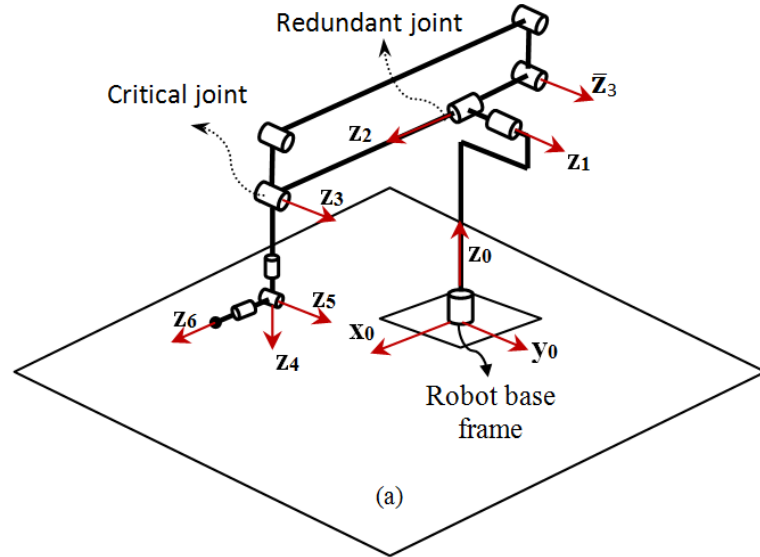


Figure 6.1 7-DOF haptic device kinematic model at home posture (a) and various sample postures (b)

6.4 Optimal Posture Control Algorithm

The proposed optimal posture control algorithm based on the passivity condition is presented in this section. Haptic systems must be passive to provide stable haptic interactions. The passivity of haptic devices means that the actuators used in the haptic system should not generate excess energy causing undesired

vibration. The major factors affecting the stability are information loss in sample/hold unit, computational delay, non-zero noise/phase-lag in velocity/acceleration estimators, non-zero noise/phase-lag in transducer signal filters, communication delays and disturbance compensation algorithms.

In the passivity based control algorithms the energy flow into the haptic system should not exceed initially stored energy as formulated in Eq.(6.1). In Chapter 4, the passivity condition was re-derived for 1-DOF haptic device as given in Eq.(6.2). This equation can also be used for each joint of a multi-DOF haptic device.

$$\begin{aligned} \frac{1}{2}I\dot{\theta}_d^2(n) + \frac{b}{T} \sum_{k=0}^{n-1} \Delta\theta_d^2(k+1) + T_c \sum_{k=0}^{n-1} \text{sgn}[\dot{\theta}_d(k)]\Delta\theta_d(k+1) \\ + \sum_{k=0}^{n-1} T_d(k)\Delta\theta_d(k+1) \geq -E_0 \end{aligned} \quad (6.2)$$

where $n, I, b, T, \Delta\theta_d, \theta_d, \dot{\theta}_d, T_c, T_d, E_0$ denote the last sampling, inertia induced in the joint, joint damping, sampling time, angular position difference, angular position, angular velocity, Coulomb friction, desired actuator torque, initially stored energy.

The first three terms in Eq.(6.2) indicate the energy contributed by passive device elements such as inertia, damping and Coulomb friction and they are always positive. The last term is the excess energy source extracted by the actuator employed in the device. If the total energy exceeds the initially stored energy, the device starts to produce undesired vibrations, which cause instability. Especially, when high impedances need to be simulated, the desired actuator torque increases and the passivity criterion cannot be met.

Eq.(6.2) shows that either the effects of passive elements should be maximized or the desired motor torque should be minimized for maximum stability. The second

approach is much more preferable, since the increasing physical inertia, damping and Coulomb friction deteriorates the transparency. Hence, the optimal posture control algorithm aims to minimize the desired actuator torque on the critical joint of the device in terms of stability. If the passivity is ensured for the critical joint, the whole system remains stable. However, at first, it should be decided that which joint is critical in 7-DOF device.

As mentioned in Chapter 4, Colgate et. al. showed that the achievable virtual wall impedance is directly related with the level of physical damping in the system [56]. Eq.(6.3) is a simplified passivity limit for haptic interfaces proposed by Colgate et. al. and indicates that the higher physical damping increases the achievable impedances as it dissipates the energy due to the instability.

$$b > \frac{KT}{2} + B \quad (6.3)$$

where b , K and B represents the physical damping of the system, virtual wall stiffness and virtual wall damping parameters respectively. T is the sampling time. Based on the passivity limit given in Eq.(6.3), the joint which has minimum physical damping can achieve only lower virtual impedances than the others; in other words, it can provide only lower desired torques than the others. Therefore, the joint which has minimum physical damping can be considered as a critical joint. A simple experiment was conducted on each joint individually to determine their physical damping. Using only stiffness parameter (K) in the virtual wall model, the passivity limit given in Eq.(6.3) can be simplified as;

$$K \leq 2b/T \quad (6.4)$$

The physical damping's (b) in the joints of the device were determined experimentally by the limits of achievable virtual stiffness (K) of those joints. In this technique, the amount of virtual stiffness was increased until an unstable interaction starts where physical damping is calculated using the simplified

equation of passivity limit. This simple virtual wall experiment was conducted for all joints of the 7-DOF haptic device individually. Sampling time (T) is 0.001 sec. in the experiments. The virtual stiffness limits of the joints (1, 2 and 3) and their corresponding physical damping values are determined as (41 Nm/rad, 29 Nm/rad, 7 Nm/rad) and (0.0205 Nms, 0.0145 Nms, 0.0035 Nms), respectively. As a result it is concluded that the critical joint of the device in the virtual wall collisions is the elbow joint shown as z_3 in Figure 6.1a. Similar result was observed in the virtual wall collision experiments implemented with 7-DOF haptic device. In these experiments, the elbow joint always caused instability first before any other joint

In the proposed algorithm, the redundant joint (z_2 in Figure 6.1a) is employed to adjust the device posture for the minimization of desired torque on the critical joint and the remaining actuating joints are utilized for 6-DOF haptic feedback. In order to provide minimum desired torque on the critical joint, optimal redundant joint angles should be estimated with an appropriate optimization technique and an effective cost function. A golden section search algorithm is an accomplished tool for such kind of problem [130]. It can be used reliably to find the global minimum of a function between two boundaries. The cost function of this problem is the minimization of critical elbow joint torque (T_{dc}) transformed from the endpoint desired force (F_d) to estimate the redundant joint angle (θ_R). The problem can be defined as given below:

Find θ_R to minimize

$$T_{dc}(\theta_R) = [\tilde{f}_r^T(\theta_R) \cdot F_d]_{(4,1)} \quad (6.5)$$

such that $\theta_L < \theta_R < \theta_U$

where F_d , T_{dc} , \hat{f}_r^T , θ_R , θ_U , θ_L , represent the desired endpoint force calculated from virtual environment, critical elbow joint torque, Jacobian matrix, redundant joint angle, redundant joint angle upper limit and lower limit, respectively.

The detailed block diagram of the proposed algorithm is shown in Figure 6.2. It comprises two parts: (1) redundant joint position controller and (2) force controller. Redundant joint adjusts the posture of the device for maximum stability while the force controller produces the required torques of the remaining joints as an impedance type force control algorithm [26]. The optimal redundant joint angles estimated from Eq.(6.5) are forwarded to the position controller as input. These optimum redundant joint angles depend on the handle position and direction of the desired force on the contact points of the virtual object surface. In this chapter, it was preferred to calculate optimal redundant joints offline before implementation since the real-time calculation produces excessive computational load. Therefore, an optimal redundant joint angles map was generated and a look-up table was formed to be used as a reference input in real-time position controller for a virtual sphere experiment. The look-up table determines the desired redundant joints according to the actual location of the handle. The block diagram shown in Figure 6.2 contains the virtual model, device dynamics, user dynamics, actuator models, force feedback controller and redundant joint position controller. Only proportional gain is employed in the force controller since the derivative and integral terms affect the force control adversely [34]. Z_v , Z_u , K_p , x_u , x_h , θ , $\dot{\theta}$, J_v , J_a , T_0^7 , F_u , τ_d , τ_m , τ_u , τ , v_a , i_m , R_m , L , K_{emf} , K_m symbols in Figure 6.3 denote the impedance of virtual environment, impedance of user hand, proportional gain of force feedback controller, position of the user hand, position of the haptic handle, joint position of the device, joint velocity of the device, virtual Jacobian matrix, actual Jacobian matrix, transformation matrix, user force, desired torque command, joint torque applied by motor, joint torque applied by user, resultant torque in joint, motor voltage, motor current, motor resistance, motor inductance, motor back EMF constant, motor torque constant respectively.

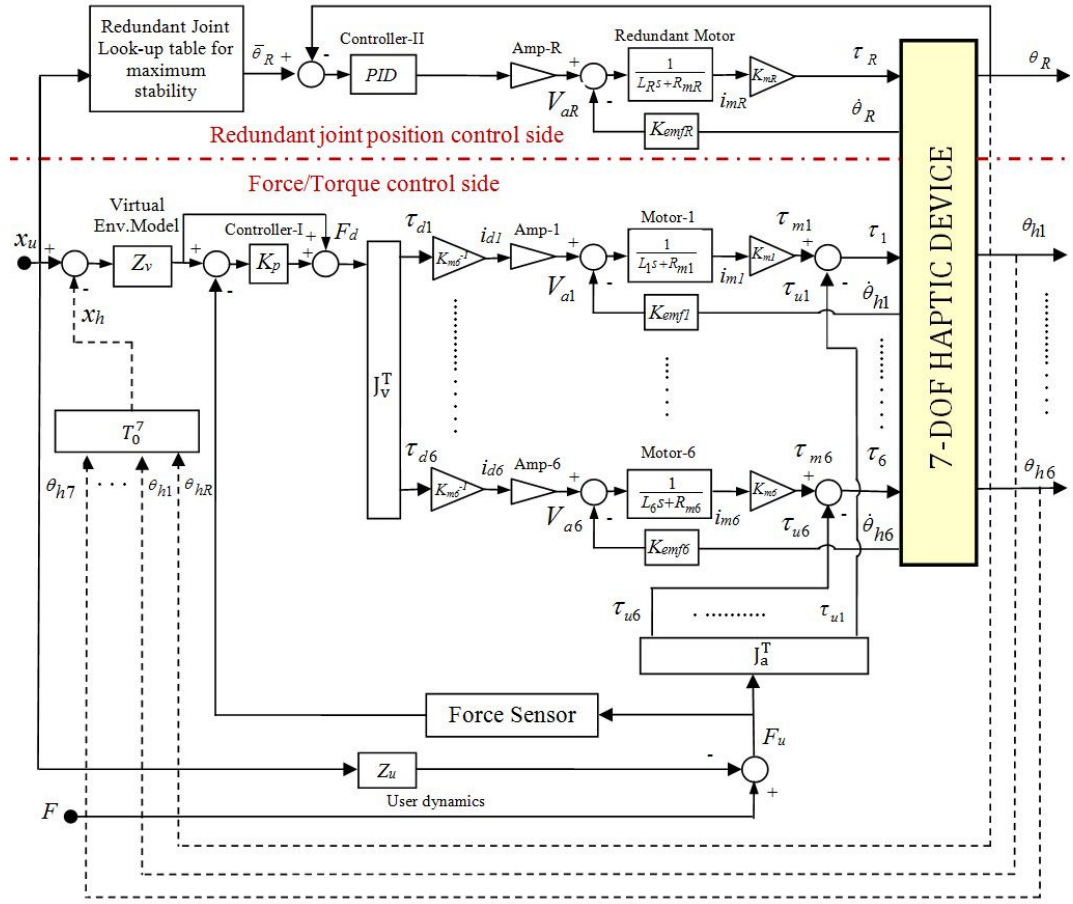


Figure 6.2 Proposed optimal posture control algorithm

6.5 Implementation of the Proposed Algorithm

This section presents a sample implementation of the proposed algorithm. In this implementation, a sample virtual environment was designed in 3D Animation Toolbox of the MATLAB Simulink® (Figure 6.3). A 50 mm radius sphere with a coordinate (100, -100, -150 mm) is located in the virtual environment. This virtual sphere was modeled by using spring-damper Voigt model lying from center to surface at each contact point. When the user moves the handle into the sphere, the device produces a force in the direction of the surface normal depending upon the penetration distance, velocity and virtual model parameters.

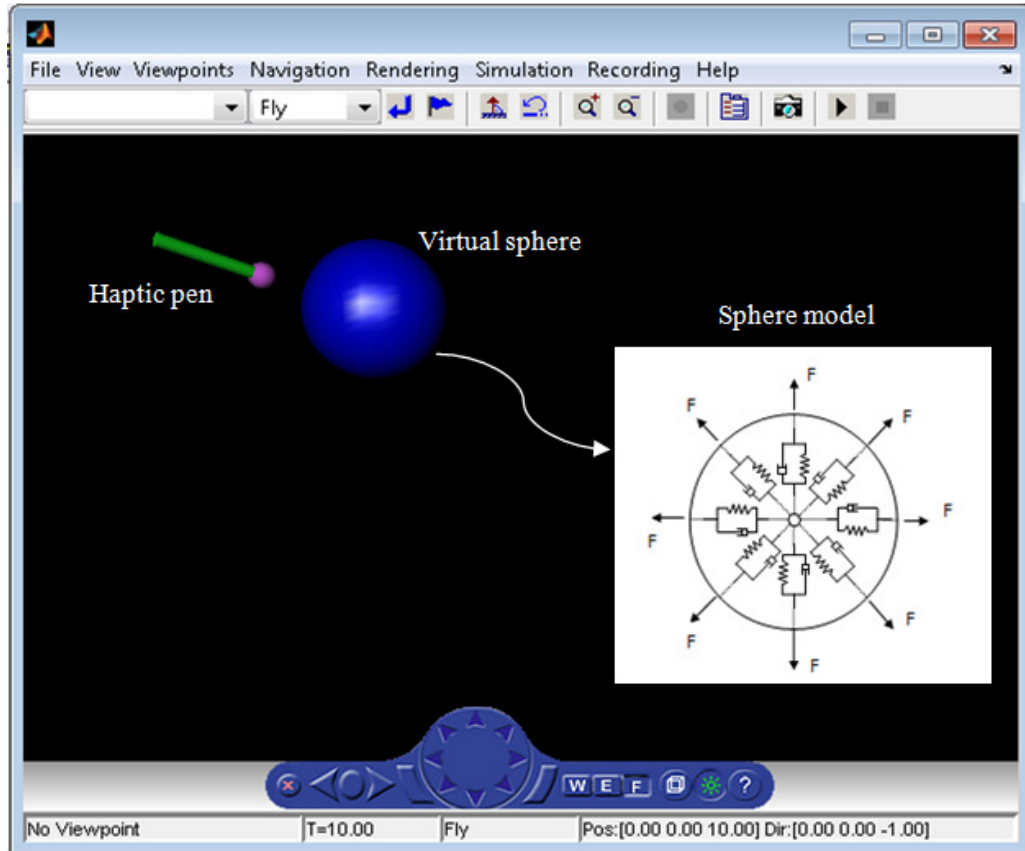


Figure 6.3 The designed virtual environment for the implementation of the proposed algorithm

6.5.1 Redundant Joint Maps

The redundant joint motor adjusts the device posture for maximum stability by using optimal redundant joint angles. One of the MATLAB[®] optimization functions, “*fminbnd*” serving as golden section search algorithm, was used for the estimation of the optimal redundant joint angle of the virtual sphere simulation. Figure 6.4 shows the initial map of redundant joint angles for the optimal postures depending upon the contact points. It can be seen from this figure that there is a ridge on the initial map. The reason of this ridge is depicted in Figure 6.5. According to the illustration, the full right posture gives the minimum torque requirement on left hemisphere and the full left posture gives it on the right. This ridge may cause the sudden change in the device posture which is not desired

since it deteriorates the transparency and may be harmful for the user. Therefore, this ridge was smoothed to avoid the sudden changes of the posture. Figure 6.6 shows this smoothed redundant joint angle map.

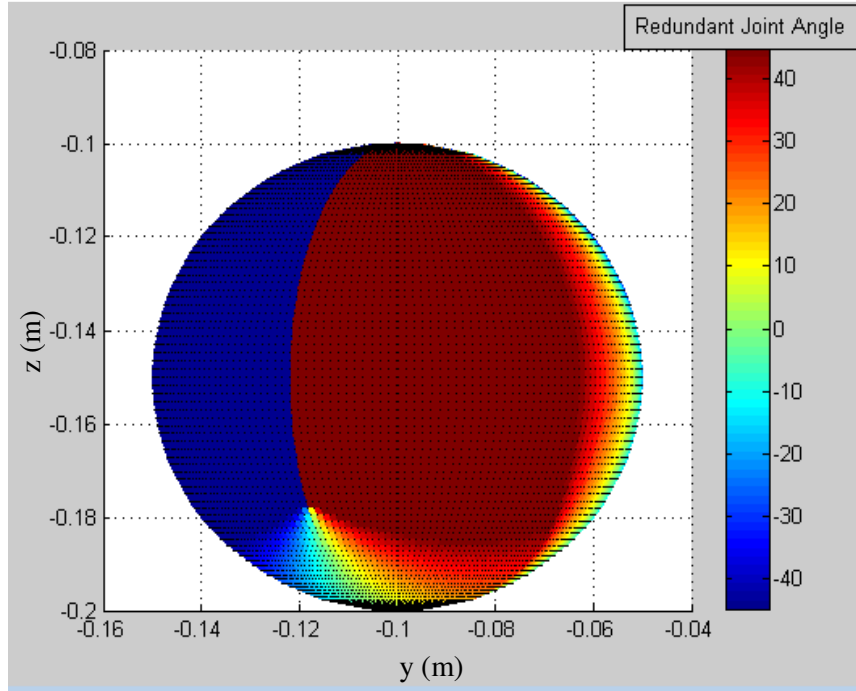


Figure 6.4 Initial map of redundant joint angles for optimal postures

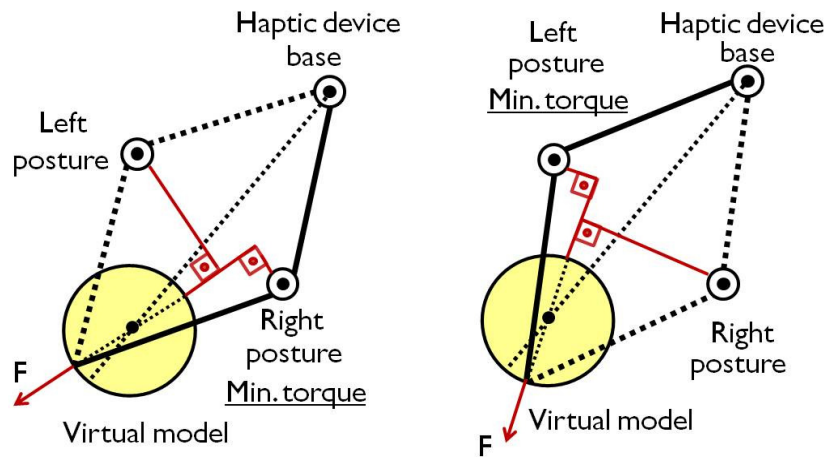


Figure 6.5 Schematic views for the reason of ridge on the redundant joint angle

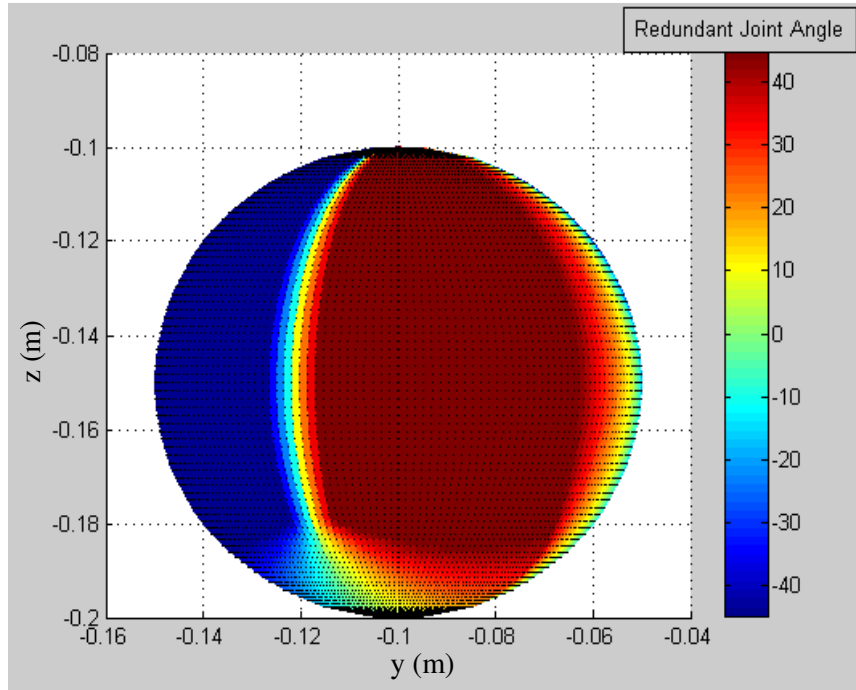


Figure 6.6 Smoothed map of redundant joint angles for optimal postures

6.5.2 Gradually Posture Adjustment

The posture adjustment should start with the first movement of the handle towards the sphere and be completed before touching the sphere. The device should transmit the contact forces with the fixed optimal posture, since the posture changing during penetration may produce the undesired inertia and deteriorate the transparent interaction. For that purpose, some spherical offsets were constructed as shown in Figure 6.7. The device adjusts the posture gradually while approaching the sphere with various redundant joint speeds increasing from outer to inner offsets. However, the innermost offset is considered as non-changing posture segment to preserve the transparency during haptic interaction. If the user wants to touch the points far away from the current contact point on the sphere, he needs to get out of the innermost offset and reenter after the new posture adjustment.

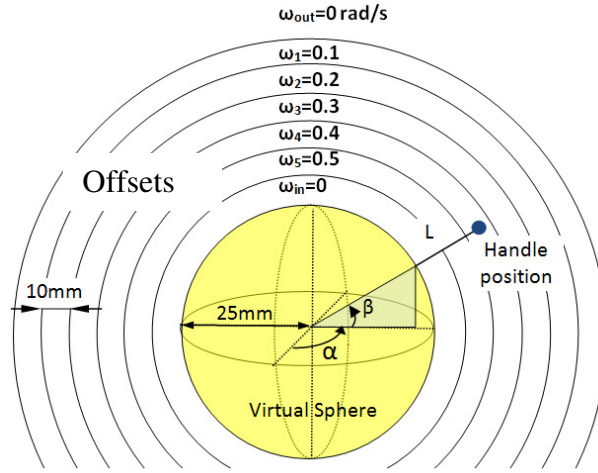


Figure 6.7 Spherical offsets for the proposed optimal posture control algorithm

6.6 Experimental Results

Stability performance of a multi-DOF haptic device is not same on every points of a virtual surface since the joint torque requirements change depending upon the force direction and location of the contact point. Hence, the stability performance of a multi-DOF haptic device should be evaluated on the different regions of the virtual model surface. In this study three different regions were selected on the virtual sphere for the stability tests and Z-width plots were generated experimentally on these regions. All details about the Z-Width stability performance metric are presented in Chapter 4. Since the default home posture of 7-DOF haptic device kinematics corresponds to 6-DOF Phantom haptic device kinematics, the proposed algorithm can be evaluated by comparing it with 6-DOF Phantom like posture of the device. Figure 6.8 shows the test regions on the sphere and their corresponding Z-width comparison plots between the optimal posture and 6-DOF Phantom like posture locked at default home posture. The results show that optimal posture control algorithm improves the achievable impedance ranges significantly on both sides and a little on lower side of the sphere.

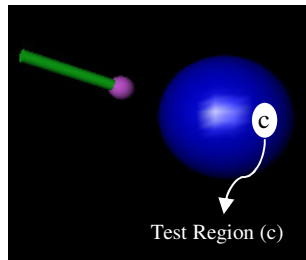
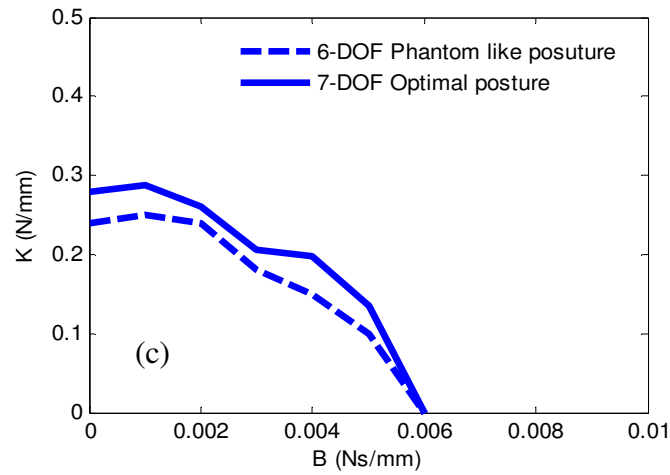
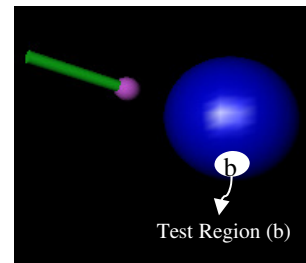
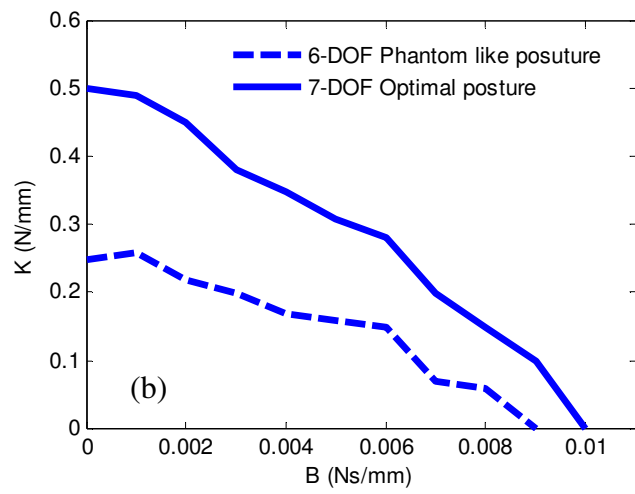
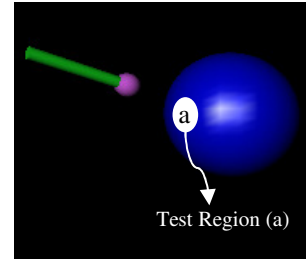
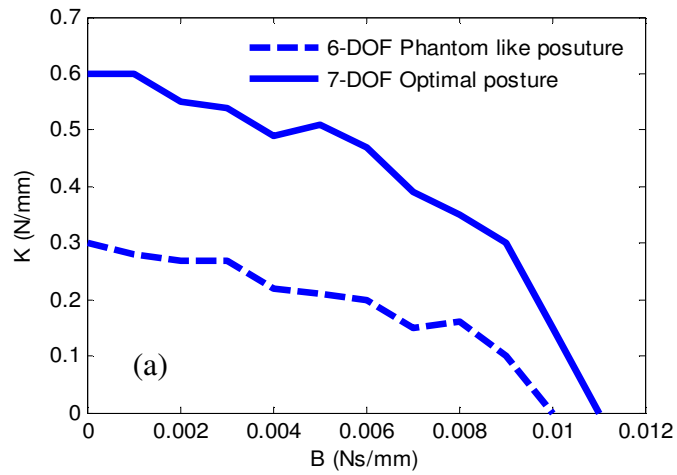


Figure 6.8 Z-width plots of 7-DOF optimal posture and 6-DOF Phantom like posture for three different regions (a, b and c) of the virtual sphere

6.7 Conclusion

Stability is indispensable in haptic interaction since unstable behavior deteriorates realistic interaction. For multi-DOF haptic devices, the passivity must be ensured in every actuator of the device for stable interaction. The occurrence of instability in any actuator makes the whole system unstable. In this chapter, an optimal posture control algorithm is proposed to improve the stability performance of the redundant haptic devices. The proposed algorithm minimizes the desired actuator torque of the critical actuator in terms of stability by using adjustable posture ability of a redundant haptic device. Golden section search algorithm is employed to estimate optimal redundant joint angles and the passivity condition is used as a cost function in the optimization. The posture of the device is adjusted online by the redundant actuator. An implementation of the proposed algorithm was carried out successfully with a 7-DOF redundant haptic device on a virtual sphere and Z-width stability performance metric is used for evaluation. The results show that the optimal posture control algorithm improves the stability performance of redundant haptic devices.

CHAPTER 7

CONCLUSION AND RECOMMENDATIONS

Haptic devices provide force/torque and tactile feedback to user for any virtual or remote environment. Sense of touch facility of haptic devices is currently used in the fields of industry, medical, education, art, aerospace and entertainment. New application fields of haptic technology are reproduced and the scope of haptic applications looks like to grow further. Therefore, the control of haptic interfaces needs to improved in terms of transparency, stability, accuracy.

The virtual environment of any virtual reality system or remote environment of any teleoperation system comprises basically physical elements such as spring, damping and mass. For accurate simulation of these physical elements by haptic devices, real-time position, velocity and acceleration measurements are required. These measurements are necessary also for model based compensators employed in haptic controllers. Usually, optical incremental encoders are used in haptic devices; however, these measurements suffer from the quantization effect introduced by sample/hold units of decoder hardware. Due to this quantization effect, accurate calculation of velocity and acceleration is not possible with numerical differentiation for every frequency range. Various methods are proposed in the literature to estimate velocity and acceleration. They are classified into two groups: fixed time and fixed position methods. In fixed time method, the number of encoder pulses is counted at a fixed sampling time for position signal and some estimation techniques are applied on this position signal. The conventional fixed time estimation methods are low-pass filters, Kalman filters

and modified state observers. They are not sufficient for every velocity range. As the best of fixed time methods, Janabi-Sharifi et. al. [27] proposed a first-order adaptive windowing technique. In this method, a first order polynomial is fitted on the position measurements in the sense of least mean squares of errors to overcome tradeoff problems among noise reduction, control delay, estimate accuracy, reliability, computational load, transient preservation for velocity estimation. However, this technique cannot estimate acceleration. Therefore, the first-order adaptive windowing technique method was enhanced to estimate both velocity and acceleration by fitting the second-order polynomial on the position measurement in the sense of least mean squares of errors. The first and second derivative of this second-order polynomial gives the velocity and acceleration estimation respectively at the current sampling time. This method is called as enhanced adaptive windowing technique in the thesis. The developed enhanced adaptive windowing technique was implemented online on a low resolution encoder (500 ppr) and compared to the offline estimations from the high resolution encoder (5000 ppr) in a 1-DOF HapticBox. The results show that the enhanced adaptive windowing technique is the best of fixed time methods for the estimation of both velocity and acceleration. On the other hand, fixed position methods that needs high-frequency clock sources such Field Programmable Gate Array's provide the good estimation except for several problems. These problems are low resolution for acceleration estimation at high frequencies and an impulsive change of acceleration estimation when the direction of motion dynamically changes. These problematic cases of fixed position method can be solved by the enhanced adaptive windowing technique. Therefore, a hybrid method is developed using both fixed position based calculation and fixed time based enhanced adaptive windowing techniques. These two methods are rolled into a single technique by applying a parametric smooth transition for the estimation of both velocity and acceleration for entire operating region. The hybrid technique was also implemented on 1-DOF HapticBox and the results show that it is the best of all fixed time and fixed position methods; however it requires high-frequency clock sources such Field Programmable Gate Array's.

Since the enhanced adaptive windowing technique can be applied by using only data acquisition board, it is used in the other parts of the thesis.

The transparency is the primary performance criteria for haptic interfaces. In haptic interactions, the transmitted impedance measured at the end-effector of the device should be close as possible to the desired virtual environment impedance for high transparency. The dynamical and frictional effects should be minimized to maximize the transparency of haptic devices. In the literature, the force feedback control algorithms and model based compensators are used for that purpose. For the force feedback control algorithms, the integral and derivative controllers are not preferred since the haptic interactions generally do not have steady state equilibrium and the transducer noise is inevitable. Besides, the proportional gain of the closed loop controller cannot be increased to high values because of the system dynamics. On the other hand, model based compensators are not sufficient for the transparency maximization. Non-precise velocity/acceleration estimation and inaccurate system model identification limit the performance of model based compensators. As an alternative, a new compensator where system model is not used was proposed. In the proposed compensation algorithm, motor current based torque feedback is employed with a secondary proportional controller to minimize the dynamical effects of the device in joint space. The proposed compensator is used together with the closed loop impedance control algorithm. The gain of main controller of the impedance algorithm is firstly set to a safe value for the stability. Then, the secondary controller gain of the motor current based torque feedback compensator is tuned to maximize transparency. This algorithm was implemented on 1-DOF HapticBox. A set of experiments was conducted with different velocities and accelerations. The results show that the transparency is improved further by the motor current based torque feedback compensator than the conventional algorithms. This proposed algorithm is implementable for multi-DOF haptic manipulators. In order to show this, a simulation study was conducted in MATLAB®/SimMechanics environment. 2-DOF planar manipulator is modeled together with artificially quantized position signals and artificial noisy transducer

signals. The proposed and conventional algorithms are applied on the simulation model with a known trajectory. The results are reasonable for the implantation of the proposed compensator to multi-DOF haptic manipulators.

Another significant performance criterion is the stability for haptic interfaces. The stability is evaluated by using Z-width plots for haptic interactions. The Z-width plot shows the impedance range (virtual stiffness- K versus virtual damping- B) of a virtual wall that can be simulated stably. The stable impedance range should be large as possible for haptic devices. In the transparency improvement studies of this thesis, it is explored that there is an inverse correlation between the transparency and stable impedance range when only active actuators are used in the haptic devices. The reason of this inverse correlation is that the transparency improvement algorithms employ noisy feedback data, which triggers the instability, and decrease physical damping of the device, which enables dissipating the unstable vibrations. An ideal haptic device should transmit wide range of virtual impedances stably and transparently. It is well known that wide range of virtual impedances can be transmitted stably by passive brakes; however, they are not sufficient for high transparency. Besides, passive brakes cause undesired sticking effect on the virtual wall due to its slow response. Using both active actuator and passive brake can increase both the stable impedance range and transparency. Accordingly, a hybrid control algorithm employing both active actuator and passive brake was developed. The developed algorithm portions the torque demand between the actuators by a task divider parameter to ensure the stability. Especially, when high impedances need to be simulated, much of the desired torque is provided by passive brake, and the remaining part of the desired torque is tuned fine by the active actuator for high transparency. The hybrid algorithm employs also a smooth transition parameter to eliminate the sticking effect of the passive brake. In this way, the proposed hybrid algorithm provides stable and transparent interaction for even high impedances. The superiority of the proposed hybrid algorithm over the conventional methods was experimentally shown on a 1-DOF hybrid haptic device. In order to interpret the experimental result much comprehensibly, the transparency Z-width plot was proposed as a

way to evaluate the stable impedance range and transparency together. On this plot, the transparency bandwidths measured for the achievable impedances are displayed as colored maps on a conventional Z-width plot. This new plot indicates the impedance limits for stable interaction and how much the transparency is under this limit.

The accuracy of pose and force control are problematic for multi-DOF capstan driven haptic manipulators. The haptic controller of these manipulators employs Jacobian matrix including kinematic parameters for pose calculation and force control. The deviations in kinematic parameters change the Jacobian matrix, and effect adversely pose and force control accuracy. Capstan driven mechanisms are frequently used in haptic devices for power transmission in the joints due to their advantages such as zero backlash, high stiffness and simplicity. However, these mechanisms introduce transmission errors in the joints, which additionally distort the pose and force control accuracy. First of all, a theoretical analysis was developed for the compensation of transmission errors resulting from the slip of the cable on the capstan drums. This theory was validated on a 1-DOF capstan drive mechanism. After that, an easy to implement calibration technique was developed to improve the pose and force control accuracy for a 7-DOF capstan driven haptic device. In this calibration technique, the transmission errors of the capstan drive mechanisms are estimated using external encoders at each joint of the device and a closed chain calibration procedure is established by using a low-cost linear cable encoder to estimate the deviations in kinematic parameters. All identified parameters for the device kinematic and transmissions were modified in the controller. Then, the pose calculation and force control experiments were conducted on the device before and after calibration. The results show that the kinematic calibration including transmission errors of capstan drives significantly improves the accuracy of pose and force control.

On a multi-DOF haptic device, the stability must be ensured for each actuator to achieve stable interaction. The main methods in the literature are to limit the actuator torque and increase the device damping to provide stable interaction.

High torque commands to the active actuators generate excess energy which triggers the unstable interaction. However, this torque limitation and increasing damping of the system distort the transparency. In redundant haptic manipulators, the device posture can be adjusted to reach any point in the workspace. The adjustable posture ability of redundant haptic devices can be used to minimize the actuator torque of critical joint in terms of stability. Using this idea, an optimal posture control algorithm is developed to increase the stable impedance range of the device. The proposed algorithm is implemented on a virtual sphere using a 7-DOF redundant haptic device. The results show that the optimal posture control approach significantly improves the stability of the redundant haptic devices for realistic haptic interaction.

Finally, this thesis aimed to improve the transparency, stability and accuracy of haptic interfaces. In this context, significant contributions have been made.

As a future work, the following recommendations can be given:

- The hybrid estimation algorithm developed in Chapter 2 of the thesis is implemented with an artificial high frequency clock in MATLAB[®] Simulink environment. This algorithm can be carried out experimentally by using a Field Programmable Gate Array and the resulting estimations can be employed in a model based compensator to improve the transparency of haptic devices.
- The motor current based torque feedback compensator developed in Chapter 3 of the thesis is implemented on a 1-DOF HapticBox and the applicability of the compensator to multi-DOF haptic devices is tested MATLAB[®]/SimMechanics environment for a planar 2-DOF manipulator. This proposed compensator can be carried out experimentally on a multi-DOF haptic device.
- The hybrid force control algorithm using both active actuator and passive brake developed in Chapter 4 of the thesis gives the promising results for a 1-DOF

hybrid haptic device. In the presented hybrid device, the actuators are coupled using sprockets and chains. In haptic device designs, the passive and active actuators can be directly coupled with specially designed equipments at the joint. Therefore, a multi-DOF hybrid driven haptic device can be designed for high stable impedance range and high transparency.

- The theoretical analysis of capstan drive transmission errors presented in Chapter 5 was developed for constant external loads. Kinematic calibration presented in the same chapter is carried out without external load. The presented theory can be improved for dynamic external loads and the corresponding kinematic calibration can be enhanced for the case of dynamic external load while being simulating virtual dynamic forces.
- The optimal posture control algorithm developed in Chapter 6 for the stability improvement of redundant haptic devices can be adapted for a different performance criterion such as minimization of inertia to maximize transparency. Besides, in the implementation of the proposed algorithm, the last shoulder joint is selected as redundant joint permanently. A new optimal posture control algorithm can be developed by exchanging redundancy between the joints of the device depending upon the virtual environment model. For instance, since the posture adjustment of the 7-DOF redundant haptic device can not change the desired torque on the base actuator, the base joint can be selected as a redundant joint when it is critical in terms of stability.

REFERENCES

- [1] A. Fisch, C. Mavroidis, Y. Bar-Cohen, and J. Melli-Huber. Haptic Devices for Virtual Reality, Telepresence and Human Assistive Robotics, Haptic and Telepresence Robotics, Chapter 4, pp. 73-101.
- [2] J. Park, O. Khatib. A Haptic Teleoperation Approach Based on Contact Force Control, The International Journal of Robotics Research, Vol. 25, No. 5–6, pp. 575-591, 2006.
- [3] G. C. Burdea. Haptic Feedback for Virtual Reality, Rutgers University, CAIP Center, 96 Frelinghuysen Rd, Piscataway, NJ, 08854, USA, 1999.
- [4] Z. Gao and I. Gibson. Haptic B-spline Surface Sculpting with a Shaped Tool of Implicit Surface, Computer-Aided Design & Applications, Vol.2, No: 1-4, pp263-272, 2005.
- [5] W. Baxter, V. Scheib, M. Lin, and D. Manocha. Interactive Haptic Painting with 3D Virtual Brushes, In Proceedings of ACM SIGGRAPH 01, pp.461-468, August 2001.
- [6] <http://home.novint.com/index.php/products/novintfalcon> (Last access date: November 28, 2012)
- [7] E. Subasi, C. Basdogan. A New Haptic Interaction and Visualization Approach for Rigid Molecular Docking in Virtual Environments, Presence: Teleoperators and Virtual Environments, MIT Press, Vol. 17, No.1, pp. 73-90, 2008.

- [8] B. Grant, A. Helser, R. M. Taylor, Adding Force Display to a Stereoscopic Head-Trackd Projection Display, IEEE Virtual Reality Annual International Symposium, , Atlanta, Georgia, 1998.
- [9] J. E. Colgate, J. M. Brown. Factors Affecting the Z-Width of a Haptic Display, Proceedings of the IEEE 1994 International Conference on Robotics & Automation, pp. 3205-3210, San Diego, CA, May 1994.
- [10] C. R. Carignan and K. R. Cleary. Closed-Loop Force Control for Haptic Simulation of Virtual Environments, Haptics-e, The Electronic Journal of Haptics Research, vol. 1, 2000.
- [11] N. L. Bernstein, D. A. Lawrence, and L. Y. Pao. Friction Modeling and Compensation for HapticInterfaces, Proceedings of the First Joint EurohapticsConference and Symposium on Haptic Interfaces for Virtual Environment and Teleoperator Systems, pp. 290-295, Pisa, Italy, 2005.
- [12] K. Ohnishi, M. Shibata, and T. Murakami. Motion control for advanced mechatronics, IEEE/ASME Trans. Mechatronics, vol. 1, no. 1, pp. 56–97, 1996.
- [13] G. Liu. On velocity estimation using position measurements, Am Control Conf. vol. 2, pp. 1115–1120, 2002.
- [14] M. Lemkin, P.H. Yang, A.C. Wuang, J. Jones, D. M. Auslander. Velocity estimation from widely spaced encoder pulses, American Control Conf. pp. 998–1002, 1995.
- [15] L. Kovudhikulrungsri, T. Koseki. Precise speed estimation from a low-resolution encoder by dual-sampling-rate observer, IEEE/ASME Trans Mechatron, vol. 11, no. 6, pp. 661–670, 2006.

- [16] P. R. Bélanger. Estimation of angular velocity and acceleration from shaft encoder measurements, IEEE Conf. Robot Automat. pp. 585–592, 1992.
- [17] R. D. Lorenz, K. W. Van Patten. High-Resolution Velocity Estimation for All-Digital, AC Servo Drives, IEEE Trans. Industry Application, vol. 27, no. 4, pp. 701–705, 1991.
- [18] M. Bodson, J. Chiasson, R. T. Novotnak. Nonlinear Speed Observer for High-Performance Induction Motor Control, IEEE Trans. Industrial Electron., vol. 42, no. 4, pp. 337–343, Aug. 1995.
- [19] S. Yang, S. Ke. Performance Evaluation of a Velocity Observer for Accurate Velocity Estimation of Servo Motor Drives, IEEE Trans. Industry Application, vol. 36, no. 1, pp. 98–104, Jan/Feb 2000.
- [20] A. Levant. Robust Exact Differentiation via Sliding Mode Technique, Automatica, vol. 34, no. 3, pp. 379–384, 1998.
- [21] A. Damiano, G. Gatto, I. Marongiu, A. Pisano, E. Usai. Rotor Speed Estimation in Electrical Drives via Digital Second Order Sliding Differentiator, European Control Conference, Karlsruhe, Germany, 1999.
- [22] A. Tilli, M. Montanari. A low-noise estimator of angular speed and acceleration from shaft encoder measurements, Automatika, vol. 42, no. 3, pp. 169–176, 2001.
- [23] S. P. Chan. Velocity estimation for robot manipulators using neural network, J Intel Robot Syst. vol. 23, no. 2, pp. 147–163, 1998.
- [24] X. Z. Gao and S. J. Ovaska. Acceleration signal estimation using neural networks, Meas. Sci. Technol. vol. 12, pp. 1611–1619, 2001.

- [25] F. Yusivar, D. Hamada, K. Uchida, S. Wakao, et al. A new method of motor speed estimation using fuzzy logic algorithm, Int. Conf. Electric Mach Drives, pp. 278–280, 1999.
- [26] R. H. Brown, S. C. Schneider, and M. G. Mulligan. Analysis of Algorithms for Velocity Estimation from Discrete Position versus Time Data, IEEE Transactions in Industrial Electronics, vol.39, no.1, February 1992.
- [27] F. Janabi-Sharifi, V. Hayward, and C. J. Chen. Discrete-Time Adaptive Windowing for Velocity Estimation, IEEE Transaction on Control System Technology, vol.8, no.6, 2000.
- [28] H. Tanaka, H. Nishi and K. Ohnishi. An Approach to Acceleration Estimation Using FPGA, IEEE International Symposium on Industrial Electronics, Cambridge, pp. 1959-1964, 2008.
- [29] E. Kilic, O. Baser, M. Dolen and E. I. Konukseven. Enhanced adaptive windowing technique for velocity and acceleration estimation using incremental position encoders, IEEE International Conference on Signal and Electronic Systems, Gliwice, Poland, 2010.
- [30] O. Baser, E. Kilic, E. I. Konukseven, M. Dolen. A hybrid technique to estimate velocity and acceleration using low-resolution optical incremental encoders, IEEE International Conference on Signal and Electronic Systems, Gliwice, Poland, 2010.
- [31] S. Jeon, M. Tomizuka. Benefits of acceleration measurement in velocity estimation and motion control, Control Engineering Practice 15, pp. 325-332, 2007.
- [32] S. Bideci. Control System Design for a Haptic Device, MS. Thesis, Middle East Technical University, Turkey, 2007.

- [33] F. Gustafsson. Determining the Initial States in Forward-Backward Filtering, *IEEE Transactions on Signal Processing*, vol. 44, no. 4, 1996.
- [34] S. T. McJunkin. Transparency Improvement for Haptic Interfaces, PhD. Thesis May 2007.
- [35] K. Vlachos and E. Papadopoulos. Transparency maximization methodology for haptic devices, *IEEE/ASME Transactions on Mechatronics*, Vol. 11, No. 3, pp. 249–255, 2006.
- [36] J. E. Colgate. Robust impedance shaping telemanipulation, *IEEE Transactions on Robotics and Automation*, Vol. 9, No. 4, pp. 374–384, 1993.
- [37] D. A. Lawrence. Stability and transparency in bilateral teleoperation, *IEEE Transactions on Robotics and Automation*, Vol. 9, No. 3, pp. 624–637, 1993.
- [38] K. B. Fite, J. E. Speich, and M. Goldfarb. Transparency and Stability Robustness in Two-Channel Bilateral Teleoperation, *Journal of Dynamic Systems, Measurement, and Control*, Vol. 123, pp. 400-407, 2001.
- [39] H. K. Lee and M. J. Chung. Adaptive Controller of a Master-Slave System for Transparent Teleoperation. *Journal of Robotic Systems*, Vol. 15, No. 8, pp. 465-475, 1998.
- [40] K. Hashtrudi-Zaad and S. E. Salcudean. Analysis of Control Architectures for Teleoperation Systems with Impedance/Admittance Master and Slave Manipulators. *The International Journal of Robotic Research*, Vol. 20, No. 6, pp. 419-445, 2001.

- [41] A. Frisoli, E. Sotgiu, C. A. Avizzano, D. Checcacci, and M. Bergamasco. Force-based Impedance Control of a Haptic Master System for Teleoperation. *Sensor Review*, Vol. 24, No. 1, pp. 42-50, 2004.
- [42] N. L. Bernstein, D. A. Lawrence, and L. Y. Pao. Friction Modeling and Compensation for Haptic Interfaces, *Proceedings of the First Joint Eurohaptics Conference and Symposium on Haptic Interfaces for Virtual Environment and Teleoperator Systems*, pp. 290-295, 2005.
- [43] S. T. McJunkin, M. K. O'Malley and J. E. Speich. Transparency of a Phantom Premium Haptic Interface for Active and Passive Human Interaction. *American Control Conference*, pp. 3060-3065, 2005.
- [44] S. T. McJunkin, Y. Li, M. K. O'Malley. Human-Machine Admittance and Transparency Adaptation in Passive User Interaction with a Haptic Interface. *Proceedings of the First Joint Eurohaptics Conference and Symposium on Haptic Interfaces for Virtual Environment and Teleoperator Systems*, pp. 283-289, 2005.
- [45] O. Baser, E. I. Konukseven, Utilization of Motor Current based Torque Feedback to Improve the Transparency of Haptic Interfaces. *Mechanism and Machine Theory*, Vol. 52, pp. 78-93, 2012.
- [46] J. J. Gil, E. Sanchez. Control Algorithms for Haptic Interaction and Modifying the Dynamical Behavior of the Interface. *2nd International Conference on Enactive Interfaces*, 2005.
- [47] N. L. Bernstein, D. A. Lawrence, and L. Y. Pao. Friction Modeling and Compensation for Haptic Interfaces. *Proceedings of the First Joint Eurohaptics Conference and Symposium on Haptic Interfaces for Virtual Environment and Teleoperator Systems*, pp. 290-295, 2005.

- [48] B. Taati, A. M. Tahmasebi, K. Hashtrudi-Zaad. Experimental Identification and Analysis of the Dynamics of a PHANToM Premium 1.5A Haptic Device. *Presence: Teleoperators and Virtual Environments*, Vol. 17, No. 4, pp. 327–343, 2008.
- [49] A. Smith, F. Mobasser, K. Hashtrudi-Zaad. Neural network based contact force observers for haptic applications. *IEEE Transactions on Robotics and Automation*, Vol. 22, No.6, pp. 1163–1175, 2006.
- [50] L. Xing, D. T. Pham, *Neural networks for identification, prediction and control*. Springer-Verlag, 1995.
- [51] J. Hollerbach, W. Khalil, M. Gautier. Model Identification in: B. Siciliano, O. Khatib, (Eds.) *Springer Handbook of Robotics*. Springer, pp. 321-344, 2008.
- [52] D. S. Kwon and K. Y. Woo. Control of haptic interface with friction compensation and its performance evaluation. *IEEE/RSJ International Conference on Intelligent Robots and Systems*, Vol.2, pp. 955-960, 2000.
- [53] L. Sciavicco, B. Siciliano. *Modelling and control of robot manipulators*. 2nd Ed. London: Springer-Verlag. 2001.
- [54] David W. Weir and J. Edward Colgate. *Haptic Rendering: Foundations, Algorithms, and Applications*, chapter 7: Stability of Haptic Displays, Ming Lin and Miguel Otaduy, Editors, pages 123–156. A.K. Peters, Boston, MA, 2008.
- [55] J. E. Colgate and G. G. Schenkel. Passivity of a Class of Sampled-Data Systems: Application to Haptic Interfaces. *J. Robot. Syst.*, Vol.14, No. 1, pp. 37–47, 1997.

- [56] J. E. Colgate and J. M. Brown. Factors affecting the Z-width of a haptic display. IEEE International Conference on Robotics and Automation, Vol. 4, pp. 3205–3210, 1994.
- [57] J. S. Mehling, J. E. Colgate, and M. A. Peshkin. Increasing the impedance range of a haptic display by adding electrical damping. IEEE First World Haptics Conference and Symposium, pp. 257– 262, 2005.
- [58] D. W. Weir, J. E. Colgate, M. A. Peshkin. Measuring and Increasing Z-Width with Active Electrical Damping. Symposium on Haptic Interfaces for Virtual Environments and Teleoperator Systems, pp. 169-175, 2008.
- [59] Y. A. Lim, H. S. Ahn, J. Ryu. Analogue input shaper for haptic interfaces. IET Control Theory and Applications, Vol. 3, No. 12, pp. 1553-1564, 2009.
- [60] K. Lee and D.-Y. Lee. Adjusting Output-Limiter for Stable Haptic Rendering in Virtual Environments. IEEE Trans. Control System Technology, Vol. 17, No.4, 2009.
- [61] B. Hannaford and J. H. Ryu. Time Domain Passivity Control of Haptic Interfaces. IEEE Trans. Robot. Automat., Vol. 18, pp. 1–10, 2002.
- [62] J.-H. Ryu, Y. S. Kim, and B. Hannaford. Sampled- and Continuous-Time Passivity and Stability of Virtual Environments. IEEE Trans. Robot. Automat., Vol. 20, No. 4, pp. 772–776, 2004.
- [63] J.-H. Ryu, C. Preusche, B. Hannaford, and G. Hirzinger. Time Domain Passivity Control with Reference Energy Following. IEEE Trans. Control Sys. Tech., Vol. 13, No. 5, pp. 737–742, 2005.
- [64] J.-P. Kim and J. Ryu. Energy Bounding Algorithm based on Passivity Theorem for Stable Haptic Interaction Control. 12th Symp.Haptic Interfaces

for Virtual Environment and Teleoperator Systems, Chicago, IL, pp. 351–357, 2004.

- [65] J. Kim and J. Ryu. Robustly Stable Haptic Interaction Control using an Energy-Bounding Algorithm. *International Journal of Robotic Research*, Vol. 29, No. 6, pp. 666-679, 2010.
- [66] J. Kim, S. Baek, and J. Ryu A Force Bounding Approach for Stable Haptic Interaction. *IEEE WorldHaptics Conference*, pp. 397-402 2011.
- [67] D. Lee and K. Huang. Passive-Set-Position-Modulation Framework for Interactive Robotic Systems. *IEEE Trans. on Robotics*, Vol. 26, No. 2, pp. 354-369, 2010.
- [68] M. Franken, S. Stramigioli, S. Misra, C. Secchi and A. Macchelli. Bilateral telemanipulation with time delays: A two-layer approach combining passivity and transparency. *IEEE Trans. on Robotics*, 27(4), 741-756, 2011
- [69] M. Franken, S. Stramigioli, R. Reilink, C. Secchi and A. Macchelli. Bridging the gap between passivity and transparency. *Proc. Robot.: Sci. Syst.*, pp. 281–288, 2009.
- [70] J. An and D. Kwon, In haptics, the influence of the controllable physical damping on stability and performance, *IEEE/RSJ Int. Conference on Intelligent Robots and Systems*, 2004.
- [71] J. An and D. Kwon, Stability and performance of haptic interfaces with active/passive actuators, *International Journal of Robotics Research*, vol. 25, pp. 1121–36, 2006.

- [72] J. Nam, M. K. Park A Hybrid Haptic Device for Wide-Ranged Force Reflection and Improved Transparency, International Conference on Control, Automation and Systems, pp. 1015-1020, Seoul, Korea, 2007.
- [73] K. Fite, J. Speich, and M. Goldfarb, Loop Shaping for Transparency and Stability Robustness in Bilateral Telemanipulation. IEEE Trans. Rob. Autom., Vol.20, No.3, pp. 620–624, 2004.
- [74] A. Gupta, M. K. O'Malley, Disturbance-Observer-Based Force Estimation for Haptic Feedback, Journal of Dynamic Systems, Measurement, and Control, Volume 133, Issue 1, 014505 pp.1-4, 2011.
- [75] <http://www.ogura-clutch.com/products/industrial/howtheywork/electromagnetic-particle-brake.html> (Last access date: November 2012)
- [76] O. Erol, B. Gonenc, D. Senkal, S. Alkan and H. Gurocak, Magnetic induction control with embedded sensor for elimination of hysteresis in magnetorheological brake, Journal of Intelligent Material Systems and Structures, Vol.23 No.4 pp.427-440, 2012.
- [77] http://scmero.ulb.ac.be/project.php?id=9&page=MR_rehabilitation_design.html (Last access date: August 2012)
- [78] J. J. Abbott and A. M. Okamura. Effects of Position Quantization and Sampling Rate on Virtual-Wall Passivity. IEEE Trans. Robot. Automat., Vol. 21, No. 5, pp. 952–964, 2005.
- [79] T. L. Brooks, Telerobotics Response Requirements, IEEE International Conference on Systems, Man and Cybernetics, pp. 113-120, 1990.
- [80] A. Bicchi, M. Raugi, R. Rizzo, and N. Sgambelluri, Analysis and design of an electromagnetic system for the characterization of Magneto-Rheological

fluids for haptic interfaces, IEEE Transactions on Magnetics, vol. 41, pp. 1876-1879, may 2005.

- [81] A. Shafer and M. Kermani, On the feasibility and suitability of MR fluid clutches in human-friendly manipulators, IEEE/ASME Transactions on Mechatronics, vol. 16-6, pp. 1073-82, 2010.
- [82] A. Grunwald and A. Olabi, Design of magneto-rheological (MR) valve, Journal of Sensors and Actuators, vol. 148, no. 1, pp. 211-223, 2008.
- [83] O. Baser, E.I. Konukseven, H. Gurocak, Stability and Transparency Improvement in Haptic Device Employing both MR-Brake and Active Actuator, 21st IEEE International Symposium on Robot and Human Interactive Communication, Paris, France, September 2012.
- [84] B. Gonenc, and H.Gurocak, Force control with hybrid actuator for virtual needle insertion, Proceedings of 2011 IEEE WorldHaptics Conference, Istanbul, Turkey, June 2011.
- [85] D Senkal, and H. Gurocak, Serpentine flux path for high torque MRF brakes in haptics applications, Mechatronics, vol. 20, pp. 377-383, February 2010.
- [86] Infolytica Corp. [Online]. Available: <http://www.infolytica.com/> (Last access date: April 2012)
- [87] A.Y. Ellata, L.P. Gen, F.L. Zhi, Y. Daoyuan, L. Fei. An Overview of Robot Calibration. Information Technology Journal 3(2), 74-78; 2004.
- [88] R.P. Judd, A.B. Knasinski. A technique to calibrate industrial robots with experimental verification. IEEE Transactions on Robotics and Automation 6(1), 20-30; 1990.

- [89] P.S. Shiakolas, K.L. Conrad, T.C. Yin. On the Accuracy, Repeatability, and Degree of Influence of Kinematics Parameters for Industrial Robots. *International Journal of Modelling and Simulation* 22(3), 245-254; 2002.
- [90] C. Gong, J. Yuan, J. Ni, Nongeometric error identification and compensation for robotic system by inverse calibration. *International Journal of Machine Tools and Manufacture* 40, 2119-2137; 2000.
- [91] C. Gatla, R. Lumia, J. Wood, G. Starr. An Automated Method to Calibrate Industrial Robots using a Virtual Closed Kinematic Chain. *Proceedings of IEEE Transactions on Robotics and Automation* 23(6), 1105-1116; 2007.
- [92] B.W. Mooring, S.S. Padavala. The effect of kinematic model complexity on manipulator accuracy. *Proceedings of the IEEE International Conference on Robotics and Automation*, 593-598; 1989.
- [93] R. Bernhardt, Approaches for commissioning time reduction. *Industrial Robot* 24(1), 62-71; 1997.
- [94] J.L. Caenen, J.C. Angue. Identification of Geometric and Non-geometric Parameters of Robots. *Proceedings of the IEEE International Conference on Robotics and Automation*, 1032-1037; 1990.
- [95] J. Chen, L.M. Chao. Positioning error analysis for robot manipulators with all rotary joints. *IEEE Journal of Robotics and Automation* RA-3(6), 539-545; 1987.
- [96] D.E. Whitney, C.A. Lozinski, J.M. Rourke. Industrial Robot Forward Calibration Method and Results. *ASME Journal of Dynamic Systems, Measurement, and Control* 108(1), 1-8; 1986.

- [97] D. Wang, Y. Bai. Improving position accuracy of robot manipulators using neural networks. Proceedings of the IEEE Instrumentation and Measurement Technology Conference; 2005.
- [98] G. Alici, B. Shirinzadeh. Laser interferometry based robot position error modeling for kinematic calibration. Proceedings of the IEEE/RSJ Int. Conference on Intelligent Robots and Systems; 2003.
- [99] J.H. Jang, S.H. Kim, Y.K. Kwak. Calibration of geometric and non-geometric errors of an industrial robot. *Robotica* 19(3), 311-321; 2001.
- [100] A. Watanabe, S. Sakakibara, K. Ban, M. Yamada, G. Shen. A Kinematic Calibration Method for Industrial Robots Using Autonomous Visual Measurement. *Annals of the CIRP* 55(1), 1-6; 2006.
- [101] J.U. Dolinsky, I.D. Jenkinson, G.J. Colquhoun. Application of genetic programming to the calibration of industrial robot. *Computers in Industry* 58(3), 255-264; 2007.
- [102] C. Lightcap, S. Hamner, T. Schmitz, S. Banks. Improved Positioning Accuracy of the PA10-6CE Robot with Geometric and Flexibility Calibration. *IEEE Transactions on Robotics* 24(2), 452-456; 2008.
- [103] W.Khalil, S. Besnard, P. Lemoine. Comparison study of the geometric parameters calibration methods. *International Journal of robotics and Automation* 15(2), 56-67; 2000.
- [104] G.A.F. Seber, C.J. Wild. *Nonlinear Regression*. JohnWiley and Sons. New York; 1989.

- [105] K. Levenberg. A Merhod for the Solution of Certain Non-Linear Problems in Least-Squares. Quarterly of Applied Mathematics-Notes 2, 164-168; 1944.
- [106] D.W. Marquardt. An Algorithm for Least-Squares Estimation of Nonlinear Parameters. Journal of the Society for Industrial and Applied Mathematics 11(2), 431-441; 1963.
- [107] N. Nathoo, M.C. Çavuşoğlu, M.A. Vogelbaum, G.H. Barnett. In Touch with Robotics: Neurosurgery for The Feature. Neurosurgery, 56(3), 421-433; 2005.
- [108] R.T. Azuma. A Survey of Augmented Reality. Presence: Teleoperators and Virtual Environments, 6(4), 355-385; 1997.
- [109] M. Slater and A. Steed. A Virtual Presence Counter. Presence: Teleoperators and Virtual Environments, 9(5), 413-434; 2000.
- [110] GHOST® SDK Programmer's Guide, Version 4.0. SensAble Technologies, Inc.® (<http://www.sensable.com/support-ghost-sdk.htm> - Last access date: July 2012).
- [111] OPENHAPTICS® Programmer's Guide, Version 3.0. SensAble Technologies, Inc.® (<http://www.sensable.com/support-openhaptics.htm> - Last access date: July 2012).
- [112] Force Dimension® SDK Programmer's Guide, (<http://www.forcedimension.com/sdk-overview> - Last access date: July 2012).

- [113] R. Ott, V. Perrot, D. Thalmann, F. Vexo. MHaptic: a Haptic Manipulation Library for Generic Virtual Environments. Cyberworlds International Conference, 338-345; 2007.
- [114] M. Harders, G. Bianchi, B. Knoerlein, G. Szekely. Calibration, Registration, and Synchronization for High Precision Augmented Reality Haptics. IEEE Transactions on Visualization and Computer Graphics, 15(1), 138-149; 2009.
- [115] B. Knoerlein, M. Harders. Comparison of tracker-based to tracker-less haptic device calibration. IEEE World Haptics Conference, 119-124; 2011.
- [116] G. Bianchi, B. Knörlein, G. Székely, M. Harders. High Precision Augmented Reality Haptics. Eurohaptics Conference, 169-178; 2006.
- [117] K. Reinig, R. Tracy, H. Glimore, and T. Mahalik, Some Calibration Information for a Phantom 1.5 a. Proc. Second PHANToM Users Group Workshop, 70-73; 1997.
- [118] M. Ikits, C. Hansen, C. Johnson. A Comprehensive Calibration and Registration Procedure for the Visual Haptic Workbench. Proc. Joint Seventh Immersive Projection Technology and Seventh Eurographics Virtual Environments Workshop, 247-254, 2003.
- [119] M.I.C. Dede, O. Selvi, T. Bilginan, Y. Kant. Design of a haptic device for teleoperation and virtual reality systems. IEEE International Conference on Systems, Man and Cybernetics, 3623-3628; 2009.
- [120] J.M. Sabater, R.J. Saltaren, R. Aracil. Design, Modelling and Implementation of a 6 URS Parallel Haptic Device. Robotics and Autonomous Systems, 47(1), 1-10; 2004.

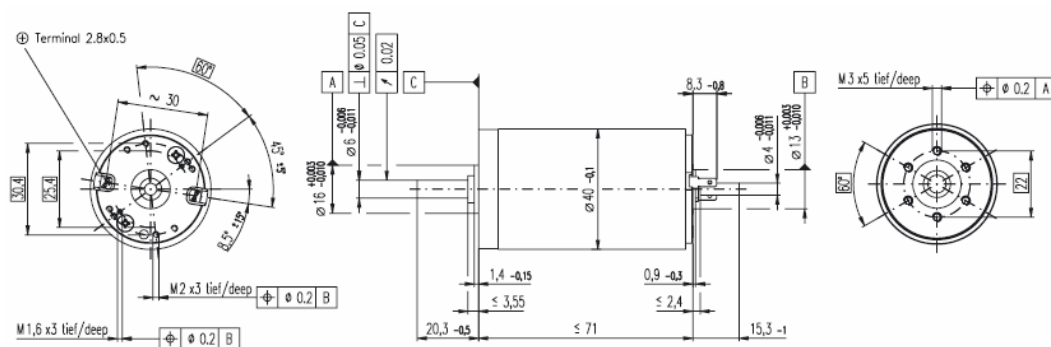
- [121] Z. Yanhe, Y. Jihong, Z. Jie, C. Hegao. Autonomous Kinematic Self-Calibration of a Novel Haptic Device. IEEE/RSJ International Conference on Intelligent Robots and Systems, 4654-4659; 2006.
- [122] O. Baser, E.I. Konukseven. Theoretical and Experimental Determination of Capstan Drive Slip Error, Mechanism and Machine Theory, 45(6), 815-827, 2010.
- [123] O. Baser, E.I. Konukseven. Kinematic Model Calibration of a 7-DOF Capstan Driven Haptic Device for Pose and Force Control Accuracy Improvement, Proceedings of the Institution of Mechanical Engineers, Part C: Journal of Mechanical Engineering Science, 0(0), 1-13, 2012.
- [124] O. Baser, E.I. Konukseven. 7 DOF Haptic Device Design, EuroHaptics Conference, 507-512; 2006.
- [125] O. Baser, E.I. Konukseven, T. Balkan. Optimal Posture Control for a 7 DOF Haptic Device Based on Power Minimization EuroHaptics Conference, 555-560; 2008.
- [126] J. Werkmeister, A. Slocum, "Theoretical and experimental determination of capstan drive stiffness" Precision Engineering 31, 55–67, 2007.
- [127] K. Schroer, S.L. Albright, A. Lisounkin. Modeling Closed-Loop Mechanisms in Robots for Purposes of Calibration. IEEE Transactions on Robotics and Automation, 13(2), 218-229; 1997.
- [128] J. Denavit, R.S. Hartenberg. A Kinematic Notation for Lower-Pair Mechanisms Based on Matrices. ASME Journal of Applied Mechanisms, 215-221; 1955.

- [129] S.A. Hayati. Robot Arm Geometric Link Calibration. Proceeding of 22nd IEEE Conference on Decision and Control, 1477-1483; 1983.
- [130] G. E. Forsythe, M. A. Malcolm, and C. B. Moler, Computer Methods for Mathematical Computations, Prentice-Hall, 1976.

APPENDIX A

HAPTIC BOX EXPERIMENTAL COMPONENTS

Specifications of electromechanical and mechanical components used in construction of the HapticBox are given in this section.



Motor Data			148877
1	Assigned power rating	W	150
2	Nominal voltage	Volt	48.0
3	No load speed	rpm	7580
4	Stall torque	mNm	2500
5	Speed / torque gradient	rpm / mNm	3.04
6	No load current	mA	69
7	Starting current	A	41.4
8	Terminal resistance	Ohm	1.16
9	Max. permissible speed	rpm	8200
10	Max. continuous current	A	3.33
11	Max. continuous torque	mNm	201
12	Max. power output at nominal voltage	W	491
13	Max. efficiency	%	92
14	Torque constant	mNm / A	60.3
15	Speed constant	rpm / V	158
16	Mechanical time constant	ms	4
17	Rotor inertia	gcm ²	134
18	Terminal inductance	mH	0.33
19	Thermal resistance housing-ambient	K / W	4.7
20	Thermal resistance rotor-housing	K / W	1.9
21	Thermal time constant winding	s	40

Figure A.1 Maxon RE40 DC Brushes Motor Specifications

Only 16mm in diameter and up to 5000 ppr. -True lines.
Up to 20000 Counts



CHARACTERISTICS

ENCODER TYPE	Micro hollow shaft encoder (blind end hollow shaft)
SMD - TECHNOLOGY	Strong compact electronics
HIGH IP-RATING	Std. IP 64 (with IDC; IP 50)
LOW CURRENT CONSUMPTION	To be connected directly to PLC'S and counters
SHORT CIRCUIT PROTECTION	Thermal shut down at 155°C
POWER SUPPLY	5 volts to 12 Volts $\pm 10\%$ (TTL) (on request up to 24 Volts)
STRONG MEC. CONSTRUCTION	Based on 2 precision ball bearings for industrial environment

ELECTRICAL SPECIFICATIONS

	At +25°C
Output	Totempole
Output waveform	Incremental (A, B)
Zero or index pulse	(Z) one pr./rev.
Supply-voltage	5 to 12 V (on request up to 24 Volts)
Current (no load)	35mA
Max. load pr. output	20mA (Short circuit protected)
V out low	Max. 500 mV at I out low = 10 mA
Operating temp.	-20°C to +70° C
Storage temp.	-20° C to +85°C
Max. pulse frequency	200 kHz
V out high	Min. (Vin -0,6) @ I = -10mA Min. (Vin -1,3) @ I = -25mA
Cable data	8-leads (0.05 mm ²) shielded or 10-leads flat band cable 0.10mm ²
Output signals	Differential (RS-422A compatible)
Certified acc. To	EN 50081-1 and EN 50082-2*

*NA with flat band cable

MECHANICAL SPECIFICATIONS

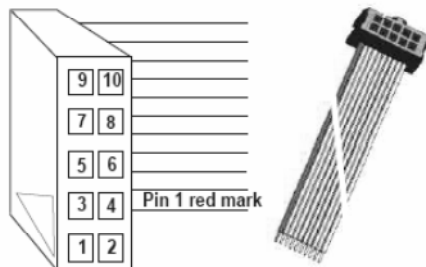
Weight, excl. Cable	About 15 g
Materials:	
Housing	Brass / Aluminum
Shaft	Brass
Bearings	Lifetime lubricated ball-bearings
Fixing clamp	Brass
H.-Shaft dimensions	ø1.5mm - ø2mm - ø3mm - 1/8"
H.-Shaft loads	Axial max. 10 N Radial max. 10 N
Max speed	12.000 rev./min.
IP-rating	IP 64 (with IDC; IP 50)
Start torque	<0,005 Nm at 25°C
Massmoment of inertia	0.25 gcm ²
Max. shock	100 G/11 ms.
Bump	10 G - 16 ms (1000 x 3axis)
Vibration	(10 - 2000 Hz)/10 G

CONNECTIONS

IDC PIN No.	Differential Output; D	Inverted Output; I (HP-compatible)
1	NC	A inv
2	Vcc	NC
3	0 volt (GND)	NC
4	NC	NC
5	A inv	NC
6	A	0-Volt
7	B inv	NC
8	B	B inv
9	Z inv	VCC
10	Z	Z

NOTE: Inverd also called HP-Standard

CABLE AND PIN OUT



MECHANICAL DIMENSIONS

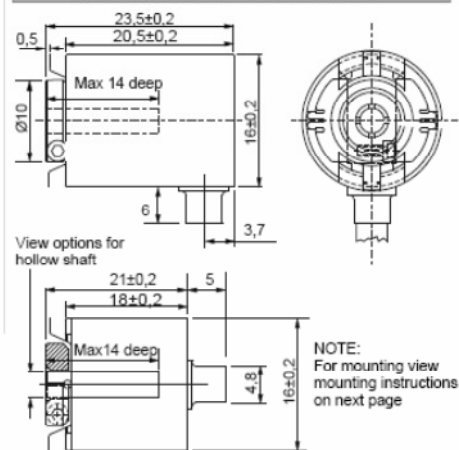


Figure A.2 Scancon Encoder Specifications

Models 412CE, 413CE, 421CE, 422CE, DC Brush Servo Amplifiers

TECHNICAL SPECS		Test conditions: 25°C ambient, Load = 200µH. in series with 1 Ω., +HV = max normal value			
MODEL		412	413	421	422
OUTPUT POWER					
Peak power		±20A @ ±80V	±30A @ ±80V	±10A @ ±170V	±20A @ ±170V
Peak time			1 sec at peak power or 2 secs. after polarity reversal		
Continuous power		±10A @ ±80V	±15A @ ±80V	±5A @ ±170V	±10A @ ±170V
OUTPUT VOLTAGE		$\pm V_{out} = \pm HV \cdot (0.97) - (R_o) \cdot (I_o)$			
		$R_o = 0.2$	$R_o = 0.15$	$R_o = 0.4$	$R_o = 0.2$
LOAD INDUCTANCE		Selectable with components on header socket: 200 µH to 40mH			
BANDWIDTH		3kHz with 200µH load at maximum supply voltage, varies with load inductance and RH20, CH18 values			
(Small signal, -3dB. freq)	Current mode:	200Hz max.			
	Voltage-feedback mode:				
PWM SWITCHING FREQUENCY		25kHz			
REFERENCE INPUT		Differential, 100K between inputs, ±20V maximum			
GAINS		X1 (Volt / Volt)			
	Input differential amplifier				
	PWM transconductance stage	$I_{peak} / 6V$ (I_{peak} = peak rated output current; 6V measured at Current Ref J2-9 or Current Monitor J2-8)			

Figure A.3 Copley 413CE Servo Amplifier

Series 5500, 5540		HEDS 5500	HEDS 5540	HEDM 5500	
Lines per revolution	N	100 - 500	100 - 500	1 000 - 1 024	
Signal output, square wave		2	2+1 Index	2	channels
Supply voltage	V _{CC}	4,5 ... 5,5			V DC
Current consumption, typical (V _{CC} = 5 V DC)	I _{CC}	17	57	57	mA
Pulse width	P	180 ± 45	180 ± 35	180 ± 45	°e
Phase shift, channel A to B	Φ	90 ± 20	90 ± 15	90 ± 15	°e
Logic state width	S	90 ± 45	90 ± 35	90 ± 45	°e
Cycle	C	360 ± 5,5	360 ± 5,5	360 ± 7,5	°e
Signal rise/fall time, typical	tr/tf	0,25 / 0,25			µs
Frequency range ¹⁾	f	up to 100	up to 100 ²⁾	up to 100	kHz
Inertia of code disc	J	0,6			gcm ²
Operating temperature range		- 40 ... + 100		- 40 ... + 70	°C
¹⁾ Velocity (rpm) = f (Hz) x 60/N					
²⁾ HEDS 5540 requires pull-up resistors of 2,7 kΩ between pins 2, 3, 5 and 4 (V _{CC})					
Ordering Information					
Encoder type	number of channels	lines per revolution	For combination with:		
HEDS 5500 C	2	100	} DC-Micromotors and DC-Motor-Tachos Series 2230, 2233, 2251 2342 2642, 2657 3242, 3257, 3557, 3863		
HEDS 5500 A	2	500			
HEDS 5540 C	2+1	100			
HEDS 5540 A	2+1	500			
HEDM 5500 B	2	1 000	} brushless DC-Servomotors Series 2036, 2444, 3056, 3564		
HEDM 5500 J	2	1 024			
Interlocking connector options: extension cables 300 mm length, on request.					

Figure A.4 HEDS 5540A Encoder



Specifications

Analog Input

Channels:	8 single-ended channels
A/D converter:	14-bit, simultaneous sampling
Conversion time:	1.6 μ s 1 channel, 1.9 μ s 2 channels, 2.5 μ s 4 channels, 3.7 μ s 8 channels
Input range:	± 10 V,
Input Impedance:	$10^{10} \Omega$
Trigger mode:	software, timer, external

Analog Output

Channels:	8 channels, 14-bit
Output Range:	± 10 V
Output current:	10 mA max.
Settling time:	31 μ s FS change to $\pm 1/2$ LSB.

Digital I/O

Input lines:	8, TTL compatible
Output lines:	8, TTL compatible

Timer/Counter

Number of channels:	4
Resolution:	32 bit, 20 ns
Modes:	PWM, counter, pulse generation

Encoder Inputs

Input channels:	4, single ended or differential
Inputs:	A, B, Index
Input frequency:	max 2.5 MHz
Resolution:	32-bit

General

Power consumption:	500 mA @ +5 V 150 mA @ +12 V 150 mA @ -12 V
Operating temperature:	0 to 50 $^{\circ}$ C (32 to 140 $^{\circ}$ F)
I/O Connector:	2 x DB-37 F
Interface:	PCI 5V or 3.3V

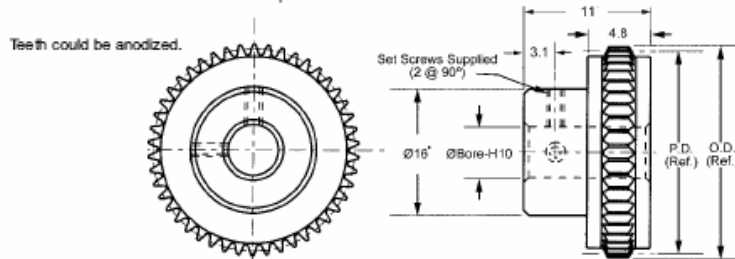
Driver Support

Microsoft Windows
32 and 64 bit C programming
Real Time Toolbox for Matlab
Real-Time Windows Target

Figure A.5 Humansoft MF624 Multifunction I/O card for PCI bus

CIR. PITCH	BORE	STYLE	MATERIAL	BERG'S ® NAME	CHAIN
2.50mm	Ø6	PIN HUB	Aluminum per DIN 3.1355 Anodized	Flex-E-Gear® Chain Drive	Operates with 32GCF Series

* For 18-24 teeth, hub diameter equals 11.9.
Other numbers of teeth available on request.

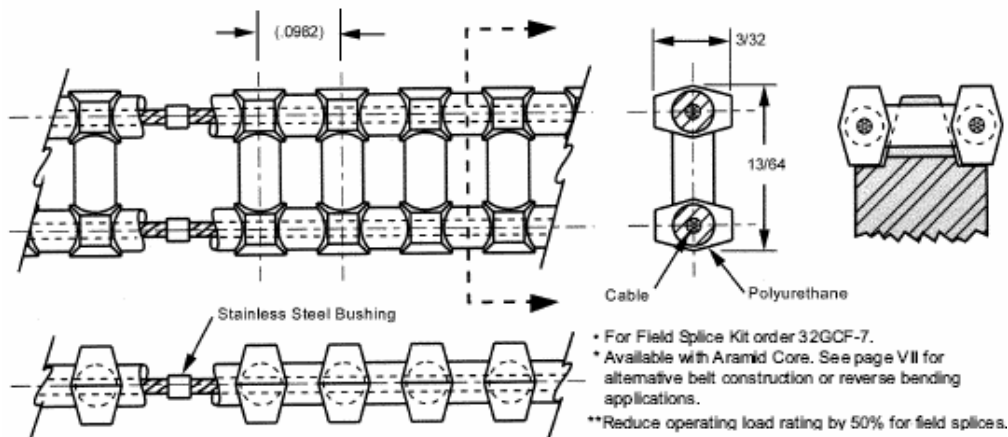


STOCK NO.	NO. OF TEETH	PITCH DIA.	OUTSIDE DIA.
32B106-18	18*	14.29	15.88
32B106-20	20*	15.88	17.47
32B106-22	22*	17.46	19.05
32B106-24	24*	19.05	20.64
32B106-26	26	20.64	22.23
32B106-28	28	22.23	23.82
32B106-30	30	23.81	25.40
32B106-32	32	25.40	26.99
32B106-36	36	28.58	30.17
32B106-40	40	31.75	33.34
32B106-48	48	38.10	39.69
32B106-56	56	44.45	46.04
32B106-64	64	50.80	52.39
32B106-72	72	57.15	58.74
32B106-80	80	63.50	65.09
32B106-88	88	69.85	71.44
32B106-96	96	76.20	77.79
32B106-112	112	88.90	90.49
32B106-128	128	101.60	103.19

WWW.WMBERG.COM

Figure A.6 W.M.Berg Sprocket Gear

PITCH	CIRCULAR PITCH	MATERIALS	BERG'S ® NAME	SPROCKET
32	.0982	Polyurethane (Blue) .018 Dia. Stainless Steel Cable*	Flex-E-Gear®	Operates with 32B, GG33 and GGF33 series.



WWW.WMBERG.COM

Figure A.7 W.M.Berg Polyurethane/Steel Cable Chain

APPENDIX B

HYBRID HAPTIC DEVICE EXPERIMENTAL COMPONENTS

Specifications of electromechanical and mechanical components used in the Hybrid Haptic Device are given in this section.

Parameter	Symbol	Units	BE230D	BE230F	BE231D	BE231F	BE232D	BE232F
Stall Torque Continuous ¹	T_{cs}	lb-in oz-in Nm	3.4 54 0.38	3.3 53 0.37	6.0 96 0.67	5.9 94 0.66	9.9 159 1.11	9.7 155 1.08
Stall Current Continuous ^{1,4,8}	$I_{cs}(\text{sine})$	Amps Peak	3.1	6.1	2.8	5.3	2.8	5.4
Stall Current Continuous ^{1,7}	$I_{cs}(\text{trap})$	Amps DC	2.7	5.3	2.4	4.6	2.4	4.7
Peak Torque ⁶	T_{pk}	lb-in oz-in Nm	10.1 161 1.13	10.0 160 1.12	18.0 289 2.02	17.7 283 1.98	29.7 476 3.33	29.0 464 3.25
Peak Current ^{1,6,8}	$I_{pk}(\text{sine})$	Amps Peak	9.4	18.2	8.2	15.9	8.4	16.3
Peak Current ^{1,7}	$I_{pk}(\text{trap})$	Amps DC	8.1	15.8	7.1	13.8	7.3	14.1
Rated Speed ²	ω_r	rpm	5000	5000	5000	5000	5000	5000
Current @ Rated Speed	$I_r(\text{sine})$	Amps Peak	2.9	5.6	2.5	4.7	2.4	4.7
Current @ Rated Speed	$I_r(\text{trap})$	Amps	2.5	4.8	2.1	4.1	2.1	4.1
Torque @ Rated Speed	T_r	lb-in oz-in Nm	2.9 47 0.33	2.9 47 0.33	5.2 83 0.58	5.1 81 0.57	8.2 131 0.92	8.0 128 0.90
Shaft Power @ Rated Speed	P_o	watts	174	174	307	300	484	473
Voltage Constant ^{3,4}	K_b	Volts/rad/s	0.140	0.072	0.286	0.145	0.461	0.232
Voltage Constant ^{3,4}	K_v	Volts/Krpm	14.66	7.53	29.90	15.18	48.28	24.29
Torque Constant ⁶	$K_t(\text{sine})$	oz-in/Amp Peak Nm/Amp Peak	17.17 0.120	8.82 0.062	35.01 0.245	17.78 0.124	56.53 0.396	28.45 0.199
Torque Constant ^{3,4}	$K_t(\text{trap})$	oz-in/Amp DC Nm/Amp DC	19.82 0.139	10.18 0.071	40.43 0.283	20.53 0.144	65.28 0.457	32.85 0.230
Resistance ⁵	R	Ohms	4.57	1.22	6.97	1.86	7.72	2.05
Inductance ⁵	L	mH	15.43	4.10	32.30	8.65	42.66	11.12
Maximum Bus Voltage	V_m	Volts DC	340	340	340	340	340	340
Thermal Res Wind-Amb	$R_{th} \text{ w-a}$	°C/watt	2.14	2.14	1.82	1.82	1.58	1.58
Motor Constant	K_m	oz-in/vwatt Nm/vwatt	9.27 0.065	9.22 0.065	15.31 0.107	15.05 0.105	23.49 0.164	22.94 0.161
Viscous Damping	B	oz-in/Krpm Nm/Krpm	0.3 1.8E-03	0.3 1.8E-03	0.4 2.5E-03	0.4 2.5E-03	0.5 3.5E-03	0.5 3.5E-03
Static Friction	T_f	oz-in Nm	0.8 5.3E-03	0.8 5.3E-03	1.3 8.8E-03	1.3 8.8E-03	2.0 1.4E-02	2.0 1.4E-02
Motor Thermal Time Constant	τ_{th}	minutes	11.6	11.6	13.3	13.3	15.0	15.0
Electrical Time Constant	τ_{elec}	milliseconds	3.38	3.36	4.63	4.65	5.53	5.42
Mechanical Time Constant	τ_{mech}	milliseconds	1.2	1.2	0.8	0.8	0.6	0.6
Intermittent Torque Duration ¹⁰	T_{int}	seconds	37	37	47	47	58	58
Peak Torque Duration ¹¹	T_{pk}	seconds	15	15	18	18	22	22
Rotor Inertia	J	lb-in-sec ² kg-m ²	4.6E-05 5.2E-06	4.6E-05 5.2E-06	8.0E-05 9.0E-06	8.0E-05 9.0E-06	1.5E-04 1.7E-05	1.5E-04 1.7E-05
Number of Poles	N_p		8	8	8	8	8	8
Motor Weight	#	lbs kg	1.5 0.7	1.5 0.7	2.0 0.9	2.0 0.9	3.1 1.4	3.1 1.4
Winding Class			H	H	H	H	H	H

Figure B.1 Parker BE232FJ brushless DC motor

Power Range	
Peak Current	15 A (10.6 A _{RMS})
Continuous Current	7.5 A (5.3 A _{RMS})
Supply Voltage	100 - 240 VAC



MODES OF OPERATION <ul style="list-style-type: none"> ▪ Current ▪ Position ▪ Velocity ▪ Hall Velocity 	INPUTS/OUTPUTS <ul style="list-style-type: none"> ▪ 3 High Speed Captures ▪ 4 Programmable Analog Inputs (16-bit/12-bit Resolution) ▪ 1 Programmable Analog Output (10-bit Resolution) ▪ 3 Programmable Digital Inputs (Differential) ▪ 7 Programmable Digital Inputs (Single-Ended) ▪ 4 Programmable Digital Outputs (Single-Ended)
COMMAND SOURCE <ul style="list-style-type: none"> ▪ PWM and Direction ▪ Encoder Following ▪ Over the Network ▪ ±10 V Analog 	COMPLIANCES & AGENCY APPROVALS <ul style="list-style-type: none"> ▪ UL ▪ cUL ▪ CE Class A (LVD) ▪ CE Class A (EMC) ▪ RoHS
FEEDBACK SUPPORTED <ul style="list-style-type: none"> ▪ Halls ▪ Incremental Encoder ▪ ±10 VDC Position ▪ Auxiliary Incremental Encoder ▪ Tachometer (±10 VDC) 	

Figure B.2 AMC-DPRANIE-015A400 Brushless DC servo amplifier

Encoder Specifications		
Mechanical	Accuracy	±2 min of arc
	Input power	5 VDC ±5%, 135 mA
Electrical	Operating frequency	250 kHz max
	Output device	26LS31
	Sink/Source, nominal	20 mA
	Suggested user interface	26LS32

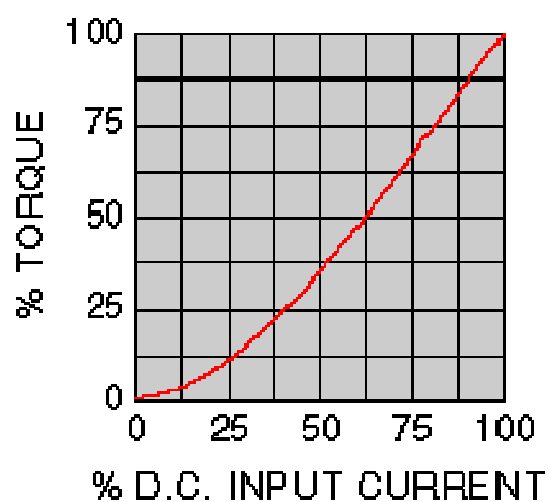
Figure B.3 Parker 2000 ppr incremental encoder



Key Features

- ✓ - 4 x 14-bit analog inputs
- ✓ - 4x 12-bit D/A voltage outputs
- ✓ - 4 quadrature encoder inputs
- ✓ - 16 programmable digital I/O channels
- ✓ - Simultaneous sampling of both analog and encoder sections
- ✓ - 2x 32-bit dedicated counter/timers
- ✓ - 4x 24-bit reconfigurable encoder counter/timers
- ✓ - 2x on-board PWM outputs
- ✓ - 32-bit, 33 MHz PCI bus interface
- ✓ - Supports Quanser real-time control software **QUARC**
- ✓ - Totem Pole digital I/O for high speed
- ✓ - Easy synchronization of multiple Q4 boards

Figure B.4 Quanser Q4 Series Multifunction I/O card for PCI bus



Torque range 3.4 to 170 newton-cm.
 Maximum RPM 2000 RPM
 Maximum heat dissipation 20 watts
 Maximum case temperature 75 degrees C
 Maximum overhung load 11 kg.
 Shaft inertia 3.8×10^{-6} kg-m²
 Response (unforced) 25 mSec.
 Response (forced) 14 mSec.
 Weight 1.1 kg.

Figure B.5 Placid BE15 Particle Magnetic Brake

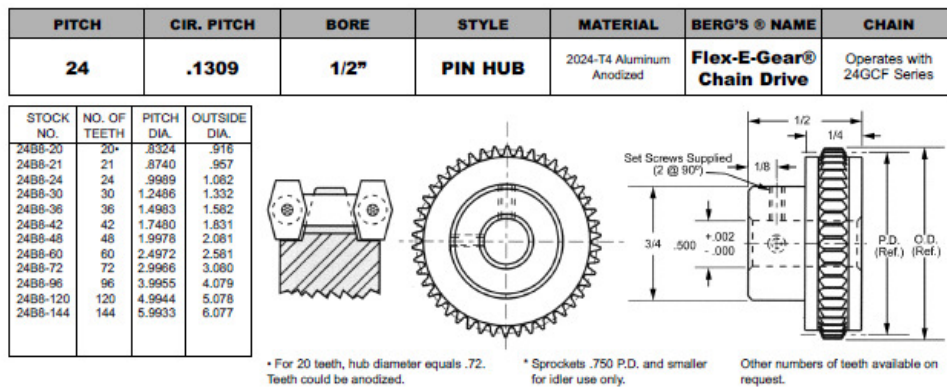


Figure B.6 W.M.Berg Sprocket Gear

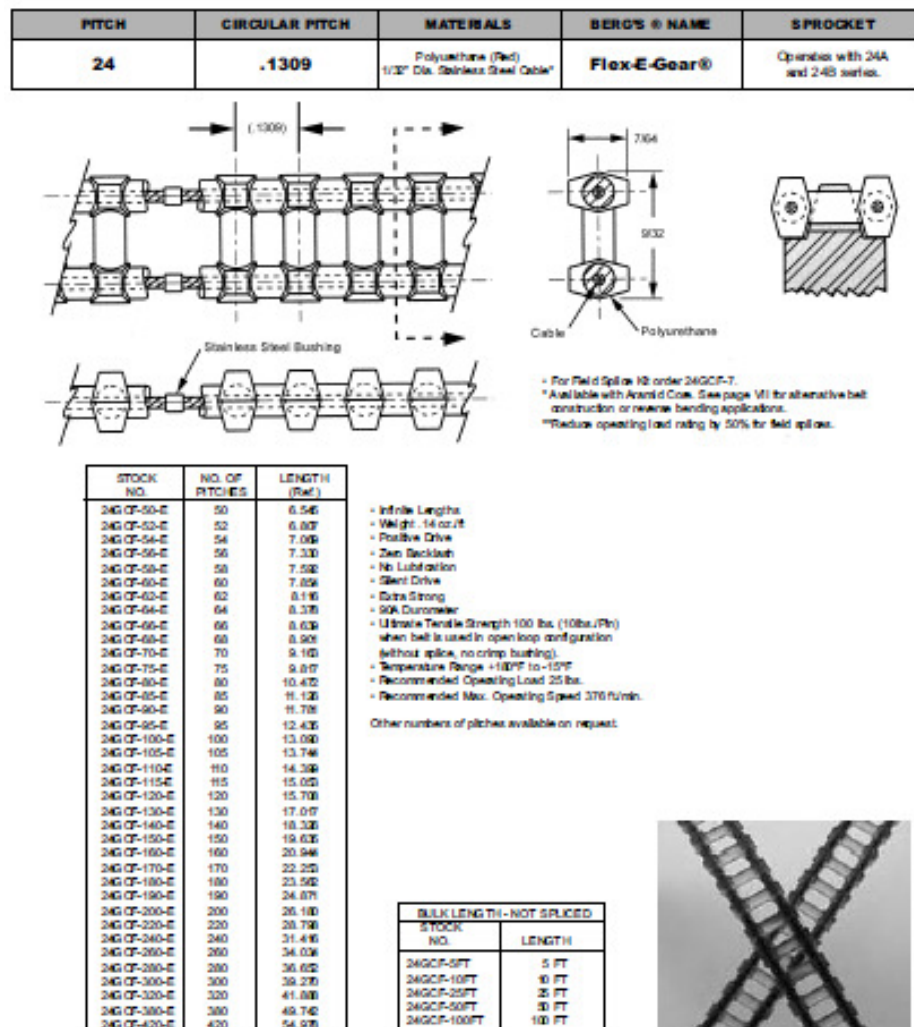


Figure B.7 W.M.Berg Polyurethane/Steel Cable Chain



SPECIFICATIONS:

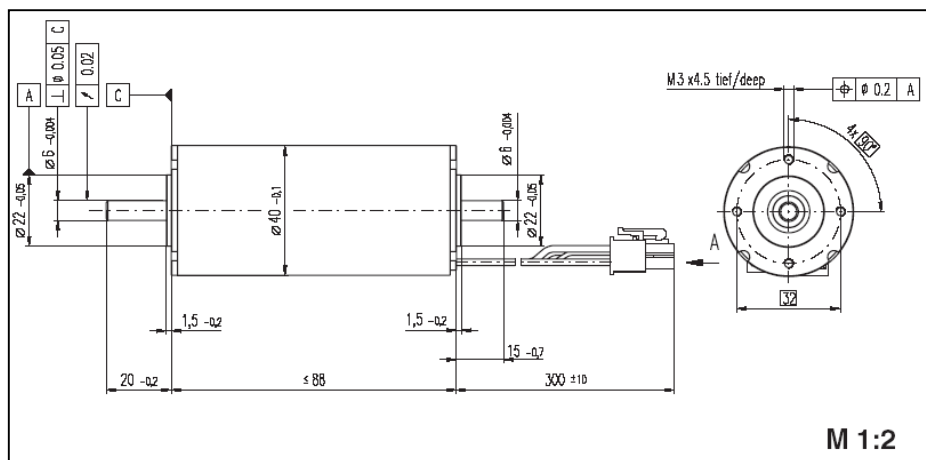
RATED OUTPUT	2 mV/V nom
SAFE OVERLOAD	150% of R.O.
ZERO BALANCE	±1% of R.O.
EXCITATION (VDC OR VAC)	5 to 11
BRIDGE RESISTANCE	350 Ω nom.
NONLINEARITY	±0.2% of R.O.
HYSTERESIS	±0.1% of R.O.
NONREPEATABILITY	±0.2% R.O.
TEMP. SHIFT ZERO	±0.01% of R.O. / °F [±0.02% of R.O. / °C]
TEMP. SHIFT SPAN	±0.01% of Load / °F [±0.02% of Load / °C]
OPERATING TEMP.	14 to 194°F [-10 to +90°C]
COMPENSATED TEMP.	41 to 122°F [+5 to +50°C]
ROTATIONAL SPEED	3000 RPM MAX
CONNECTOR:	6 pin Binder Series #581 (09-0323-99-06)
ACCESSORIES AND RELATED INSTRUMENTS AVAILABLE	
CALIBRATION (STD)	Certificate of Conformance
CALIBRATION (AVAILABLE)	5pt CW and CCW
SHUNT CAL VALUE (INTERNAL)	87K ohm
CALIBRATION TEST EXCITATION	10VDC
SHUNT CALIBRATION	With sensor fully connected jump Pins 1 & 6 to generate 2 mV/V nom output.

Figure B.8 Futek FSH01987 torque transducer with ±10Nm range

APPENDIX C

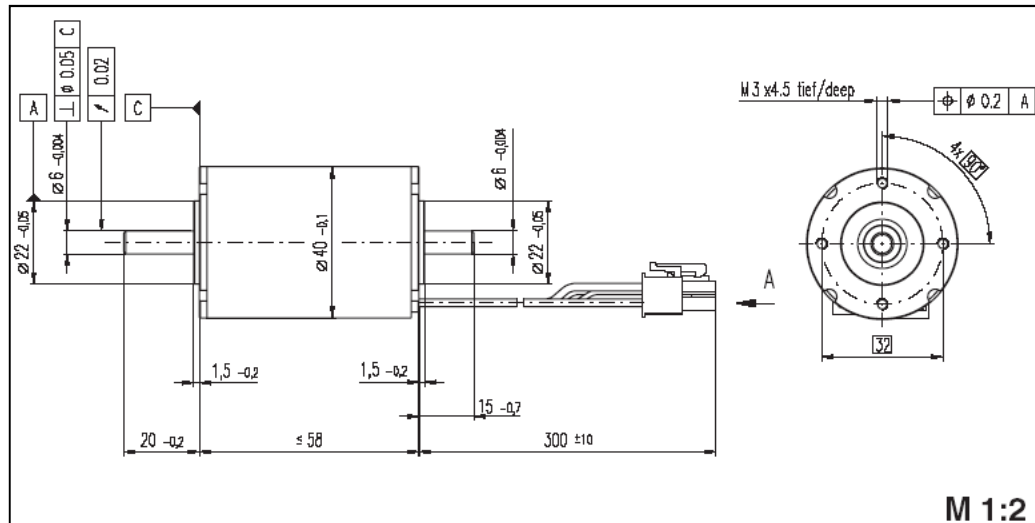
7-DOF HAPTIC DEVICE EXPERIMENTAL COMPONENTS

Specifications of electromechanical and mechanical components used in the 7-DOF Haptic Device are given in this section.



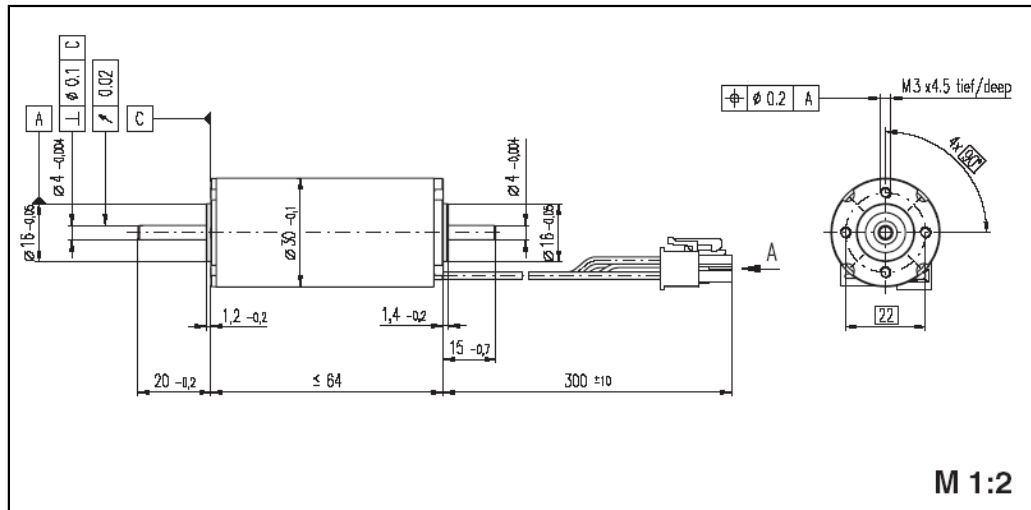
Motor Data (provisional)		
1	Assigned power rating	W 120
2	Nominal voltage	Volt 48.0
3	No load speed ¹⁾	rpm 10000
4	Stall torque ¹⁾	mNm 2190
5	Speed / torque gradient ¹⁾	rpm / mNm 4.61
6	No load current ¹⁾	mA 306
7	Terminal resistance phase to phase	Ohm 0.999
8	Max. permissible speed	rpm 12000
9	Max. continuous current at 5000 rpm ¹⁾	A 4.8
10	Max. continuous torque at 5000 rpm	mNm 186
11	Max. efficiency ¹⁾	% 85
12	Torque constant	mNm / A 45.5
13	Speed constant	rpm / V 210
14	Mechanical time constant	ms 4.9
15	Rotor inertia	gcm ² 101
16	Terminal inductance phase to phase	mH 0.196
17	Thermal resistance housing-ambient	K / W 3.5
18	Thermal resistance winding-housing	K / W 0.29
19	Thermal time constant windings	s 3.8
20	Thermal time constant stator	s 952

Figure C.1 Maxon EC-max 40 Brushless DC Motor -120W



Motor Data (provisional)		
1	Assigned power rating	W 70
2	Nominal voltage	Volt 48.0
3	No load speed ¹⁾	rpm 9080
4	Stall torque ¹⁾	mNm 640
5	Speed / torque gradient ¹⁾	rpm / mNm 14.3
6	No load current ¹⁾	mA 124
7	Terminal resistance phase to phase	Ohm 3.75
8	Max. permissible speed	rpm 12000
9	Max. continuous current at 5000 rpm ¹⁾	A 1.92
10	Max. continuous torque at 5000 rpm	mNm 84.9
11	Max. efficiency ¹⁾	% 82
12	Torque constant	mNm / A 50
13	Speed constant	rpm / V 191
14	Mechanical time constant	ms 7.7
15	Rotor inertia	gcm ² 51
16	Terminal inductance phase to phase	mH 0.468
17	Thermal resistance housing-ambient	K / W 4.6
18	Thermal resistance winding-housing	K / W 0.54
19	Thermal time constant windings	s 4.1
20	Thermal time constant stator	s 917

Figure C.2 Maxon EC-max 40 Brushless DC Motor – 70W



Motor Data (provisional)		
1	Assigned power rating	W 60
2	Nominal voltage	Volt 24.0
3	No load speed ¹⁾	rpm 9740
4	Stall torque ¹⁾	mNm 447
5	Speed / torque gradient ¹⁾	rpm / mNm 22.1
6	No load current ¹⁾	mA 210
7	Terminal resistance phase to phase	Ohm 1.25
8	Max. permissible speed	rpm 15000
9	Max. continuous current at 5000 rpm ¹⁾	A 2.98
10	Max. continuous torque at 5000 rpm	mNm 60.8
11	Max. efficiency ¹⁾	% 80
12	Torque constant	mNm / A 23.3
13	Speed constant	rpm / V 410
14	Mechanical time constant	ms 5.1
15	Rotor inertia	gcm ² 21.9
16	Terminal inductance phase to phase	mH 0.124
17	Thermal resistance housing-ambient	K / W 5.9
18	Thermal resistance winding-housing	K / W 0.55
19	Thermal time constant windings	s 2.8
20	Thermal time constant stator	s 669

Figure C.3 Maxon EC-max 30 Brushless DC Motor - 60

Series 1524 ... SR								
	1524 T	003 SR	006 SR	009 SR	012 SR	018 SR	024 SR	
1 Nominal voltage	U _N	3	6	9	12	18	24	V
2 Terminal resistance	R	1,1	5,1	10,4	19,8	44	79,6	Ω
3 Output power	P _{out max}	1,92	1,7	1,88	1,75	1,78	1,75	W
4 Efficiency, max.	η _{max}	77	77	77	76	77	78	%
5 No-load speed	n ₀	10 800	9 700	10 100	9 900	9 900	9 900	rpm
6 No-load current (with shaft ø 1,5 mm)	I ₀	0,047	0,021	0,014	0,011	0,007	0,005	A
7 Stall torque	M _{st}	6,8	6,68	7,12	6,76	6,86	6,75	mNm
8 Friction torque	M _f	0,12	0,12	0,12	0,13	0,12	0,11	mNm
9 Speed constant	k _v	3 660	1 650	1 140	840	560	419	rpm/V
10 Back-EMF constant	k _e	0,273	0,607	0,877	1,19	1,79	2,38	mV/rpm
11 Torque constant	k _M	2,61	5,8	8,37	11,4	17,1	22,8	mNm/A
12 Current constant	k _i	0,384	0,172	0,119	0,088	0,059	0,044	A/mNm
13 Slope of n-M curve	Δn/ΔM	1 590	1 450	1 420	1 460	1 440	1 470	rpm/mNm
14 Rotor inductance	L	17	70	150	250	560	1 000	μH
15 Mechanical time constant	τ _m	10	10	10	10	10	10	ms
16 Rotor inertia	J	0,6	0,66	0,67	0,65	0,66	0,65	gcm ²
17 Angular acceleration	α _{max}	110	100	110	100	100	100	10 ⁴ rad/s ²
18 Thermal resistance	R _{th1} / R _{th2}	4,5 / 31						K/W
19 Thermal time constant	τ _{th1} / τ _{th2}	2,4 / 300						s
20 Operating temperature range:								
– motor		-30 ... +85 (optional version -55 ... +125)						°C
– rotor, max. permissible		+125						°C
21 Shaft bearings		sintered bearings (standard)		ball bearings (optional version)		ball bearings, preloaded (optional version)		
22 Shaft load max.:								
– with shaft diameter		1,5		1,5		1,5		mm
– radial at 3 000 rpm (3 mm from bearing)		1,2		5		5		N
– axial at 3 000 rpm		0,2		0,5		0,5		N
– axial at standstill		20		10		10		N
23 Shaft play								
– radial	r _r	0,03		0,015		0,015		mm
– axial	r _a	0,2		0,2		0		mm
24 Housing material		steel, black coated						
25 Weight		21						g
26 Direction of rotation		clockwise, viewed from the front face						
Recommended values – mathematically independent of each other								
27 Speed up to	n _{0 max}	10 000	10 000	10 000	10 000	10 000	10 000	rpm
28 Torque up to	M _{0 max}	2,5	2,5	2,5	2,5	2,5	2,5	mNm

Orientation with respect to motor terminals not defined

Side view dimensions: 6x M1,6 1,4 deep, ø10, 23,8, 0,75, 2,1, 6±0,3, 8,1±0,3, ø15⁰_{-0,052}, ø13, ø6⁰_{-0,05}, ø1,5^{-0,004}_{-0,009}, ø3,5, ø2,38⁰_{-0,04}, 1,1, 2,1, 4,3±0,3.

Front view dimensions: 10,6, 4,2±0,5, 2, 10±0,3, 1,4 deep, 6x ø0,07, 3,04, DIN 58400 m=0,2 z=9 R=0,25.

1524 T ... SR

1524 E ... SR

Figure C.4 Faulhaber 1524012SR Coreless DC Motor



Operating modes	
	Speed controller, current controller
Electrical Data	
Operating voltage V_{CC}	12 - 50 VDC
Max. output voltage	$0.9 \times V_{CC}$
Max. output current I_{max}	15 A
Continuous output current I_{cont}	5 A
Switching frequency of power stage	50 kHz
Max. efficiency	92 %
Band width current controller	1 kHz
Max. speed (1 pole pair)	25 000 rpm
Built-in motor choke per phase	160 μ H / 5 A
Input	
Set value configurable (1024 Steps)	-10...+10 W0...+5 V
"Enable"	+2.4...50 V
Digital 1 (Switch "Monitor n" / "Monitor I")	+2.4...50 V
Digital 2 (Switch speed- / current controller)	+2.4...50 V
STOP	+2.4...50 V
Encoder signals	A, A', B, B', I, I' max. 1 MHz 3-channel encoder is required
Hall sensor signals	H1, H2, H3
Output	
Monitor configurable	-10...+10 W0...+5 V
Status reading "Ready"	Open Collector, max. 30 V ($I_L < 20$ mA)
Voltage outputs	
Encoder supply voltage	+5 VDC, max. 100 mA
Hall sensors supply voltage	+5 VDC, max. 50 mA
Auxiliary voltage	
Interface	
RS232	RxD; TxD (max. 115 200 bit/s)
CAN	high; low (max. 1 Mbit/s)
Trim potentiometer	n_{max} , Offset, I_{max} , gain
Indicator	Bi-colour LED, green = READY, red = ERROR
Ambient temperature and humidity range	
Operation	-10...+45°C
Storage	-40...+85°C
No condensation	20...80%
Mechanical Data	
Weight	Approx. 430 g
Dimensions (L x W x H)	180 x 103 x 26 mm (see page 308)
Mounting threads	Flange for M4-screws
Connections	See page 308

Figure C.5 DES 50/5 4-Q-EC-Servoamplifier



Operating modes	
	ixR compensation, voltage control, encoder speed control, DC tach speed control, current control
Electrical Data	
Operating voltage V_{CC}	12 - 30 VDC
Max. output voltage	$V_{CC} - 5\text{ V}$
Max. output current I_{out}	2 A
Continuous output current I_{out}	2 A
Switching frequency of power stage	
Max. efficiency	
Built-in motor choke	
Input	
Set value	Configurable, -10 ... +10 V, -3.9 ... +3.9 V
Enable	«Disable» Disable min. $V_{CC} - 1\text{ V}$, Enable max. GND + 1 V
DC tach	min. 2 VDC, max. 50 VDC
Encoder signals	Channel A and channel B, max. 100 kHz, TTL
Output	
Status reading «Ready»	Open Collector, max. 30 VDC ($I_L < 20\text{ mA}$)
Monitor current «Monitor I»	
Monitor speed «Monitor n»	
Voltage outputs	
Auxiliary voltages	+3.9 VDC, -3.9 VDC, max. 2 mA
Encoder supply voltage	+5 VDC, max. 80 mA
Trim potentiometer	ixR compensation, Offset, n_{out} , I_{out} , gain
Protective functions	Protected against thermal overload
Indicator	Green LED = READY, red LED = ERROR

Figure C.6 LSC 4-Q-DC-Servoamplifier



NANO17

Product Advantages

One of the Smallest 6-axis Sensors in the World:
The Nano17 fits into restricted spaces of research applications.

Extremely High Strength:

- EDM wire-cut from high yield-strength stainless steel.
- Maximum allowable single-axis overload values are 4.4 to 19.5 times rated capacities.

High Signal-to-Noise Ratio: Silicon strain gauges provide a signal 75 times stronger than conventional foil gauges. This signal is amplified, resulting in near-zero noise distortion.

Typical Applications

- Dental research
- Robotic surgery
- Robotic hand research
- Finger-force research



The Nano17 F/T transducer

The transducer is made of hardened stainless steel, with integral interface plates made from high-strength aircraft aluminum.

English Calibrations	SENSING RANGES	Calibrations					
	Axes	US-3-1		US-6-2		US-12-4	
	Fx, Fy (\pm lbf)	3		6		12	
	Fz (\pm lbf)	4.25		8.5		17	
	Tx, Ty (\pm lbf-in)	1		2		4	
	Tz (\pm lbf-in)	1		2		4	
	RESOLUTION	System Type*					
	Axes	CON	DAQ	CON	DAQ	CON	DAQ
	Fx, Fy (lbf)	1/640	1/5120	1/320	1/2560	1/160	1/1280
	Fz (lbf)	1/640	1/5120	1/320	1/2560	1/160	1/1280
Tx, Ty (lbf-in)	1/4000	1/32000	1/2000	1/16000	1/1000	1/8000	
Tz (lbf-in)	1/4000	1/32000	1/2000	1/16000	1/1000	1/8000	

Metric Calibrations	SENSING RANGES	Calibrations					
	Axes	SI-12-0.12		SI-25-0.25		SI-50-0.5	
	Fx, Fy (\pm N)	12		25		50	
	Fz (\pm N)	17		35		70	
	Tx, Ty (\pm Nmm)	120		250		500	
	Tz (\pm Nmm)	120		250		500	
	RESOLUTION	System Type*					
	Axes	CON	DAQ	CON	DAQ	CON	DAQ
	Fx, Fy (N)	1/160	1/1280	1/80	1/640	1/40	1/320
	Fz (N)	1/160	1/1280	1/80	1/640	1/40	1/320
Tx, Ty (Nmm)	1/32	1/256	1/16	1/128	1/8	1/64	
Tz (Nmm)	1/32	1/256	1/16	1/128	1/8	1/64	

Contact ATI for complete loading information. Resolutions are typical. All Sensors calibrated by ATI. *CON: Controller F/T System, DAQ: 16-bit DAQ F/T System

Figure C.7 SI-50-0.5 Nano 17 6-DOF Force/Torque Transducer



Specifications

Analog Input

Channels:	8 single-ended channels
A/D converter:	14-bit, simultaneous sampling
Conversion time:	1.6 μ s 1 channel, 1.9 μ s 2 channels, 2.5 μ s 4 channels, 3.7 μ s 8 channels
Input range:	± 10 V,
Input Impedance:	$10^{10} \Omega$
Trigger mode:	software, timer, external

Analog Output

Channels:	8 channels, 14-bit
Output Range:	± 10 V
Output current:	10 mA max.
Settling time:	31 μ s FS change to $\pm 1/2$ LSB.

Digital I/O

Input lines:	8, TTL compatible
Output lines:	8, TTL compatible

Timer/Counter

Number of channels:	4
Resolution:	32 bit, 20 ns
Modes:	PWM, counter, pulse generation

Encoder Inputs

Input channels:	4, single ended or differential
Inputs:	A, B, Index
Input frequency:	max 2.5 MHz
Resolution:	32-bit

General

Power consumption:	500 mA @ +5 V 150 mA @ +12 V 150 mA @ -12 V
Operating temperature:	0 to 50 °C (32 to 140 °F)
I/O Connector:	2 x DB-37 F
Interface:	PCI 5V or 3.3V

Driver Support

Microsoft Windows
32 and 64 bit C programming
Real Time Toolbox for Matlab
Real-Time Windows Target

Figure C.8 Humansoft MF624 Multifunction I/O card for PCI bus

Series 5500, 5540

		HEDS 5500	HEDS 5540	HEDM 5500	
Lines per revolution	N	100 - 500	100 - 500	1 000 - 1 024	channels
Signal output, square wave		2	2+1 Index	2	V DC
Supply voltage	V _{CC}	4,5 ... 5,5			mA
Current consumption, typical (V _{CC} = 5 V DC)	I _{CC}	17	57	57	°e
Pulse width	P	180 ± 45	180 ± 35	180 ± 45	°e
Phase shift, channel A to B	Φ	90 ± 20	90 ± 15	90 ± 15	°e
Logic state width	S	90 ± 45	90 ± 35	90 ± 45	°e
Cycle	C	360 ± 5,5	360 ± 5,5	360 ± 7,5	°e
Signal rise/fall time, typical	tr/tf	0,25 / 0,25			μs
Frequency range ¹⁾	f	up to 100	up to 100 ²⁾	up to 100	kHz
Inertia of code disc	J	0,6			gcm ²
Operating temperature range		- 40 ... + 100		- 40 ... + 70	°C

¹⁾ Velocity (rpm) = f (Hz) x 60/N
²⁾ HEDS 5540 requires pull-up resistors of 2,7 kΩ between pins 2, 3, 5 and 4 (V_{CC})

Ordering Information

Encoder type	number of channels	lines per revolution	For combination with:
HEDS 5500 C	2	100	DC-Micromotors and DC-Motor-Tachos Series 2230, 2233, 2251 2342 2642, 2657 3242, 3257, 3557, 3863
HEDS 5500 A	2	500	
HEDS 5540 C	2+1	100	
HEDS 5540 A	2+1	500	
HEDM 5500 B	2	1 000	
HEDM 5500 J	2	1 024	
			brushless DC-Servomotors Series 2036, 2444, 3056, 3564

Interlocking connector options: extension cables 300 mm length, on request.

Figure C.9 Maxon HEDS 5540 Encoder

Series IE2 – 512

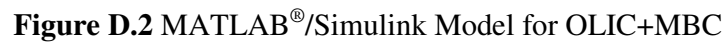
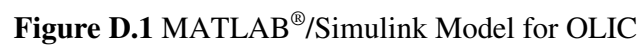
		IE2 – 64	IE2 – 128	IE2 – 256	IE2 – 512	
Lines per revolution	N	64	128	256	512	channels
Signal output, square wave		2				V DC
Supply voltage	V _{DD}	4,5 ... 5,5				mA
Current consumption, typical (V _{DD} = 5 V DC)	I _{DD}	typ. 6, max. 12				°e
Output current, max. ¹⁾	I _{OUT}	5				°e
Pulse width	P	180 ± 45				°e
Phase shift, channel A to B	Φ	90 ± 45				°e
Signal rise/fall time, max. (C _{LOAD} = 50 pF)	tr/tf	0,1 / 0,1				μs
Frequency range ²⁾ , up to	f	20	40	80	160	kHz
Inertia of code disc	J	0,09				gcm ²
Operating temperature range		- 25 ... + 85				°C

¹⁾ V_{DD} = 5 V DC: Low logic level < 0,5 V, high logic level > 4,5 V: CMOS and TTL compatible

²⁾ Velocity (rpm) = f (Hz) x 60/N

Figure C.10 Faulhaber IE 512 Encoder

TULIK MODELS USED IN THE EXPERIMENTS



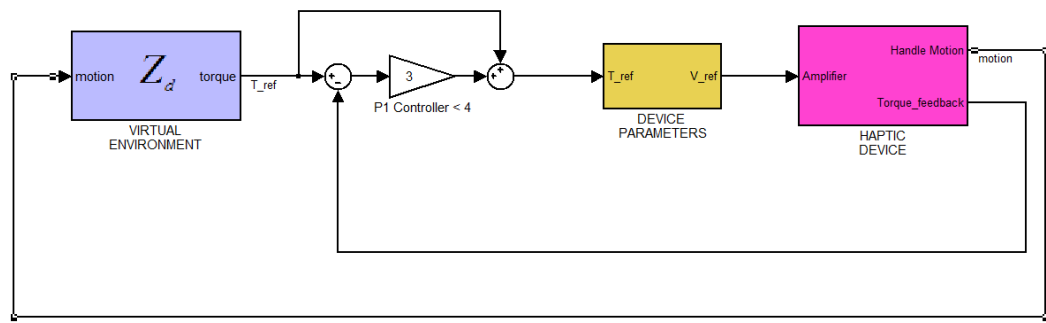


Figure D.3 MATLAB®/Simulink Model for CLIC

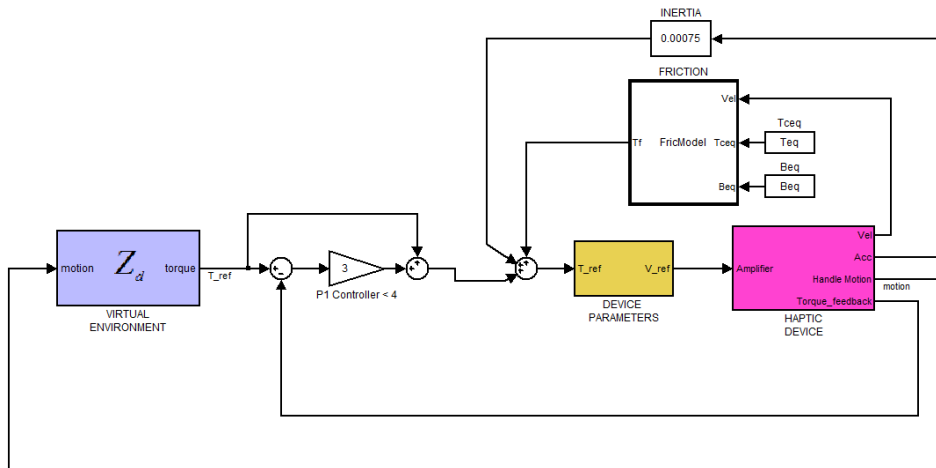


Figure D.4 MATLAB®/Simulink Model for CLIC+MBC

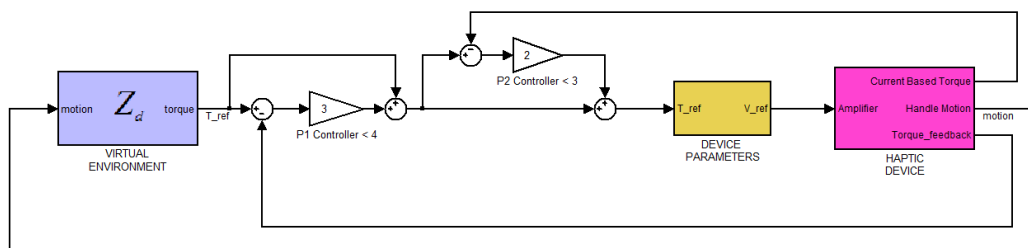


Figure D.5 MATLAB®/Simulink Model for CLIC+MCBC

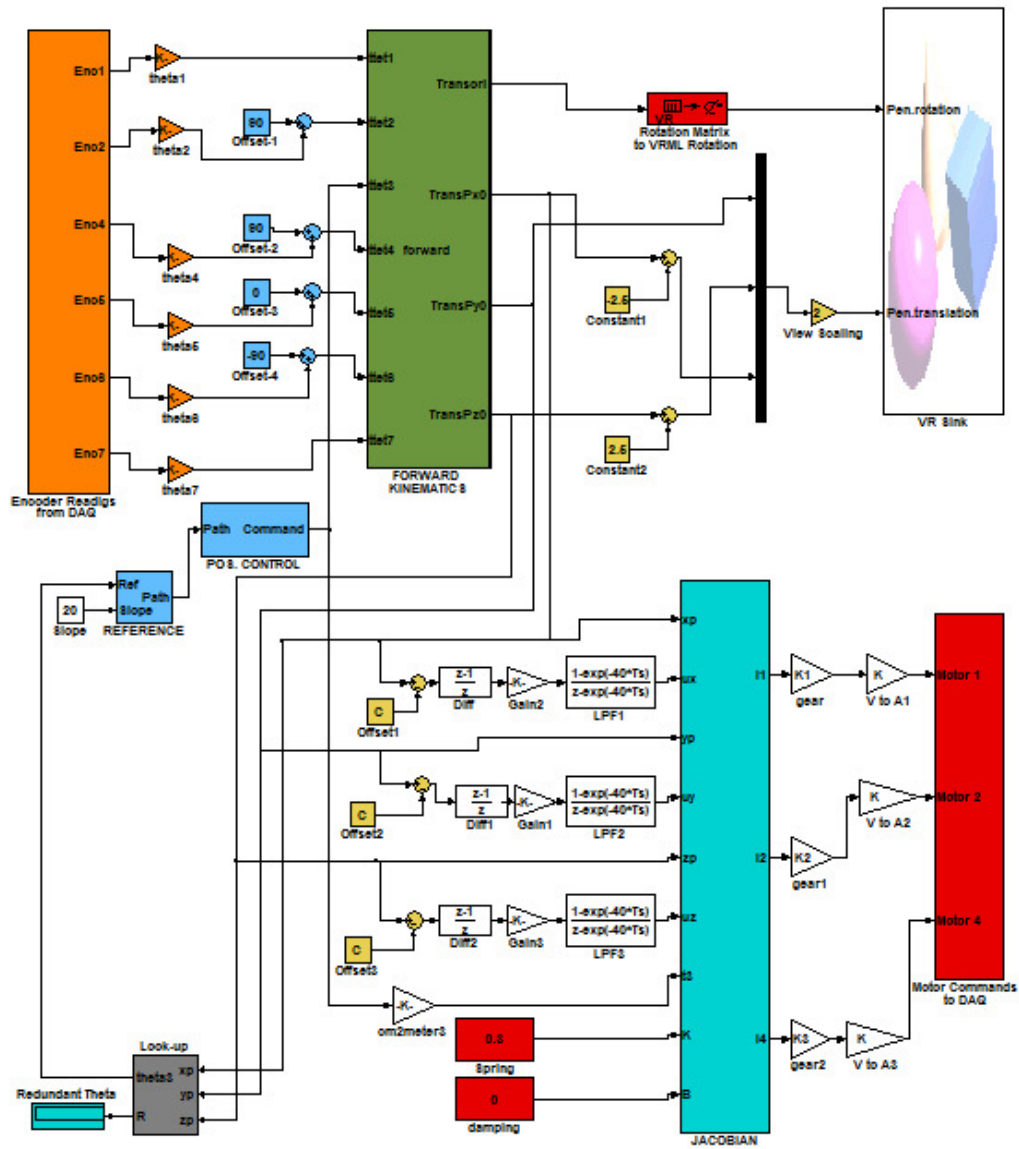


Figure D.11 MATLAB®/Simulink Model for Optimal Posture Control of 7-DOF Haptic Device

APPENDIX E

MATLAB M-FILES USED IN THE CALIBRATION EXPERIMENTS

```
function OB_CL(CLm,theta)

%Calibration Main Function that executes the overall calibration files
%OB_CL(CLm,theta), opt_CL(dh,CLm,theta,n) forward_CL(theta,alpha,a,d)
%CLm : Cable encoder measurements and heta : Encoder measurements

n =200; % Measurement number

%D-H parameters - nominal values
alpha = [-pi/2, -pi/2, pi/2, -pi/2, pi/2, -pi/2, pi/2, 0];
a = [-0.2107, 0, 0, 0, 0, 0, 0, 0.0259];
d = [0, 0.371, 0, 0.245, 0, 0.250, 0, 0.0322];

%D-H parameters - initial values
alpha0=[-pi/2, pi/2, -pi/2, pi/2, -pi/2, pi/2];
a0= [-0.2107, 0, 0, 0, 0, 0, 0, 0.0259];
d0=[0.371, 0, 0.245, 0, 0.250, 0, 0.0322];
tet0=[0, 0, 0, 0, 0, 0];

%Optimization
options = ptimset('MaxFunEvals',1e10,'LevenbergMarquardt','on','TolX',1e-
10,'TolFun',1e-10,'MaxIter',200,'Display','iter');

%Optimization parameter limit values
alpha00=[0.1, 0.1, 0.1, 0.1, 0.1, 0.1];
a00= [0.01, 0.01, 0.01, 0.01, 0.01, 0.01, 0.01, 0.01];
d00=[0.01, 0.01, 0.01, 0.01, 0.01, 0.01, 0.01, 0.01];
tet00=[0.1, 0.1, 0.1, 0.1, 0.1, 0.1];
tol=[alpha00 a00 d00 tet00];

x0 = [alpha0 a0 d0 tet0];

%Optimization parameter bounds
lb = x0 - tol;
ub = x0 + tol;

[DHp]=lsqnonlin(@(dh) opt_CL(dh,CLm,theta,n),x0,lb,ub,options);

o_alpha=[-pi/2,DHp(1),DHp(2),DHp(3),DHp(4),DHp(5),DHp(6),0];
o_a = [DHp(7),DHp(8),DHp(9),DHp(10),DHp(11),DHp(12),DHp(13),DHp(14)];
o_d = [0,DHp(15),DHp(16),DHp(17),DHp(18),DHp(19),DHp(20),DHp(21)];
o_tet = [0,DHp(22),DHp(23),DHp(24),DHp(25),DHp(26),DHp(27),DHp(28)];

%Displaying the Results
display(' ');
display('DH variations found after optimizaiton');
display(' ');

display(sprintf('o_alpha = [ %f %f %f %f %f %f %f %f]',o_alpha(1)-
alpha(1),o_alpha(2)-alpha(2),o_alpha(3)-alpha(3),o_alpha(4)-
alpha(4),o_alpha(5)-alpha(5),o_alpha(6)-alpha(6),o_alpha(7)-
alpha(7),o_alpha(8)-alpha(8)));
```

```

display(sprintf('o_a = [ %f %f %f %f %f %f %f %f]',o_a(1)-a(1),o_a(2)-
a(2),o_a(3)-a(3),o_a(4)-a(4),o_a(5)-a(5),o_a(6)-a(6),o_a(7)-a(7),o_a(8)-
a(8)));

display(sprintf('o_d = [ %f %f %f %f %f %f %f %f]',o_d(1)-d(1),o_d(2)-
d(2),o_d(3)-d(3),o_d(4)-d(4),o_d(5)-d(5),o_d(6)-d(6),o_d(7)-d(7),o_d(8)-
d(8)));
display(sprintf('o_tet = [ %f %f %f %f %f %f %f %f]',o_tet(1), o_tet(2),
o_tet(3), o_tet(4), o_tet(5), o_tet(6), o_tet(7), o_tet(8)));
function error = opt_CL(dh,CLm,theta,n)

% Optimization function that uses only cable encoder measurements

o_alpha = [-pi/2, dh(1), dh(2), dh(3), dh(4), dh(5), dh(6), 0];
o_a = [dh(7), dh(8), dh(9), dh(10), dh(11), dh(12), dh(13), dh(14)];
o_d = [0, dh(15), dh(16), dh(17), dh(18), dh(19), dh(20), dh(21)];
o_tet = [ 0, dh(22), dh(23), dh(24), dh(25),dh(26), dh(27), dh(28)];

for i = 1 : 1 : n
o_theta(i,:)=theta(i,:)+o_tet;
end

for i = 1 : 1 : n
CL(i,:) = forward_CL(o_theta(i,:),o_alpha,o_a,o_d);%o_cable);
end

%Objective function
i = 1 : n;
error(i,:)= CL(i,:)-CLm(i,:);

```

```

function [CL] = forward_CL(theta,alpha,a,d)%cable)

%FORWARD Calculates forward kinematics of the 7DOF Haptic device

% This function takes joint angles from the vector theta and the DH
% parameters from alpha, a and d and
% returns the position of the end effector.

% OFFSET

offset=[0, 0, pi/2, 0, pi/2, 0, -pi/2, 0];

theta=theta+offset;

% Preallocate the matrix A
A = zeros(4,4,8);

% For all seven joints, calculate the matrix A
for i = 1 : 1 : 8

T = [1 0 0 a(i);0 1 0 0;0 0 1 d(i);0 0 0 1];
Rx = [1 0 0 0;0 cos(alpha(i)) -sin(alpha(i)) 0; 0 sin(alpha(i))
cos(alpha(i)) 0;0 0 0 1];
Rz = [cos(theta(i)) -sin(theta(i)) 0 0;sin(theta(i)) cos(theta(i)) 0 0;0
0 1 0;0 0 0 1];
A(:,:,i) = Rz * T * Rx;

end

% Calculate the Transformation
Trans = A(:,:,1) * A(:,:,2) * A(:,:,3) * A(:,:,4) * A(:,:,5) *
A(:,:,6)*A(:,:,7)*A(:,:,8);

```

CIRRICULUM VITAE

PERSONEL INFORMATION:

Name : Özgür Başer
Place of Birth : Aydın
Adress : Middle East Technical University,
Mechanical Engineering Department,
D-102, 06800, Ankara.
GSM : [+90] (505) 671 03 08
e-mail : ozgrbasr@gmail.com

EDUCATION:

2006 –2012 : Ph.D. Programme at METU
CPGA: 3.67/4
2003 – 2006 : M.Sc. Programme at METU
CPGA: 3.07/4
1997 – 2001 : B.Sc. Programme at KTU
CPGA: 3.30/4 (Honor Student)
1994 – 1997 : High School Degree from Nazilli Mehmet Akif Ersoy Lisesi,
Aydın

LANGUAGES:

Turkish (native), English

WORK EXPERIENCE:

2003 –2012 : Teaching Assistant at ME Department, METU, Ankara.

COMPUTER SKILLS:

Autodesk\ AutoCAD	: Medium
ProEngineer	: Medium
SolidWorks	: Professional
KeyCreator	: Professional
MATLAB	: Professional
VBasic	: Medium

INTERNATIONAL JOURNAL PAPERS:

- **O. Baser**, E.I. Konukseven, *Theoretical and Experimental Determination of Capstan Drive Slip Error*. Mechanism and Machine Theory, 45(6), 815-827, 2010.
- **O. Baser**, E.I. Konukseven, *Utilization of Motor Current based Torque Feedback to Improve the Transparency of Haptic Interfaces*. Mechanism and Machine Theory, Vol. 52, pp. 78-93, 2012.
- **O. Baser**, E.I. Konukseven, *Kinematic Model Calibration of a 7-DOF Capstan Driven Haptic Device for Pose and Force Control Accuracy Improvement*. Proceedings of the Institution of Mechanical Engineers, Part C: Journal of Mechanical Engineering Science, 0(0), 1-13, 2012.
- **O. Baser**, H. Gurocak, E.I. Konukseven *Hybrid Control Algorithm to Improve Both Stable Impedance Range and Transparency in Haptic Devices*. Mechatronics, (Accepted, 2012)
- **O. Baser**, E.I. Konukseven, *7 DOF Haptic Device and Interface Design*, Turkish Journal of Electrical Engineering and Computer Sciences, (Accepted, In Press, 2012)
- **O. Baser**, E.I. Konukseven, *Kinematic Calibration of PHANTOM Premium 1.5/6DOF Haptic Device*, Key Engineering Materials Vol. 486, 2011.

TURKISH JOURNAL PAPERS:

- **O. Baser**, E.I. Konukseven, “Dokunsak Kuvvet Geri Beslemeli Cihaz Tasarımı”, Makina Tasarım ve İmalat Dergisi, Cilt 7, Sayı 2, s.68-78, Kasım 2005

INTERNATIONAL CONFERENCE PAPERS:

- **O. Baser**, E.I. Konukseven, *7 DOF Haptic Device Design*, Eurohaptics 2006 Conference, Paris, France, pp 507-512, July 3-6, 2006.
- **O. Baser**, E.I. Konukseven, T. Balkan, *Optimal Posture Control for a 7 DOF Haptic Device Based on Power Minimization*, Eurohaptics 2008 Conference, Madrid, Spain, pp.555-661, June 10-13, 2008.
- **O. Baser**, E. Kilic, E.I. Konukseven, M. Dolen, *A Hybrid Technique to Estimate Velocity and Acceleration Using Low-Resolution Optical Incremental Encoders*. IEEE International Conference on Signal and Electronic Systems, Gliwice, Poland, 2010.
- E. Kilic, **O. Baser**, M. Dolen and E.I. Konukseven, *Enhanced Adaptive Windowing Technique for Velocity and Acceleration Estimation Using Incremental Position Encoders*. IEEE International Conference on Signal and Electronic Systems, Gliwice, Poland, 2010.
- **O. Baser**, E.I. Konukseven, *Kinematic Calibration of a 7-DOF Haptic Device*. IEEE 15th International Conference on Advanced Robotics (ICAR), Tallinn, Estonia, June 2011.
- **O. Baser**, E.I. Konukseven, H. Gurocak, *Stability and Transparency Improvement in Haptic Devices Employing both MR-Brake and Active Actuator*. IEEE 21st International Symposium on Robot and Human Interactive Communication, Paris, France, September 2012.

AWARDS

- **Awarded 1st Place**, Suleyman Demirel University, ISPARTEK 2012, Technological Machines, Devices and Materials, Project Title: 7-DOF haptic device and optimal posture control interface design.
- **Awarded 1st Place**, TMMOB Chamber of Mechanical Engineers, I. Necdet Eraslan Project Competition 2005, Science and Technology in Robotics-I, Project Title : Haptic touch sense and force feedback interface system design.
- **Awarded 2nd Place**, IZOCAM, Intercollegiate Heat Isolation Competition 2001.